

Development of advanced energy harvesters: Theoretical and experimental studies

by

Mohammad Khorsand

*Thesis
Submitted to Flinders University
for the degree of*

Doctor of Philosophy
College of Science and Engineering
December 2020

Declaration

I certify that this thesis does not incorporate without acknowledgement any material previously submitted for a degree or diploma in any university; and that to the best of my knowledge and belief it does not contain any material previously published or written by another person except where due reference is made in the text.

Mohammad Khorsand

18/09/2020

Parts of this thesis have been published in the following journal articles

- [1] Artificial intelligence enhanced mathematical modeling on rotary triboelectric nanogenerators under various kinematic and geometric conditions, *Nano energy*, 75 (2020) 104993.
- [2] Simulation of high-output and lightweight sliding-mode triboelectric nanogenerators, *Nano energy*, 66 (2019) 104115.
- [3] Thermal analysis and electro-elastic response of multilayered spherical vessels, *International Journal of Pressure Vessels and Piping*, 171 (2019) 194-206.
- [4] Durable pyroelectric shell structures for energy scavenging applications, *Acta Mechanica*, 231 (2020) 205-220.

Acknowledgements

I would like to acknowledge my supervisor, Professor Youhong Tang, for the patient advice, continuous encouragement, and guidance he generously offered to me during my PhD journey. From the very beginning, he was drawing a nice plan for my PhD study. He provided all required software and hardware resources and arranged weekly meeting discussion to meet all challenges throughout my time as his student. I would like to thank all the technical staff from Flinders Microscopy and Microanalysis (FMMA), Institute for NanoScale Science and Technology, and Engineering Service Team of College of Science and Engineering, Flinders University for their supports.

I would like to express my gratitude to Dr Javad Tavakoli, Mr Kudzai Kamanya, and Mr Haowen Guan for their unwavering support, energy and for all kind of technical and non-technical discussions. This achievement would have not been possible without them.

I heartily thank my parents for all great support through my life. I sincerely gratitude my wife for supporting me during my studies and always believing in me. Without them, I could never have reached this level of success in my studies.

Contents

Introduction.....	1
1.1 Motivation.....	1
1.2 Mechanical energy harvesting strategies	2
1.3 Organization of thesis	3
Energy harvesting mechanisms	5
2.1 Background.....	5
2.2 Energy Harvesting Strategies	5
2.2.1 Piezoelectric Energy Harvesters.....	5
2.2.1.1 Cantilever beam energy harvester	7
2.2.1.2 Wearable energy harvester	8
2.2.1.3 Nanowire energy harvester	10
2.2.1.4 Biomedical energy harvesters.....	12
2.2.2 Electromagnetic Energy Harvesters.....	15
2.2.3 Electrostatic Energy Harvesters	19
2.2.4 Triboelectric Energy Harvesting	23
2.2.4.1 Sliding-mode TENGs	27
2.2.4.2 Contact-Separation TENGs	28
2.3 Possible Applications of TENGs	29
2.3.1 Biomechanical Energy Harvesters	30
2.3.2 Wind Based Energy Harvesters	33
2.3.3 Water Based Energy Harvesters.....	36
2.3.4 Wearable Energy Harvesters.....	39
2.3.5 Self-powered Sensors	41
2.4 Optimization techniques	48

2.4.1 Iterative methods.....	49
2.4.2 Heuristics	49
2.4.2.1 Differential evolution	49
2.4.2.2 Artificial bee colony	50
2.4.2.3 Genetic algorithm	50
2.4.2.4 Particle swarm optimization.....	51
2.4.2.5 Grey wolf method.....	51
2.5 Significance of the research.....	52
Piezoelectric energy harvesters.....	55
3.1 Introduction.....	55
3.2 FGMs	55
3.3 Spherical piezoelectric smart shells.....	56
3.3.1 Piezoelectric layers	57
3.3.2 Host layer.....	59
3.3.3 Heat conduction analysis	60
3.3.4 Interface interactions and boundary bonds	60
3.3.5 Solution methodology.....	61
3.3.5.1 Differential quadrature	62
3.3.5.2 Choices of sampling grid points.....	64
3.3.6 Numerical results and discussion.....	65
3.3.6.1 Evaluation.....	65
3.3.6.2 FG host layer laminated with sensor layer	68
3.3.6.3 FG host layer laminated with actuator and sensor layers	75
3.4 Cylindrical smart shells	79
3.4.1 Thermo-electro-elastic formulation	79

3.4.2 Optimization formulation.....	81
3.4.3 Method of solution.....	84
3.4.3.1 Generalized integral quadrature	84
3.4.3.2 Co-evolutionary particle swarm optimization.....	85
3.4.3.3 Grey wolf optimization method.....	87
3.4.4 Numerical results and discussions	90
3.4.4.1 Evaluation study	91
3.4.4.2 Evaluation of the GWO with PSO	92
3.4.4.3 Homogeneous and inhomogeneous vessels	93
3.4.4.4 Effects of thermal loading	96
3.5 Summary.....	99
Sliding triboelectric nanogenerators	102
4.1 Motivation.....	102
4.2 Experimental setup	103
4.3 Load resistance analysis of TENGs.....	106
4.4 Simulation process.....	109
4.5 Simulation results	112
4.5.1 Validity evaluation.....	112
4.5.2 Prediction of TENG's outputs	118
4.5.3 Study of the thickness of dielectric films.....	123
4.5.4 Investigation of optimal load resistance	127
4.6. Summary.....	129
Rotary triboelectric nanogenerators.....	131
5.1. Introduction.....	131
5.2. Theoretical principles of rotary TENGs	132

5.2.1 Mechanism of operation for rotary TENGs	132
5.2.2 Experimental setup.....	135
5.2.3 Fundamental mathematics of TENGs.....	137
5.3. Solution strategy	140
5.4. Results and discussion	143
5.4.1 Evaluation	143
5.4.2 Prediction and sensitivity analysis of TENG	148
5.4.3 Study on grating number.....	152
5.4.4 Investigation on the angular velocity	155
5.4.5 Investigation on the tribo-surface spacing	158
5. Concluding remarks.....	160
Conclusion and Future plans	162
6.1 Conclusion	162
6.2 Future plans	163
6.2.1 Improvement in generated current.....	164
6.2.2 Hybridization of TENGs.....	164
6.2.3 Bulk energy generation.....	164
Reference	166

Abbreviation

CPSO	Co-evolutionary particle swarm optimization
FGMs	Functionally graded materials
GW	Grey wolf
ITO	Indium tin oxide
LED	Light emitting diodes
MEMS	Microelectromechanical systems
NEMS	Nanoelectromechanical systems
PSO	Particle swarm optimization
PVDF	Polyvinylidene fluoride
PZT	Lead zirconate titanate
SEM	Scanning electron microscope
TEM	Transmission electron microscope
TENG	Triboelectric nanogenerator
FEP	Fluorinated ethylene propylene
DE	Differential evolution
GA	Genetic algorithm
ABC	Artificial bee colony
AFM	Atomic force microscope
FGMs	functionally graded materials
NWs	Nanowires
GIQ	Generalized integral quadrature
DQ	Differential quadrature

Symbols

a	Inner radius of the shell
a_c	Acceleration
$A^{(n)}$	Weighting coefficients of the n^{th} order derivative in piezo shell
b	Outer radius of the shell
$B^{(n)}$	Weighting coefficients of the n^{th} order derivative in host shell
c	Specific heat
C	Capacitance
C_{ij}	Elasticity tensor
d	Thickness
D	Electric displacement
e	Piezoelectric tensor
E	Young's modulus
g	Gravity
h	Tribo-spacing distance
I_{sc}	Short circuit current
K	Thermal conductivity
L	Length
M	Number of mesh point in the geometry
N	Grating number
P	Pyroelectric tensor
P_{ave}	Average output power
Q	Transferred charge
Q_t	Number of mesh point in time domain
Q_{sh}	Short circuit current

r	Radial direction
R	Resistance load
S	Mid-plane radial to the thickness of the shell
t	Time
T	Temperature
T_t	Time period
u	Radial displacement
U	Stored energy in piezoelectric cells
V	Voltage
V_{oc}	Open circuit voltage
w	Width
W	Weight
Y_i	Material properties at the inner and outer surfaces

Greek letters

β	Grading index
ε	Strain field
ε_0	Permittivity of the space
ε_r	Permittivity of the dielectrics
η	Dielectric permittivity
θ	Tangential direction
λ	Thermal elastic coupling tensor
ρ	Density
σ	Stress field
τ	Dimensionless time
ω	Angular velocity
Ω	Electric field

List of Figures

- Fig. 2.1:** Piezoelectric effects. (a) piezoelectric material free of any electric charge or mechanical pressure, (b) and (c) represent direct piezoelectric effect, (d) and (e) depict inverse piezoelectric effect, and (f) exhibits this fact that if we apply AC signal, material will vibrate. 6
- Fig. 2.2:** Cantilever-based piezoelectric energy harvester; S is strain, V stands for voltage, M shows the mass [3]. 7
- Fig. 2.3:** (a) Top view of the piezoelectric energy scavenger, (b) side illustration of the design, and (c) generated voltage versus various frequencies [4] 8
- Fig. 2.4:** Possible wearable energy harvesting sources in human body [10] 9
- Fig. 2.5:** Shoe-based piezoelectric energy harvester [11]. 9
- Fig. 2.6:** (a) The fabricated device, and (b) undergoing the finger motion [15]. 10
- Fig. 2.7:** ZnO based energy harvester (a) SEM of aligned ZnO nanowires, (b) TEM of ZnO nanowires, and (c) experimental setup [25]. 11
- Fig. 2.8:** Flexible piezoelectric nanogenerator: (a) scheme of the flexible nanogenerator (NG) base on ultrathin aluminium foil, (b) view of the flexible NG, and (c) SEM image of cross section of the NG [26]. 12
- Fig. 2.9:** Energy harvesting from human biologics [33]. 13
- Fig. 2.10:** (a) Schematic view of helical piezoelectric energy scavenger, (b) sublayers of the device, and (c) SEM of cross section of the sandwich layers [34]. 13
- Fig. 2.11:** (a) Fabricated piezoelectric nanogenerator, and (b) wrapping the device around the aorta [35]. 14
- Fig. 2.12:** (a) Mounting the energy harvester on bovine lung, (b) on diaphragm, (c) generated voltage from lung, and (d) from diaphragm [36]. 15
- Fig. 2.13:** Schematic of the prototype [38] 16

Fig. 2.14: Illustrating a schematic view of the prototype [40].	17
Fig. 2.15: Generating electricity during human walking [41].	17
Fig. 2.16: Design of micro energy harvester [42].	18
Fig. 2.17: (a) Inner section of the generator, and (b) AA size micro power generator (Copyright © 2003 IEEE) [43].	18
Fig. 2.18: Various mechanical designs for electrostatic energy harvesters [44].	19
Fig. 2.19: View of the design including the triangular electrode elements and the direction of motion [45].	20
Fig. 2.20: Schematic drawing of (a) micro electret generator, and (b) working mechanism of electret generator (Copyright © 2006, IEEE) [46].	21
Fig. 2.21: Illustration of different parts of the electrostatic energy harvester [47].	21
Fig. 2.22: Application of nonlinear springs for energy scavenging: (i) schematic view of the final design, (ii) impacts of nonlinearity on the spring force, and (iii) the electrostatic energy harvester connected to a nonlinear spring [48].	22
Fig. 2.23: Work functions of different metals: (a) before contact, and (b) after contact [51].	23
Fig. 2.24: Triboelectric series [53, 54].	24
Fig. 2.25: Schematic of electron-cloud-potential-well model, (a) before contact, (b) in contact, (c) after contact, and (d) charge release from the atom at elevated temperatures [57].	26
Fig. 2.26: Mechanism of the sliding-mode TENGs. (a-d) form a loop and the iteration of the loop generates electrical power [60].	28
Fig. 2.27: Operating mechanism of the contact-mode TENGs.	29
Fig. 2.28: Rhombic TENGs, (a) schematic view of the geometry, and (b) implementation of TENGs in a backpack [63].	30

Fig. 2.29: Multilayered TENGs for scavenging energy from human motions, (a) schematic view, (b) bent TENG with finger, and (c) generated power during normal walking [64].	31
Fig. 2.30: TENG system for harvesting breathing energy, (a) and (b) the attached TENGs to live rat's diaphragm, and (c) enlarged photograph of the TENGs [69].	32
Fig. 2.31: (a) Working mechanism of the proposed TENG, (b) in vivo application of TENG, and (c) measured in vivo voltage [70].	32
Fig. 2.32: Rotary TENGs for harvesting wind power [71].	33
Fig. 2.33: High output rotary TENGs, (a) rotator, (b) stator, (c) lighting LEDs up, and (d) lighting up a globe [72].	34
Fig. 2.34: TENGs for air cleaning, (a) view of the design, (b) principle for SO ₂ removal, and (c) removal based on electrostatics [73].	35
Fig. 2.35: Schematic drawing of wind tunnel and the structural design of a flutter driven TENGs [74].	36
Fig. 2.36: (a) Schematic drawing of the proposed TENG, (b) and (c) SEM images of dielectric materials, and (d) working mechanism of the TENG [75].	37
Fig. 2.37: Large scale electricity generation by TENG, (a) illustration of the TENG, (b) fabricated TENG, and (c) SEM images of PTFE and aluminum electrode [76].	37
Fig. 2.38: Photograph of the proposed TENG, (a) schematic drawing, (b) SEM image of cross section of the TENG, (c) AFM image of PTFE layer, and (d) contact angle of the PTFE film [77].	38
Fig. 2.39: Water based TENG, (a) schematic, and (b) generating power [78].	39
Fig. 2.40: Stretchable wavy-TENG, (a) fabricated design, and (b) applications on human hand and neck [79].	40
Fig. 2.41: Design of foldable TENG, (a) schematic of the wearable TENG, and (b)	40

operation of a remote control [80].	
Fig. 2.42: Illustrations of stretchable fabrics for TENGs [81].	41
Fig. 2.43: The working principle of ZnO-based piezoelectric nanogenerator [25]	42
Fig. 2.44: (a) Illustration of the self-powered system, and (b) detected electric signal [83]	42
Fig. 2.45: (a) Fabrication of ZnO nanowires on flexible Kapton substrate, and (b) circuit diagram, and (c) detection results [84]	43
Fig. 2.46: The output and some applications of tactile triboelectric sensor [93].	44
Fig. 2.47: Self-powered skin based TENGs, (a) fabricated design, (b) SEM of PDMS surface, and (c) and (d) touch pad applications of the sensor [94].	45
Fig. 2.48: (a) Schematic of the TENG sensor, (b) SEM of TiO ₂ nanowires, and (c) fabricated TENG [95].	46
Fig. 2.49: Triboelectric based sensors for detection of Hg ²⁺ ions [96].	47
Fig. 2.50: Active sensors for human health assessment, (a) drawing of TENG sensor, and (b) application of sensor in human neck, chest and wrist [97].	47
Fig. 2.51: Self-powered triboelectric sensor for angel monitoring, (a) illustration of the TENG device, (b) rotator, (c) stator, (d) SEM image of PTFE, and (e) SEM image of Cu film [98].	48
Fig. 3.1: Sectional view of geometry and coordinates of the laminated shell of (a) shell 1, a host FGM layer covered with a layer of PZT-4 bonded to its outer surface, and (b) shell 2, one-layer FGM host covered by a film of Ba ₂ NaNb ₅ O ₁₅ and a layer of PZT-4 to its inner and outer surfaces respectively.	57
Fig. 3.2: Compatibility conditions between k th and (k+1) th layers, including radial stress, electric displacement and thermal flux terms.	61
Fig. 3.3: Evaluation study of the presented method with the literature for a thick FG	66

spherical shell (a) radial distribution of the circumferential stress, and (b) radial displacement through the thickness.

Fig. 3.4: Comparison between the presented results with those of the finite element analysis for an FG sphere (a) radial stress, (b) radial displacement, and (c) electric potential. 68

Fig. 3.5: Effects of inhomogeneity on the dimensionless (a) radial stress, (b) circumferential stress, and (c) radial displacement (at $\tau=2.5\times 10^{-6}$). 70

Fig. 3.6. Impacts of inhomogeneity on the dimensionless (a) radial distribution of the electric potential, and (b) temperature through the thickness. 71

Fig. 3.7: Effects of thermal gradient on dimensionless (a) radial stress, (b) circumferential stress, (c) radial displacement, and (d) electric potential (at $\tau=2.5\times 10^{-6}$). 73

Fig. 3.8: A survey of the effects of the shell thickness S on the profile of (a) circumferential stress, and (b) radial displacement (at $\tau=2.5\times 10^{-6}$). 74

Fig. 3.9: Impacts of the geometric parameter on the dimensionless (a) radial stress, and (b) electric potential. 75

Fig. 3.10: Effects of the electrical potential on (a) radial stress, (b) circumferential stress, and (c) radial displacement (at $\tau=2.5\times 10^{-6}$). 76

Fig. 3.11: Impacts of h_{FGM}/h_{piezo} on the dimensionless (a) radial stress, (b) circumferential stress, and (c) electric potential (at $\tau=2.5\times 10^{-6}$). 77

Fig. 3.12: Effects of h_{FGM}/h_{piezo} on (a) radial displacement, and (b) temperature. 78

Fig. 3.13: Sectional plot of the pyroelectric shell (a) coordinates and loadings, and (b) variation of material properties along the thickness. 79

Fig. 3.14: Specifications of the optimization study. 82

Fig. 3.15: Flow chart of *PSO* method. 86

Fig. 3.16: Steps of the <i>GWO</i> method.	89
Fig. 3.17: Comparison of the response of FG smart vessel with those of reference [165] for radial distribution of the (a) circumferential stress, and (b) electric potential.	92
Fig. 3.18: Comparison of results of the <i>GWO</i> method with those of the traditional <i>PSO</i> .	93
Fig. 3.19: Inhomogeneity impacts on (a) radial stress, (b) circumferential stress, (c) radial displacement, and (d) electric potential.	95
Fig. 3.20: Inhomogeneity impacts on radial distribution of the (a) temperature, and (b) thermal gradient.	96
Fig. 3.21: Impacts of thermal loading on (a) radial stress, (b) tangential stress, (c) radial displacement, (d) electric potential, and (e) thermal flux.	98
Fig. 4.1: The experiment set up design of TENG including (a) a schematic of the sliding process and components, (b-e) multi-orientation images of the setup. The experiment setup was mainly consisted of 5 major parts: part 1: the sliding segment including PTFE; part 2: sliding segment including Nylon; part 3: actuator to convert rotary motion of a motor to a reciprocal movement, part 4: base, part 5: top plate, and (f) serially connected LEDs being turned on during reciprocal motion.	104
Fig. 4.2: SEM images captured from the cross-section of Nylon film (a) without, and (b) with coating. The upper and lower surfaces of the Nylon film (b) were coated with gold and chromium, respectively. (c) and (d) SEM cross-section images captured at higher magnifications from the upper surface coated with gold.	106
Fig. 4.3: The optimization procedure of the sliding-mode TENGs.	111
Fig. 4.4: Comparison of results obtained for (a) current and (b) voltage with those of Ref. [55].	113

Fig. 4.5: Induced charges generated in four cycles.	115
Fig. 4.6: Comparison of the simulation results with our experiment (a) temporal response of the current for $R=8\text{ M}\Omega$, (b) temporal response of the voltage for $R=8\text{ M}\Omega$, (c) maximum current, and (d) maximum voltage.	116
Fig. 4.7: The SEM images of the Nylon surface (a) before and (b) after gold coating and the coated surface after (c)1000 cycles, (d) 15,000 cycles and (e) 30,000 cycles of sliding.	118
Fig. 4.8: Dependence of TENG's outputs on the resistor and thickness of the triboelectric films: (a) voltage, (b) current, and (c) average power output.	119
Fig. 4.9: Variation of the average power output in respect to (a) resistor and (b) thickness of triboelectric films.	120
Fig. 4.10: Impacts of the resistor and contact area on outputs of the TENG, including (a) voltage, (b) current, and (c) average power output.	121
Fig. 4.11: Variation of the average power output in respect of (a) resistor and (b) contact area.	121
Fig. 4.12: Comparing the impacts of the thickness of the dielectric films and contact area for different load resistances: (a) $R= 100\text{ M}\Omega$, (b) $R= 1\text{ G}\Omega$, and (c) $R= 10\text{ G}\Omega$.	122
Fig. 4.13: Convergence study of the proposed algorithm.	124
Fig. 4.14: Variation of the optimum thickness of dielectric films with resistor.	125
Fig. 4.15: Results of different resistors on electrical outputs of dielectric-to-dielectric sliding-mode NTEGs (a) charge, (b) current, (c) voltage, (d) power, and (e) energy.	126
Fig. 4.16: Variation of optimum load resistance and average power output with the thickness of the dielectric film.	128
Fig. 4.17: Effects of the thickness of dielectric film on electrical outputs of	129

dielectric-to-dielectric sliding-mode TENGs (a) charge, (b) current, (c) voltage, (d) power, and (e) energy.

Fig. 5.1: Operating mechanism of rotary TENGs: (a) schematic view, where θ_0 and θ represent the segment and rotation angles in radian, and N , h , and ω stand for grating number, tribo spacing, and rotational speed, respectively, (b) initial physical contact of dielectrics, (c) separation of dielectric films, (d) rotation outwards, (e) full separation of segments, and (f) rotation towards the adjacent segment. (Note: Figures (b-f) show the cross-sectional profile of one segment of a rotary TENGs.)

Fig. 5.2: SEM images of the surface (a) before and (b) after contact rotation for 10,000 cycles, (c) photograph of the device, (d) driving serially connected LEDs, and (e) the output power of rotary TENGs after undergoing some cycles.

Fig. 5.3: Flow chart of the proposed algorithm for characterizing the contact-mode TENGs.

Fig. 5.4: Comparison of results obtained for (a) current and (b) voltage with those of Ref. [177] with inner and outer radii of 5 mm and 50 mm, grating number of 4, triboelectric layers thickness of 100 μm and tribo spacing h of zero.

Fig. 5.5. Temporal response of the current for a whole rotation.

Fig. 5.6: Comparison of the simulation results with our experimental results (a) temporal response of the current for $R=1 \text{ G}\Omega$, (b) temporal response of the voltage for $R=1 \text{ G}\Omega$, (c) maximum obtained current, and (d) maximum obtained voltage.

The geometry parameters are $r_1=5 \text{ mm}$, $r_2=50 \text{ mm}$, $N=4$, $d_1=d_2=250 \mu\text{m}$, and $h=0$.

Fig. 5.7: Dependence of TENG outputs on the resistor and (a) angular velocity, (b) tribosurface spacing, and (c) number of gratings. Dot points represent the experimental data obtained in this study with $r_1=5 \text{ mm}$, $r_2=50 \text{ mm}$, $d_1=d_2=250 \mu\text{m}$, angular velocity of 100, 300, 500 and 700 rpm, h of 0, 0.5 and 1 mm, and N of 2 and

4, respectively.

Fig. 5.8: Sensitivity analysis of TENG's generated power with (a) resistance vs different N , (b) angular velocity, (c) resistance vs different ω , (d) number of gratings, (e) resistance vs different h , and (f) tribo-surface spacing. 152

Fig. 5.9: Convergence study of the proposed algorithm. 153

Fig. 5.10: Results of optimized average power output and resistors for different N . 154

Fig. 5.11: Impacts of the grating number on electrical outputs of rotary NTEGs: (a) charge, (b) current, (c) voltage, and (d) power. 155

Fig. 5.12: Distribution of the optimized load resistance and average power output with ω . 156

Fig. 5.13: Effects of angular velocity on electrical outputs of rotary TENGs: (a) charge, (b) current, (c) voltage, and (d) power. 157

Fig. 5.14: Optimized curves for variation of tribo spacing, h ($r_1=5$ mm, $r_2=50$ mm, $N=4$ and $d_1=d_2=250$ μm). 159

Fig. 5.15: Impacts of tribo spacing of rotary TENGs on (a) charge, (b) current, (c) voltage, and (d) power with geometry parameters of $r_1=5$ mm, $r_2=50$ mm, $N=4$, and $d_1=d_2=250$ μm . 160

List of Tables

Table 3.1: Elastic and thermal material properties of TiC and Ni [172].	67
Table 3.2: Electro-thermo-elastic properties of PZT-4 and Ba ₂ NaNb ₅ O ₁₅ [173, 174].	67
Table 3.3: Thermo-electro-elastic properties of PZT-5H [182].	91
Table 3.4: Effects of inhomogeneity on weight and stored energy of FG shell structures.	94
Table 3.5: Results of the optimization algorithm for different temperature excitations.	97
Table 4.1: Properties of dielectric films [61].	112
Table 4.2: Simulation results for the optimum dielectric thickness of different resistor values.	124
Table 4.3: Optimum load resistance of sliding-mode TENGs for different geometries.	127
Table 5.1: Material properties of dielectric films [61].	146
Table 5.2: Optimum outputs of rotary TENGs for different values of the grating number.	153
Table 5.3: Optimized specification of rotary TENGs for different angular velocity.	156
Table 5.4: Optimized results for different tribo spacings.	158

Summary

This thesis deals with advanced energy harvesting approaches including piezoelectric-based energy harvesters and triboelectric nanogenerators (TENGs). As a traditional strategy, piezoelectric materials have extensively been used in many energy harvesting systems. Since piezoelectric and pyroelectric materials respond excellently to pressure and temperature variations, pressure-based piezoelectric energy harvesters are designed in the current study. The cylindrical and spherical geometries were considered, and the patterns of field variables were graphically drawn. It was demonstrated that the harvested energy can go up by 74% with a proper design.

Next, the study was shifted on the most modern method for powering electronics in micro/nano scales. TENGs have been proposed as an effective approach to harvest mechanical energy from various sources in the ambient environment. TENGs have a wide range of applications in sensors, biomedical, defense technology, environmental monitoring, and personal electronics. This thesis deals with in-plane sliding and contact-separation configurations to scavenge mechanical energy. A high-output and lightweight sliding-mode TENG was designed to improve the efficiency of the TENGs system. The TENGs output was numerically simulated with the help of analytical methods and optimization theories. A great match between the experiment data and simulation results was reported. The sliding-mode TENG successfully generated a peak voltage and current of 150 V and 0.9 μ A respectively. The new design was found to harvest 3.65 mJ at each cycle where the weight is almost 43 g. Meanwhile, a sensitivity analysis was shown that the resistor, contact area and thickness of dielectric film are respectively the most important design parameters in the sliding-mode TENG. Because of the prevalence of rotation in the environment, the rotary TENGs were fabricated and simulated to harvest the maximum accessible energy. The device can work in fully contact mode as well as the non-contact mode. Through the rotation, measurement

showed a peak of 30 V and 0.6 μA , respectively. It was demonstrated that the spacing, grating number and angular velocity can significantly affect the TENG' performance. A general algorithm was introduced to achieve the best performance for the rotary system with appropriate values for design parameters. It was concluded that the optimized TENGs can scavenge almost 0.369 mJ at each cycle.

Introduction

1.1 Motivation

Obviously, today's life is highly dependent on the electrical energy. Humans have increasingly been surrounded by personal electronics, for example, mobile phones, personal computers, medical electrical equipment (e.g. heart rate monitor, biosensors, etc), industrial electronic parts (e.g. sensors, actuators, etc), and so on. Miniaturization of electronics is driving this trend forward. Evidently as the use of electronic devices grows, the technical challenge of powering these devices is imposed. Traditionally, battery has been used to wirelessly power electronics. However, its limitation in charge storage, and its disposal after lifetime remain a critical challenge.

To meet the above-mentioned problems, energy scavenging was introduced in this era. Energy scavenging means the procedure in which other versions of energy for like solar power, thermal energy, vibration, etc are skilfully converted into the electrical energy to run low-consumed energy electronics. Solar energy is very common in energy harvesting strategies, but it depends on some parameters such as weather, time, and location. The thermal based energy harvesters are still low efficient, and highly depend on the hot and cold temperatures. Most of the mechanical energy, in specific pressure, friction and vibration energy, can be easily captured and converted to electrical energy. Therefore, the focus of many researches was on improving the self-powering technology to present self-powered microelectromechanical systems (MEMS) and nanoelectromechanical systems (NEMS) operating wirelessly and independently without the use of any energy suppliers.

1.2 Mechanical energy harvesting strategies

Mechanical energy is ubiquitously available in our surrounding. This type of energy can be a result of human activity (walking, hand movements, heart beating, blood flow, speaking, etc), environmental phenomena (wind power, wave energy, etc), and human-made inventions (vibration of tires, vibration of household appliances e.g. washing machine, etc). To harvest mechanical energy, traditionally, there are three main energy scavenging approaches including: electromagnetic, electrostatic and piezoelectric energy conversion principles.

Electromagnetic energy harvesters operate based on Faraday's law. This type of energy harvester is only practical in large-scale energy production [1]. Electrostatic-based energy harvesters work on the charge transfer procedure between two parallel plates. Any change in the gap will lead to the flow of charges. Comparing to other energy harvesters, the output is very low, and another external voltage resource is required, then this technique is not popular in particular for wireless MEMS/NEMS. As the third version, piezoelectric energy harvesters are the most popular mechanism working on the ground of the property of materials known as piezoelectricity. Some common piezoelectric materials are lead zirconate titanate (PZT), zinc oxide (ZnO) and aluminum nitride (AlN). The bottlenecking matters of piezoelectric energy harvesters are fabrication complexity and the cost of materials.

A new sub-division is triboelectric-based energy harvesters. This type operates based on the charge generation during the electrification process. The advent of triboelectric nanogenerators (TENGs) has radically revolutionized energy harvesting approaches due to its unique merits. Firstly, TENGs use organic materials, which were already considered as waste materials for electricity generation. The second advantage is that TENGs are producing sustainable power output for wireless electronics. Furthermore, TENGs require a highly simple fabrication process in comparison with other energy harvesters. More details on working mechanism are mentioned in the next chapters.

1.3 Organization of thesis

This thesis deals with advanced energy harvesting approaches including piezoelectric and triboelectric based energy harvesters. For commercializing any technology, it is of the great importance to be low cost and high efficiency. In fact, the amount of scavenged energy is a function of various parameters. The current study first explains the working mechanism of the TENGs in different configurations. Next, it recognizes the key factors affecting the output of energy harvesters, then attempts to attribute proper values to the design parameters, aiming at maximizing the harvested power. The designed products have various applications where there is no power supplier. The organization of this thesis is described below.

In Chapter 2, a comprehensive literature review is presented to show the background of all four energy harvesting methods. Since the focus of the current study is development of the piezoelectric and triboelectric energy harvesters, more details are explained for the piezoelectric and triboelectric mechanisms.

Because piezoelectric reflects a high sensitivity to pressure, pressure-based piezoelectric energy harvesters are designed to increase the harvested energy. Chapter 3 deals with design process of cylindrical and spherical shells made of piezoelectric materials for energy harvesting purposes. The application is highly wide from a small scale (such as stents in blood vessels) up to a large scale (such as pressure vessels). The chapter is based on publications of in “Thermal analysis and electro-elastic response of multilayered spherical vessels, *International Journal of Pressure Vessels and Piping*, 171 (2019) 194-206” and “Durable pyroelectric shell structures for energy scavenging applications, *Acta Mechanica* 231 (2020) 205-220”.

In Chapter 4, a high output and lightweight sliding-mode TENG is developed. The theoretical study is conducted to predict behavior of TENGs under different working conditions. With the help of artificial intelligence, a new design is presented to increase the

harvested energy at each cycle of the movement. The chapter comes from the publication of “Simulation of high-output and lightweight sliding-mode triboelectric nanogenerators, Nano energy 66 (2019) 104115”.

Rotation is another prevalent type of mechanical energy. Chapter 5 explores rotary TENGs. The governing mathematics is derived, and output power is introduced as a function of angular velocity, grating number and spacing. The optimum design for disk-shaped TENGs is presented; meanwhile, experimental setup is also fabricated. The chapter is based on the publication of “Artificial intelligence enhanced mathematical modeling on rotary triboelectric nanogenerators under various kinematic and geometric conditions, Nano energy 75 (2020) 104993”.

Chapter 6 summarizes the thesis with key findings and developments on piezoelectric and triboelectric based energy harvesters. This chapter also proposes some further works which help to understand triboelectric effect in other configurations and develop more efficient TENGs.

Energy harvesting mechanisms

2.1 Background

Converting mechanical energy into electrical form is the most applicable strategy to charge and drive electronics wirelessly. In this chapter, a comprehensive literature review is presented for possible energy harvesting approaches to understand their working mechanism and significance of the current study. Generally, energy scavenging strategies was divided into four main categories including piezoelectric energy harvesters, electromagnetic-based energy harvesters, electrostatic energy harvesters and triboelectric-based energy harvesters. First, an in-depth description will be presented on the working mechanisms of the first three approaches, and their previously developed devices are reviewed. Next, the chapter shifts to the last sub-division, TENGs. In this case, more details on different mechanisms, materials candidates, and fabrication techniques are presented. A review also is conducted to show the applicability of TENGs in various applications e.g. vibration based TENGs, wind and water based TENGs, biomechanical TENGs, and the area of sensors.

2.2 Energy Harvesting Strategies

2.2.1 Piezoelectric Energy Harvesters

Properties of the smart materials can be changed by external motivations such as pressure, humidity, pH and magnetic field. Piezoelectric materials are one of the most favorable options in smart systems. These smart systems operate based on the property of material known as piezoelectricity. Piezoelectrics can provide electric voltage while tolerate mechanical loads, and can supply the system with deflections, if we apply electric excitation.

Piezoelectric materials have much great attractiveness because of its simple structure, light weight and high ability in control aims. These materials can be divided into two main categories: piezoceramics and piezopolymers. Most of piezoceramics are a combination of lead zirconate titanate (PZT), which their properties are dependent on ratio of zirconate to titanat. The most prevalent piezopolymer is polyvinylidene fluoride (PVDF). In fact, PZT has high stiffness, resulting in suitable ability in actuating aims, and PVDF has high damping ability; thus, we can use PVDF as sensor. When we apply mechanical motivations like pressure, piezoelectics produce electric potential; this phenomenon refers to direct piezoelectric effect. Vice versa, by applying electric charge in piezoelectics, system will experience some deflections; this ability is inverse piezoelectric effect. Fig. 2.1 shows piezoelectric effects.

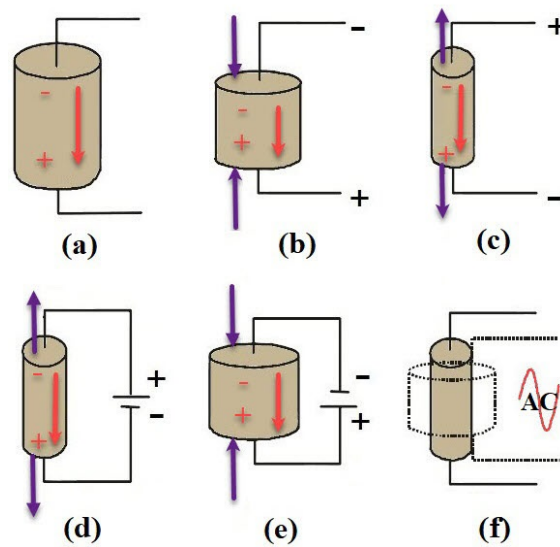


Fig. 2.1: Piezoelectric effects. (a) piezoelectric material free of any electric charge or mechanical pressure, (b) and (c) represent direct piezoelectric effect, (d) and (e) depict inverse piezoelectric effect, and (f) exhibits this fact that if we apply AC signal, material will vibrate.

2.2.1.1 Cantilever beam energy harvester

The most traditional piezoelectric energy harvester is that of the cantilever beam configuration [2, 3], depicted in Fig. 2.2. The piezoelectric beam is fixed on the one side while is free to vibrate on the other side. When the cantilever experiences vibration, it will go under compression and tension periodically. Hence, some voltage will be generated on electrodes. The mass at the tip increases the amplitude of the vibration, resulting in higher voltage.

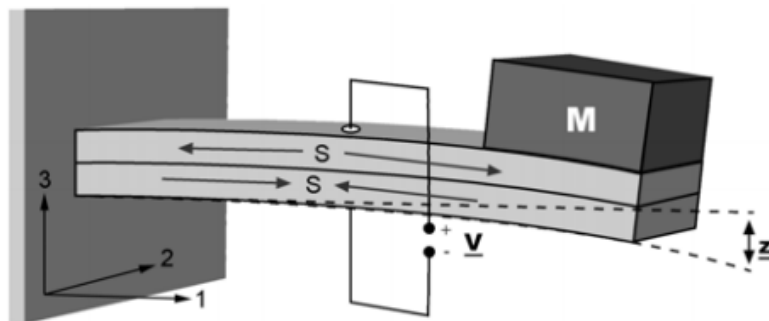


Fig. 2.2: Cantilever-based piezoelectric energy harvester; S is strain, V stands for voltage, M shows the mass [3].

An electronically connected array of thin piezoelectric films were proposed for low frequency energy harvesting purposes by Liu et al. [4]. A schematic illustration is depicted in Fig. 2.3. The study showed the series and parallel deliver the same level of the output power. However, the required optimum resistance is less in case of electrically parallel connection.

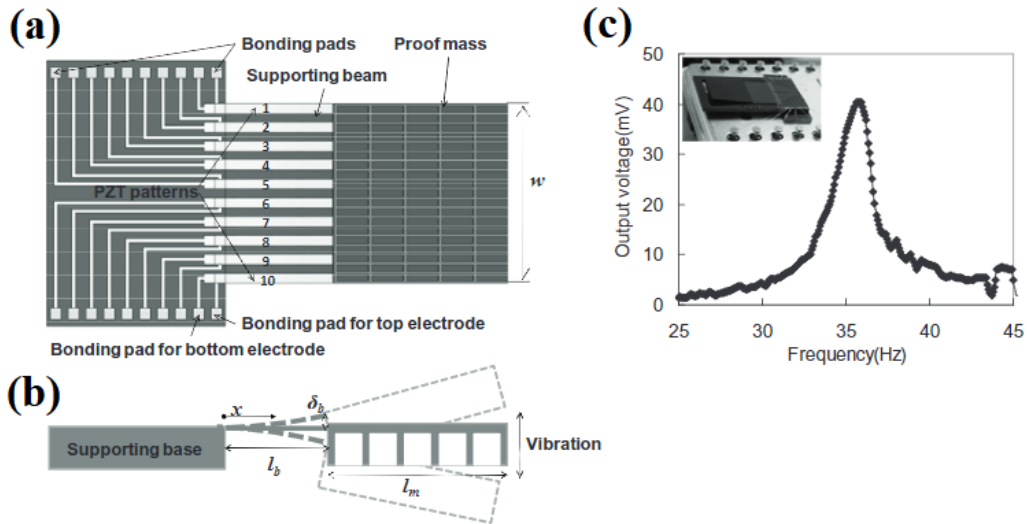


Fig. 2.3: (a) Top view of the piezoelectric energy scavenger, (b) side illustration of the design, and (c) generated voltage versus various frequencies [4].

Many studies attempted to modify the characteristics of the piezoelectric cantilevered beam energy harvesters by means of finite element analysis [5], optimization theories [6], strain distribution extension [7], innovative shapes [8, 9], etc.

2.2.1.2 Wearable energy harvester

Different parts of human body can produce mechanical energy, depicted in Fig. 2.4. Then, merging the human motion and nanogenerators introduces an important research discipline. Wearable nanogenerators are one of the most promising approaches to generate some micro/nano scale amount of power which can be used to run mobile electronics.

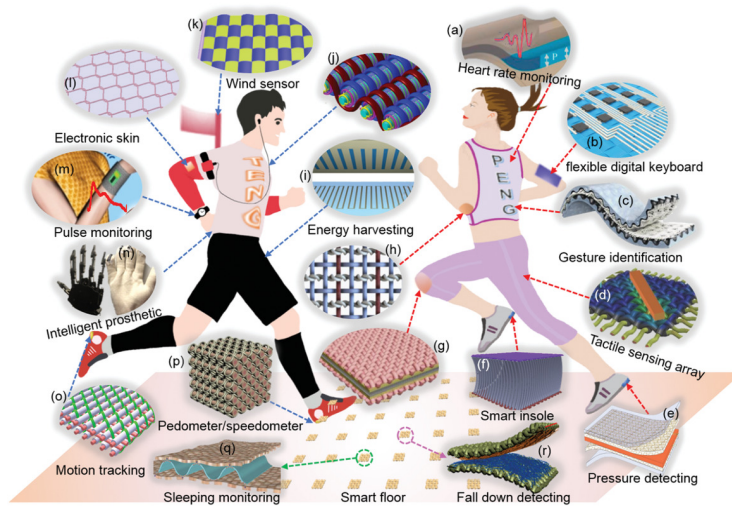


Fig. 2.4: Possible wearable energy harvesting sources in human body [10].

One of the most interesting applications is that of the wearable piezoelectric energy harvester [11]. Fig. 2.3 depicts the configuration. The produced energy is limited, but the presented device still benefits low power applications (for example, radio-frequency identification tag).

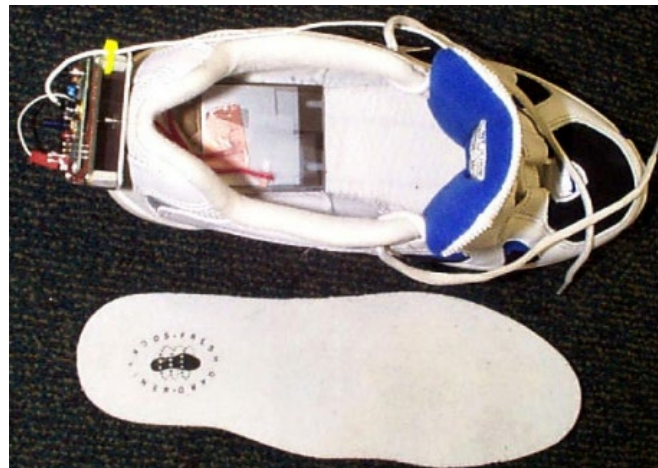


Fig. 2.5: Shoe-based piezoelectric energy harvester [11].

Later the energy conversion was improved through different studies. By designing a curved geometry [12], testing various durable piezoelectrics [13], and optimizing the

electrical characteristics [14], more efficient piezoelectric shoes have been presented. Furthermore, piezoelectric nanogenerators can generate power based on human motion. Guido [15] presented the idea of piezoelectric flexible skin generating some power by finger motion, depicted in Fig. 2.6. the results were verified by finite element method, and a peak-to-peak voltage of 0.7 V was reported.

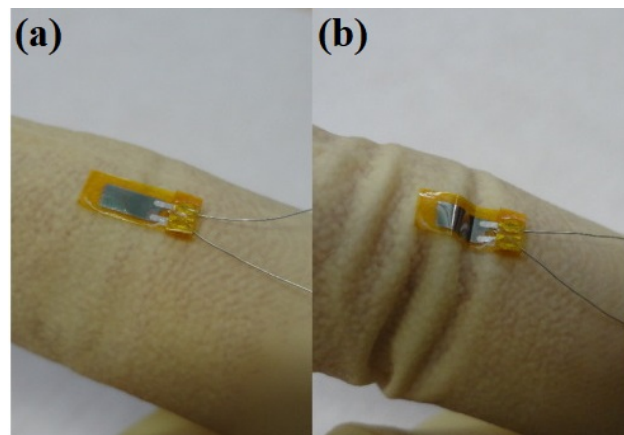


Fig. 2.6: (a) The fabricated device, and (b) undergoing the finger motion [15].

In the recent years, many attempts were dedicated to introduce skin-conformability piezoelectric nanogenerators for human motion monitoring; some are summarized as embedding BaTiO_3 particles into Ecoflex matrix [16], using onion skin as piezoelectric material [17], design a coaxial piezoelectric fibre [18].

2.2.1.3 Nanowire energy harvester

Generally, zinc oxide (ZnO) offers some merits to be used in energy harvesting purposes: (i) It is a biocompatible element and keeps the chance to be utilized in biomedical electronics [19]; (ii) It possesses both piezoelectric and semiconducting properties [20]; and (iii) It can be in various configurations such as nanowires (NWs), nanorings, nanobelts, and nanobows [21-24]. These advantages introduce ZnO arrays as a potential candidate to be grown on a

substrate and convert low frequency vibration into electricity. Wang and Song showed that an array of ZnO NWs can generate some power [25]. A schematic of the configuration was depicted in Fig. 2.7. The working mechanism is based on bending a ZnO nanowire with the atomic force microscopy's tip. The introduced energy harvester has capability to be embedded in implantable biomedical electronics, remote sensors, and portable electronic devices for new self-powering nanotechnology.

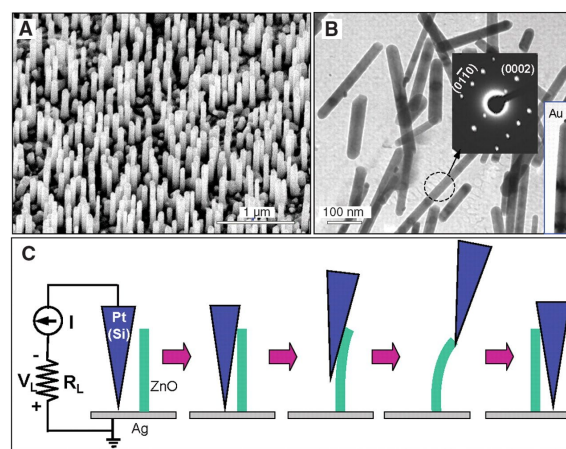


Fig. 2.7: ZnO based energy harvester (a) SEM of aligned ZnO nanowires, (b) TEM of ZnO nanowires, and (c) experimental setup [25].

In order to increase the output power, Lee et al. [26] fabricated a flexible piezoelectric nanogenerator by coating aluminum (Al) foil with polymethyl methacrylate (PMMA) layer before the growth of ZnO NWs, as shown in Fig. 2.8. The presented device generated a voltage and current of 50 mV and 200 nA, respectively.

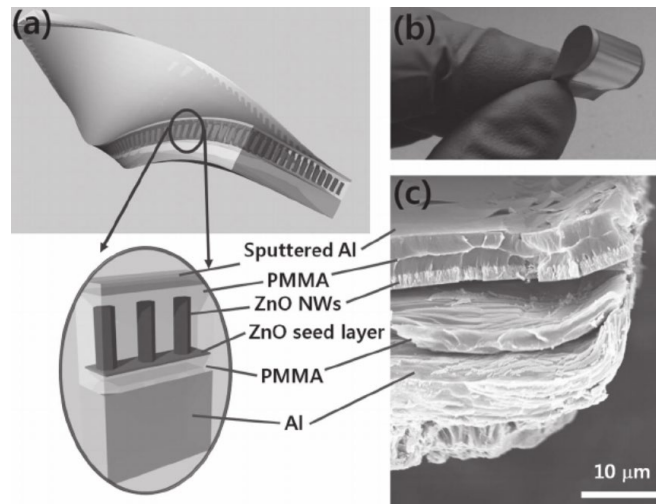


Fig. 2.8: Flexible piezoelectric nanogenerator: (a) scheme of the flexible nanogenerator (NG) base on ultrathin aluminium foil, (b) view of the flexible NG, and (c) SEM image of cross section of the NG [26].

Many researches attempted to improve the efficiency of NWs via hybridizing the piezoelectric NWs with other energy scavengers [27, 28], employing materials with better piezoelectric properties [29-31], and developing the structure [32].

2.2.1.4 Biomedical energy harvesters

Recent advancement in MEMS and NEMS highlighted the applications of implantable medical electronics. As diagnostic tools, these devices can monitor the heart rate, blood pressure and temperature. The following figure depicts some sources of mechanical energy in human body and its possible applications.

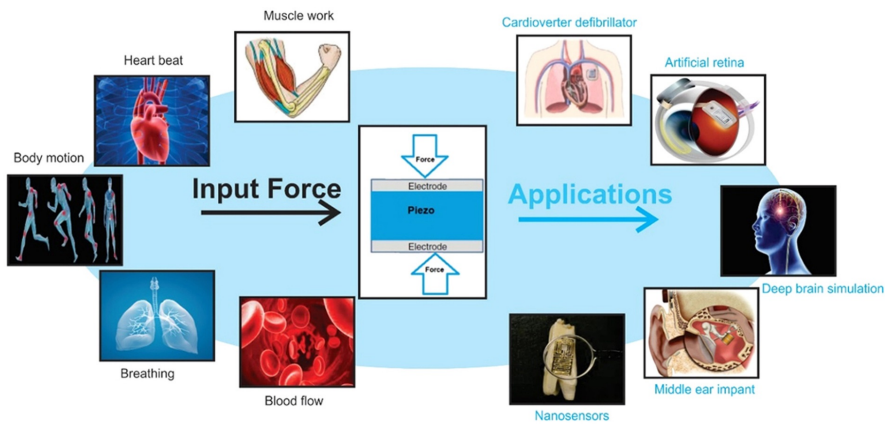


Fig. 2.9: Energy harvesting from human biologics [33].

Dong et al. [34] integrated porous piezoelectric films with a pacemaker, extending the lifetime of the device up to 1.5 years. Fig. 2.10 shows the helical configuration for the piezoelectric design, delivering an output voltage of 0.65 V. The simulation results found in a good agreement with those of the experimental data.

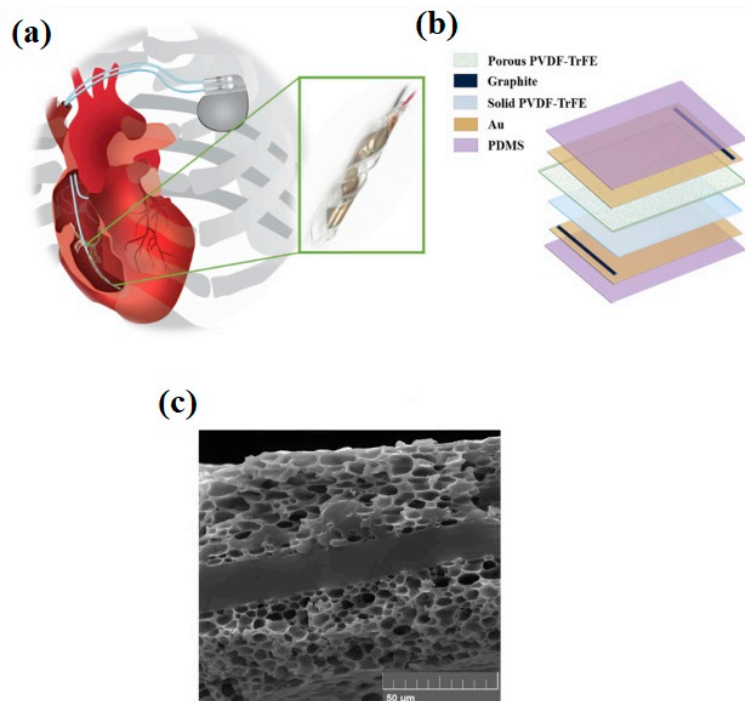


Fig. 2.10: Schematic view of helical piezoelectric energy scavenger, (b) sublayers of the device, and (c) SEM of cross section of the sandwich layers [34].

Zhang et al. [35] fabricated piezoelectric energy scavenger working based on pulsating of the ascending aorta, as shown in Fig. 2.11. Vivo study demonstrates a maximum voltage and current of 1.5 V and 300 nA with a heartbeat of 120 bpm. The piezoelectric generator circularly wrapped around the ascending aorta, reducing the risk of stroke, expansion of aorta, and blocking blood flow.

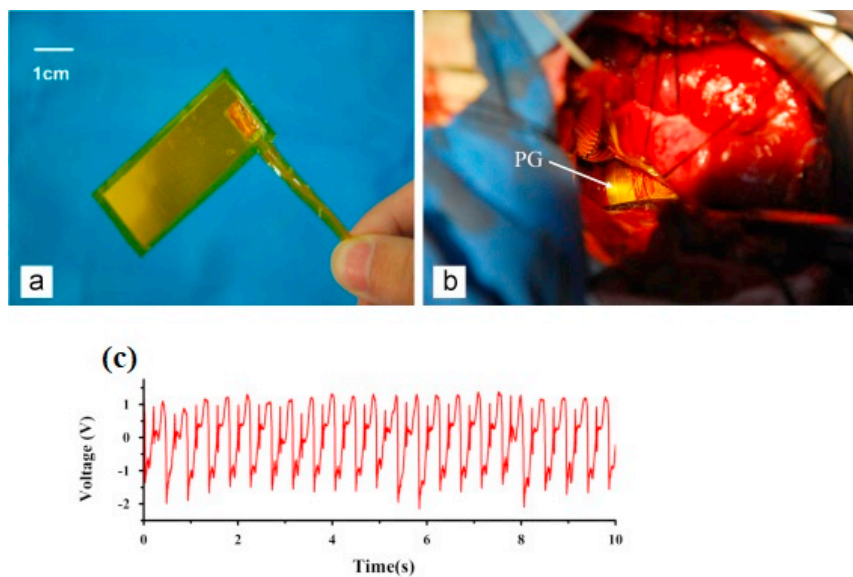


Fig. 2.11: (a) Fabricated piezoelectric nanogenerator, and (b) wrapping the device around the aorta [35].

A piezoelectric nanogenerator was fabricated to scavenge the power from bovine lung and diaphragm by Dagdeviren et al. [36], as shown in Fig. 2.12. The harvested voltage from lung and diaphragm reached 4 and 2 V respectively. The study showed the applicability of the piezoelectric energy harvesters from motion of internal organs.

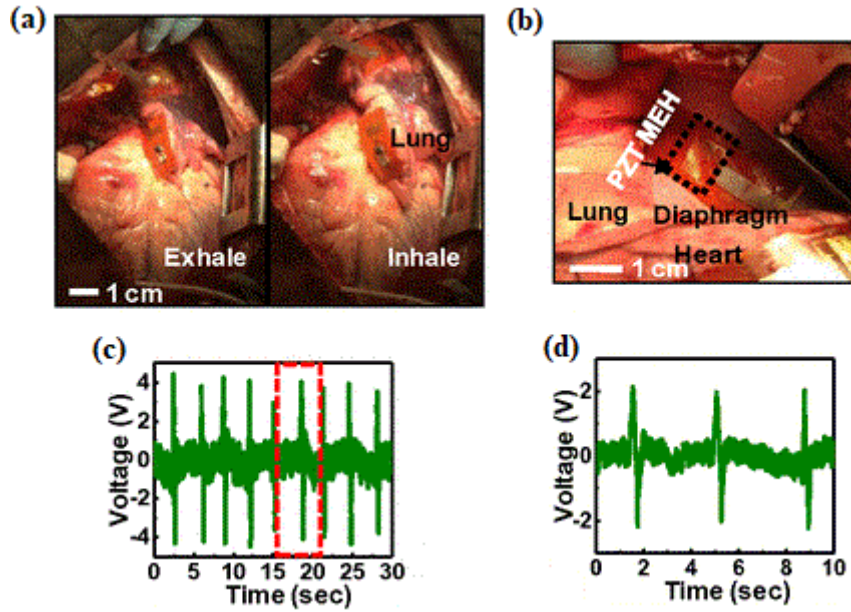


Fig. 2.12: (a) Mounting the energy harvester on bovine lung, (b) on diaphragm, (c) generated voltage from lung, and (d) from diaphragm [36].

The above-mentioned introduction shows some applications of piezoelectric energy harvesters. However, from technological point of view, this field face some bottlenecking challenges. Limited choice of materials, low current output along with complex fabrication process remain problems.

2.2.2 Electromagnetic Energy Harvesters

Electromagnetic energy harvesters operate based on the Faraday's law [37]. This law describes the interaction between a magnetic field and an electric circuit. Most electrical motors and generators work on this basic principle. A schematic view of electromagnetic energy harvester is shown in Fig. 2.13. This type of energy harvesters utilizes the relative motion between the coil and magnet to generate some electric power. The amount of scavenged power depends on the number of coil turns, resistor, and the electromagnetic damping. The size of these parameters can significantly affect the extracted electricity. In

fact, shrinking the device leads to low magnetic fields and subsequently the generated current in the coil decreases.

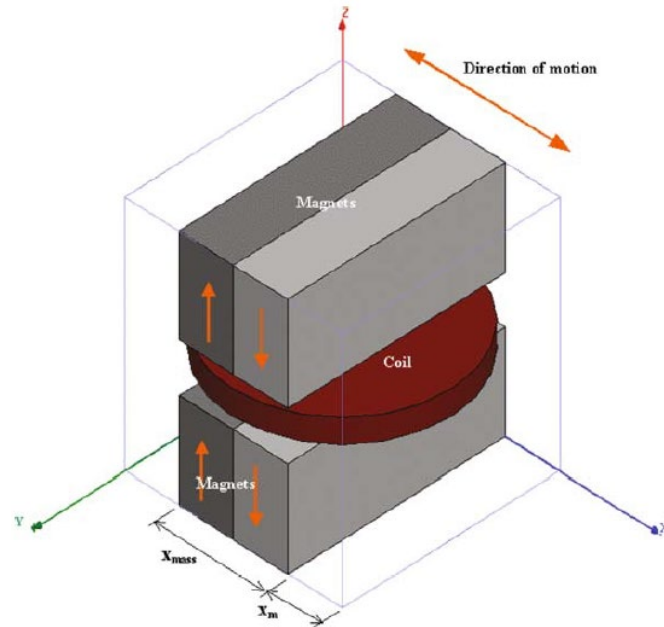


Fig. 2.13: Schematic of the prototype [38].

Electromagnetic energy harvesters are a sustainable candidate in large-scale energy harvesting systems. However, recently some plans have been also presented in small-scale systems. As a pioneer, Williams et al. [39] fabricated a small-sized electromagnetic energy harvester consisted of samarium-cobalt permanent magnet and planar gold coils. The device successfully produced $0.3 \mu\text{W}$. Kulkarni et al. [40] developed electromagnetic microgenerators with the help of integrating polarized NdFeB between two electroplated copper coils. Fig. 2.14 shows a schematic view of the prototype. With an acceleration of 8.829 m/s^2 , the presented design generated a power of 586 nW when resistor was 110Ω .

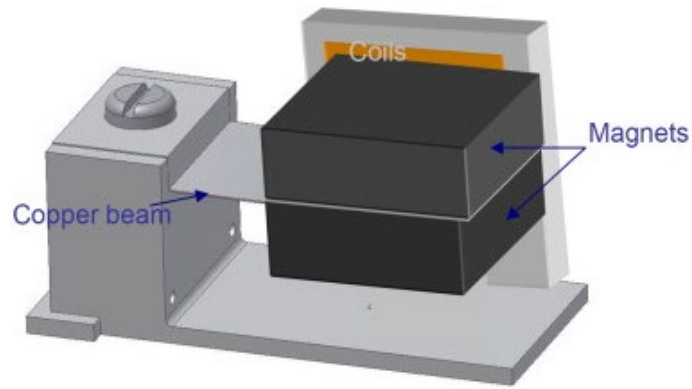


Fig. 2.14: Illustrating a schematic view of the prototype [40].

Donelan et al. [41] developed a cost-effective biomechanical energy harvester producing some electricity during human walking. The working mechanism is depicted in Fig. 2.15. The device mounted at the knee assists deceleration of the joint. The design can produce an output power of 5 W on each leg. One of the most promising application lies at prosthetic knees and ankles to help disabled people with walking.

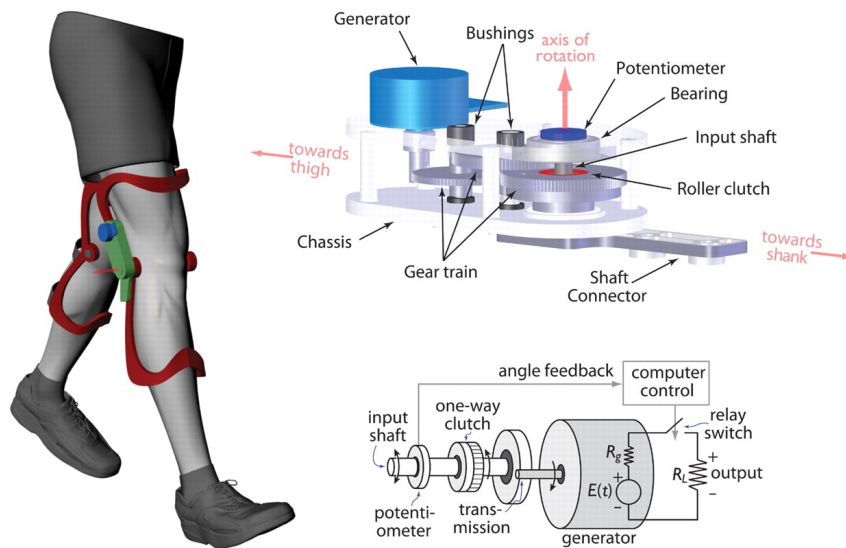


Fig. 2.15: Generating electricity during human walking [41].

With combination of multiple magnetic circuits and serpentine coil, a flat micro energy harvester, in millimeter scale, was fabricated by Cepnik and Wallrabe [42]. Fig. 2.16 shows the harvester generating an average power of $12 \mu\text{W}$. The design improved the generated power via increasing the flux gradient and maximizing the copper filling factor.

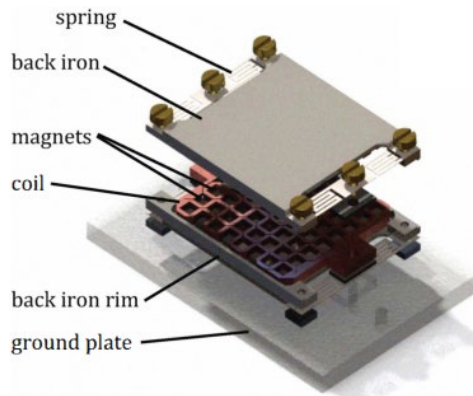


Fig. 2.16: Design of micro energy harvester [42].

Lee et al. [43] theoretically and experimental designed a standard AA size micro energy transducer. The device, shown in Fig. 2.17, was integrated with a power-management circuit. The generator consists of a spring mass system which uses laser-micromachined copper springs to convert vibration into output power.

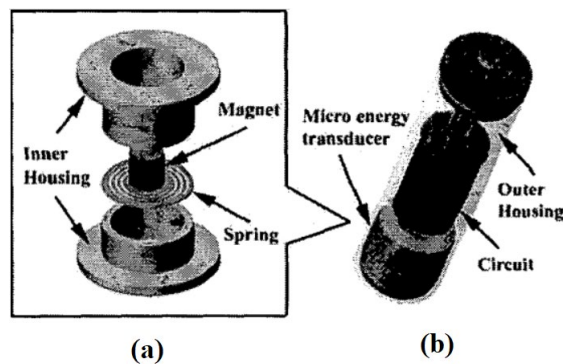


Fig. 2.17: (a) Inner section of the generator, and (b) AA size micro power generator (Copyright © 2003 IEEE) [43].

Briefly, electromagnetic energy harvesters are suitable choices for large-scale electricity production. But in micro and nanoscale, the size of structure, i.e. coil and magnet, is a bottlenecking problem.

2.2.3 Electrostatic Energy Harvesters

Electrostatic energy harvesters harness the mechanical energy done against the electrostatic force of a variable parallel capacitor. In other words, any vibration from the environment generates some electricity due to variation of capacitance of the parallel plate capacitor. The electrostatic energy harvesters can be fabricated in various configurations, as depicted in Fig. 2.18. The mechanism of all possible configurations is based on the motion of the central mass in respect to the substrate.

The most irritating problem with this type of energy harvesters is the fact that always an external motivation is needed to initiate the setup. One candidate can be the usage of an external voltage supplier. Another option is using electrets to generate a potential difference between plates.

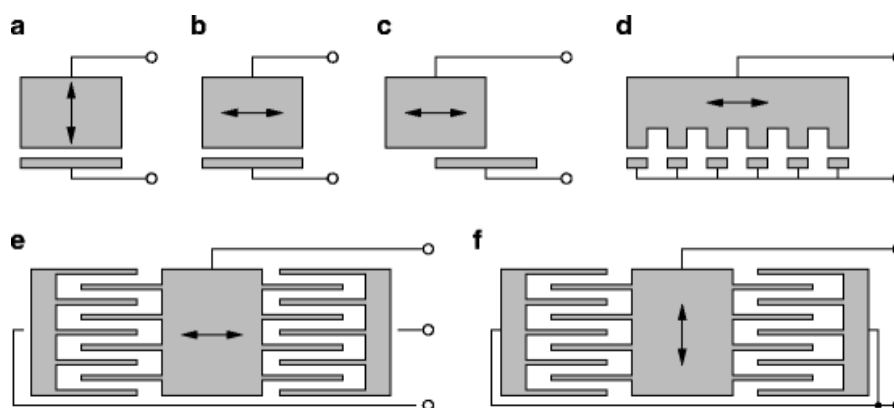


Fig. 2.18: Various mechanical designs for electrostatic energy harvesters [44].

In order to develop the capacitance of the traditional electrostatic energy harvesters, Hoffmann et al. [45] presented the triangular electrode structures, as shown in Fig. 2.19. This configuration for electrodes has two main merits. First, it provides a higher capacitance value. Furthermore, the presented design produces a nonlinear frequency response which is useful for broadband vibrations. Experimentally a 20 μF capacitor was charged to feed a transmission module.

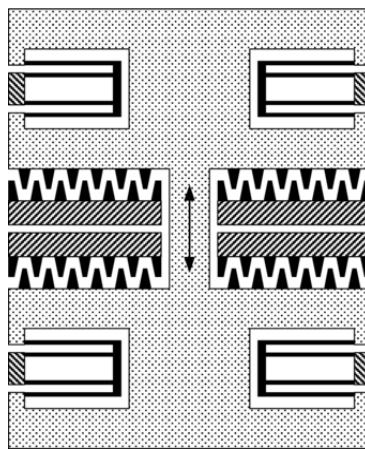


Fig. 2.19: View of the design including the triangular electrode elements and the direction of motion [45].

Tsutsumino et al. [46] used CYTOP as electret, and developed micro electric generators, as shown in Fig. 2.20. Because of the variation in the overlapping region, some charges move in the external circuit. In the setup, a spring is used to increase the amplitude of the oscillations. An output power of 37.7 mW and a voltage of 150 V during vibrations was reported.

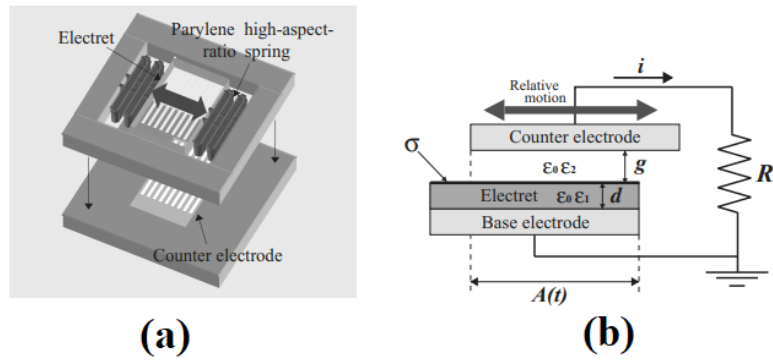


Fig. 2.20: Schematic drawing of (a) micro electret generator, and (b) working mechanism of electret generator (Copyright © 2006 IEEE) [46].

A rotary comb electrostatic energy harvester, depicted in Fig. 2.21, was presented by Yang et al. [47]. The energy harvester includes fixed and movable combs, ladder springs, and centric mass. When undergoing the vibration, the movable combs will engage inside the fixed combs from one side (i.e., side A), while moving away from another side (i.e., side B). this movement changes the capacitance and results in charge transfer between electrodes. The device converts low frequency planar vibrations from the ambient environment into an output power of $0.35 \mu\text{W}$ at matched resistors.

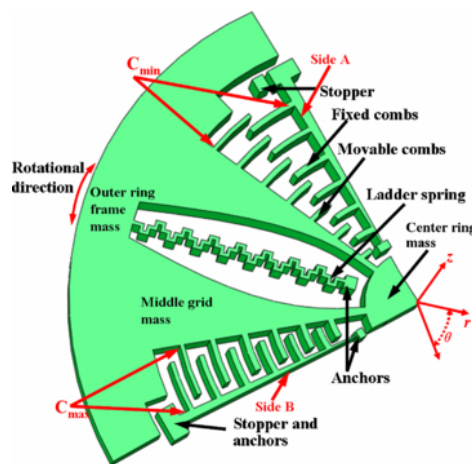


Fig. 2.21: Illustration of different parts of the electrostatic energy harvester [47].

The ambient environment offers a wide range of frequencies. Traditionally, the conventional energy harvesters are linearly designed. To meet the non-ideal cases, Nguyen and Halvorsen [48] suggested the usage of nonlinear springs for vibration energy harvesters, as shown in Fig. 2.22. They successfully harvested an average output power of 180 nW at an acceleration of 0.488 g. It was concluded that the nonlinear spring delivers more power comparing to the linear spring.

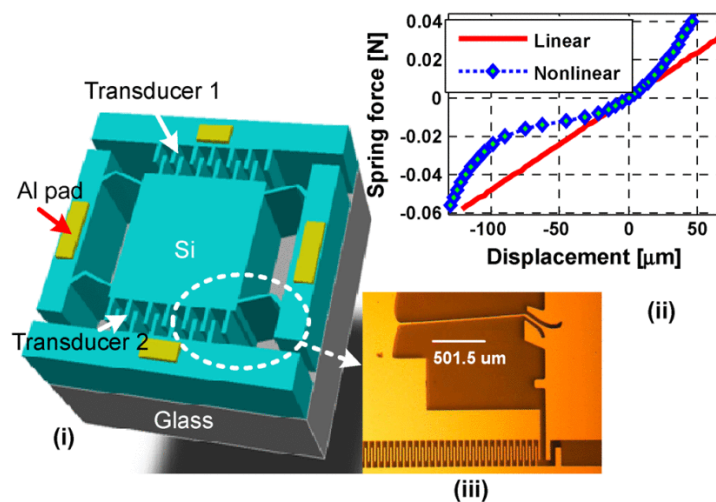


Fig. 2.22: Application of nonlinear springs for energy scavenging: (i) schematic view of the final design, (ii) impacts of nonlinearity on the spring force, and (iii) the electrostatic energy harvester connected to a nonlinear spring [48].

To summarize, because of some restrictions, electrostatic energy harvesters are not in the top priority for energy harvesting purposes. The first limitation is the low generated power output. Furthermore, for launching the system, the system relies on the external power supplier.

2.2.4 Triboelectric Energy Harvesting

Triboelectrification, as the procedure of transferring small-scale static electricity charges generated by friction contact between dissimilar films, has frequently been considered as an approach for accumulating energy from organic materials. During the contact, the triboelectrification phenomenon leaves some charges with opposite polarities on each surface. Those triboelectric charges can be generated between nearly any arbitrary pair of materials, encompassing semiconductors, conductors such as metals, and insulators such as non-ionic materials.

Triboelectric energy harvesters, as the most advanced technology for harvesting the electrical energy in micro/nano scales, work based on the triboelectrification principle. Some models in the literature have described contact electrification in detail [49-52]. Matsusaka et al. [51] explained the electron transfer during the metal-metal contact by utilizing the work functions (ϕ_1 and ϕ_2) and thermodynamic equilibrium law, as schematically drawn in Fig. 2.23.

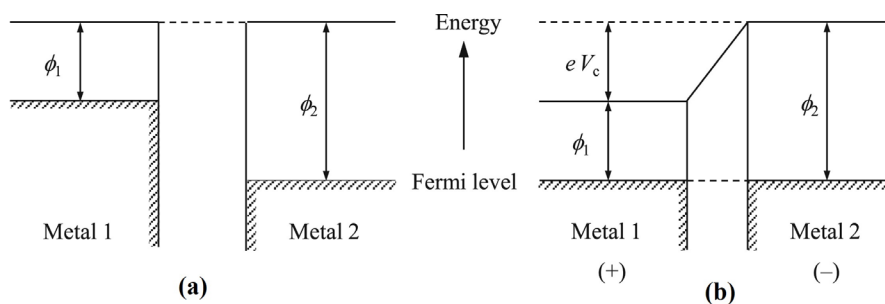


Fig. 2.23: Work functions of different metals: (a) before contact, and (b) after contact [51].

In their model, the transferred charge was expressed as the product of the potential difference and the capacitance between the two metals. When two different materials become into the physical contact, some charges with opposite sign are left on their surfaces. This phenomenon is because different metals and dielectric materials show different tendencies in

electron absorption or donation. This tendency can be categorized in a specific order known as triboelectric series [53, 54], as shown in Fig. 2.24.

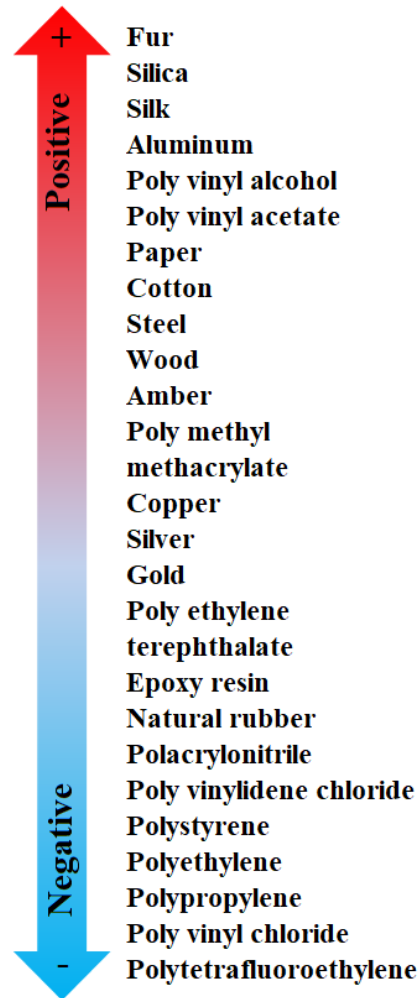


Fig. 2.24: Triboelectric series [53, 54].

When materials from the top and bottom of the triboelectric series are brought into contact, the top elements will acquire positive charges. Fig. 2.24 demonstrates which material acquires positive or negative charges. Furthermore, the greater the distance between positive and negative materials in the triboelectric series, the higher the value of surface charge density generated during the physical contact. Generally, triboelectric nanogenerators are categorized into two classes: in-plane sliding mechanism or in short as sliding mechanism

and out-of-plane contact-separation mechanism, shortly known as contact-separation mechanism. In the following sections, the working mechanism of both configurations are described.

Recently some attempts have been dedicated to unravelling fundamental working principle of nanogenerators. It was found that the output of nanogenerators can be described within Maxwell's displacement current [55]. Maxwell's displacement current is composed of two terms, i.e. ($J = \epsilon_0 \partial E / \partial t + \partial P / \partial t$). The first part ($\epsilon_0 \partial E / \partial t$) explains electromagnetic wave and the theory of light. Its application goes through radar, radio, and more importantly wireless communication. The second term ($\partial P / \partial t$) refers to polarization of media. This component is the base for introduction of nanogenerators, capacitors, self-powered sensors, and all new energy technologies. Then, the electric current of TENGs can be scrutinized by this term. Another theoretical development for nanogenerator was adding a new term (P_s) into the displacement vector [56]. This term contributes to electrostatic charges generating in triboelectricity and piezoelectricity. Considering this non-electric term, new formulation was driven to explain dynamics of nanogenerators. The new theoretical platform can extend Maxwell's theory in case of energy and sensors.

Many works have been presented to figure out contact-electrification phenomenon. However, a general platform to unravel charge transfer mechanism, particularly in case of metal-polymer and polymer-polymer, was still lack. Recently, electron-cloud-potential-well model proposed by Wang can explain the contact-electrification in all materials [57]. The suggested theory assume that the electron clouds are composed of localized electrons in specific atoms and molecules. Before contacting of dielectric materials, electrons cannot transfer since they are stuck in potential well, as shown in Fig. 2.25a. When materials become into touch, electron cloud hop from atom of the first material to atom of the second material, depicted in Fig. 2.25b. At lower temperatures, when materials are separated, most transferred

electrons are kept in the second material because these electrons face energy barrier to go back to the first material. Here, first material gets negative charges while the second one gets positive charges, as shown in Fig. 2.25c. As temperature increases, electrons can easily hop out of potential well, and go back to the original place or emit to air, illustrated in Fig. 2.25d. It should be pointed out that the proposed model introduces electron transfer as the dominant process in charge transfer.

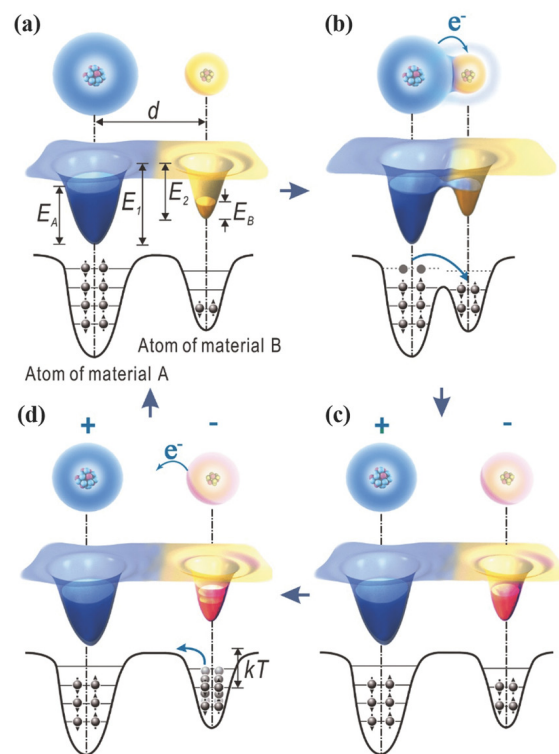


Fig. 2.25: Schematic of electron-cloud-potential-well model, (a) before contact, (b) in contact, (c) after contact, and (d) charge release from the atom at elevated temperatures [57].

Later, the model was extended into liquid-solid and liquid-gas conditions [58, 59]. To analyze charge transfer in the liquid-solid case, a two-step process was proposed. Initially, molecules in liquid have electron cloud overlap with atoms in solid. After that, ion transfer is the next step and the dominant process. In the liquid-gas state, gas molecules strike the liquid surface and make the electron cloud under pressure.

2.2.4.1 Sliding-mode TENGs

The sliding-mode mechanism of TENGs is schematically drawn in Fig. 2.26. Based on the contact charge and electrostatic induction, the theory of this type of TENGs is explained. First, some key points should be taken into consideration: (i) Dielectric substrates have different tendencies to accept or donate electrons, which, in its turn, lead to the aggregation of the net negative charges on the first layer (i.e., polytetrafluoroethylene (PTFE)) and the net positive charges on another part (i.e., polyamide (Nylon 66)); (ii) It is vitally important to consider that charges will remain on the contact region of triboelectric films due to the insulation properties of the polymers; and (iii) The generated positive and negative charges have the same density.

In the first half cycle of the sliding, two initially distinct dielectric films are in physical contact, as shown in Fig. 2.26a. In the fully overlapping position, the electric potential difference between the top and bottom electrode films is approximately negligible because the charges are formed at the surface of polymers. Therefore, as depicted in Fig. 2.26b, when the top substrate moves outward in relative to the bottom counterpart, the contact area of contact between the two polymers gradually decreases; hence, the opposite charges are separated, and a flow occurs between electrodes. The current continues as the outward sliding proceeds until both dielectrics are fully separated. This step leads to the aggregation of induced positive and negative charges on each electrode. Current output is measured by the relative sliding rate of the two films. The reverse procedure is depicted in Fig. 2.26d. Once top dielectric layer begins to slide inward, the charges that had appeared on the surface of the electrodes revert, due to the electrostatic equilibrium law. Thus, the flow is reversed, from the second to the first electrode, until the two surfaces completely overlap, i.e. Fig. 2.26a [60].

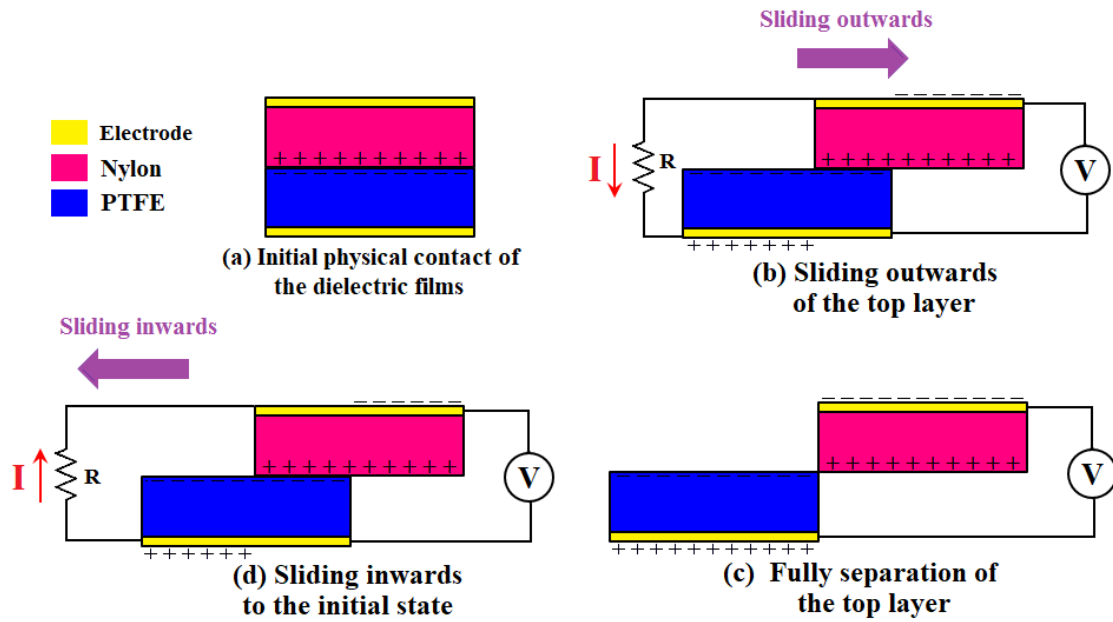


Fig. 2.26: Mechanism of the sliding-mode TENGs. (a-d) form a loop and the iteration of the loop generates electrical power [60].

2.2.4.2 Contact-Separation TENGs

Here, a brief description is given on mechanism of the contact-mode TENGs. Fig. 2.27 shows a schematic process of the contact-mode TENGs. The mechanism of this type of TENGs is similar to electrostatic energy harvesters. However, unlike to electrostatic energy harvesters which require to an external power supplier, the system is initialized through the electrification process. Initially, an external mechanical force is required to bring the top dielectric film on the bottom layer (Fig. 2.27a). As mentioned, when polymer substrates are in physical touch, the triboelectric effect will leave some positive charges on the first surface, while accumulating the absolute negative charges on the second layer, and only the surface of each dielectric film meets the generated positive and negative charges which have the same density. As soon as the top surface begins to separate in the direction normal, some electrons relocate from the top electrode to the bottom one, as shown in Fig. 2.27b. The more distance between two dielectrics, the more produced current. Generally, the value of the produced

current depends on different parameters including the contact area, thickness of the dielectrics, material of dielectric layers, and resistance load. When two dielectric films fully separate, the electron flow will stop. Fig. 2.27c shows the maximum position of the top dielectric at separation procedure, corresponding to the maximum expected charge. As the top film starts coming back to its initial position (drawn in Fig. 2.27d), the current is reversed, and will be zero when two dielectric films are brought into a full contact, as depicted in Fig. 2.27a.

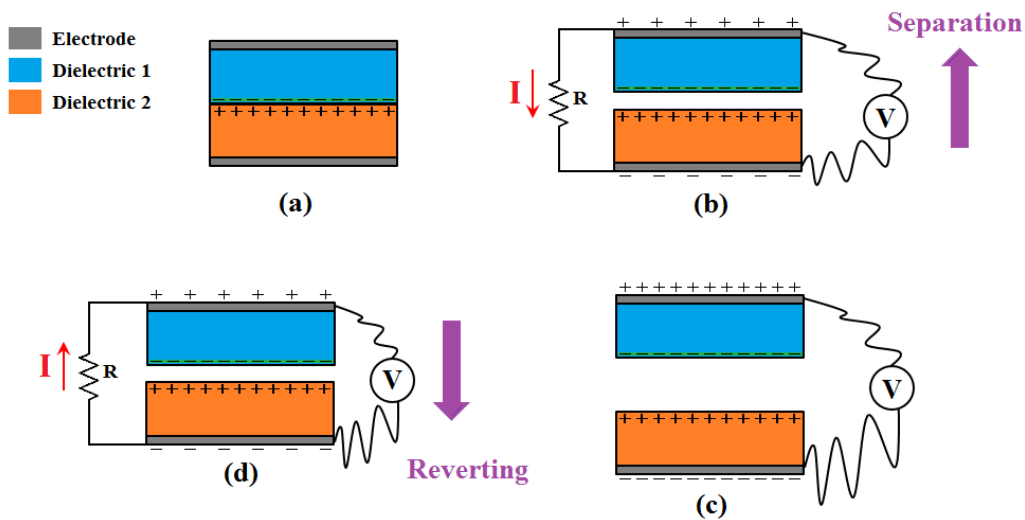


Fig. 2.27: Operating mechanism of the contact-mode TENGs.

2.3 Possible Applications of TENGs

Wang's research group at Georgia Institute of Technology, US is predominantly the precursor of the TENGs technology. At first, they presented the experimental and theoretical study of sliding-mode TENGs [61]. Nylon 66 and PTFE was used as dielectric layers and set up an experiment to find the pattern of voltage and current for sliding-based TENGs. Furthermore, they firstly introduced out-of-plane TENGs consisted of Al and Kapton as thin dielectric films [62]. The voltage-current response of TENG highlighted the ability of this

type of TENGs to be used in wireless MEMS/NEMS. In the following sections, a review is presented to reflect applications of the TENG system in the ambient environment.

2.3.1 Biomechanical Energy Harvesters

Energy harvesting from human motion and human biologics is highly interesting. Biomechanical energy has attracted attention of researchers to develop devices generating electricity from daily activities. The produced power is sustainable enough to drive watches, smartphones, wearable sensors, and implantable medical devices. External body movement, such as hand and foot motions, is a rich source for low-power generation aims. For harvesting vibration from human walking, Yang et al. [63] designed robust TENGs possessing rhombic gridding structures. Fig. 2.28 shows a schematic drawing and real application of the design. The fabricated TENGs working based on both contact-separation and sliding mode concepts was successfully implemented into a backpack to charge a mobile phone. The suggested paradigm considerably enhanced the output voltage and current outputs because of the application of multiplied rhombic gridding cells.

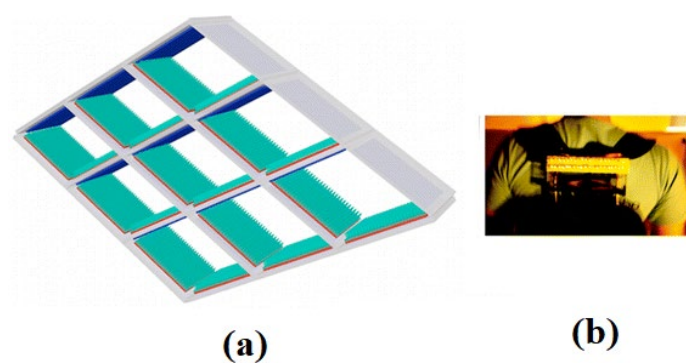


Fig. 2.28: Rhombic TENGs, (a) schematic view of the geometry, and (b) implementation of TENGs in a backpack [63].

In order to harvest mechanical energy, Bai et al. [64] fabricated flexible integrated TENGs. The proposed structure is depicted in Fig. 2.29. To increase the output power, the design has a multilayered zigzag structure. The TENGs was attached onto a shoe pad and commercial LEDs were successfully lighted up. A short circuit current (I_{sc}) and the open circuit voltage (V_{oc}) of 0.66 mA and 215 V was reported.

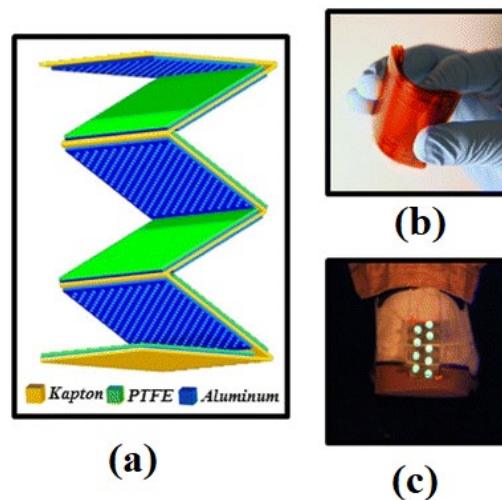


Fig. 2.29: Multilayered TENGs for scavenging energy from human motions, (a) schematic view, (b) bent TENG with finger, and (c) generated power during normal walking [64].

Besides the external body movement, as electronics progresses, implementation of devices and sensor in human and animal body is more prevalent for remote monitoring of patients, aiding organs etc. Human biologics periodically produces renewable source of energy in terms of heart beating [36, 65], breathing [66], lungs [67], and legs [68]. Zheng et al. [69] utilized vivo vibrations in breathing and drove a pacemaker. Fig. 2.30 shows the device. A pyramid patterned was selected for PDMS and Al as dielectric films to increase the output power. A power density of 8.44 mW/m² was reported. This study demonstrates the sustainability of TENGs towards implantable self-powered medical devices.

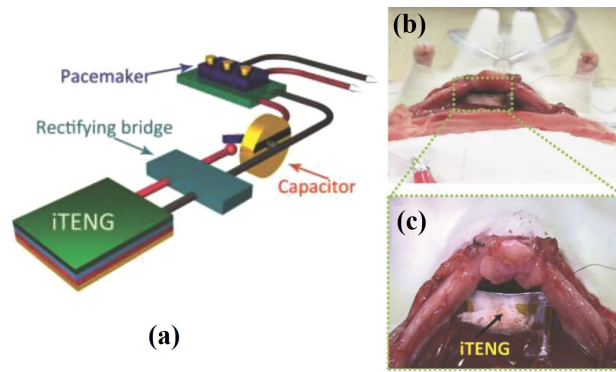


Fig. 2.30: TENG system for harvesting breathing energy, (a) and (b) the attached TENGs to live rat's diaphragm, and (c) enlarged photograph of the TENGs [69].

A triboelectric based pacemaker was fabricated and embedded in Pig's body by Ouyang et al. [70], as shown in Fig. 2.31. Corona discharge technology was used to increase the surface charge density on the contacting area. Biocompatibility and stability of the device was demonstrated through fatigue test and water penetration test. An in vivo open circuit voltage and short circuit current of ~ 65.2 V and 0.5 μ A was measured.

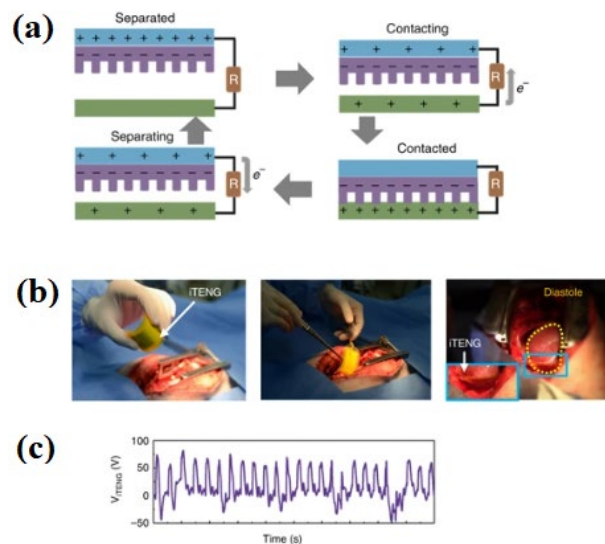


Fig. 2.31: (a) Working mechanism of the proposed TENG, (b) in vivo application of TENG, and (c) measured in vivo voltage [70].

2.3.2 Wind Based Energy Harvesters

Wind power as a ubiquitous and natural power source has been broadly utilized in large scale energy harvester systems. Wind energy turbines are the most well-established energy harvesters used to produce bulk amount of output power. However, complex setup and extravagant costs are the most challenges in the field. Recently, it was demonstrated that TENGs have the capability of power generation at the small scale from wind energy. The generated power can be used to drive some electronics and wireless sensors. Xie et al. [71] presented a rotary TENG to harvest wind energy. As shown in Fig. 2.32, the prototype includes a cup to convert wind power into rotational energy. Then, the produced rotational energy makes physical contact between PTFE and Al as triboelectric layers. At a wind speed of 15 m/s, the open circuit voltage, short circuit current and power density reach 250 V, 0.25 mA, and 39 W/m² respectively.

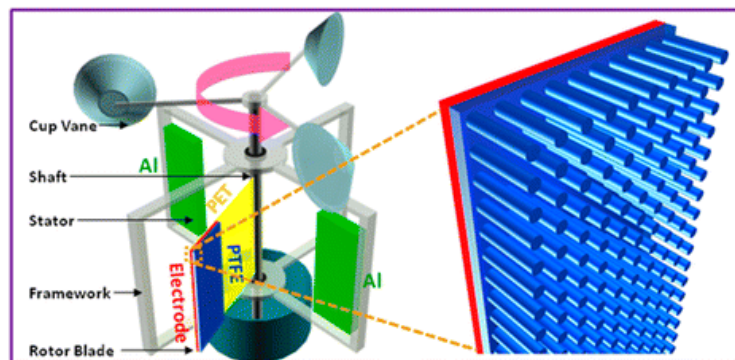


Fig. 2.32: Rotary TENGs for harvesting wind power [71].

A robust rotary TENG is presented by Zhu et al. [72] to harvest wind energy. The geometry, shown in Fig. 2.33, encompasses a rotator and stator consisted of fluorinated ethylene propylene (FEP) and copper as dielectric materials. The working mechanism is based on relative rotation between rotor and stator, leading to electron flow between electrodes. At a rotation of 1000 rpm, a globe light and 20 spotlights were driven. An output

power of 1.5 W was generated, and the device can effectively convert mechanical energy from wind power, tap water flow and normal body movement.

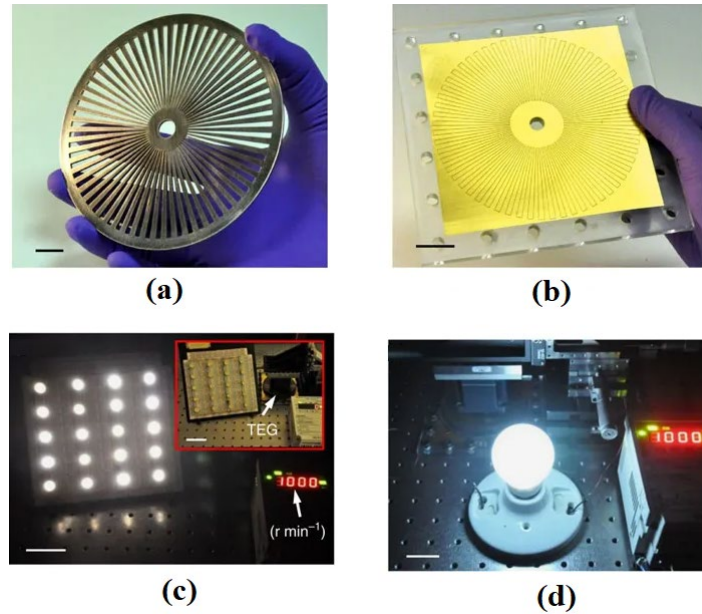


Fig. 2.33: High output rotary TENGs, (a) rotator, (b) stator, (c) lighting LEDs up, and (d) lighting up a globe [72].

Chen et al. [73] presented self-powered air cleaning system working based on sulfur dioxide (SO_2) and dust removal, as shown in Fig. 2.34. The system generates some electrical power from wind energy by means of a rotating TENG consisted of Kapton, copper and a grating structure for electrodes. The proposed air cleaner collects dust particles in air and oxidizes SO_2 without any byproduct. One potential application of such a device is for haze-fog environments.

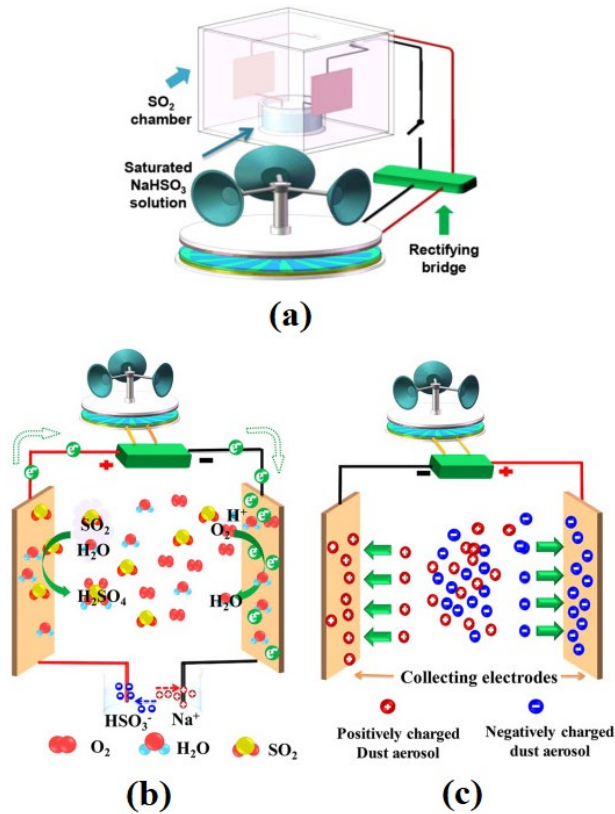


Fig. 2.34: TENGs for air cleaning, (a) view of the design, (b) principle for SO_2 removal, and (c) removal based on electrostatics [73].

Bae et al. [74] presented a flexible wind based triboelectric generator which uses flutter motion to scavenge wind energy. As Fig. 2.35 shows, a gold coated woven fabric was used to fabricate the triboelectric film. The flag periodically moves (similar to pendulum motion), and touches the plate, eventuating a flow of electrons between electrodes. With dimensions of $7.5 \text{ cm} \times 5.0 \text{ cm}$ at wind speed of 15 m/s , the TENG generated an output voltage, current and average power density of 200 V , $60 \mu\text{A}$ and 0.86 mW respectively.

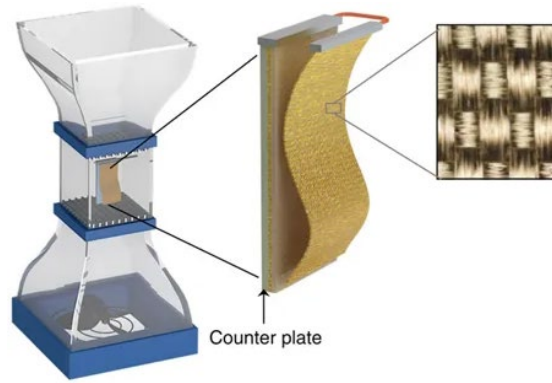


Fig. 2.35: Schematic drawing of wind tunnel and the structural design of a flutter-driven TENGs [74].

2.3.3 Water Based Energy Harvesters

Water energy is a renewable and clean type of energy which can be found in many locations. Many researchers have attempted to generate electricity from water energy. In order to harvest the water energy, Lin et al. [75] presented a new generation of TENG with interdigitative electrodes producing multiple electric outputs. Fig. 2.36 depicts different parts of the TENG and its working principle. A copper rod coated with polyurethane (PU) forwardly and backwardly roles on a PTFE layer covered with nine pairs of interdigitative electrodes. The surfaces of the PU and PTFE films are fabricated as porous structures and nanowire arrays, which provide an advantages of large contact area and efficient separation. A power density of 1.1 W/m^2 was obtained through one water wave impact.

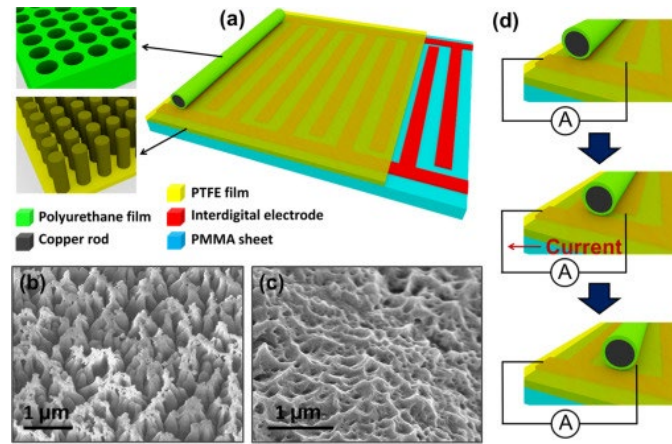


Fig. 2.36: (a) Schematic drawing of the proposed TENG, (b) and (c) SEM images of dielectric materials, and (d) working mechanism of the TENG [75].

Chen et al. [76] introduced a network design of TENGs to convert random wave energy into electricity, as shown in Fig. 2.37. The TENGs consists of Al and PFTE as dielectric materials coated with Cu as electrodes. The Al film was fixed at the middle, while two PTFE counterparts undergo periodic contact-separation movements. The proposed plan floated on the water surface and demonstrated the ability to produce large scale electricity. Based on the measured output of a single TENG, the TENG is expected to give an average power output of 1.15 MW from a 1 km² surface area.

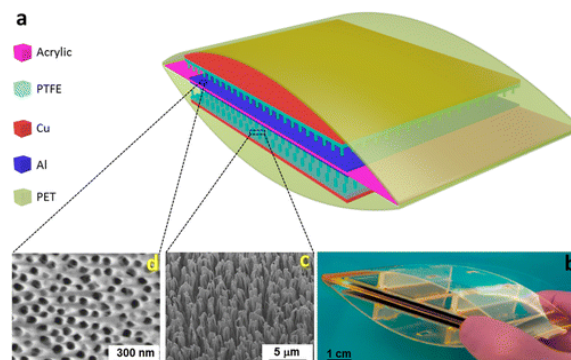


Fig. 2.37: Large scale electricity generation by TENG, (a) illustration of the TENG, (b) fabricated TENG, and (c) SEM images of PTFE and aluminum electrode [76].

For water wave energy harvesting, Liang et al. [77] introduced a transparent TENGs, depicted in Fig. 2.38. A glass substrate was chosen to guarantee transparency. PTFE is one dielectric material, and water here is another part. Becoming into physical contact, water will charge positively, while PTFE getting charged negatively. Based on the single electrode mechanism, the current will be appeared between electrode and the ground. A power density of 11.56 mW/m^2 was reported. This type of TENG can be integrated with silicon based solar cell, building glass, and car glass to use the energy of water flow.

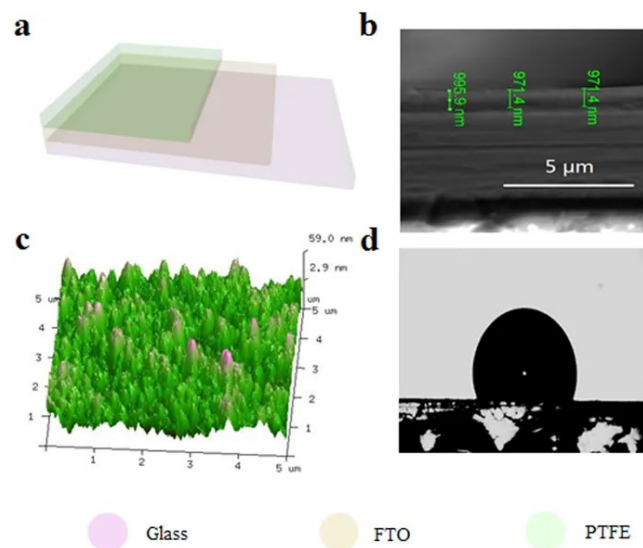


Fig. 2.38: Photograph of the proposed TENG, (a) schematic drawing, (b) SEM image of cross section of the TENG, (c) AFM image of PTFE layer, and (d) contact angle of the PTFE film [77].

Initially, TENGs were introduced to take the advantage of contact between two solid surfaces to generate some power. Another possibility is using water as a dielectric counterpart. Lin et al. [78] presented water based TENGs operating based on the contact electrification between PDMS and water (Fig. 2.39). During the contact, water was positively charged while PDMS got negative charges. Deionized water, tap water, and 0.6 M sodium

chloride were chosen as liquid dielectric layer. It was demonstrated that the deionized water delivers better performance than others, an open circuit voltage of 52 V, a short circuit current density of 2.45 mA/m² and a peak power density of nearly 0.13 W/m² were reported.

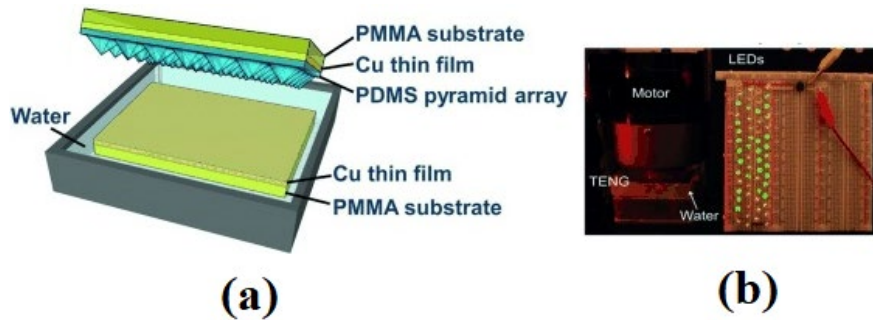


Fig. 2.39: Water based TENG, (a) schematic, and (b) generating power [78].

2.3.4 Wearable Energy Harvesters

Wearable energy scavengers harvest energy from human daily activities. Fabric based nanogenerators have been the focus of some research. Yang et al. [79] presented stretchable TENGs working at compressive as well as the stretching mode, as shown in Fig. 2.40. The device was made of two single-electron TENGs. PDMS substrates coated with copper as electrodes physically contacted with a wavy Kapton, resulted in a flow of electron between electrodes and the ground. The wavy structure for Kapton film was obtained by high-temperature annealing process. The designed TENG generated an open circuit voltage of 700 V, a short-circuit current of 75 μ A, and a power density of 5 W/m².

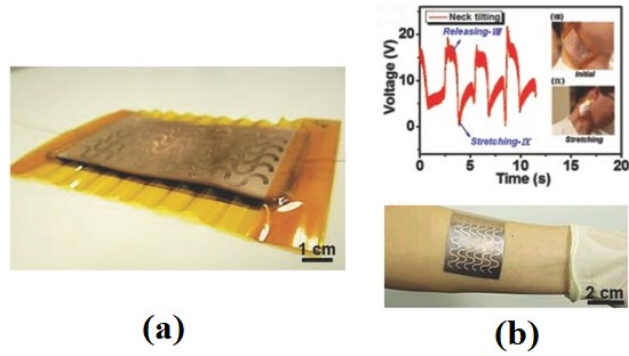


Fig. 2.40: Stretchable wavy-TENG, (a) fabricated design, and (b) applications on human hand and neck [79].

A high-output foldable wearable TENG was reported by Seung et al. [80], as shown in Fig. 2.41. The electricity generation relies on relative contact-separation movement of Ag-coated textile and nanopatterned PDMS structure on a textile. When Ag-coated textile touches the PDMS-based textile, some electrons flow from the Ag-coated textile to PDMS-based textile. Separating from each other, electrons moves to Ag-coated textile electrode. This contact-separation generates AC current. During measurement, a voltage and current of approximately 120 V and 65 μ A were collected.

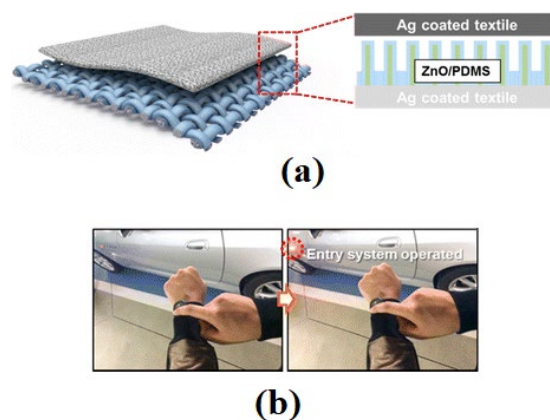


Fig. 2.41: Design of foldable TENG, (a) schematic of the wearable TENG, and (b) operation of a remote control [80].

Kim et al. [81] weaved fibers made of PDMS tubes and Al wires and introduced fabric-structured TENGs, depicted in Fig. 2.42. These fibers present high aspect ratio nanotextured properties resulted in stretchable and high output energy harvesters. The study showed that the internment of Al radius and PDMS tube radius leads to a high electric power. Sustainable voltage and current of 40 V and 210 μ A were obtained.

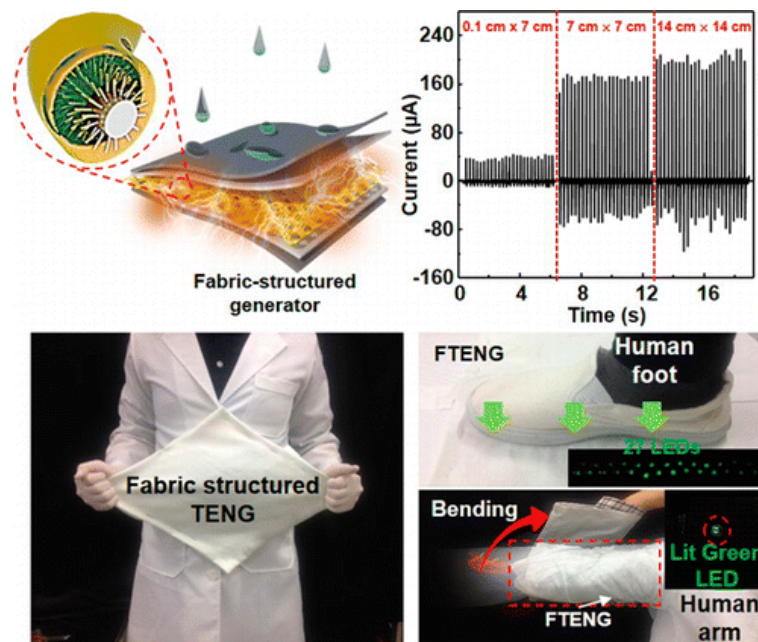


Fig. 2.42: Illustrations of stretchable fabrics for TENGs [81]

2.3.5 Self-powered Sensors

Sensors are being vastly used in various engineering circle to detect any change in properties such as force, pressure, vibration, etc. Sensors usually need external power suppliers to run. It is desirable for wireless nanosystems to be self-powered. This concept was first proposed by Wang in 2006 [25, 82]. The aligned ZnO nanowires were deflected when touched by an atomic force microscope tip. When nanowires bend, the piezoelectric and semiconducting properties of ZnO results in electrical current. The working principle is depicted in Fig. 2.43.

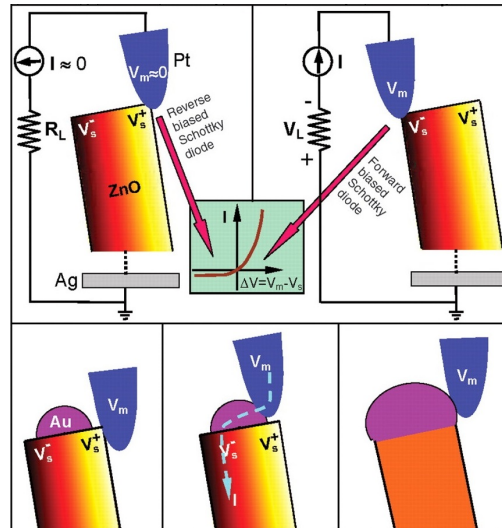


Fig. 2.43: The working principle of ZnO-based piezoelectric nanogenerator [25]

Next, a self-powered wireless transmitter was designed to demonstrate the adaptability and mobility of self-powered nanosensors [83]. A diagram of the self-powered system is depicted in Fig. 2.44. The system includes a nanogenerator, capacitor, and wireless transmitter. An external signal was detected by a phototransistor as a sensor. Then, the detected electric signal was wirelessly transmitted by a radio frequency transmitter. This work proved the applicability of self-powered systems for long distance data transmission.

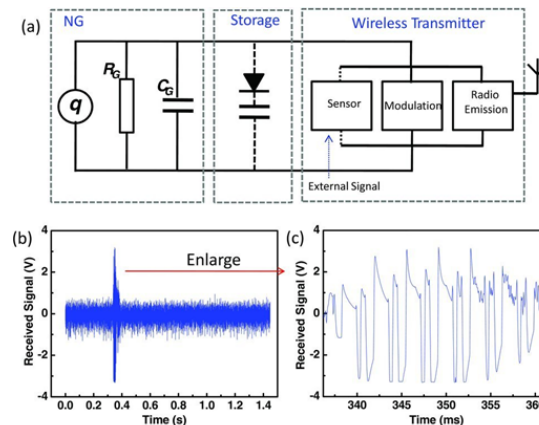


Fig. 2.44: (a) Illustration of the self-powered system, and (b) detected electric signal [83].

For further development of self-powered sensors, Wang's research group designed a self-powered environmental sensor for Hg^{2+} detection purposes, shown in Fig. 2.45 [84]. The proposed system includes ZnO nanowire-based nanogenerator, capacitor, and Hg^{2+} sensor. A flexible Kapton substrate was employed to enhance the number of contacting nanowires and Au electrodes. The sensor was composed of single-walled carbon nanotube networks. When mercury ions approached the networks, a current flow appears in the circuit, and LED will be lit up.

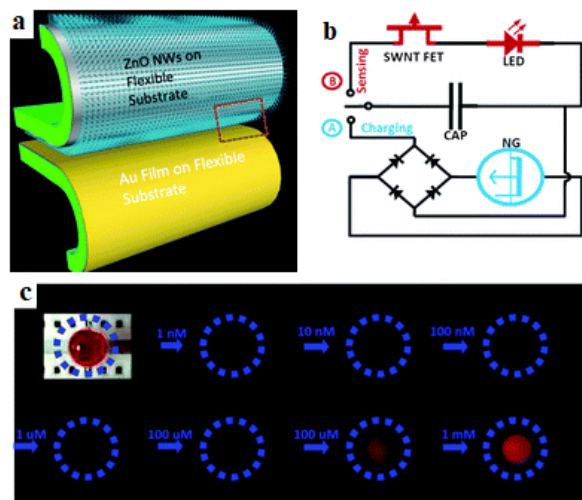


Fig. 2.45: (a) Fabrication of ZnO nanowires on flexible Kapton substrate, and (b) circuit diagram, and (c) detection results [84].

Since 2006, some other distinguished works have also been presented to develop application of self-powered systems, particularly emerge of vertically and laterally aligned ZnO nanowires-based nanogenerators [85, 86], self-powered patterned electrochromic supercapacitor [87], cantilevered-based self-powered sensors [88, 89], and flexible self-powered sensors [90-92].

As already mentioned, triboelectric mechanisms produce some electrical output when undergoing mechanical excitations. These structures can be considered as self-powered

sensors. Zhu et al. [93] designed a flexible triboelectric sensor generating a signal while coming into a physical touch. In fabrication process, FEP is the triboelectric film, and indium tin oxide (ITO) films play the role of electrode. When an object touches the TENG, FEP negatively is charged (Since FEP is at bottom of the triboelectric series) and the object gets some positive charges. After separation, the remained negative charges on the FEP makes an electric field between the top and bottom electrodes. Fig. 2.46 shows some applications of the proposed sensor. The proposed TENG sensor showed a high-pressure sensitivity of 44 mV/Pa in response to a low-pressure region (<0.15 KPa).

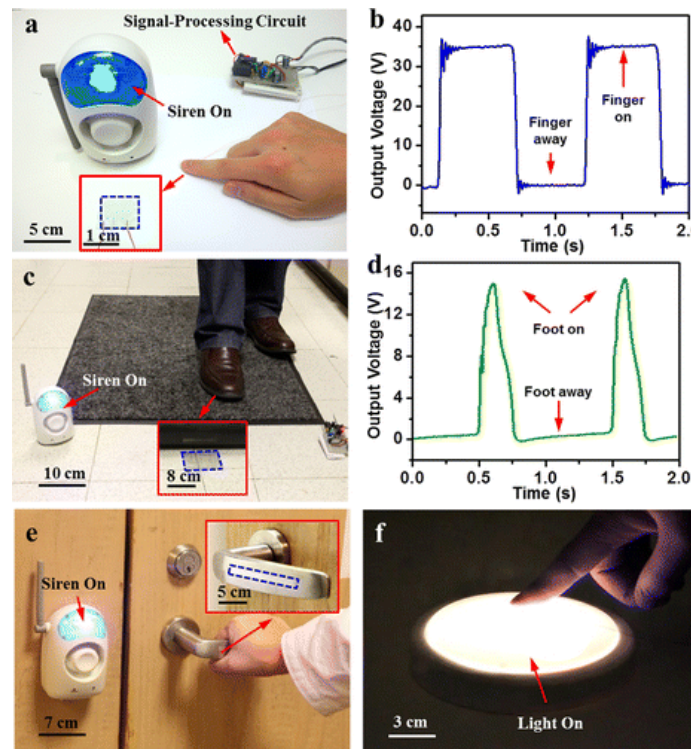


Fig. 2.46: The output and some applications of tactile triboelectric sensor [93].

Yang et al. [94] fabricated a skin based TENG sensor for touch pad applications. The working mechanism is based on the touch of human skin with a pyramid-surface PDMS connected to ITO films as electrode. As Fig. 2.47 shows, the device is highly flexible and transparent. The pressure and location of the touch can be estimated, opening a new horizon

in human-machinery applications. The sensitivity of the device is almost 0.29 V/kPa, with a generated power density of 500 mW/m².

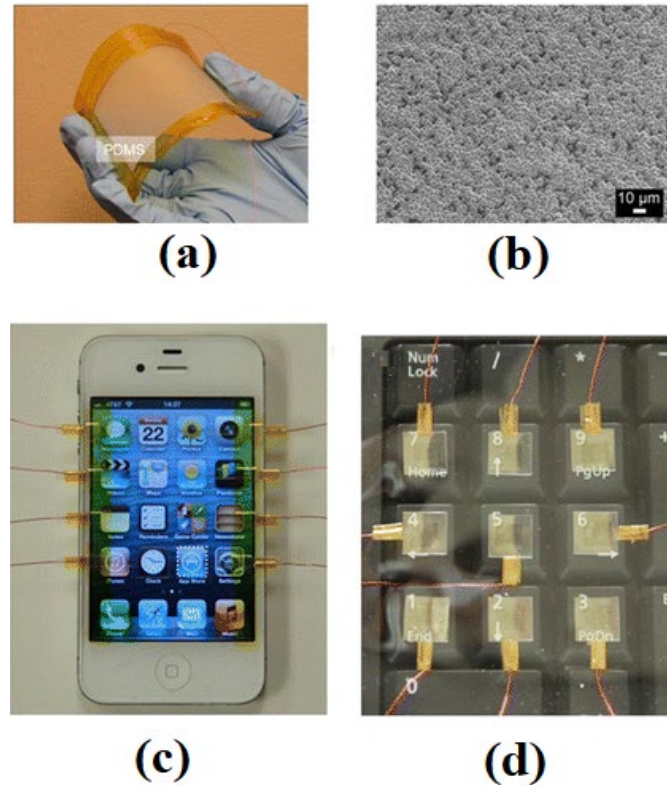


Fig. 2.47: Self-powered skin based TENGs, (a) fabricated design, (b) SEM of PDMS surface, and (c) and (d) touch pad applications of the sensor [94].

Another rich research area for TENG devices is detection of chemical changes. Li et al. [95] presented a novel self-powered sensor for phenol detection and electrochemical degradation. The device, shown in Fig. 2.48, uses titanium dioxide (TiO₂) nanowires and PTFE as triboelectric layers. β -cyclodextrin molecules were injected onto the TiO₂ film to enhance the triboelectrification process. To be specific, the surface charge density increases via some charge transfer from β -cyclodextrin to TiO₂. As a result, with a concentration of 80 μ M of β -cyclodextrin, the open circuit voltage and short circuit current surged by ten and six times, respectively. When TiO₂ and PTFE are become into physical contact, positive and

negative charges appear on TiO₂ and PTFE respectively. Then, cyclical contact and separation will result in AC current through an external resistance. To investigate the phenol detection, different concentrations of phenol were dropped on TiO₂ surface, leading to a decrease in the voltage and current with increment of phenol concentration. The proposed device showed a detection sensitivity of 0.01 μM⁻¹.

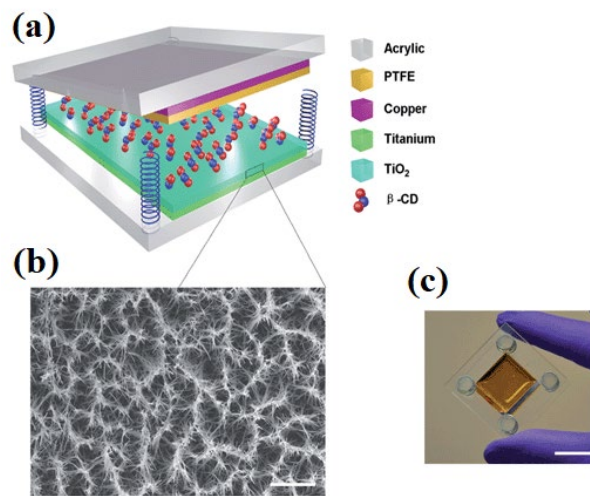


Fig. 2.48: (a) Schematic of the TENG sensor, (b) SEM of TiO₂ nanowires, and (c) fabricated TENG [95].

Lin et al. [96] presented triboelectric sensors for the detection of mercury (Hg²⁺) ions which are non-biodegradable and highly dangerous for human body. As depicted in Fig. 2.49, the TENG operating in contact-separation mode is composed of PDMS and Au films as triboelectric layers. 3-mercaptopropionic acid (3-MPA) was assembled onto Au nanoparticles as recognition element. Various concentrations of Hg²⁺ were dropped on Au film, then the TENG device was operated. While having Hg²⁺ on Au film, the surface current density decreases from 63 to 8 μA/cm². When detecting Hg²⁺ ions, the TENG cannot light up any LEDs. The device demonstrated a high-power density of 6.9 mW/cm², and the fabricated sensor has excellent potential for the detection of Hg²⁺ ions in the environment.

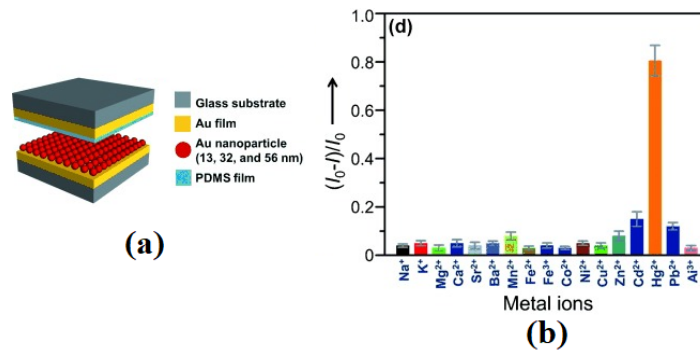


Fig. 2.49: Triboelectric based sensors for detection of Hg^{2+} ions [96].

The self-powered sensors for cardiovascular system characterization and voice detection were presented by Yang et al. [97], as shown in Fig. 2.50. The structure is simple and cost-effective since PTFE and Nylon were used as dielectric materials, and a thin film of ITO as electrode. When external force is applied on the PTFE surface, it gets physical contact with the Nylon film, resulting in charge transfer in the ITO film. The device was embedded on human body to measure arterial pulse and reflection of carotid artery. The sensor has the capability to be used in human health assessment and biometric authentication.

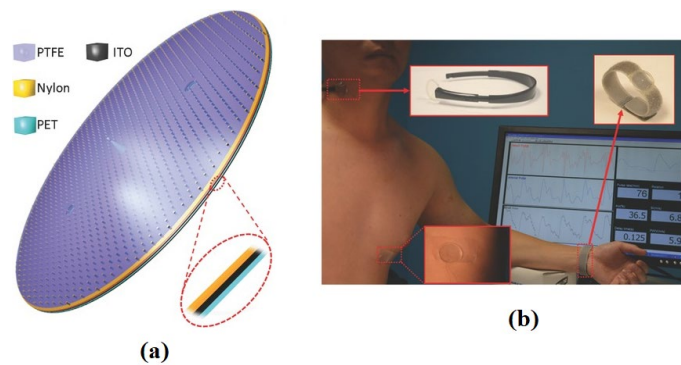


Fig. 2.50: Active sensors for human health assessment, (a) drawing of TENG sensor, and (b) application of sensor in human neck, chest and wrist [97].

Wu et al. [98] fabricated self-powered sensors for angular measurement using triboelectrification phenomenon (Fig. 2.51). The TENG mechanism has the single-electrode

configuration, encompassing a rotor rotating on a stator which is connected to copper film as electrode. It was demonstrated that the sensor generates a maximum open circuit voltage of 60 V.

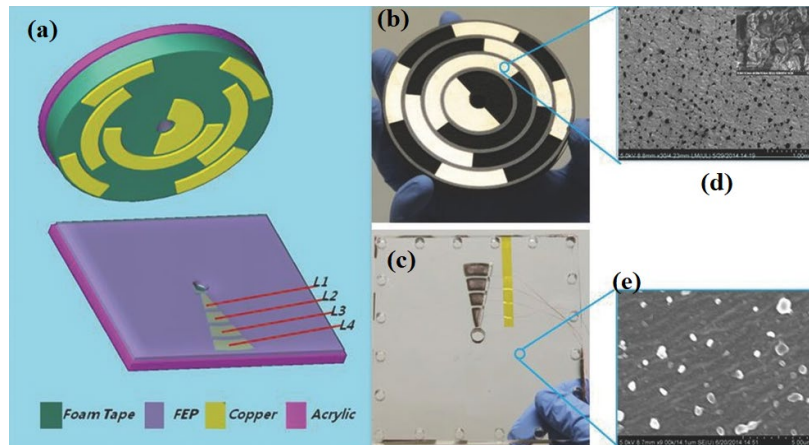


Fig. 2.51: Self-powered triboelectric sensor for angel monitoring, (a) illustration of the TENG device, (b) rotator, (c) stator, (d) SEM image of PTFE, and (e) SEM image of Cu film [98].

2.4 Optimization techniques

Optimization is obviously one of the most critical ingredients of intelligent systems. As a mathematical approach, optimization theory is a platform seeking for the “best” solution in the problem’s search space. In an engineering circle, optimization provides algorithms to meet well-structured problems in conjunction with the analysis of those algorithms. Firstly, problems are required to be scrutinized in terms of variables, objective function, and constraints. Then, based on the provided information, the problem can be treated as constrained or unconstrained optimizations. In unconstrained problems, the best solutions for objective function are found without any constraints. However, in unconstrained cases, solutions are sought on the search space restricted by some inequality constraints. Generally

computational optimization techniques can be mainly summarized into classes: iterative methods and heuristics. The recent advancement on these methods are reviewed here.

2.4.1 Iterative methods

Iterative optimization approaches utilize an initial guess to deliver an optimum in finite number of steps. The most popular methods are Newton's method, Ellipsoid method, Interpolation method, Interior-point method and coordinate descent [99, 100]. Because of some bottlenecking issues, including low rate convergency, requiring solving a large system of equations at each step, and no guarantee on a converge solution, these classic methods are not popular in advanced engineering problems. Besides the iterative solutions, heuristics are employed to recognize the local and global optimum within the pre-defined search space.

2.4.2 Heuristics

Heuristics is an efficient substitute to optimize engineering problems where classic methods fail to deliver the optimum. The most popular ones are reviewed here.

2.4.2.1 Differential evolution

Differential evolution (DE) is an evolutionary algorithm suits for non-differentiable, non-continuous, and non-linear optimization problems. This method works based on the mutation, recombination, and selection [101]. The algorithm has been developed to solve various engineering problems, but not limited to: presenting a multi-view version of differential evolution to solve engineering problems [102], developing an adaptive relaxation of constraints [103], adapting differential evaluation for managing flexibility in capacity planning for engineering systems [104], presenting high convergent rate of differential evolution for non-linear chemical processes [105]. Although DE presented some merits into

optimization theories, it still suffers from issues like non-linear separable functions [106] and getting stuck in local optimum regions [107].

2.4.2.2 Artificial bee colony

Artificial bee colony (ABC) algorithm was proposed by inspiring from social behavior of honeybee swarm. In this method, three different of bees, namely employed bees, onlookers and scouts, work together to deliver the best solution [108, 109]. This algorithm has met some structural optimization problems, encompassing: improving generated power of photovoltaic systems [110], maximizing the power generation of hybrid photovoltaic-wind systems [111], marine dynamic positioning system [112], energy management for industrial mobile devices [113], enhancing the fatigue life of alloys [114], image processing aims [115], optimize the fuel cost and emission in power systems [116], and so on. Although the ABC algorithm shows a very good exploration, its exploitation is still insufficient [117, 118]. Moreover, getting stuck into a local optimum region and also slow convergence rate is another issue [119].

2.4.2.3 Genetic algorithm

Genetic algorithm (GA) was inspired by theory of natural evolution. Three main principles include: (i) selection rules to choose the individuals as parents to generate next generation, (ii) Crossover rules to combine parents, and (iii) Mutation rules to make some changes in parents. Here, the next generations are produced by selecting the fittest agents through crossover and mutation process [120, 121]. This algorithm has successfully met many engineering problems such as: optimizing a torque arm [122], analyzing control systems [123], fixing transportation problems [124], minimizing energy consumption in warehouses [125], etc. It should be noticed that GA cannot meet some optimization categories. The first

issue is that of the GA-deceptive functions [126], leading to unsuitable chromosomes. The second prevalent problem is genetic drift [127]. It often occurs when attributing small population to GA, making GA falling into local optimization regions. Other unfavorable problems are no guarantee on response time and performance of individuals [128, 129].

2.4.2.4 Particle swarm optimization

Particle swarm optimization (PSO) is a population-based optimization strategy inspired by behavior of social animals such as flocks of birds. It guesses a solution in the search space, and based on the governing mathematics, it iteratively attempts to converge towards the global best [130-132]. Over the last decade, researchers have implemented this approach to optimize the wind turbine [133], enhance the energy efficiency for tissue paper mill [134], improve heating ventilating and air-conditioning systems [135], develop micro-grid power systems [136], improve renewable energy penetration from wind and solar power sources [137], etc. Comparing to traditional optimizers, PSO has been gaining a wide attention in optimization purposes due to (i) bright robustness and applicability, (ii) excellent distribution ability, (iii) rapid convergency rate, and (iv) adaptability to hybridize with other algorithms [138, 139].

2.4.2.5 Grey wolf method

Grey wolf (GW) is a recently-established optimization algorithm motivated by hunting mechanism of grey wolf [140]. For simulation purpose, four agents including alpha, beta, delta and omega are engaged in searching for prey, encircling prey, and attacking prey. The algorithm was tested on 29 different functions, presenting better performance comparing to other optimizer approaches [140]. Some engineering optimization cases were also analysed by the GW method. Taking advantages of the GW method, Shilaja and Arunprasath

optimized the power loss of renewable energy systems working based wind and solar sources [141]. Lara-Montaña and Gómez-Castroa [142] conducted a study to find optimized characteristics for a heat exchanger, offering the minimum cost for heat energy transmission systems. Miao and Hossain [143] presented an efficient numerical platform working based on the GW method and introduced the optimum location and size of the micro-grid storage system. The optimality system was derived for hybrid power generation to minimize the costs by Yahiaoui et al. [144]. Comparing to other traditional strategies, the total costs has been significantly reduced by attributing a proper value to the number of PV panels. Various studies demonstrated the superiority of the GW method over other metaheuristic algorithms in terms of local optima avoidance, accuracy, and convergence [140, 145-147].

2.5 Significance of the research

Form the above-mentioned introduction, piezoelectric and triboelectric based energy harvesters are the most efficient strategy for supplying electrical energy for electronic components. Electricity generation based on the triboelectric effects is a green and renewable pathway generating sufficiently power output for wireless micro/nano electronic devices. The theories regarding the working mechanism have been extensively explored, though the urgent need for improving the characteristics of energy harvesters still lacks. The main effort of the current research is **“How different strategies can be applied in order to improve sustainability and efficiency of the current energy harvesters?”**. To meet this problem, at first, mechanisms of piezoelectric and triboelectric generators are fully recognized. Then, the active parameters affecting the output response are determined. These parameters range from geometry issue to inherent characteristics.

In case of piezoelectric energy harvesters, an effort is dedicated to scrutinizing how material properties synthesize new smart systems exhibiting higher levels of electrical energy

while possessing considerably lower weight. To achieve such an aim, it is assumed that the material properties of the piezoelectric medium would be graded through the thickness and the mechanical, electrical, and thermal fields would have their own independent gradient indexes. If we nominate the grading indexes as design variables, the material elements of the solid should be appropriately functionalized, avoiding any problems stemming from the low electrical outputs of shell structures in energy-harvesting applications.

Moreover, the output power of TENG system is highly dependent on the electrification process and its characteristics. The material of dielectrics considerably affects the surface charge density generated on the surface. As it was mentioned, highly positive and negative selection from triboelectric series results in higher surface charge density. The choice of materials depends on the availability of materials, application, fabrication restrictions and cost. In addition, geometry of the TENGs is another dominant parameter affecting the efficiency and output power. The geometry includes the type of the configuration, the thickness of the dielectric films, and the contact area. The kinematics of the motion of the TENGs, i.e., acceleration and speed rates, is the next crucial factor. Usually, the higher rate of motion, the higher harvested energy. The last design step is that of the electrical specifications of the TENGs which needs to be scrutinized in order to scavenge the maximum electrical power.

As already mentioned, Wang's research group, at Georgia Institute of Technology, is the pioneer and the most productive place for fabricating the TENG devices, resulted in many patents and innovations in biomedical devices, wearable electronics, water/wind based energy harvesters, and self-powered sensors. A review on his publications shows they have being focused on experimental studies on the TENG devices. Undeniably, experimentally investigation on different materials, working conditions, electrical specification, and geometry parameters is time-consuming and needs different experimental setups. To fill the

gap, simulation and optimization approaches can be employed to predict the TENGs' output and introduce the optimized values for TENGs' characteristics.

For simulation purposes, merged algorithms of advanced optimization schemes with mathematical solvers are presented to discover all possible search space. Analysing the active parameters under such advanced platform leads to promising nanogenerators producing higher level of power output for micro/nano electronic devices. The concept discussed in this thesis, is a general outline, which can easily be extended to all configurations of TENGs and piezoelectric energy harvesters. The presented results significantly improve the power density, obtained voltage and current of nanogenerators, opening a new horizon for straightforwardly and cost-effectively fabrication process of TENGs and piezoelectric nanogenerators.

Piezoelectric energy harvesters

3.1 Introduction

The previous chapter showed some applications of piezoelectric materials in energy harvesting approaches. In fact, piezoelectrics are highly sensitive to the external pressure. As it was already mentioned, when piezoelectric materials undergo the external force, some electric power will be generated. Furthermore, thermal gradient can also result in some power output in piezoelectric systems. Here, we use the piezoelectric materials undergoing pressure and thermal gradient in order to introduce high performance energy harvesters. For novelty purposes, we take the advantages of functionally graded materials (FGMs) to introduce piezoelectric-based energy scavengers with non-uniform materials properties, harvesting more electrical output.

3.2 FGMs

Conventional engineering materials cannot meet the required material properties in critical applications such as microelectronics, power generation, bioengineering and aerospace. In such applications, a higher resistance against electro-thermo-elastic stresses or chemical resistance is required. For example, gears not only should be sufficiently tough inside to resist the fracture, but also should be hard enough on outside to withstand wear [148]. In fact, multiple functions of materials properties is required. Traditional techniques, such as surface treatment or hardening techniques, were initially used to improve the properties. However, issues such as abrupt interface or interfacial stresses are still remained [149]. Later alloying and powder metallurgy were used to arrange various properties within a media [150]. As a

modern approach, composite materials tailor the material properties over the entire geometry. But for laminated structures, the problems of inter-laminar stresses and interface discontinuity are remained.

In 1984, the concept of FGMs was applied in design process of space shuttle in order to improve the thermal resistance [151]. Generally, FGMs provide a platform to control material response to deformation, fracture, wear, etc [152]. They also offer many benefits compared to conventional composite materials including utilizing different material systems e.g. ceramic/metals [153], removing interface problem in multi-laminar structures [154], and offering bio-applications opportunity to engineering designs.

Here we use the FGMs concept to introduce piezoelectric-based energy harvesters scavenging energy based on the applied pressure and thermal motivations. The grading index of the FGMs makes a link between the thermo-elastic and electric fields. Two case study are investigated in this chapter. The first one is spherical shells made of FG piezoelectric materials, undergoing mechanical pressure and thermal excitation. The role of the FG piezoelectrics as sensor and actuator is examined, and thermo-electro-static responses are drawn. In the second study, a cylindrical geometry is chosen. An optimization platform is presented to maximize the electric output by means of the FG rule.

3.3 Spherical piezoelectric smart shells

Two laminated smart shell types are considered in this study, called shell 1 and shell 2. Shell 1 is a two-layered shell made of a host FGM layer covered with a layer of PZT-4 perfectly bonded to its outer surface. Shell 2 is a includes three layers, with one-layer FGM host covered by a film of $\text{Ba}_2\text{NaNb}_5\text{O}_{15}$ and a layer of PZT-4 perfectly bonded to its inner and outer surfaces respectively. A sectional view of shell 1 and shell 2 and the spherical coordinates are shown schematically in Fig. 3.1.

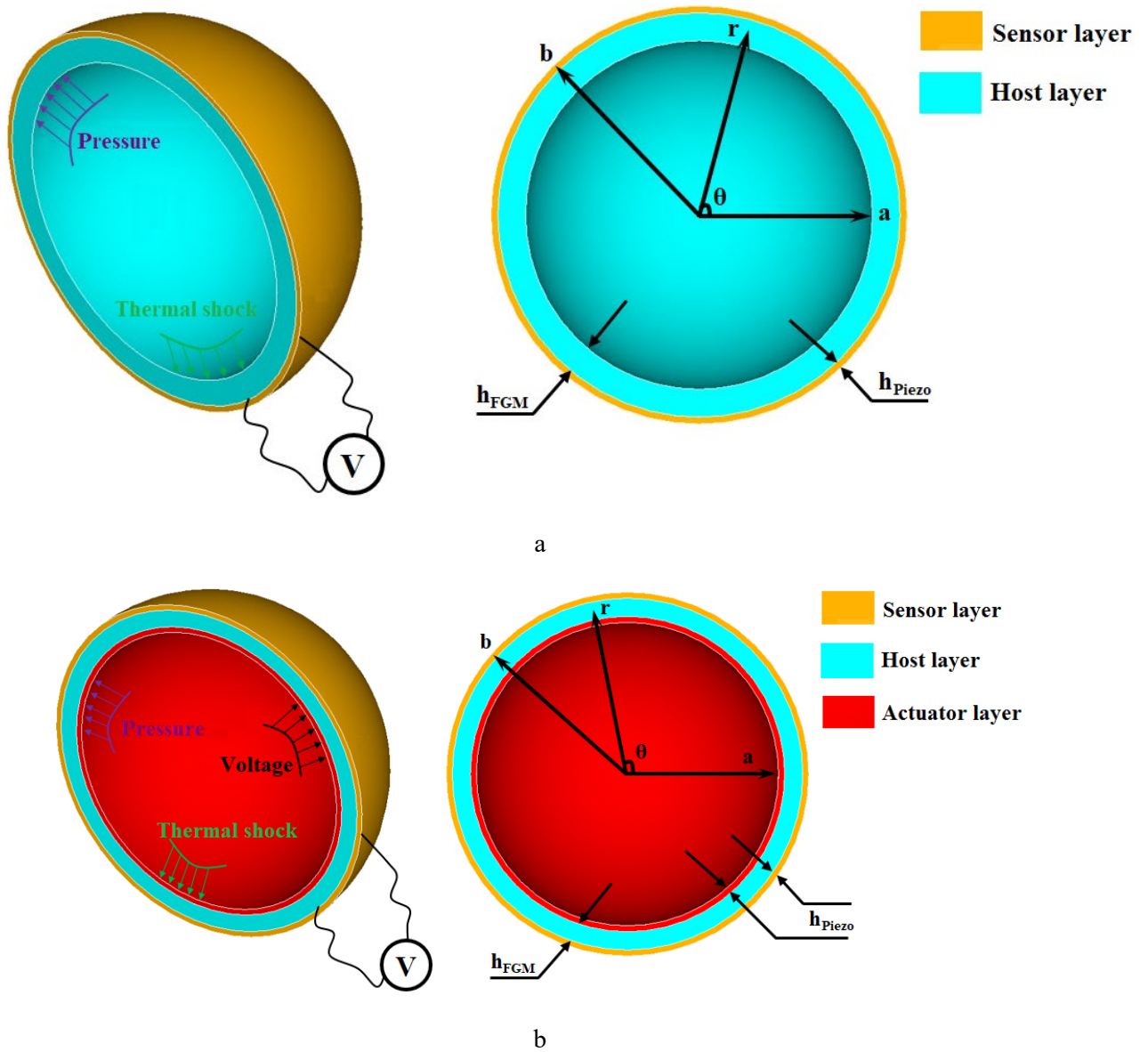


Fig. 3.1: Sectional view of geometry and coordinates of the laminated shell of (a) shell 1, a host FGM layer covered with a layer of PZT-4 bonded to its outer surface, and (b) shell 2, one-layer FGM host covered by a film of $Ba_2NaNb_5O_{15}$ and a layer of PZT-4 to its inner and outer surfaces respectively.

3.3.1 Piezoelectric layers

The linear constitutive relations of a piezoelectric material subjected to mechanical stress and electric and thermal fields are considered as [155]:

$$\boldsymbol{\sigma} = C\boldsymbol{\varepsilon} - e^T \boldsymbol{\Omega} - \lambda T, \quad \mathbf{D} = e\boldsymbol{\varepsilon} + \eta\boldsymbol{\Omega} + PT \quad (3.1)$$

where $\boldsymbol{\sigma}$ and $\boldsymbol{\varepsilon}$ denote stress and strain fields, respectively; C , e , η , λ and P represent elasticity, piezoelectric, dielectric permittivity, thermal elastic coupling and pyroelectric tensors, respectively. The radial components of the electric displacement (\mathbf{D}) and electric ($\boldsymbol{\Omega}$) fields are D_r and Ω_r , respectively. Also, T explicates the temperature change of the spherical shell.

The constitutive equation, Eq. (3.1), expresses the converse and direct piezoelectric effects. For a shell made of non-piezoelectric material, $e=\eta=P=0$ are set. In essence, the real application of the proposed study lies at heart of structural health monitoring, damage detection and sensory and actuary utilizations. In such applications, a thin film of piezoelectric materials is deposited on the structure. Here, in comparison with FG layer, a very thin film of piezoelectric materials has been implemented into the structure ($h_{\text{piezo}}/h_{\text{FG}} \approx 0.1$). The following references can evidently confirm the assumption [156-158]. Then, the properties of piezoelectric materials are assumed to be constant and independent of the temperature. It is also noted that the piezoelectric sphere is spherically isotropic [159, 160].

The governing equation of the spherical coordinate system in the absence of body force is [161]:

$$\frac{\partial \sigma_r}{\partial r} + \frac{2(\sigma_r - \sigma_\theta)}{r} = \rho \frac{\partial^2 u}{\partial t^2} \quad (3.2)$$

where ρ and t represent the density of the shell and time respectively. The governing equation of the electrostatic charge is:

$$\frac{\partial D_r}{\partial r} + \frac{2D_r}{r} = 0 \quad (3.3)$$

In our studies, the thickness of the piezo film is 5% of the host layer, and the ratio of the mid-plane radial to the thickness is almost 5. Then, thick shell theory is used to drive the strain-displacement equation for the geometry [162]. The strain-displacement and the electric field-electric potential relations of a spherically isotropic pyroelectric medium are defined as:

$$\varepsilon_r = \frac{\partial u}{\partial r}, \quad \varepsilon_\theta = \varepsilon_\varphi = \frac{u}{r}, \quad \Omega_r = -\frac{\partial \psi}{\partial r} \quad (3.4)$$

where u and ψ account for the radial displacement and electric potential, respectively. By combining Eqs. (3.4) with (3.1), the definitions of the radial stress, circumferential stress and electrical displacement components are obtained in terms of the radial displacement, electric potential, and temperature fields.

$$\begin{aligned} \sigma_r &= C_{11} \frac{\partial u}{\partial r} + 2C_{12} \frac{u}{r} + e_{11} \frac{\partial \psi}{\partial r} - \lambda_{11} T \\ \sigma_\theta &= C_{12} \frac{\partial u}{\partial r} + (C_{22} + C_{23}) \frac{u}{r} + e_{12} \frac{\partial \psi}{\partial r} - \lambda_{12} T \\ D_r &= e_{11} \frac{\partial u}{\partial r} + 2e_{12} \frac{u}{r} - \eta_{11} \frac{\partial \psi}{\partial r} + P_{11} T \end{aligned} \quad (3.5)$$

By substituting parameters of the above equations into Eq. (3.2), governing equations are obtained in terms of the displacement fields, electric potentials, and temperatures of the piezoelectric layer. Hence, the piezoelectric field equations are found to be:

$$\begin{aligned} C_{11} \frac{\partial^2 u}{\partial r^2} + 2C_{12} \left\{ \frac{1}{r} \frac{\partial u}{\partial r} - \frac{1}{r^2} u \right\} + e_{11} \frac{\partial^2 \psi}{\partial r^2} - \lambda_{11} \frac{\partial T}{\partial r} + \frac{2}{r} \{ C_{11} \frac{\partial u}{\partial r} + 2C_{12} \frac{u}{r} + e_{11} \frac{\partial \psi}{\partial r} - \lambda_{11} T \} \\ - \{ C_{12} \frac{\partial u}{\partial r} + (C_{22} + C_{23}) \frac{u}{r} + e_{12} \frac{\partial \psi}{\partial r} - \lambda_{12} T \} = \rho \frac{\partial^2 u}{\partial t^2} \end{aligned} \quad (3.6)$$

$$e_{11} \frac{\partial^2 u}{\partial r^2} + 2e_{12} \left\{ \frac{1}{r} \frac{\partial u}{\partial r} - \frac{1}{r^2} u \right\} - \eta_{11} \frac{\partial^2 \psi}{\partial r^2} + P_{11} \frac{\partial T}{\partial r} + \frac{2}{r} \{ e_{11} \frac{\partial u}{\partial r} + 2e_{12} \frac{u}{r} - \eta_{11} \frac{\partial \psi}{\partial r} + P_{11} T \} = 0 \quad (3.7)$$

3.3.2 Host layer

It is assumed that the host shell is made of isotropic and FG material. Hence, it has only three material parameters in addition to the thermal conductivity, K , namely the Young's modulus, E , the Poisson's ratio, ν , and the coefficient of thermal expansion, α . It is assumed that the sphere is made of material that is FG in the radial direction, except for the Poisson's ratio which is assumed to be constant through the shell thickness. All material properties are temperature independent. The stress components of an isotropic shell are defined in terms of displacement components and the temperature field as:

$$\begin{aligned}
\sigma_r &= \frac{E\nu}{(1+\nu)(1-2\nu)} \left\{ \frac{\partial u}{\partial r} + \frac{2u}{r} \right\} + \frac{E}{(1+\nu)} \frac{\partial u}{\partial r} - \left\{ \frac{3E\nu}{(1+\nu)(1-2\nu)} + \frac{E}{(1+\nu)} \right\} \alpha T \\
\sigma_\theta &= \frac{E\nu}{(1+\nu)(1-2\nu)} \left\{ \frac{\partial u}{\partial r} + \frac{2u}{r} \right\} + \frac{E}{(1+\nu)} \frac{u}{r} - \left\{ \frac{3E\nu}{(1+\nu)(1-2\nu)} + \frac{E}{(1+\nu)} \right\} \alpha T
\end{aligned} \tag{3.8}$$

By substituting components of Eq. (3.8) into Eq. (3.2), the dominant equation for the host layer is developed in terms of the displacement and temperature fields of the FG spherical layer, as follows:

$$\begin{aligned}
&\frac{E\nu}{(1+\nu)(1-2\nu)} \left\{ \frac{\partial^2 u}{\partial r^2} + \frac{2}{r} \frac{\partial u}{\partial r} - \frac{2u}{r^2} \right\} + \frac{\nu \frac{\partial E}{\partial r}}{(1+\nu)(1-2\nu)} \left\{ \frac{\partial u}{\partial r} + \frac{2u}{r} \right\} + \frac{E}{(1+\nu)} \frac{\partial^2 u}{\partial r^2} + \frac{\frac{\partial E}{\partial r}}{(1+\nu)} \frac{\partial u}{\partial r} - \left\{ \frac{3E\nu}{(1+\nu)(1-2\nu)} \right. \\
&+ \left. \frac{E}{(1+\nu)} \right\} \frac{\partial \alpha}{\partial r} T - \left\{ \frac{3E\nu}{(1+\nu)(1-2\nu)} + \frac{E}{(1+\nu)} \right\} \alpha \frac{\partial T}{\partial r} - \left\{ \frac{3\nu \frac{\partial E}{\partial r}}{(1+\nu)(1-2\nu)} + \frac{\frac{\partial E}{\partial r}}{(1+\nu)} \right\} \alpha T + \frac{2E}{(1+\nu)r} \left\{ \frac{\partial u}{\partial r} - \frac{1}{r} u \right\} = \rho \frac{\partial^2 u}{\partial t^2}
\end{aligned} \tag{3.9}$$

3.3.3 Heat conduction analysis

In this work, transient heat conduction without internal heat source is considered; hence, the governing equation of the transient temperature field is defined as [163]:

$$\frac{1}{r^2} \frac{\partial}{\partial r} \left\{ r^2 K \frac{\partial T}{\partial r} \right\} = \rho c \frac{\partial T}{\partial t} \tag{3.10}$$

where K and c are the thermal conductivity and specific heat respectively.

3.3.4 Interface interactions and boundary bonds

For a laminated structure, the energy balance must be met at the interface of each adjacent layer, i.e., between the k^{th} . and the $(k+1)^{th}$. layers. A schematic view is presented in Fig. 3.2.

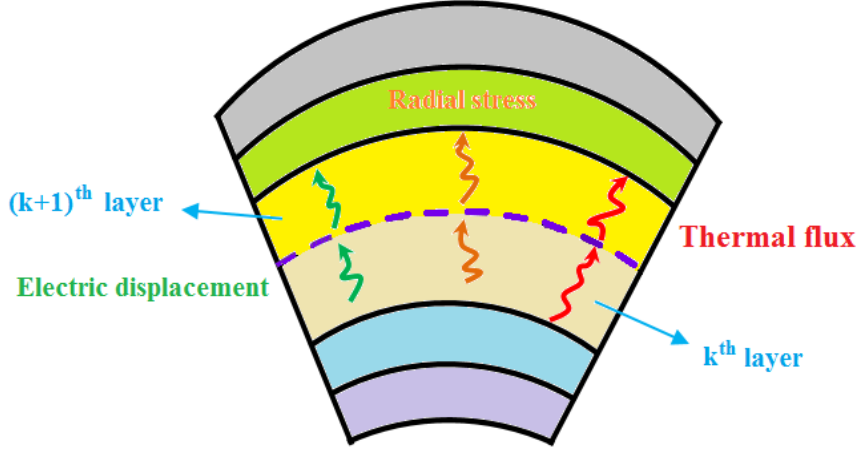


Fig. 3.2: Compatibility conditions between k^{th} and $(k+1)^{\text{th}}$ layers, including radial stress, electric displacement and thermal flux terms.

The corresponding interface equilibrium and compatibility conditions are written as [164]:

$$\sigma_r|_k = \sigma_r|_{k+1}, u|_k = u|_{k+1}, D_r|_k = D_r|_{k+1}, \psi|_k = \psi|_{k+1}, T|_k = T|_{k+1}, K \frac{\partial T}{\partial r}|_k = K \frac{\partial T}{\partial r}|_{k+1} \quad (3.11)$$

The surface boundary conditions of the outer piezoelectric shell, i.e. $r=b$, are considered to be free of traction and the temperature is assumed to be zero. Also, the inner surface is subjected to transient pressure and thermal excitations. Under these circumstances, the boundary conditions are drafted as:

$$\begin{aligned} \text{at } r=a: \quad & \sigma_r = P(t), \quad T = T(t); \\ \text{at } r=b: \quad & \sigma_r = D = 0, \quad T = 0 \end{aligned} \quad (3.12)$$

3.3.5 Solution methodology

In this study, the differential quadrature (DQ) method is used to approximate the derivatives of the displacement and temperature fields with respect to the spatial and time domains and to discretize the governing partial differential equations into series form.

3.3.5.1 Differential quadrature

Researchers face a set of partial differential and integral equations describing the characteristics of the problem. Many low-order computational methods have been presented, suffering from inadequate accuracy and time-consuming computer operation. However, the highly accurate outcomes of DQ , which uses the coordinates of all mesh points for approximating the derivatives of a desirable function, revolutionized the computational research area. If $A^{(n)}$, x , and M stand for the weighting coefficients of the n^{th} order derivative, mesh points and the number of grid points, we have:

$$\left. \frac{\partial^n \psi}{\partial x^n} \right)_i \approx \sum_{l=1}^M A^{(n)}_{il} \psi_l \quad (3.13)$$

In fact, the accuracy of the weighting coefficients specifies the accuracy level of the DQ . The polynomial expansion based differential quadrature that was introduced in the approach of Quan and Chang [165, 166] is employed to define the first and second order derivatives of the function in the physical domain. Several polynomial based differential quadratures have been developed by researchers [167-170]; however, the most useful approach uses Lagrange interpolation polynomials.

For the weighting coefficients of n^{th} order for $\phi(x)$, an explicit formula based on the Lagrange interpolation function was derived as:

$$A_{ij}^n = \frac{d}{dx^n} l_j(x_i) \quad , \quad i, j = 1, 2, \dots, M \quad (3.14)$$

and:

$$l_j(x) = \frac{\phi(x)}{(x - x_k) \phi^{(1)}(x_k)} \quad , \quad \phi(x) = \prod_{k=1}^M (x - x_k) \quad (3.15)$$

$$\phi^{(1)}(x_i) = \frac{d\phi(x_j)}{dx} = \prod_{\substack{k=1 \\ k \neq i}}^M (x_i - x_k)$$

By employing the differential quadrature method, the governing equations (3.6) and (3.7) can be discretized into the following forms.

$$\begin{aligned}
& C_{11} \sum_{l=1}^{M_1} A^{(2)}_{il} u_l + 2C_{12} \left\{ \frac{1}{r_i} \sum_{l=1}^{M_1} A^{(1)}_{il} u_l - \frac{1}{r_i^2} u_i \right\} + e_{11} \sum_{l=1}^{M_1} A^{(2)}_{il} \psi_l - \lambda_{11} \sum_{l=1}^{M_1} A^{(1)}_{il} T_l \\
& + \frac{2}{r_i} \left\{ C_{11} \sum_{l=1}^{M_1} A^{(1)}_{il} u_l + 2C_{12} \frac{u_i}{r_i} + e_{11} \sum_{l=1}^{M_1} A^{(1)}_{il} \psi_l - \lambda_{11} T_i \right\} - \left\{ C_{12} \sum_{l=1}^{M_1} A^{(1)}_{il} u_l + (C_{22} + C_{23}) \frac{1}{r_i} u_i \right. \\
& \left. - e_{21} \sum_{l=1}^{M_1} A^{(1)}_{il} \psi_l - \lambda_{12} T_i \right\} = \rho \sum_{n=1}^{Q_1} C^{(2)}_{in} u_n
\end{aligned} \tag{3.16a}$$

$$\begin{aligned}
& e_{11} \sum_{l=1}^{M_1} A^{(2)}_{il} u_l + 2e_{21} \left\{ \frac{1}{r_i} \sum_{l=1}^{M_1} A^{(1)}_{il} u_l - \frac{1}{r_i^2} u_i \right\} - \eta_{11} \sum_{l=1}^{M_1} A^{(2)}_{il} \psi_l + P_{11} \sum_{l=1}^{M_1} A^{(1)}_{il} T_l \\
& + \frac{2}{r_i} \left\{ e_{11} \sum_{l=1}^{M_1} A^{(1)}_{il} u_l + 2e_{12} \frac{1}{r_i} u_i - \eta_{11} \sum_{l=1}^{M_1} A^{(1)}_{il} \psi_l + P_{11} T_i \right\} = 0
\end{aligned} \tag{3.16b}$$

where $A^{(i)}$ and $C^{(i)}$ ($i=1,2$) explain the weighting coefficients of the i^{th} order derivative in the piezoelectric layer and time domain respectively. The right side of this equation (3.16a) discretizes the inertia effects. In current study, thermoelastic loads sharply change over the time, then time varying characteristics, including displacement, temperature, and electric potential, are investigated in space and time domains parallelly. The dynamics of piezoelectric films are broken to small time intervals through the solution algorithm, and all these time intervals interactively work to present the final temporal response.

The governing equation of the host shell corresponding to Eq. (3.9) is:

$$\begin{aligned}
& \frac{E}{(1+\nu)(1-2\nu)} \left\{ \sum_{m=1}^{M_2} B^{(2)}_{im} u_m + \frac{1}{r_i} \sum_{m=1}^{M_2} B^{(1)}_{im} u_m - \frac{1}{r_i^2} u_i \right\} + \frac{E}{(1+\nu)} \sum_{m=1}^{M_2} B^{(2)}_{im} u_m \\
& + \frac{\nu \frac{\partial E}{\partial r}}{(1+\nu)(1-2\nu)} \left\{ \sum_{m=1}^{M_2} B^{(1)}_{im} u_m + \frac{1}{r_i} u_i \right\} + \frac{\frac{\partial E}{\partial r}}{(1+\nu)} \sum_{m=1}^{M_2} B^{(1)}_{im} u_m - \left\{ \frac{3E\nu}{(1+\nu)(1-2\nu)} \right. \\
& \left. + \frac{E}{(1+\nu)} \right\} \frac{\partial \alpha}{\partial r} T_i - \left\{ \frac{3E\nu}{(1+\nu)(1-2\nu)} + \frac{E}{(1+\nu)} \right\} \alpha \sum_{m=1}^{M_2} B^{(1)}_{im} T_m - \left\{ \frac{3\nu \frac{\partial E}{\partial r}}{(1+\nu)(1-2\nu)} + \frac{\frac{\partial E}{\partial r}}{(1+\nu)} \right\} \alpha T_i \\
& + \frac{2E}{(1+\nu)r_i} \left\{ \sum_{m=1}^{M_2} B^{(1)}_{im} u_m - \frac{1}{r_i} u_i \right\} = \rho \sum_{n=1}^{Q_1} C^{(2)}_{in} u_n
\end{aligned} \tag{3.17}$$

where $B^{(i)}$ ($i=1, 2$) elucidates the weighting coefficients of i^{th} order derivative in the host layer.

The transient temperature field in the host shell and the piezoelectric layers are represented as:

$$\begin{aligned} & \frac{2K_{FGM}}{r_i} \sum_{m=1}^{M_2} B^{(1)}_{im} T_m + K_{FGM} \sum_{m=1}^{M_2} B^{(2)}_{im} T_m + \frac{\partial K_{FGM}}{\partial r} \sum_{m=1}^{M_2} B^{(1)}_{im} T_m \\ & = \rho_{FGM} c_{FGM} \sum_{n=1}^{Q_1} C^{(1)}_{in} T_n \end{aligned} \quad (3.18a)$$

$$\frac{2K_{Piezo}}{r_i} \sum_{l=1}^{M_1} A^{(1)}_{il} T_l + K_{Piezo} \sum_{l=1}^{M_1} A^{(2)}_{il} T_l = \rho_{Piezo} c_{Piezo} \sum_{n=1}^{Q_1} C^{(1)}_{in} T_n \quad (3.18b)$$

where K_{FGM} , ρ_{FGM} , c_{FGM} , and K_{Piezo} , ρ_{Piezo} , c_{Piezo} are the thermal conductivity, density, and specific heat for the host and piezoelectric layers respectively.

The boundary conditions of the piezoelectric and shell layers as defined in Eq. (3.12) are dictated as:

$$\begin{aligned} \sigma_r|_{FGM} &= \frac{E\nu}{(1+\nu)(1-2\nu)} \left\{ \sum_{m=1}^{M_2} B^{(1)}_{im} u_m + \frac{1}{r_i} u_i \right\} + \frac{E}{(1+\nu)} \sum_{m=1}^{M_2} B^{(1)}_{im} u_m \\ &- \left\{ \frac{3E\nu}{(1+\nu)(1-2\nu)} + \frac{E}{(1+\nu)} \right\} \alpha T_i + P(t) = 0 \\ \sigma_r|_{piezo} &= C_{11} \sum_{l=1}^{M_1} A^{(1)}_{il} u_l + 2C_{12} \frac{1}{r_i} u_i + e_{11} \sum_{l=1}^{M_1} A^{(1)}_{il} \psi_l - \lambda_{11} T_i = 0 \\ D_r &= e_{11} \sum_{l=1}^{M_1} A^{(1)}_{il} u_l + 2e_{12} \frac{1}{r_i} u_i - \beta_{11} \sum_{l=1}^{M_1} A^{(1)}_{il} \psi_l + P_{11} T_i = 0 \end{aligned} \quad (3.19)$$

3.3.5.2 Choices of sampling grid points

In order to carry out numerical computation, sampling points in the spatial coordinates are assumed to be distributed according to Chebyshev-Gauss-Lobatto polynomials. For a time domain, uniform, distributed grid points are used.

$$\begin{aligned}
r_{k_1} &= a + \frac{b-a}{2} \left\{ 1 - \cos\left(\frac{k_1-1}{M-1}\pi\right) \right\}, & k_1 &= 1, \dots, M \\
t_{k_2} &= t_T \left(\frac{k_2-1}{Q_1-1}\right), & k_2 &= 1, \dots, Q_1
\end{aligned} \tag{3.20}$$

where t_T clarifies the total time of the transient analysis.

3.3.6 Numerical results and discussion

3.3.6.1 Evaluation

To proceed with calculations, evaluation of the outputs of the present method is first carried out. The results for a FG thick-walled sphere subjected to mechanical and thermal loads are obtained using the presented algorithm and are then compared with the results published by Eslami *et al.* [171]. Variations of the material properties are assumed to be obeying the following power law formulation:

$$Y(r) = Y_i \left(\frac{r}{a}\right)^\beta \tag{3.21}$$

where Y_i elucidates the material properties at the inner radius. Results are presented for the same loading and boundary conditions described in [171].

The radial distribution of the hoop stress and radial displacement fields calculated by the present method are compared with the data reported in [171]. As can be seen from Fig. 3.3, the thermo-elastic response of the FG spherical shells obtained by the proposed technique shows very good agreement with that of the reference [171].

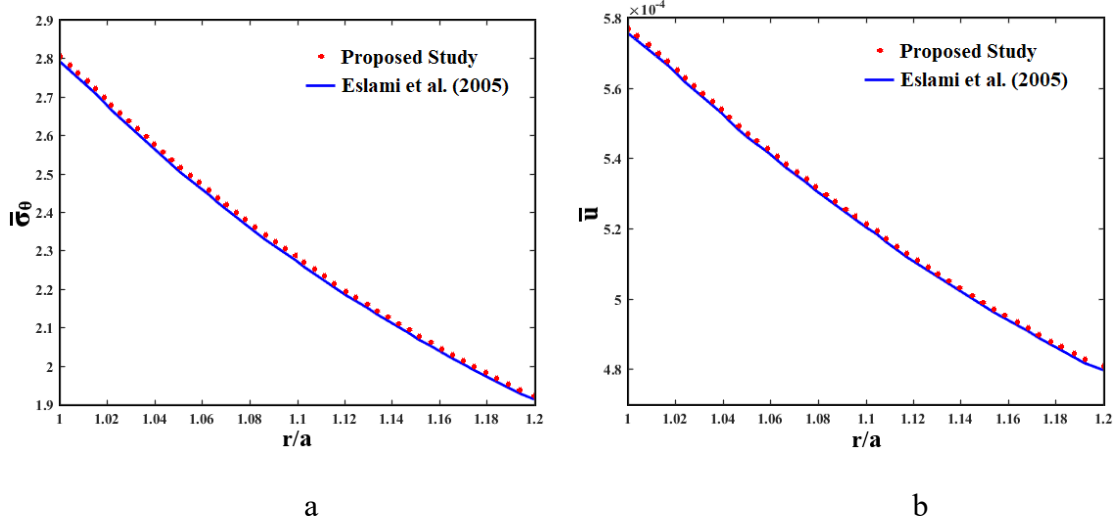


Fig. 3.3: Evaluation study of the presented method with the literature for a thick FG spherical shell (a) radial distribution of the circumferential stress, and (b) radial displacement through the thickness.

In this work, results are marked in dimensionless form. The following dimensionless parameters are defined for the components of stress, displacement, temperature, and electric fields.

$$\{\bar{\sigma}_r, \bar{\sigma}_\theta\} = \frac{1}{P} \{\bar{\sigma}_r, \bar{\sigma}_\theta\}, \bar{u} = \frac{1}{a} u, \bar{T} = \frac{T}{T_a}, \bar{\psi} = \frac{\beta_{11} \times \alpha_r}{P_{11} \times h_{FGM}} \psi, \tau = \frac{K}{\rho \times c \times h_{FGM}^2} t \quad (3.22)$$

For the host shell, variation of the material properties in the radial direction is defined by a power law, as:

$$Y(r) = Y_i \left\{ 1 - \left(\frac{r-a}{b-a} \right)^\beta \right\} + Y_o \left(\frac{r-a}{b-a} \right)^\beta \quad (3.23)$$

where Y_i and Y_o denote the material properties at the inner and outer surfaces of the FG shell (i.e. a and b) respectively and β is the grading parameter labeling the change of the volume fraction of two constituents. It is assumed that the inner and outer surfaces are made of TiC and Ni respectively. The properties of these materials are listed in Table 3.1.

Table 3.1: Elastic and thermal material properties of TiC and Ni [172].

Property	E (GPa)	ν	α ($10^{-6}/^{\circ}\text{C}$)	K (W/m. $^{\circ}\text{C}$)	ρ (kg/m^3)	c ($\text{j}/\text{kg. }^{\circ}\text{C}$)
TiC	460	0.336	7.4	20	4930	530
Ni	199.5	0.312	18	90.5	8908	440

The material properties of the piezoelectric layers used in the present study are listed in Table 3.2.

Table 3.2: Electro-thermo-elastic properties of PZT-4 and $\text{Ba}_2\text{NaNb}_5\text{O}_{15}$ [173, 174].

Material	Elastic constant (GPa)				Piezoelectric constant (C/m^2)		Permittivity ($10^{-9}\text{C}^2/\text{Nm}^2$)	Pyroelectric constant ($10^{-5}\text{C}/\text{m}^2\text{ }^{\circ}\text{C}$)
	C_{11}	C_{12}	C_{22}	C_{23}	e_{11}	e_{12}	β_{11}	P_{11}
PZT-4	139	78	139	74	-5.2	-5.2	6.5	5.4
$\text{Ba}_2\text{NaNb}_5\text{O}_{15}$	239	104	247	52	-0.4	-0.3	1.96	5.4
	Thermal modulus ($10^5 \text{ GPa}/^{\circ}\text{C}$)		Thermal conductivity ($\text{W}/\text{m }^{\circ}\text{C}$)		Density (kg/m^3)	Specific heat ($\text{J}/\text{kg }^{\circ}\text{C}$)		
	λ_{11}	λ_{12}	K		ρ	C		
PZT-4	6.7	2	1.5		7500	200		
$\text{Ba}_2\text{NaNb}_5\text{O}_{15}$	15	2.6	13.9		5300	350		

Next, for the sake of further verification, a study is conducted in order to compare the accuracy of the proposed method with that of the finite element analysis (ANSYS). The curve responses of the radial stress and displacement, and electric potential are drawn in Fig. 3.4. As can be clearly seen, outputs of the implemented algorithm are in a good agreement with those of the finite element analysis.

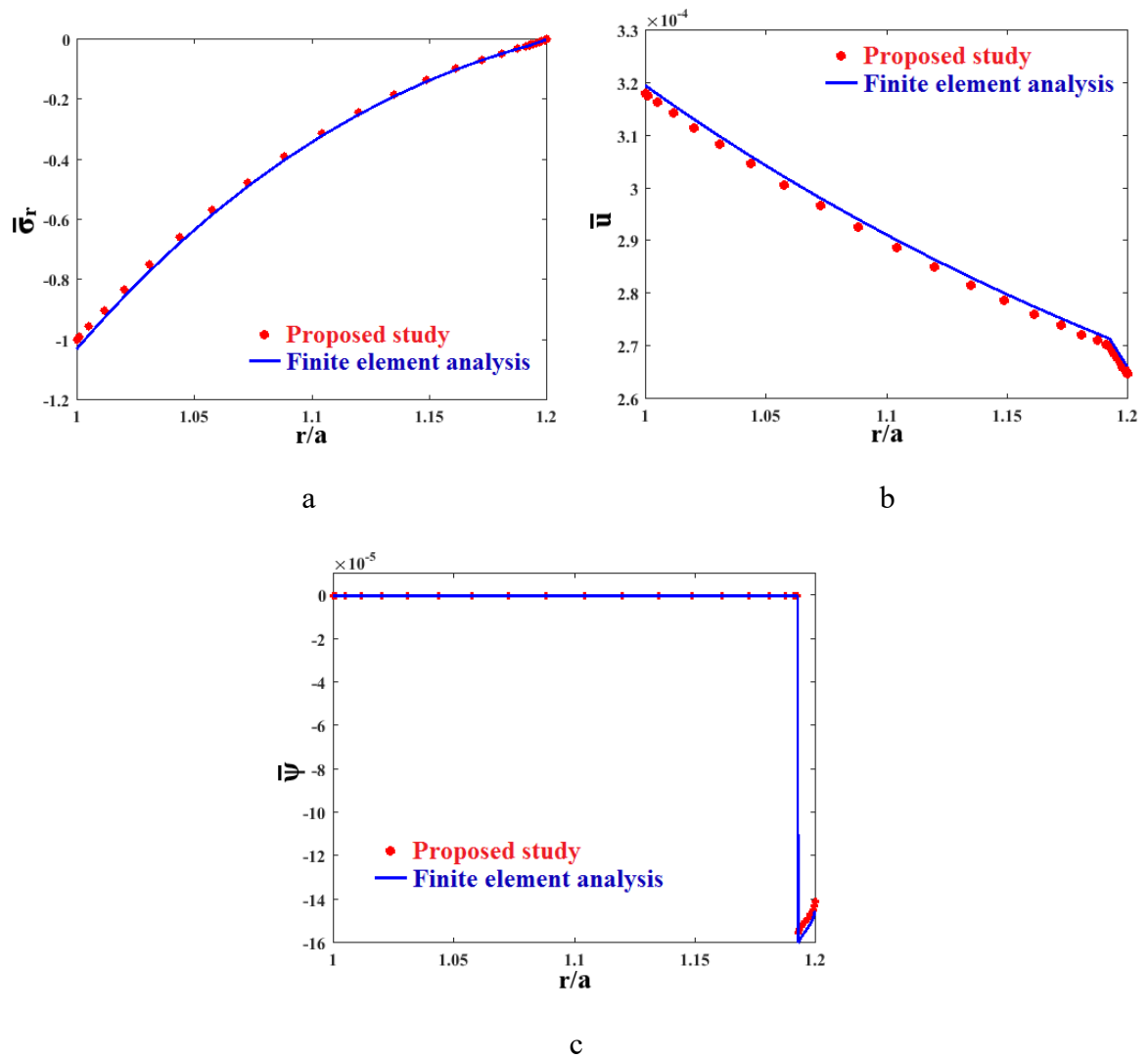


Fig. 3.4: Comparison between the presented results with those of the finite element analysis for an FG sphere (a) radial stress, (b) radial displacement, and (c) electric potential.

3.3.6.2 FG host layer laminated with sensor layer

In this section, transient thermo-electro-elastic feedback of shell 1 is investigated. In essence, the piezoelectric layer plays the role of a sensor layer. By the application of mechanical and thermal motivations to the FG host layer, electric output is produced that reflects direct a piezoelectric effect in the sensor layer. This electric potential can be used for various purposes such as vibration control and structural health monitoring.

The effect of the grading parameter β on the distribution through the thickness of the dimensionless radial and circumferential stresses and radial displacement is plotted in Fig. 3.5. It is observed from Figs. 3.5a and 3.5c that the interface continuity conditions and the boundary conditions for the radial stress and the radial displacement are fully satisfied. It is also shown in Fig. 3.5a that the absolute value of the radial stress is almost constant for $\beta=5$ and $\beta=-5$. Moreover, the value of the hoop stress decreases in the sensor layer as β increases. Circumferential stress is one of the main reasons for failure, especially in brittle materials. Fracture can be tackled by knowing and controlling the value of this stress. Another important point about Fig. 3.5b is the discontinuity of the circumferential stress at the common interface of the host and the sensor layers. It is realized from Fig. 3.5c that as β drops, the dimensionless radial displacement increases monotonously, with its maximum value at the inner surface.

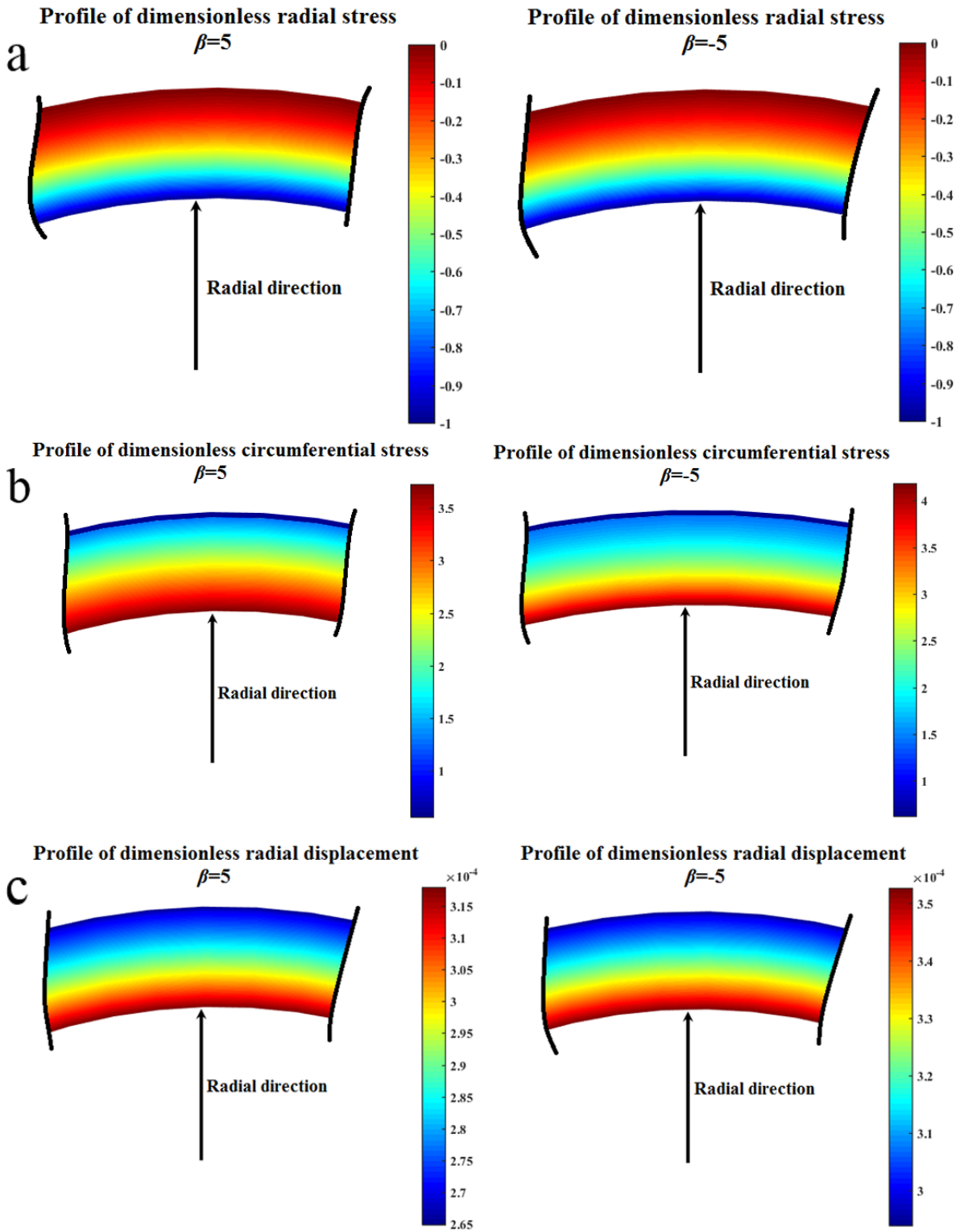


Fig. 3.5: Effects of inhomogeneity on the dimensionless (a) radial stress, (b) circumferential stress, and (c) radial displacement (at $\tau=2.5 \times 10^{-6}$).

Next, the responses of the electric potential and temperature of shell 1 are depicted in Fig. 3.6. The dimensionless electric potential is drawn in Fig. 3.6a and clarifies that the sensor layer senses the high absolute voltages as the grading parameter β declines. Likewise, this graph reflects a zero-electric potential in the FGM host layer, as expected. The electrical output of the sensor layer can be used in structural health monitoring of the shell structures for quantifying the severity of damage. The dimensionless temperature distribution is displayed in Fig. 3.6b, exhibiting a significant decrease in its values as the grading index increases. Furthermore, this figure illuminates a nonlinear distribution through the thickness of the FGM shell, attributable to the power law grading of its material properties, but a linear distribution is observed through the sensor layer. In general, the statistical data illustrated here would be helpful in designing laminated smart FG shell structures with an appropriate grading parameter that ensured smooth distribution of stresses in the entire structure.

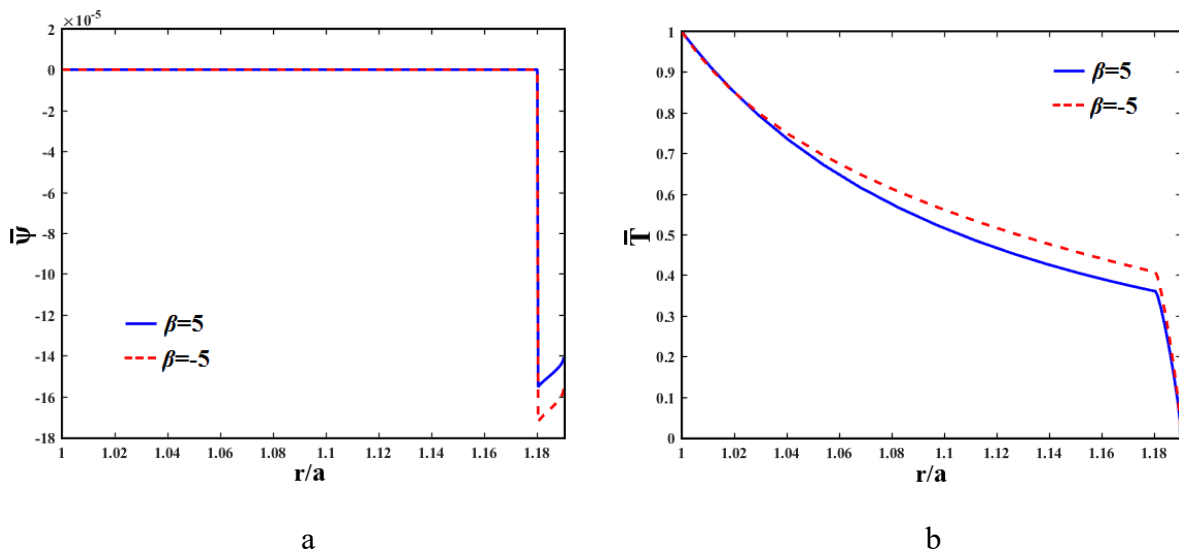


Fig. 3.6. Impacts of inhomogeneity on the dimensionless (a) radial distribution of the electric potential, and (b) temperature through the thickness.

Here, the effects of the temperature gradient (i.e. $T_a = \partial T / \partial t$) at two surfaces of the shell 1 on the dimensionless stresses, radial displacement, and electric potential are displayed in Fig. 3.7. The temperature of the outer surface assumed to be fixed, i. e., $T(b)=0$ °C and the temperature of the inner surface varies sinusoidally with time as a parameter. Material properties are assumed to vary linearly in the radial direction, i.e. $\beta =1$. From Fig. 3.7a, it is revealed that the values of dimensionless radial stress increase gradually as the temperature difference increases. Fig. 3.7b illustrates that the hoop stress declines in the FG host and sensor layers as the thermal gradient rises. Variations of the dimensionless radial displacement and electric potential are illustrated in Figs. 3.7c and 3.7d, highlighting an increase magnitude as T_a increases.

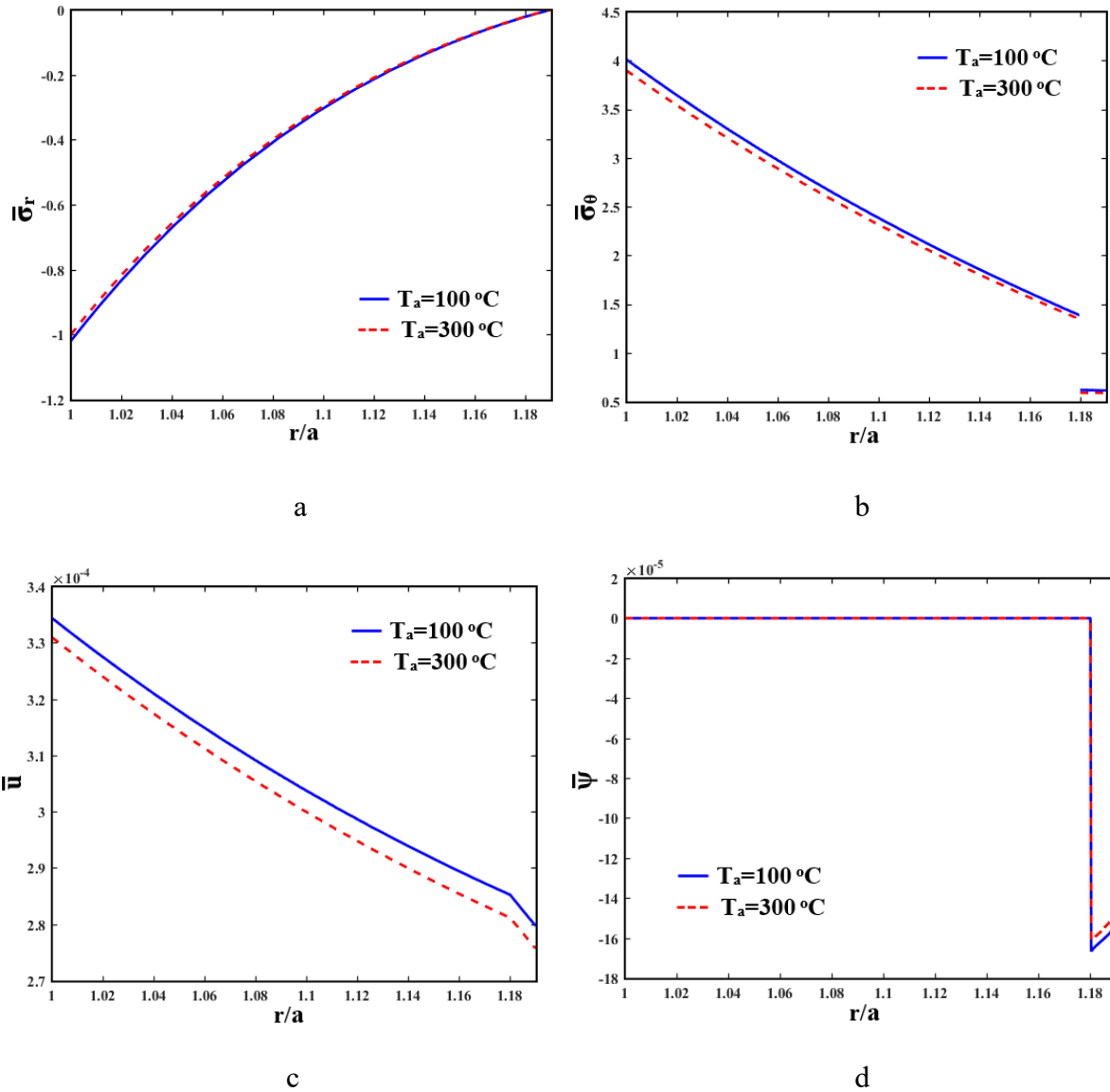


Fig. 3.7: Effects of thermal gradient on dimensionless (a) radial stress, (b) circumferential stress, (c) radial displacement, and (d) electric potential (at $\tau=2.5 \times 10^{-6}$).

One of the most important features of the shell structure is the ratio of the mid-plane radial to the thickness (S) of the shell [162, 175, 176]. Transient responses of the dimensionless σ_θ and u of shell 1 are shown in Figs. 3.8. These figures show that as S increases, the tangential stress, and displacement fields substantially increase. It is noteworthy that, with representation of the transient variations of the stress and displacement fields at different

points in the shell structures, critical points of damage in engineering materials can be discerned.

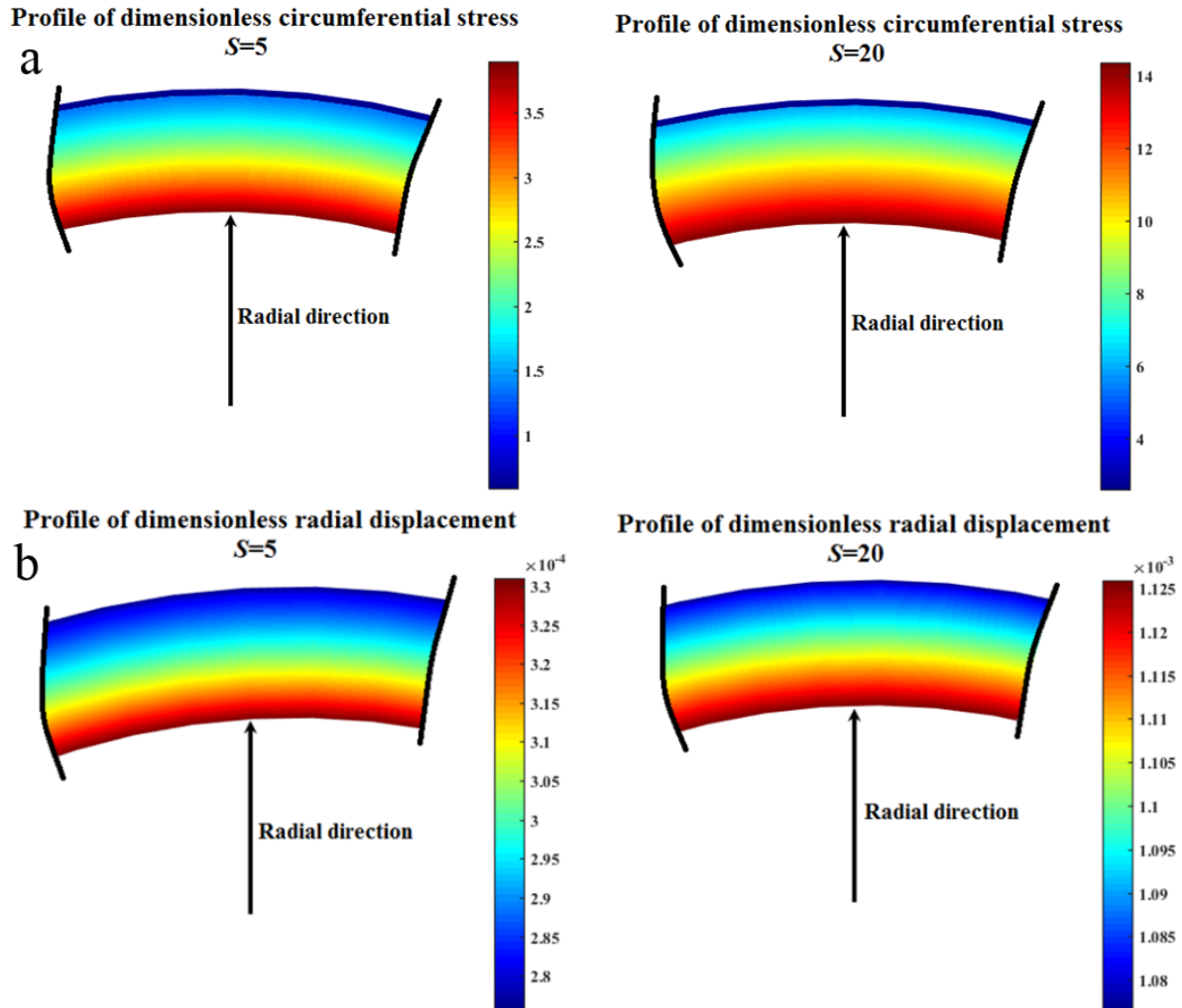


Fig. 3.8: A survey of the effects of the shell thickness S on the profile of (a) circumferential stress, and (b) radial displacement (at $\tau=2.5 \times 10^{-6}$).

Next, a study is conducted of the impacts of the ratio of the mid-plane radial to the thickness on the radial stress and the sensed electric potential. The thermo-elastic response is depicted in Fig. 3.9. As expected, the sensed electric output in the sensor layer is dramatically affected by S . Moreover, the FG host layer displays considerably higher values of the stress field when S increases.

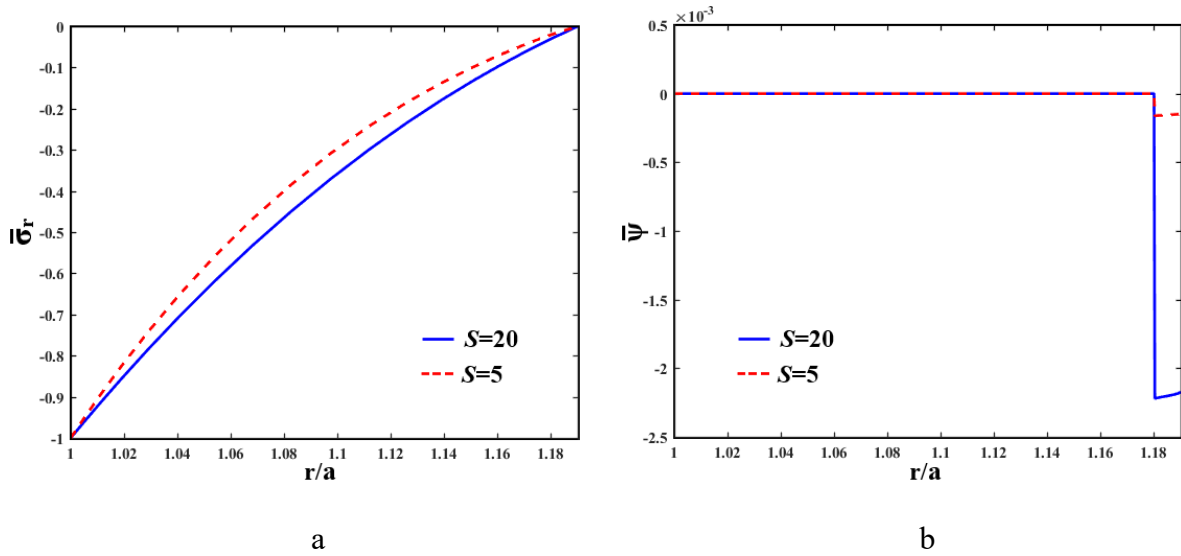


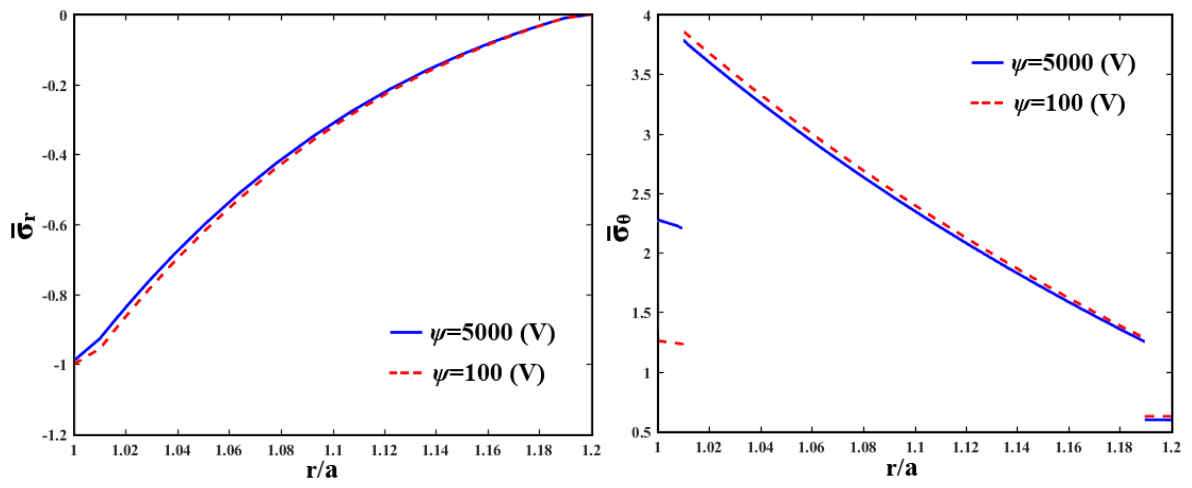
Fig. 3.9: Impacts of the geometric parameter on the dimensionless (a) radial stress, and (b) electric potential.

3.3.6.3 FG host layer laminated with actuator and sensor layers

Now, the thermo-electro-elastic interactions of FG shells bonded with thin piezoelectric layers are examined. Piezoelectric layers on the inner and outer surfaces of the host FG shell are involved as actuator and sensor layers, respectively. Transient mechanical, thermal, and electrical loadings are applied on the actuator layer, and deformations and electric output are observed in the whole structure. The application of an electric load as input and production of deformations throughout layers demonstrate the converse piezoelectric effect.

The effects of the electric excitation, i.e. variation of the electric potential on the characteristics of shell 2 are studied and the results are shown in Fig. 3.10. The electric excitation is assumed to vary as a parameter, i.e. $\psi=0.1$ and 5 KV . Indeed, by applying an electric excitation, stress and displacement fields are produced that reflect the converse piezoelectric effect. From Fig. 3.10a, it is evident that the values of dimensionless radial stress increase as the electric excitation increases. The tangential stress curve is plotted in Fig.

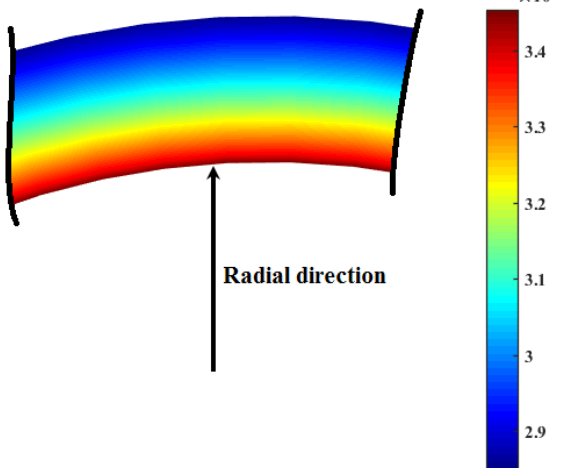
3.10b. This figure highlights an overwhelming increment in the σ_θ values in the actuator layer with the increase in ψ ; however, the pattern is reversed for the FG and sensor counterparts. The dimensionless distribution of u in Fig. 3.10c shows that, with an increase in electric motivation, the level of radial displacement decreases.



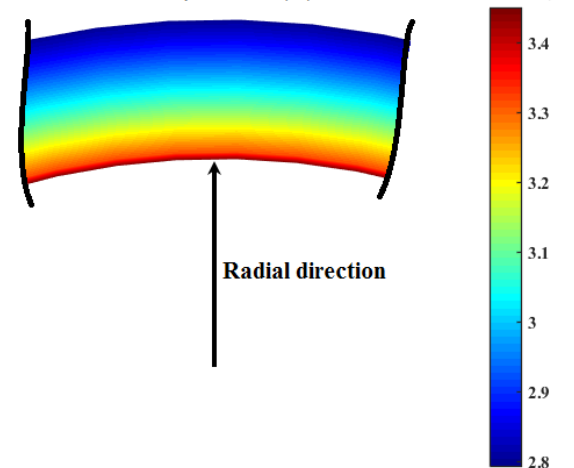
a

b

Profile of dimensionless radial displacement
 $\psi=100$ (V)



Profile of dimensionless radial displacement
 $\psi=5000$ (V)



c

Fig. 3.10: Effects of the electrical potential on (a) radial stress, (b) circumferential stress, and (c) radial displacement (at $\tau=2.5 \times 10^{-6}$).

In this section, the effects of the ratio of the thickness of the FG layer to the thickness of the piezoelectric layer (*i.e.* h_{FGM}/h_{piezo}) for the shell 2 are explored. This ratio has significant effect on direct and converse piezoelectric effects [157, 158]. As observed in Fig. 3.11a, the absolute values of the dimensionless radial stress through the thickness show an initial reduction and then a smooth increment. As observed in Fig. 3.11b, the dimensionless circumferential stress in actuator and sensor layers decreases as the thickness of the FG layer increases. The r -distribution of the radial displacement is displayed in Fig. 3.11c, indicating that as the thickness of the piezoelectric layer decreases, the electric potential values in the sensor and actuator layers decrease dramatically.

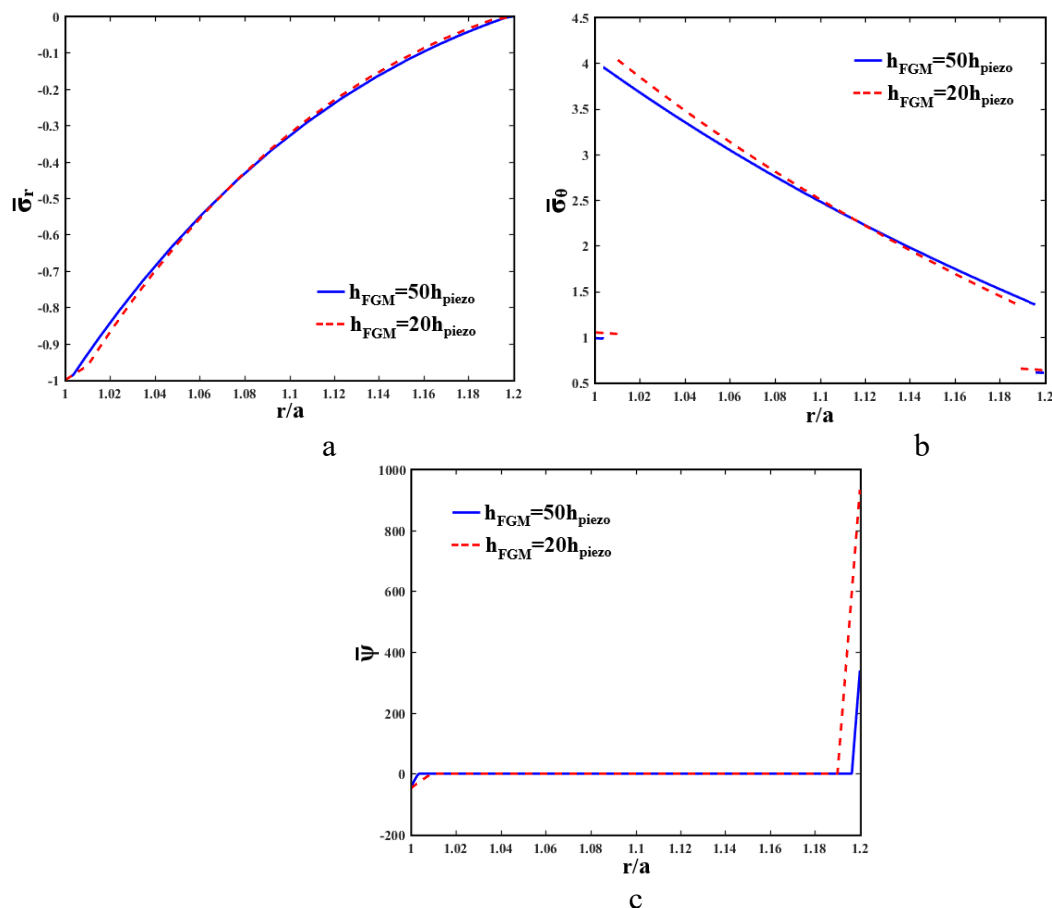


Fig. 3.11: Impacts of h_{FGM}/h_{piezo} on the dimensionless (a) radial stress, (b) circumferential stress, and (c) electric potential (at $\tau=2.5 \times 10^{-6}$).

Finally, the r -distribution of the radial displacement and electric potential is probed, and the outcomes are shown in Fig. 3.12. Clearly, from Fig. 3.12a, as the thickness of the FG layer increases, the values of radial displacement decrease moderately. The temperature distribution through the thickness is sketched in Fig. 3.10b, denoting that with an increase in h_{FGM}/h_{Piezo} , the grid values of temperature decrease in the laminated shell structure. As the final point, from Figs. 3.11 and 3.12, compared with other parameters, the effect of the geometric parameter is greatest on the distribution of the electric potential. Furthermore, the effect of piezoelectric layers becomes negligibly small as the thickness of piezoelectric layers decreases to a value of about $h_{FGM}=50h_{Piezo}$.

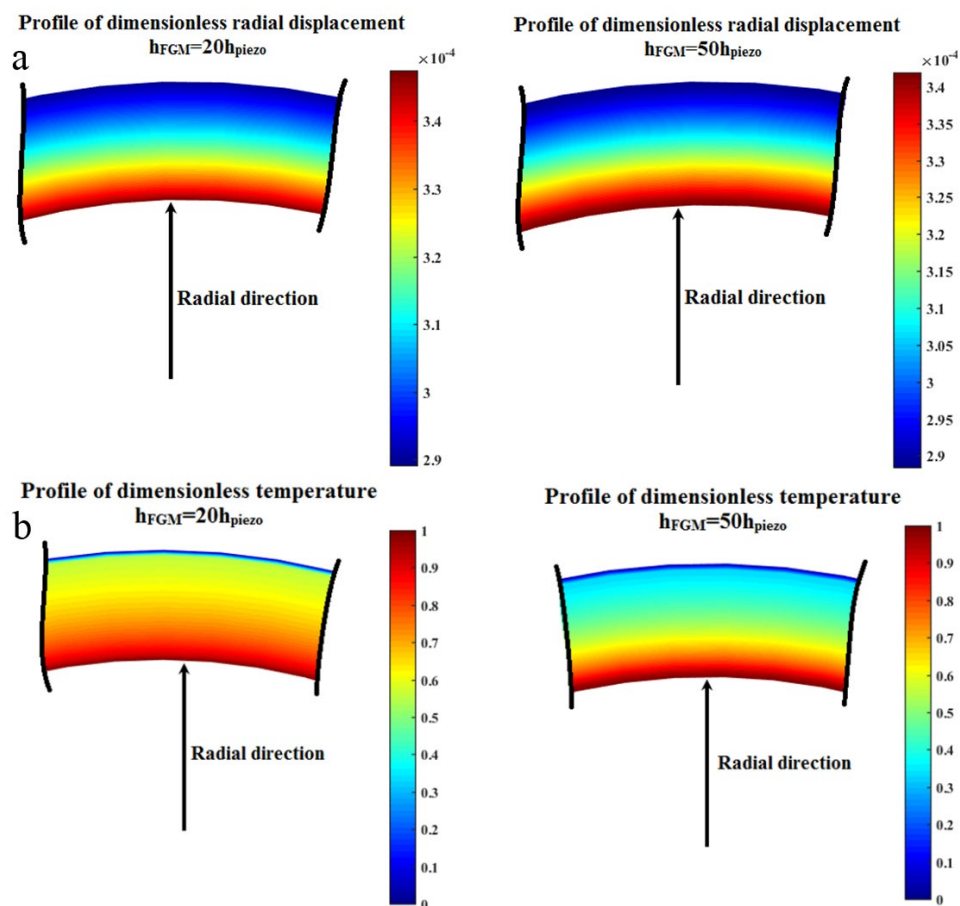


Fig. 3.12: Effects of h_{FGM}/h_{piezo} on (a) radial displacement, and (b) temperature.

3.4 Cylindrical smart shells

In this section, the applicability of cylindrical shells in energy harvesting purposes is examined. We assumed that the shell is made of FGMs. Then, the relevant formulations are presented. An optimization platform is presented in order to maximize the scavenged energy while minimizing the weight of the shell. One of the most important application of the proposed strategy lies at heart of design process of the lightweight shell structures for portable energy harvesters.

3.4.1 Thermo-electro-elastic formulation

Here the constitutive equations of pyroelectric shells under mechanical, electrical and thermal excitations are presented. Sectional views of the geometry of the structure are plotted in Fig. 3.13.

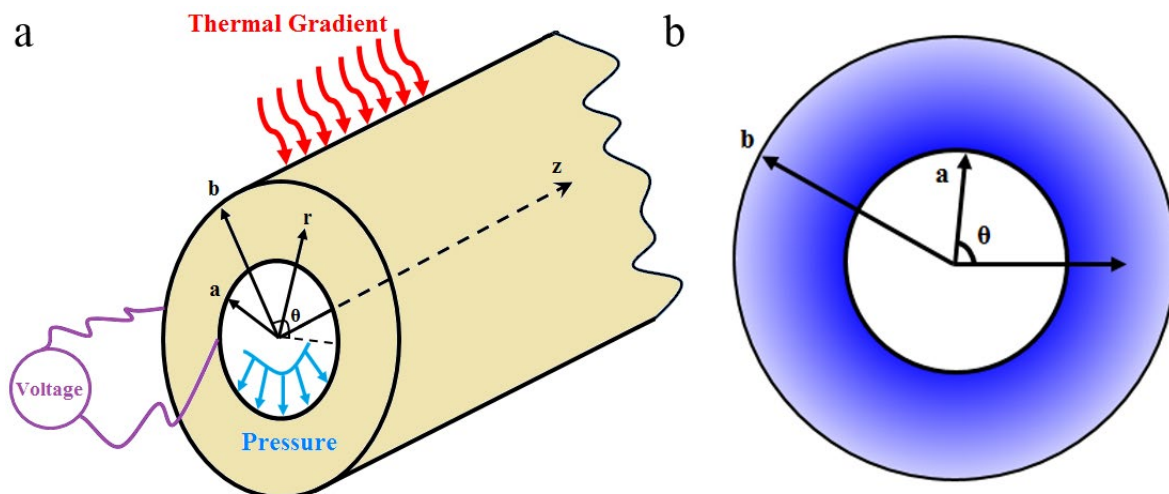


Fig. 3.13: Sectional plot of the pyroelectric shell (a) coordinates and loadings, and (b) variation of material properties along the thickness.

As mentioned, it is assumed that the piezoelectric vessel is made of an FGM. Mechanical, electrical and thermal material parameters have their own special gradient indexes, namely β_l

for the elastic modulus, β_2 for the piezoelectric constant and the dielectric constant, and β_3 for the thermal modulus, the pyroelectric constant and the thermal conductivity (K). The gradings of material properties thorough the thickness are written as:

$$\begin{aligned} c_{ij}(r) &= c_{ij}^0 \left(\frac{r}{a}\right)^{\beta_1} \quad , \quad \rho(r) = \rho^0 \left(\frac{r}{a}\right)^{\beta_1} \\ e_{ij}(r) &= e_{ij}^0 \left(\frac{r}{a}\right)^{\beta_2} \quad , \quad \eta_{ij}(r) = \eta_{ij}^0 \left(\frac{r}{a}\right)^{\beta_2} \\ p_i(r) &= p_i^0 \left(\frac{r}{a}\right)^{\beta_3} \quad , \quad \beta_i(r) = \beta_i^0 \left(\frac{r}{a}\right)^{\beta_3} \quad , \quad K_i(r) = K_i^0 \left(\frac{r}{a}\right)^{\beta_3} \end{aligned} \quad (3.24)$$

where $c_{ij}^0, \rho^0, e_{ij}^0, \eta_{ij}^0, P_i^0$ and K_i^0 stand for the elastic modulus, density, piezoelectric constant, dielectric constant, pyroelectric constant and the thermal conductivity at the inner surface, and β_1, β_2 and β_3 are mechanical, electrical and thermal grading variables thorough the thickness, respectively.

In our case study, the body force does not exist; hence, the equation of equilibrium in cylindrical coordinates of the shell is:

$$\frac{\partial \sigma_r}{\partial r} + \frac{\sigma_r - \sigma_\theta}{r} = 0 \quad (3.25)$$

and according to electrostatic rules, the governing equation for electric field can be derived as [155]:

$$\frac{\partial D_r}{\partial r} + \frac{D_r}{r} = 0 \quad (3.26)$$

By merging Eqs. (3.4) and (3.1) in spherical coordinate, the stress and electrical displacement vectors are expanded as below:

$$\begin{aligned} \sigma_r &= c_{33} \frac{\partial u}{\partial r} + c_{13} \frac{u}{r} + e_{33} \frac{\partial \psi}{\partial r} - \beta_r T \\ \sigma_\theta &= c_{13} \frac{\partial u}{\partial r} + c_{11} \frac{u}{r} + e_{31} \frac{\partial \psi}{\partial r} - \beta_\theta T \\ D_r &= e_{33} \frac{\partial u}{\partial r} + e_{31} \frac{u}{r} - \eta_{33} \frac{\partial \psi}{\partial r} + p_r T \end{aligned} \quad (3.27)$$

Next by inserting the stress and electrical displacement vectors into the equations of equilibrium, stress equilibrium equation and electrostatic equation can be derived:

Stress equilibrium equation:

$$\begin{aligned}
& c_{33} \frac{\partial^2 u}{\partial r^2} + c_{13} \left\{ \frac{1}{r} \frac{\partial u}{\partial r} - \frac{1}{r^2} u \right\} + e_{33} \frac{\partial^2 \psi}{\partial r^2} - \beta_r \frac{\partial T}{\partial r} + \frac{\partial c_{33}}{\partial r} \frac{\partial u}{\partial r} + \frac{\partial c_{13}}{\partial r} \frac{u}{r} \\
& + \frac{\partial e_{33}}{\partial r} \frac{\partial \psi}{\partial r} - \frac{\partial \beta_r}{\partial r} T + \frac{1}{r} \left\{ c_{33} \frac{\partial u}{\partial r} + c_{13} \frac{u}{r} + e_{33} \frac{\partial \psi}{\partial r} - \beta_r T - c_{13} \frac{\partial u}{\partial r} \right. \\
& \left. - c_{11} \frac{1}{r} u - e_{31} \frac{\partial \psi}{\partial r} + \beta_\theta T \right\} = 0
\end{aligned} \tag{3.28}$$

Electrostatic equation:

$$\begin{aligned}
& e_{33} \frac{\partial^2 u}{\partial r^2} + e_{31} \left\{ \frac{1}{r} \frac{\partial u}{\partial r} - \frac{1}{r^2} u \right\} - \eta_{33} \frac{\partial^2 \psi}{\partial r^2} + p_r \frac{\partial T}{\partial r} + \frac{\partial e_{33}}{\partial r} \frac{\partial u}{\partial r} + \frac{\partial e_{31}}{\partial r} \frac{u}{r} - \frac{\partial \eta_{33}}{\partial r} \frac{\partial \psi}{\partial r} \\
& + \frac{\partial p_r}{\partial r} T + \frac{1}{r} \left\{ e_{33} \frac{\partial u}{\partial r} + e_{31} \frac{1}{r} u - \eta_{33} \frac{\partial \psi}{\partial r} + p_r T \right\} = 0
\end{aligned} \tag{3.29}$$

Derivatives of the material properties are defined according to their respective functions.

In this study, we assumed that there is no heat generation in the system, and all derivatives in respect to time is zero. Then, the heat transfer analysis is confined to the below:

$$\frac{1}{r} \frac{\partial}{\partial r} \left(rK \frac{\partial T}{\partial r} \right) = 0 \tag{3.30}$$

Here we describe the boundary conditions. FG structure undergoes the internal pressure.

The electric potential is kept zero at surfaces. The temperature motivation is applied to the inner radius. In summary, the surface conditions of the FG piezoelectric vessel are written:

$$\begin{aligned}
& \text{at } r = a: \sigma_r = P, T = T(a), \psi = 0 \\
& \text{at } r = b: \sigma_r = 0, T = 0, \psi = 0
\end{aligned} \tag{3.31}$$

3.4.2 Optimization formulation

Here, we introduce the optimization prospect. It is obvious that lighter smart structures reproducing higher electric outputs are preferred for energy-harvesting systems. Simultaneously, as structures become lighter through reduction in dimensions or decreases in material strength, they will be put at risk of failure. Then, the aim of this study is to present

an optimized version of FG smart shells which can store the maximum level of energy while having the minimum weight. Fig. 3.14 depicts the main concept of this study. Grading indexes of the mechanical, electrical and thermal fields (β_1 , β_2 and β_3) constitute the search space of the problem. It is expected to achieve the following goals throughout our design:

- The weight of the structure can be reduced by means of decrement in the value of β_1 .
- Increment in β_2 means that the energy stored in the piezoelectric cells increases, leading to higher values of electrical output (voltage and electrical energy).
- Lower values of β_3 result in higher values of electrical output.

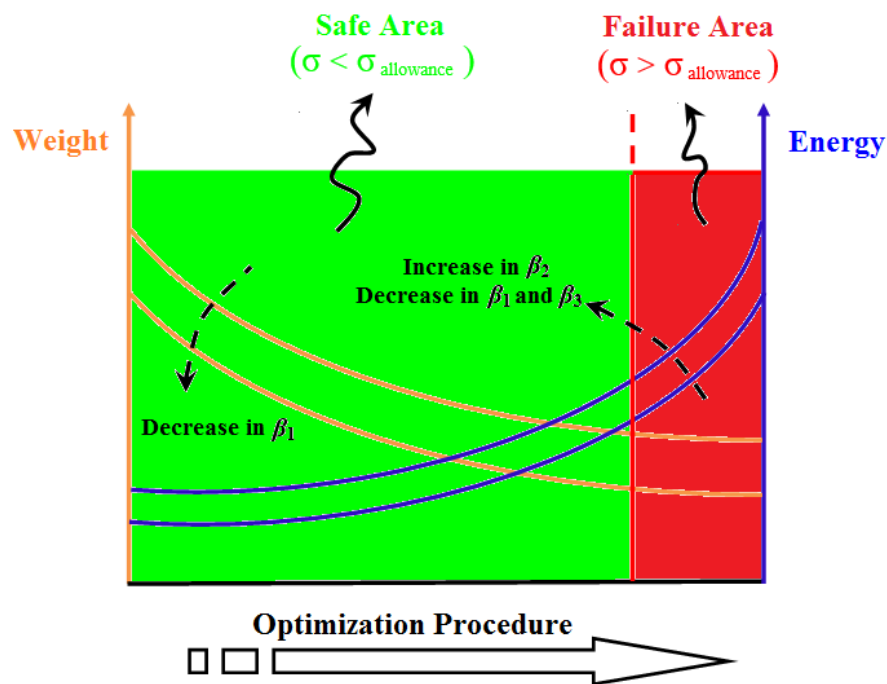


Fig. 3.14: Specifications of the optimization study.

Here, we formulate the optimization problem. Calculation is presented per length unit. If γ shows specific gravity, the weight of the structure can be calculated by the following integral between the boundary surfaces:

$$W = \int_{r=a}^{r=b} \gamma dV = \int_{r=a}^{r=b} \rho(r)gdV \quad (3.32)$$

where $g = 9.81 \text{ m/s}^2$.

It is also assumed that the density of the vessel varies through the thickness in accordance with Eq. (3.24). Then, the whole weight (density * volume) of the shell can be found:

$$W = \int_{r=a}^{r=b} 2\pi\rho(r)grdr = 2\pi\rho_0g \int_{r=a}^{r=b} \left(\frac{r}{a}\right)^{\beta_1} rdr \quad (3.33)$$

On the other hand, the stored electrical energy in pyroelectric cells is derived by taking the integration of dot product of the electric field and electric displacement, as below [177]:

$$U = \int_V E.Ddv \quad (3.34)$$

where v shows the integration on the volume of the body

$$U = \int_V E.Ddv = \int_{r=a}^{r=b} 2\pi E.Drdr = 2\pi \int_{r=a}^{r=b} E.Drdr \quad (3.35)$$

For calculating the above integral, generalized integral quadrature (*GIQ*) as a semi-analytical integral method is used. Finally, the goal function of the present study can be written as:

$$\text{Goal Function} = W + \frac{1}{U} = 2\pi\rho_0g \int_{r=a}^{r=b} \left(\frac{r}{a}\right)^{\beta_1} rdr + \frac{1}{2\pi \int_{r=a}^{r=b} E.Drdr} \quad (3.36)$$

The gradient index (including β_1 , β_2 and β_3) should be found in order to minimize the weight and simultaneously to maximize the value of the electrical energy (U). In addition, to guarantee the structural integrity of the smart structure, it is supposed that the torsions of the pyroelectric structure remain within the allowance stress limitation. The optimization approach should be considered under the following bonds:

$$\begin{aligned}
\text{Constraints:} \quad & \sigma_\theta \leq \sigma_{yield} \\
\text{Search Space:} \quad & \begin{cases} \beta_1|_{\min} \leq \beta_1 \leq \beta_1|_{\max} \\ \beta_2|_{\min} \leq \beta_2 \leq \beta_2|_{\max} \\ \beta_3|_{\min} \leq \beta_3 \leq \beta_3|_{\max} \end{cases}
\end{aligned} \tag{3.37}$$

As it was mentioned, the structure is made of an FGM with varying properties through the thickness according to Eq. (3.24). Because of the inhomogeneity, failure analysis is a hard task and seems to be a function of some variables. In reality, PZT-5H should be treated as brittle, and fracture mechanics techniques are required to determine the failure point. Here, situation is more complicated due to the applied thermal shocks and inhomogeneity. It may change the materials behaviour as a quasi-brittle one. Since real failure analysis is out the scope of this thesis, a simplified strategy was used to judge the failure.

3.4.3 Method of solution

To solve the optimization problem of the pyroelectric medium and present numerical simulation, we use the *GWO* and *PSO* methods to find solutions under the law of constraints. Furthermore, the *DQ* and *GIQ* methods, as powerful approaches in solving differential equations, are employed along with the *GWO* method to send the results to the goal function.

3.4.3.1 Generalized integral quadrature

In certain engineering problems, particularly calculations of the surface or of the volume of a body, we confront integration of functions over the physical domain. Analytical calculation of such integrations is a difficult task. Here, numerical integration methods can be helpful. In a similar manner to that used for partial differential derivatives, the approximation of the integration of a desired function over the arbitrary domain can be derived as:

$$\int_{x_i}^{x_j} f(x)dx \approx \sum_{l=1}^N A_l^{ij} f(x_l) \quad (3.38)$$

where A denotes the weighting coefficients.

Different rules have been applied for the calculation of weighting coefficients, resulting in various approximations. Preferably, to achieve accurate results a high order approach should be employed. In this work, *GIQ* is used to approximate the stored electrical energy in the structure's cells. The main idea is based on approximation of the function by high order polynomials involving the functional values of all grid points. The following formula is used for the weighting coefficients:

$$A_l^{ij} \approx w_{jl}^I - w_{il}^I \quad (3.39)$$

where $w^{(I)}$ is the inversion of the weighting coefficients matrix of the *DQ*.

3.4.3.2 Co-evolutionary particle swarm optimization

As an evolutionary computation technique, *PSO* has been comprehensively investigated by other researchers. Briefly, some random particles are defined in the search space. Each particle has its own position and velocity, as $x_{i,j}$ and $v_{i,j}$. At every step, each particle obtains its own best position, i.e., $p_{i,j}$, and at every step of the algorithm the global best will be updated ($p_{g,j}$). New positions and velocity of particles can be updated via the formula:

$$\begin{aligned} v_{i,j}(t+1) &= wv_{i,j}(t) + c_1r_1(p_{i,j} - x_{i,j}(t)) + c_2r_2(p_{g,j} - x_{i,j}(t)) \\ x_{i,j}(t+1) &= x_{i,j}(t) + v_{i,j}(t+1) \end{aligned} \quad (3.40)$$

where c_1 and c_2 are constant; r_1 and r_2 show independent random numbers in $[0, 1]$, and w is the inertia factor. Briefly, Fig. 3.15 depicts the different steps in the conventional *PSO* method.

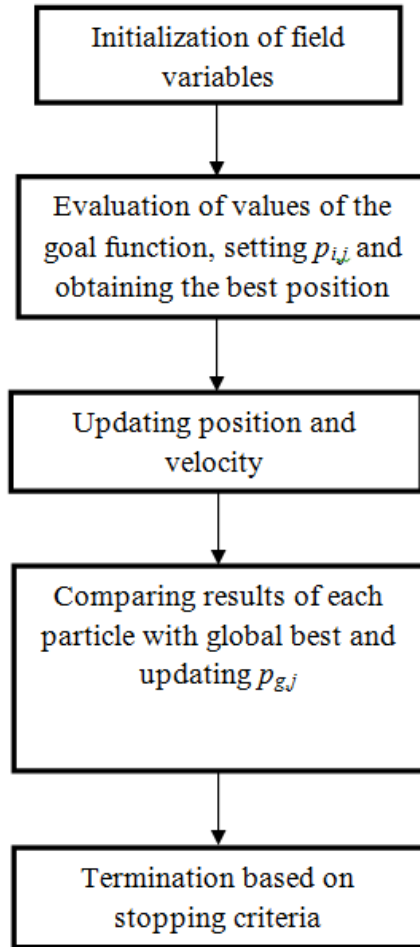


Fig. 3.15: Flow chart of *PSO* method.

In engineering sciences and physics circles, optimization problems are usually engaged with a collection of goal functions including restrictions. A general definition of an optimization study containing some constraints is written as:

$$\begin{aligned}
 & \text{Goal Function: } \text{Minimize } f(x) \\
 & \text{Constraints: } \quad g_i(x) \leq 0 \quad , \quad h_i(x) = 0 \\
 & \text{Search Space: } \quad x = [x_1, x_2, \dots, x_n]
 \end{aligned} \tag{3.41}$$

For meeting the restrictions of the dominant problem, application of the penalty functions is the most prevalent method [178, 179]. Here, we take advantage of the method described in reference [180]. The mechanism is based on two simultaneous *PSOs* cooperating interactively; the internal loop seeks out optimization variables in the predefined search space

while the external loop exerts the penalty limitations. In the current study, the penalty functions are assumed to be [181]:

$$\text{Internal PSO: } F_i(x) = f_i(x) + \text{sum_viol} \times w_1 + \text{num_viol} \times w_2$$

$$\text{External PSO: } \begin{cases} -\text{If there is any feasible solution in internal PSO:} \\ P(B_j) = \frac{\sum f_{feasible}}{\text{num_feasible}} - \text{num_feasible} \\ -\text{If there is no feasible solution in internal PSO:} \\ P(B_j) = \max(P_{valid}) + \frac{\sum \text{sum_viol}}{\sum \text{num_viol}} - \sum \text{num_viol} \end{cases} \quad (3.42)$$

where $f_i(x)$, num_viol and sum_viol stand for objective value, number of violations, and the sum of all violations in the inner loop. Moreover, $\sum f_{feasible}$ and num_feasible account for the sum of the objective functions of the feasible solutions and the number of feasible solutions in the inner *PSO*, and $\max(P_{valid})$ shows the maximum fitness value of the valid particles in the outer *PSO*. Also, w_1 and w_2 denote the penalty factors calculated by the external *PSO*.

3.4.3.3 Grey wolf optimization method

The *GWO* algorithm is based on mimicking the hunting behaviour of grey wolves in nature. The method contains three main steps: seeking the prey, encircling the prey, and attacking the prey. Furthermore, to simulate the leadership hierarchy, four different grey wolf variable types, including alpha, beta, delta, and omega, are implemented. In this method, the first level of grey wolves is alpha. The second major responsible variable is beta, helping alpha in decision-making. The lowest important grey wolf variable for making decisions is omega, which submits to all other wolves. The last wolf is known as delta. This kind of wolf submits to alpha and beta wolves while dominating omega. Briefly, the following mathematical formulas show the governing mathematics [140]:

$$\begin{aligned}
D &= \left| C X_p(t) - X(t) \right| \\
X(t+1) &= X_p(t) - AD \\
A &= 2a r_1 - a \\
C &= 2r_2
\end{aligned} \tag{3.43}$$

here, t represents the iteration; X and X_p show position of a grey wolf and the prey, respectively. $|\cdot|$ returns the absolute value. Based on this algorithm, r_1 and r_2 are accidental numbers within the [0-1] interval, and values of a are fall from 2 to 0 in iterations.

Positions of wolves are updated as below:

$$\begin{aligned}
D_\alpha &= \left| C_1 \cdot X_\alpha - X \right|, D_\beta = \left| C_2 \cdot X_\beta - X \right|, D_\delta = \left| C_3 \cdot X_\delta - X \right| \\
X_1 &= X_\alpha - A_1 \cdot (D_\alpha), X_2 = X_\beta - A_2 \cdot (D_\beta), X_3 = X_\delta - A_3 \cdot (D_\delta) \\
X(t+1) &= \frac{X_1 + X_2 + X_3}{3}
\end{aligned} \tag{3.44}$$

Briefly, the different steps in the *GWO* method are depicted in Fig. 3.16.

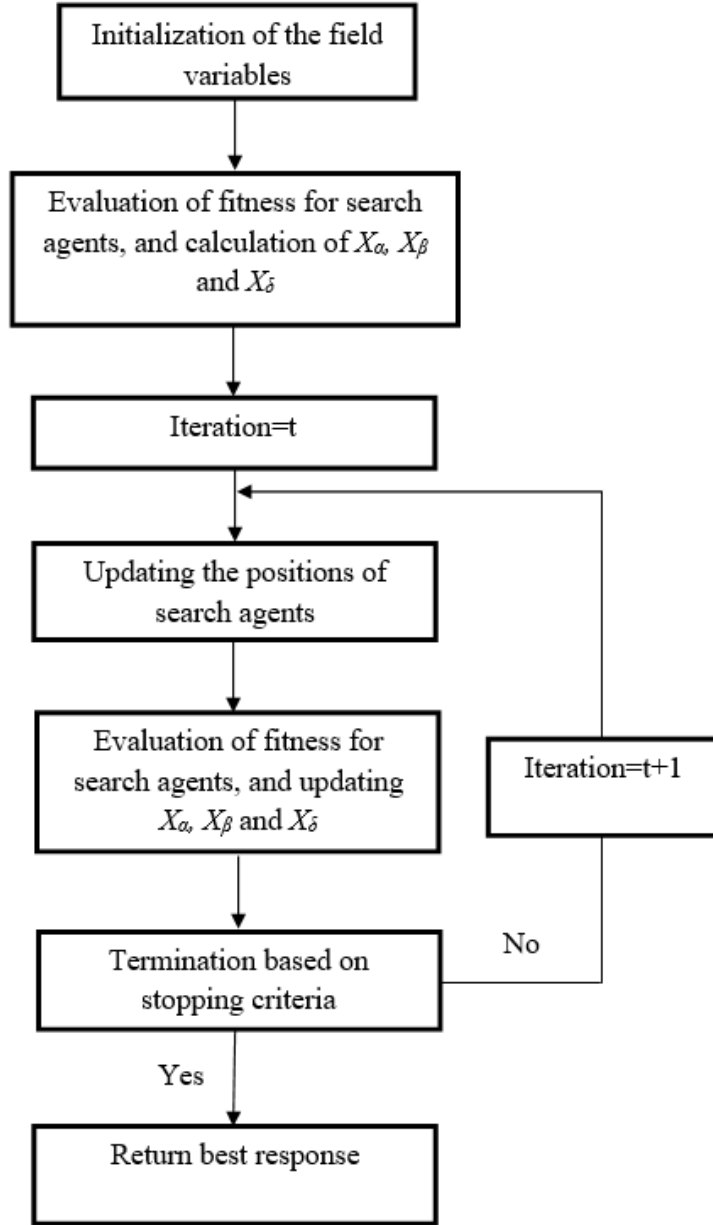


Fig. 3.16: Steps of the *GWO* method.

With the help of quadrature method, the first governing equation of the pyroelectric shell is expressed as:

$$c_{33} \sum_{l=1}^{M_1} A^{(2)}_{il} u_l + c_{13} \left\{ \frac{1}{r_i} \sum_{l=1}^{M_1} A^{(1)}_{il} u_l - \frac{1}{r_i^2} u_i \right\} + e_{33} \sum_{l=1}^{M_1} A^{(2)}_{il} \psi_l - \beta_r \sum_{l=1}^{M_1} A^{(1)}_{il} T_l \quad (3.45)$$

$$\begin{aligned}
& + \frac{\partial c_{33}}{\partial r} \sum_{l=1}^{M_1} A^{(1)}_{il} u_l + \frac{\partial c_{13}}{\partial r} \frac{u_i}{r_i} + \frac{\partial e_{33}}{\partial r} \sum_{l=1}^{M_1} A^{(1)}_{il} \psi_l - \frac{\partial \beta_r}{\partial r} T_i + \frac{1}{r_i} \left\{ c_{33} \sum_{l=1}^{M_1} A^{(1)}_{il} u_l \right. \\
& + c_{13} \frac{1}{r_i} u_i + e_{33} \sum_{l=1}^{M_1} A^{(1)}_{il} \psi_{ljk} - \beta_r T_i - c_{13} \sum_{l=1}^{M_1} A^{(1)}_{il} u_l - c_{11} \frac{1}{r_i} u_i - e_{31} \sum_{l=1}^{M_1} A^{(1)}_{il} \\
& \left. + \beta_\theta T_i \right\} = 0
\end{aligned}$$

The discretised electrostatic equation is:

$$\begin{aligned}
& e_{33} \sum_{l=1}^{M_1} A^{(2)}_{il} u_l + e_{31} \left\{ \frac{1}{r_i} \sum_{l=1}^{M_1} A^{(1)}_{il} u_l - \frac{1}{r_i^2} u_i \right\} - \eta_{33} \sum_{l=1}^{M_1} A^{(2)}_{il} \psi_l \\
& + p_r \sum_{l=1}^{M_1} A^{(1)}_{il} T_l + \frac{\partial e_{33}}{\partial r} \sum_{l=1}^{M_1} A^{(1)}_{il} u_l + \frac{\partial e_{31}}{\partial r} \frac{u_i}{r_i} - \frac{\partial \eta_{33}}{\partial r} \sum_{l=1}^{M_1} A^{(1)}_{il} \psi_l \\
& + \frac{\partial p_r}{\partial r} T_i + \frac{1}{r_i} \left\{ e_{33} \sum_{l=1}^{M_1} A^{(1)}_{il} u_l + e_{31} \frac{1}{r_i} u_i - \eta_{33} \sum_{l=1}^{M_1} A^{(1)}_{il} \psi_l + p_r T_i \right\} = 0
\end{aligned} \tag{3.46}$$

In the same way, the steady state heat transfer analysis is similarly discretised as:

$$\frac{K}{r_i} \sum_{l=1}^{M_1} A^{(1)}_{il} T_l + K \sum_{l=1}^{M_1} A^{(2)}_{il} T_l + \frac{\partial K}{\partial r} \sum_{l=1}^{M_1} A^{(1)}_{il} T_l = 0 \tag{3.47}$$

Meanwhile, the surface interactions are discretised in series format:

$$c_{11} \sum_{l=1}^{M_1} A^{(1)}_{il} u_l + c_{12} \frac{1}{r_i} u_i + e_{11} \sum_{l=1}^{M_1} A^{(1)}_{il} \psi_l - \beta_r T_i + P(r) = 0 \tag{3.48}$$

3.4.4 Numerical results and discussions

First, all simulation data are graphically obtained in dimensionless format. The below non-dimensional formulas are used for field parameters:

$$\begin{aligned}
(\bar{\sigma}_r, \bar{\sigma}_\theta) &= \frac{1}{P}(\sigma_r, \sigma_\theta) \quad , \quad \bar{u} = \frac{1}{b}u \\
\bar{T} &= \frac{T}{T_a} \quad , \quad \bar{\psi} = \frac{\eta\alpha}{Pb}\psi \quad , \quad \bar{q} = \frac{b\alpha}{K}q \\
\bar{U} &= \frac{U}{U_{\text{Homogeneous}}} \quad , \quad \bar{W} = \frac{W}{W_{\text{Homogeneous}}}
\end{aligned} \tag{3.49}$$

here α stands for the thermal expansion coefficient; also, q shows the thermal flux.

The inner surface of the smart vessel is made of PZT-5H, and material properties vary across the thickness according to Eq. (3.24). Li *et al.* listed the properties of PZT-5H [112], as shown in Table 3.3.

Table 3.3: Thermo-electro-elastic properties of PZT-5H [182].

Elastic modulus, GPa			Piezoelectric constants, C/m ²	
c_{11}^0	c_{33}^0	c_{13}^0	e_{31}^0	e_{33}^0
126	117	53	-6.5	23.3
Permittivity	Pyroelectric constant	Density	Thermal conductivity	
$10^{-9}\text{C}^2/\text{Nm}^2$	$10^{-5}\text{C}/\text{m}^2\text{k}$	kg/m^3	w/mk	
η_{33}^0	p_{11}^0	p_{22}^0	ρ^0	K_r^0
13	5.4	5.4	7500	2

3.4.4.1 Evaluation study

In this section, validity of the results is confirmed. Outputs of the proposed work are compared with results of the smart shell discussed by Li *et al.* [182]. The vessel is polarized in the radial direction, and its material properties are orthotropic and nonhomogeneous. The calculated circumferential stress and electrical outputs are plotted in Fig. 3.17, indicating the accuracy of the utilized semi-analytical algorithm. Specifically, the proposed algorithm can be easily applied to any arbitrary variation of material properties, where presenting the

analytical solution is impossible. Moreover, this algorithm can be implemented in complex geometries as well as the nonlinear problems at which usually analytical solutions cannot be straightforwardly found [182].

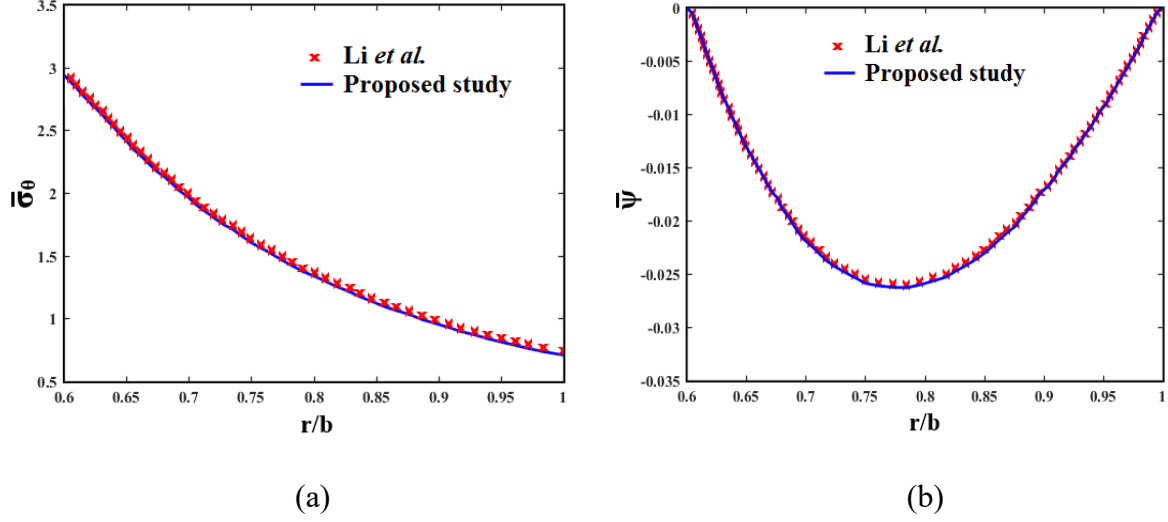


Fig. 3.17: Comparison of the response of FG smart vessel with those of reference [182] for radial distribution of the (a) circumferential stress, and (b) electric potential.

3.4.4.2 Evaluation of the GWO with PSO

Next, results of the *GWO* are compared with those of *PSO*. As an evolutionary iterative-based approach, *PSO* has been applied in many engineering simulations. After assigning the initial values to particles, *PSO* begins searching in the search space, while the positions ($x_{i,i}$) and velocities ($v_{i,i}$) of particles are upgraded at every step, as discussed in references [130, 132]:

$$\begin{aligned} v_{i,j}(t+1) &= wv_{i,j}(t) + c_1r_1(p_{i,j} - x_{i,j}(t)) + c_2r_2(p_{g,j} - x_{i,j}(t)) \\ x_{i,j}(t+1) &= x_{i,j}(t) + v_{i,j}(t+1) \end{aligned} \quad (3.50)$$

Here, $p_{i,j}$ stands for the best response in the history for the particle; $p_{g,j}$ is the global best; c_1 and c_2 account for the learning factors and are constant; w expresses the inertia modulus; r_1 and r_2 denote the arbitrary random numbers in the interval of $[0, 1]$.

Results of the *GWO* and *PSO* methods are obtained and are delineated in Fig. 3.18, showing that the weight obtained is almost the same for both algorithms, whereas the electrical energy obtained by the *GWO* method is almost 3% greater than that obtained by the *PSO* approach. From this figure, it can be concluded that the *GWO* algorithm can be employed in solving complex engineering problems involving mixed partial differential and integral equations.

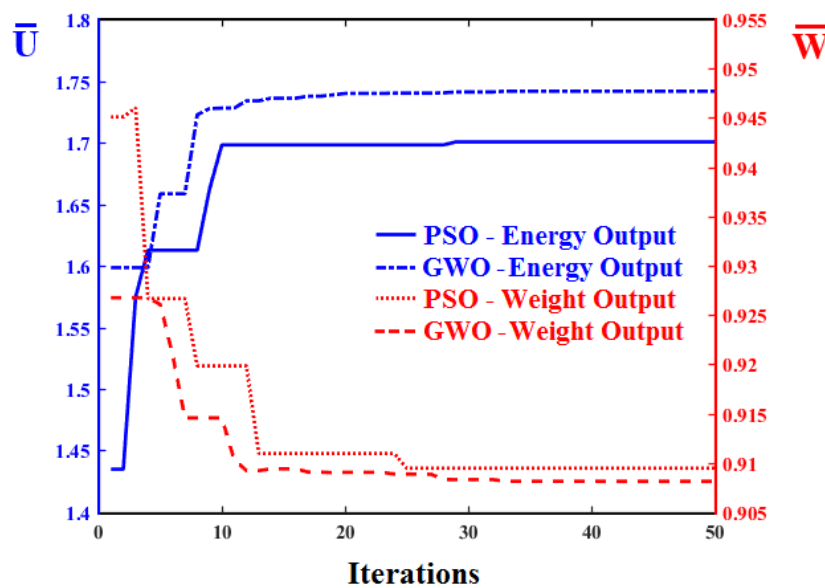


Fig. 3.18: Comparison of results of the *GWO* method with those of the traditional *PSO*.

3.4.4.3 Homogeneous and inhomogeneous vessels

As already mentioned, in the energy extraction application of smart structures, there are two key parameters, i.e., the electrical energy output and the weight of the structure. It is a demanding task to compare the energy production performance of homogeneous piezoelectrics with their inhomogeneous counterparts. Results of the *GWO+DQ+GIQ* algorithm are presented in Table 3.4. The results demonstrate that the optimized responses of the FG smart shells generate a remarkable growth in energy output (75%) while a significant decrement is observed in weight (9.1%). These outstanding results mean that the proposed

design can be implemented in energy scavenging structures to solve the problem of low-power generation of smart devices.

Table 3.4: Effects of inhomogeneity on weight and stored energy of FG shell structures.

	β_1	β_2	β_3	\bar{W}	Weight reduction	\bar{U}	Energy increment
Homogeneous shell	0	0	0	1	-	1	-
FG vessel	-3.7352	5	-1.6151	0.909	9.1%	1.75	75%

Next, for homogeneous and inhomogeneous vessels, the results for variations of elastic and electrical fields through the r -direction are presented in Fig. 3.19. From this figure, it can be appreciated that the boundary conditions of the problem have been satisfied perfectly, demonstrating the high accuracy of the proposed method in solving complex interactions of mechanical, electrical and thermal interactions. Also, the dimensionless distributions of radial and circumferential stresses signify that the structure is in the safe region, demonstrating that the proposed algorithm works well. As shown in Fig. 3.19d, the electric potential rises considerably, producing higher values of electrical energy.

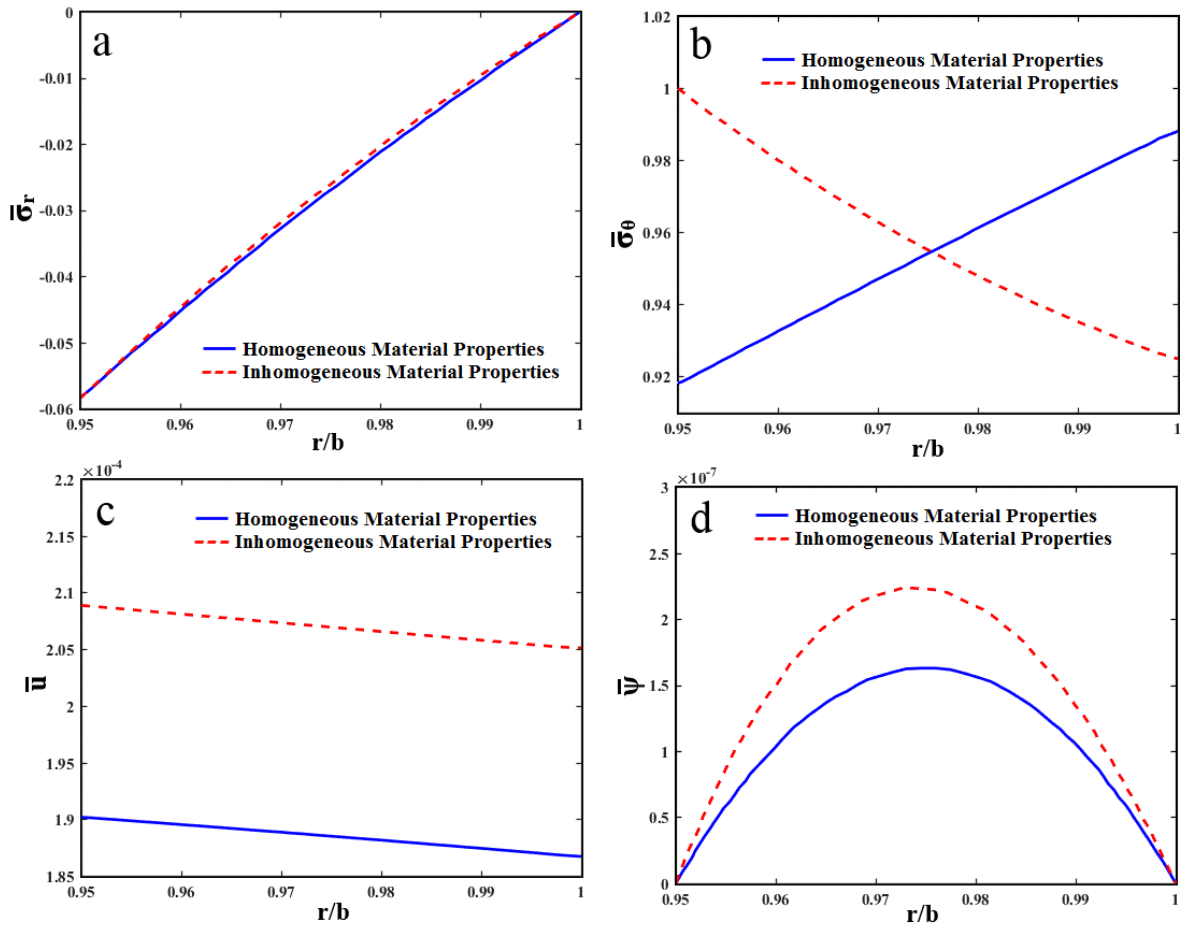
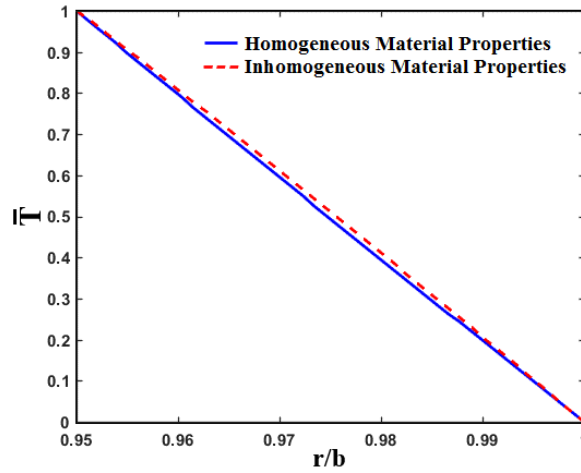
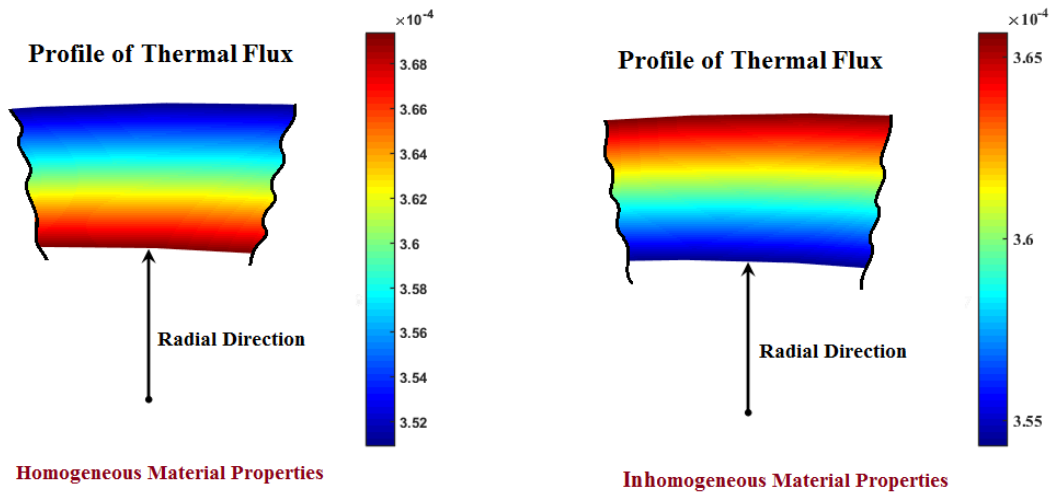


Fig. 3.19: Inhomogeneity impacts on (a) radial stress, (b) circumferential stress, (c) radial displacement, and (d) electric potential.

Impacts of inhomogeneity on the thermal field are presented in Fig. 3.20. Since the thermal conductivity varies through the thickness in accordance with the power law, temperature has a nonlinear distribution for the inhomogeneous structure. Fig. 3.20b shows the dimensionless distribution of the thermal flux. It is interesting to note that for a homogeneous structure, the maximum amount of thermal flux occurs in the inner section, whereas inhomogeneous shells tolerate the maximum flux at the outer radius, due to the shaping and refining of the material elements by the proposed algorithm.



(a)



(b)

Fig. 3.20: Inhomogeneity impacts on radial distribution of the (a) temperature, and (b) thermal gradient.

3.4.4.4 Effects of thermal loading

Lastly, the effects of thermal excitations on the dimensionless curves of elastic, electrical and temperature fields are investigated. The results showing a decrease in weight and increase in electrical energy are presented in Table 3.5. As expected, for lower values of thermal excitation, simulation presents smart structures with less weight and higher electrical output.

Table 3.5: Results of the optimization algorithm for different temperature excitations.

	β_1	β_2	β_3	\bar{W}	Weight Reduction	\bar{U}	Energy Increment
$T(a)=12\text{ }^\circ\text{C}$	-4.4560	5	-3.1132	0.892	10.8%	1.74	74%
$T(a)=15\text{ }^\circ\text{C}$	-2.8439	5	0.12379	0.929	7.1%	1.56	56%

The impacts of the thermal shock on behaviour of the mechanical, electrical and thermal fields are examined in Fig. 3.21. All calculations are done with a variable temperature at inner radius while a constant temperature is applied at the outer boundary condition. The thermal field has increased the thermal stresses, as displayed in Figs. 3.21a and 3.21b. Moreover, Figs. 3.21a and 3.21b show that the values of the thermal stresses are in the permitted range, guaranteeing the impeccability of the structure. The response of the radial displacement and electric potential are highlighted in Figs. 3.21c and 3.21d. It is observed that the of deflection values decline as the temperature difference increase. Also, the maximum values of radial displacement happen at inner section where the thermal excitation is maximized. In the last analysis, profiles of the thermal flux are calculated and plotted in Fig. 3.21e. It is noteworthy that with lower temperature inputs, the maximum thermal flux can be observed at $r=a$, whereas with higher thermal excitations the maximum position of the thermal flux shifts to $r=b$. This behaviour is due to changes in the grading index of the thermal conductivity coefficient (i.e., β_3). From the figure, this trend can be extracted by applying different thermal loadings, where various values of the electric output can be introduced to demonstrate the pyroelectric effect.

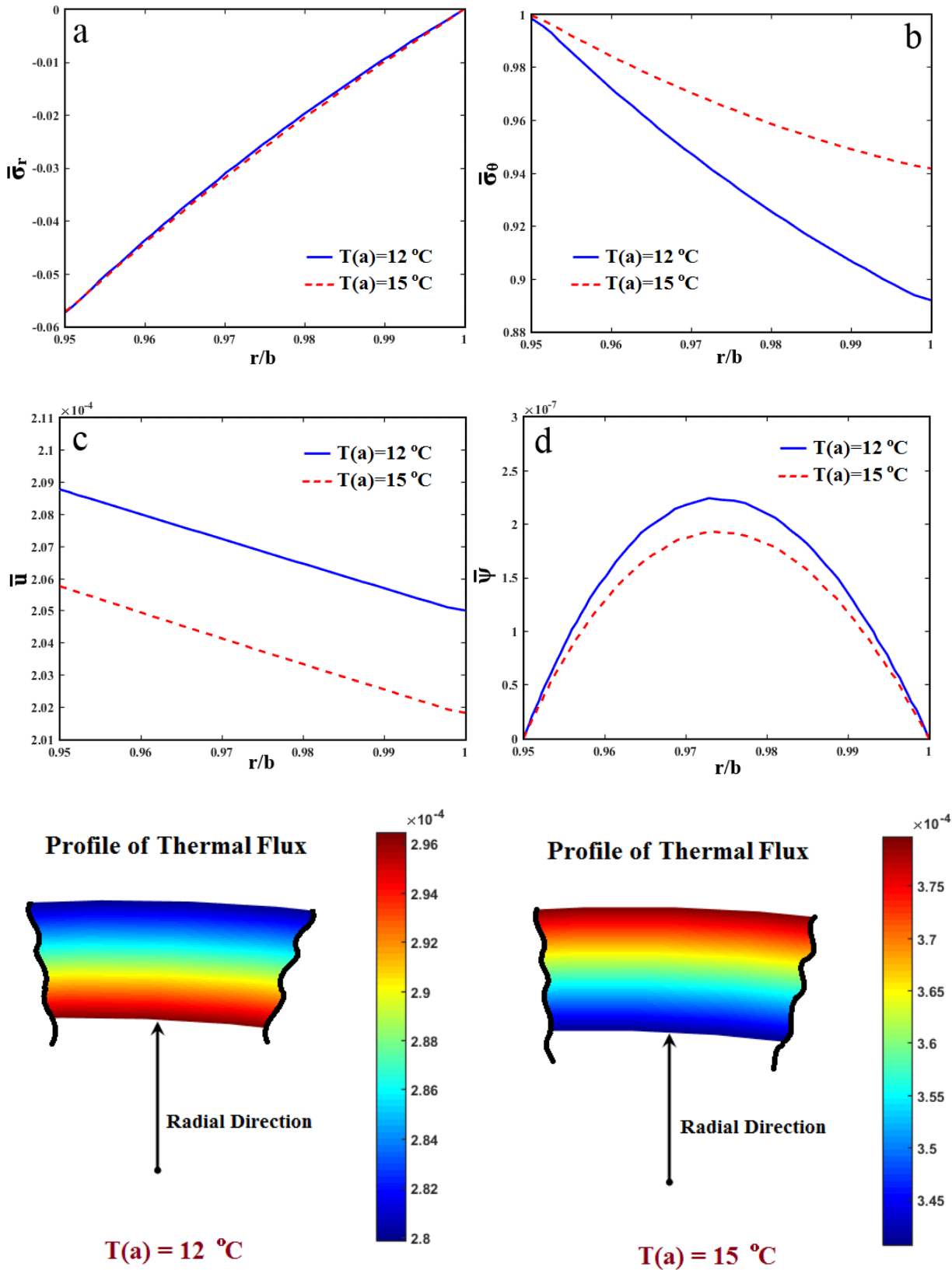


Fig. 3.21: Impacts of thermal loading on (a) radial stress, (b) tangential stress, (c) radial displacement, (d) electric potential, and (e) thermal flux.

3.5 Summary

Given the urgent demands of current lifestyle for electrical energy, it is enormously important to introduce new generations of smart systems that efficiently generate the electrical form of energy. To meet this demand, we introduce a smart system which is sufficiently capable of storing high amounts of electrical energy in its elements while the weight of the structure is substantially reduced. For numerical simulation, it was supposed that the properties of the vessel change through the r direction, while the mechanical, electrical and thermal fields of the pyroelectric shell have their own independent gradient indexes (i.e., β_1 , β_2 and β_3). The energy interactions among mechanical, electrical and thermal excitations were analysed through an adroit combination of the *GWO* method with *DQ* and *GIQ* approaches. The *GWO* scheme searches for the best values of the grading index to refine the elements of the material, while the *DQ* and *GIQ* methods solve the boundary bonds and the governing partial differential and integral equations. It was shown that the proposed algorithm could work efficiently to attribute appropriate values to the grading index of FG smart shells, rendering higher electrical energy corresponding to a noticeable decrease in weight. Furthermore, a study was presented to show the effects of inhomogeneity and temperature excitations on the obtained electrical energy and the weight. Boundary conditions at the edges were perfectly satisfied. All calculations were accomplished while maintaining the structure away from failure regions. Generally, cracking and yielding can happen when dimensionless deflections reach a determined critical level. Therefore, the concept discussed here is a fundamental source for energy-harvesting applications of shell structures. This work highlights the potential of properly functionalized smart materials to maintain the safety and structural integrity of FG smart shells while maximizing the electrical output and minimizing the weight.

In the structural health monitoring of mechanical systems, smart materials, particularly piezoelectric materials, have shown strong performance because of their light weight, structural simplicity, and excellent coupling characteristics between mechanical and electrical fields. In the current study, the coupled transient interactions among thermal, electrical, and elastic fields of laminated spherical shells including an FG host layer and piezoelectric substrates were carefully extricated. In investigation of transient heat transfer and electrostatic charge constraints, governing equations of FG vessels and smart counterparts of the system were derived. A semi-analytical technique, the quadrature method, was exploited to find the solutions for stress, displacement, and electric fields of laminated FG spherical shells with piezoelectric covering at the interior and exterior surfaces as actuator and sensor layers. Graphic outputs of the simulations demonstrated that the interface compatibility conditions between adjacent layers and boundary bonds at the edges were fully satisfied. Also, in general, cracking and yielding of mechanical structures occurred when the stresses reached a determined value great enough to exceed the critical value of materials. The patterns obtained through the proposed algorithm could be of considerable assistance by presenting the timed responses of the variations of stress and displacement at different points in the structure. Moreover, it was demonstrated that the grading index of materials, thermal and electrical excitation, and geometry of the shell played important roles in the distribution of stress, displacement, electric, and thermal fields. It was found that the values of stresses and displacement could be managed by selecting a suitable grading parameter. The values of the deflections and sensed electric potential were sharply affected as the thermal gradient changed. The effects of the ratio of the thickness of the FG host layer to the thickness of the piezoelectric layers on the electric potential were greater than those of other field parameters. Furthermore, the effect of piezoelectricity became negligibly small as the thickness of the piezoelectric layers decreased to about 2% of the thickness of the host shell. Finally, electric

excitation had a marked effect on the field parameters in the actuator layer; their distributions were almost linear, due to constant properties through the radial direction.

Sliding triboelectric nanogenerators

4.1 Motivation

It was already mentioned that piezoelectric energy harvesters can produce a relatively acceptable voltage when experiencing physical motivation. However, some serious challenges remain to be solved. The first problem is low current output particularly when the size of piezo films is shrunk. Also, we have a limited choice of materials to be implemented in the harvesting design. Integrate such issues with required complex fabrication process, especially in micro/nano scales, and susceptibility to properties change over the time, a more efficient and sustainable energy harvesting approach is vital.

Triboelectrification, as the procedure of transferring small-scale static electricity charges generated by friction contact between dissimilar films, has frequently been considered as an approach for accumulating energy from organic materials. During the contact, the triboelectrification phenomenon leaves some charges with opposite polarities on each surface. Those triboelectric charges can be generated between nearly any arbitrary pair of materials, encompassing semiconductors, conductors such as metals, and insulators such as non-ionic materials. The electrification phenomenon has been the focus of some researches. In fact, different materials show different tendencies to accept or donate electrons. In detail, the materials on the top side of the series have a great tendency to donate electrons, while the materials in negative side accept the electrons easily. It can be concluded that farther the two materials in positive and negative sides, higher is the surface charge density generated during the physical contact. This parameter can significantly affect the output of the TENGs. Generally, we have two version of TENGs, including: (i) Sliding mechanism, (ii) Contact-

separation mechanism. The working principle of both mechanisms is described in next section.

4.2 Experimental setup

In our experiment, PTFE and Nylon were used as a pair of triboelectric films of the same size (L=10 cm, W=10 cm and t=250 μ m). The schematic presented in Fig. 4.1a illustrates the sliding process and details of the sliding surfaces. The two dielectric materials were placed at opposite sides of the triboelectric series. Figs. 4.1b-4.1f indicate the experimental setup and the row of serially connected LEDs successfully lit up. In experimental setup, PTFE was positioned at the surface of the mechanism as the bottom dielectric film and Nylon was glued to a free-moving acrylic glass attached to a rotating disk. A drill attached to the rotating disk was used to create the linear motion (Figs. 4.1b-4.1e). This setup was found to be much cheaper than a linear actuator, and it could provide various rates of acceleration.

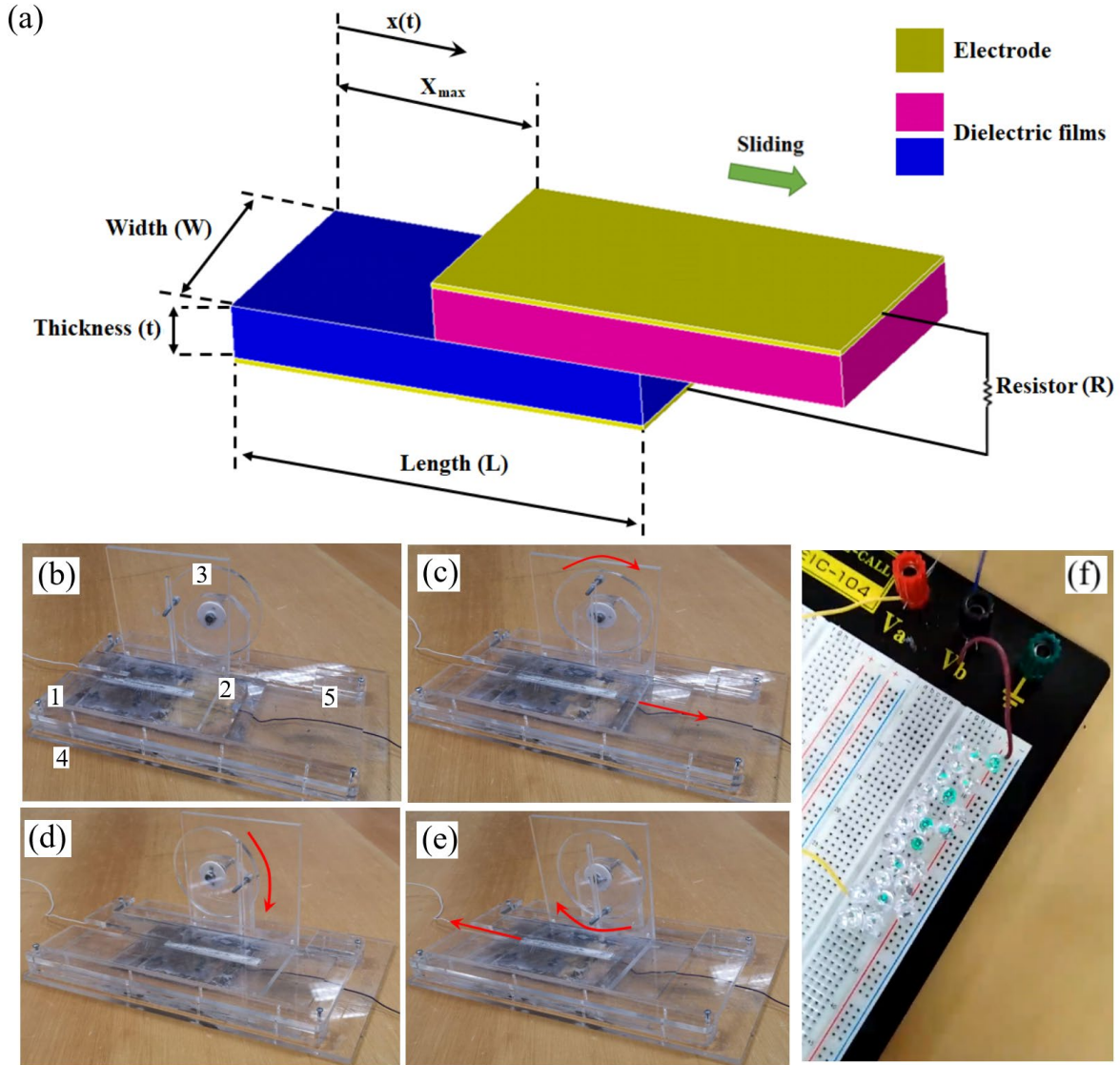


Fig. 4.1: The experiment set up design of TENG including (a) a schematic of the sliding process and components, (b-e) multi-orientation images of the setup. The experiment setup was mainly consisted of 5 major parts: part 1: the sliding segment including PTFE; part 2: sliding segment including Nylon; part 3: actuator to convert rotary motion of a motor to a reciprocal movement, part 4: base, part 5: top plate, and (f) serially connected LEDs being turned on during reciprocal motion.

A metal electrode layer (chromium, $t=50$ nm) was deposited on the external surface of each triboelectric film, known as electrodes. To enhance the charge transfer between

electrodes, the in-contact surfaces of the sliding triboelectric films were coated with gold ($t=200$ nm). Before coating, the triboelectric films were twice washed carefully with ethanol and dried under a fume hood. A dual-target sputter coater (Q300T-D, Quorum, UK) was used for coating under the vacuum condition. The presence of coating was evaluated by scanning electron microscopy (SEM, Inspect F50, FEI, USA) by comparing the surfaces of the triboelectric film of Nylon before (Fig. 4.2a) and after (Fig. 4.2b) coatings. As seen in Fig. 4.2b, the upper surface (top surface) of the triboelectric film (Nylon) was coated with gold and the lower surface (bottom surface) was coated with chromium. SEM images of the gold-coated surface was also captured under higher magnifications (Figs. 4.2c and 4.2d) to identify the structures of the in-contact surfaces of the sliding triboelectric films. As shown in Fig. 4.2c, the in-contact surface of the films comprised gold layers that were parallel to the contact surface and sliding direction.

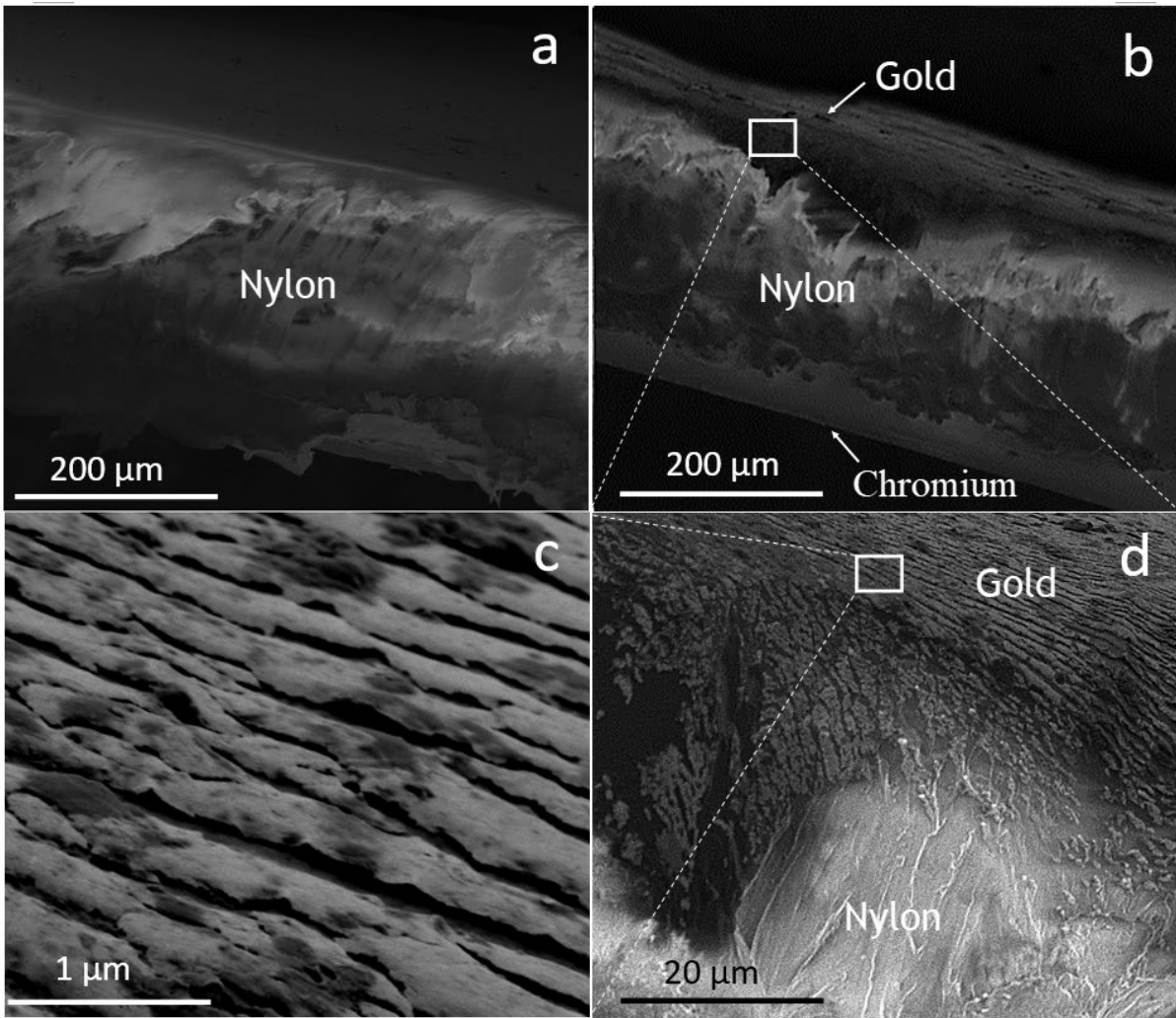


Fig. 4.2: SEM images captured from the cross-section of Nylon film (a) without, and (b) with coating. The upper and lower surfaces of the Nylon film (b) were coated with gold and chromium, respectively. (c) and (d) SEM cross-section images captured at higher magnifications from the upper surface coated with gold.

4.3 Load resistance analysis of TENGs

The open-circuit condition shows a situation in which the resistor value goes to the infinity, resulting in no current. Also, the short circuit state reflects a condition in which the resistance is negligible, leading to zero voltage along the connection. The fact should be considered that both short circuit and open circuit conditions indicate the ideal current and voltage outputs of the device. In practical applications, TENGs are connected to different resistors. Then,

analysis of the TENG's resistor circuit is highly important. Nominating the capacitance and open-circuit voltage as C and V_{oc} , the basic formulation describing the relationship between voltage (V) and the transferred charges between electrodes (Q) can be written as [61, 62]:

$$V = \frac{-1}{C}Q + V_{oc} \quad (4.1)$$

To derive the formula for capacitance, it is assumed that the length and the width of the dielectric substrate are considerably greater than its thickness. Then, the behavior of the electrodes can be considered as two parallel infinite plates. The general formula for the capacitance is thus:

$$C = \frac{\epsilon_r S}{D} \quad (4.2)$$

where S represents the contact area; D is the distance between electrodes; ϵ_r is the permittivity of the space. Depending on the region of overlap between PTFE and Nylon, the capacitance can be formulated as:

$$C = \frac{\epsilon_0 w(l - x(t))}{\frac{d_1}{\epsilon_1} + \frac{d_2}{\epsilon_2}} \quad (4.3)$$

where d_1 and d_2 stand for the thickness of the dielectric films; ϵ_1 and ϵ_2 are the permittivity of the dielectric films. l and w are the length and the width of the dielectric films, respectively. Also, $x(t)$ shows the sliding distance in sliding-mode TENGs, respectively.

In sliding-mode TENGs, at non-overlapping sections of dielectrics, the value of surface charge density is assumed to be σ . In the open-circuit condition, the total charge in the electrode layer must be zero; then the absolute value of surface charge density can be calculated simply, as $\sigma x/(l-x)$. Combining the surface charge density and electric field into the Gauss theorem [183], the open-circuit voltage for TENGs can be written as:

$$V_{OC} = E_1 d_1 + E_2 d_2 = \frac{\sigma x(t)}{\varepsilon_0(l-x(t))} \left\{ \frac{d_1}{\varepsilon_1} + \frac{d_2}{\varepsilon_2} \right\} \quad (4.4)$$

Now, merging the equations of the capacitance and the open-circuit voltage with the V - Q relationship results in:

$$V = \frac{-1}{C} Q + V_{OC} = \frac{-1}{\varepsilon_0 w(l-x(t))} \left\{ \frac{d_1}{\varepsilon_1} + \frac{d_2}{\varepsilon_2} \right\} Q + \frac{\sigma x(t)}{\varepsilon_0(l-x(t))} \left\{ \frac{d_1}{\varepsilon_1} + \frac{d_2}{\varepsilon_2} \right\} \quad (4.5)$$

A short circuit condition denotes the condition at which voltage across the electrodes must be set to zero; hence, the short circuit charge (Q_{sc}) can be calculated by:

$$Q_{sc} = \sigma w x(t) \quad (4.6)$$

Also, the short circuit current can be evaluated by taking the time-derivative of the short circuit charge, i.e.:

$$I_{sc} = \frac{dQ_{sc}}{dt} = \sigma w \frac{dx}{dt} = \sigma w v(t) \quad (4.7)$$

As already mentioned, TENGs in real applications are supposed to be attached to an external resistor. Then, based on Ohm's law in circuit analysis, the V - I relationship is expressed as:

$$V = RI = R \frac{dQ}{dt} \quad (4.8)$$

where R represents a resistor. Merging Eqs. (4.5) and (4.8) leads to:

$$R \frac{dQ}{dt} = \frac{-1}{\varepsilon_0 w(l-x(t))} \left\{ \frac{d_1}{\varepsilon_1} + \frac{d_2}{\varepsilon_2} \right\} Q + \frac{\sigma x(t)}{\varepsilon_0(l-x(t))} \left\{ \frac{d_1}{\varepsilon_1} + \frac{d_2}{\varepsilon_2} \right\} \quad (4.9)$$

The better strategy in power evaluation of TENGs is measuring the average power produced over time:

$$P_{ave} = \frac{\int_0^T V I dt}{T_t} = \frac{\int_0^T R I^2 dt}{T_t} \quad (4.10)$$

where T_t is the total time of the analysis.

4.4 Simulation process

The principal task of the present study would be efficiently harvesting the electrical energy from our surroundings. To meet this need, a comprehensive study is conducted on characteristics of the available energy harvesters. Behaviours of triboelectric-based energy harvesters under different work conditions are scrutinized to represent a modified generation of old-fashion nanogenerators. As an inseparable ingredient of the present technology, an effective optimization scheme should be implemented into our calculations.

In engineering and physic circles, artificial intelligence plays a vital role in reduction of the hidden marginal costs and augmentation of inherent characteristics of any problem. To achieve this goal, energy harvesting theories should be merged with advanced artificial intelligence techniques, leading to high performance nanogenerators. In detail, electrical, mechanical and material specifications of energy harvesters determine the level of produced voltage and current from nano up to micro units. The more rational choice for these parameters, the more economical and productive electricity generation approach.

So far, various mathematical techniques have been developed for modelling. In conventional artificial intelligence methods, high-level heuristic procedure was being applied to find the best solution with limited computational efforts. The major limitation was the fact that algorithm got stuck in local optimized regions. However, in early 21st century, some new ideas have been presented to decrease the error and greatly decline the cost function of the optimization study. In this thesis, the emphasis is on exploiting the recently established approaches to compensate the inherently low efficiency of nanogenerators. The basic idea is on dividing the whole domain into sub-domains; initializing the particles in the search region; and finding the best solution based on the local and general populations' feedback.

Increasing the output power of TENGs and decreasing the size of the system are of great importance. Here, we introduce a simulation process in which the generated power is

increased, and the size is miniaturized. Specifically, the first scheme finds the exact value of the resistance circuit for a predefined geometry. The second scheme is the identification of the smallest dimension of dielectric layers while the power output is fixed.

Previously, we [132] presented a powerful merged algorithm that was based on a semi-analytical solver and an iteration-based advanced optimization scheme for solving the coupled optimization and dominant equations for large-scale engineering structures. Here, that algorithm is implemented into micro/nanoscale problems to investigate the characteristics of triboelectric nanogenerators. The flowchart of the procedure is presented in Fig. 4.3. The capability of this algorithm with other artificial intelligence methods in [132] were compared, showing a greater performance. Here, we use the two PSO method in parallel, (i.e. *CPSO*), to find the best result for TENG's parameters. The internal loop seeks out optimization variables in the predefined search space while the external loop exerts the penalty limitations. Meanwhile, the governing mathematics should be solved in every step of each loop. The artificial intelligence and the governing mathematics were coded in MATLAB.

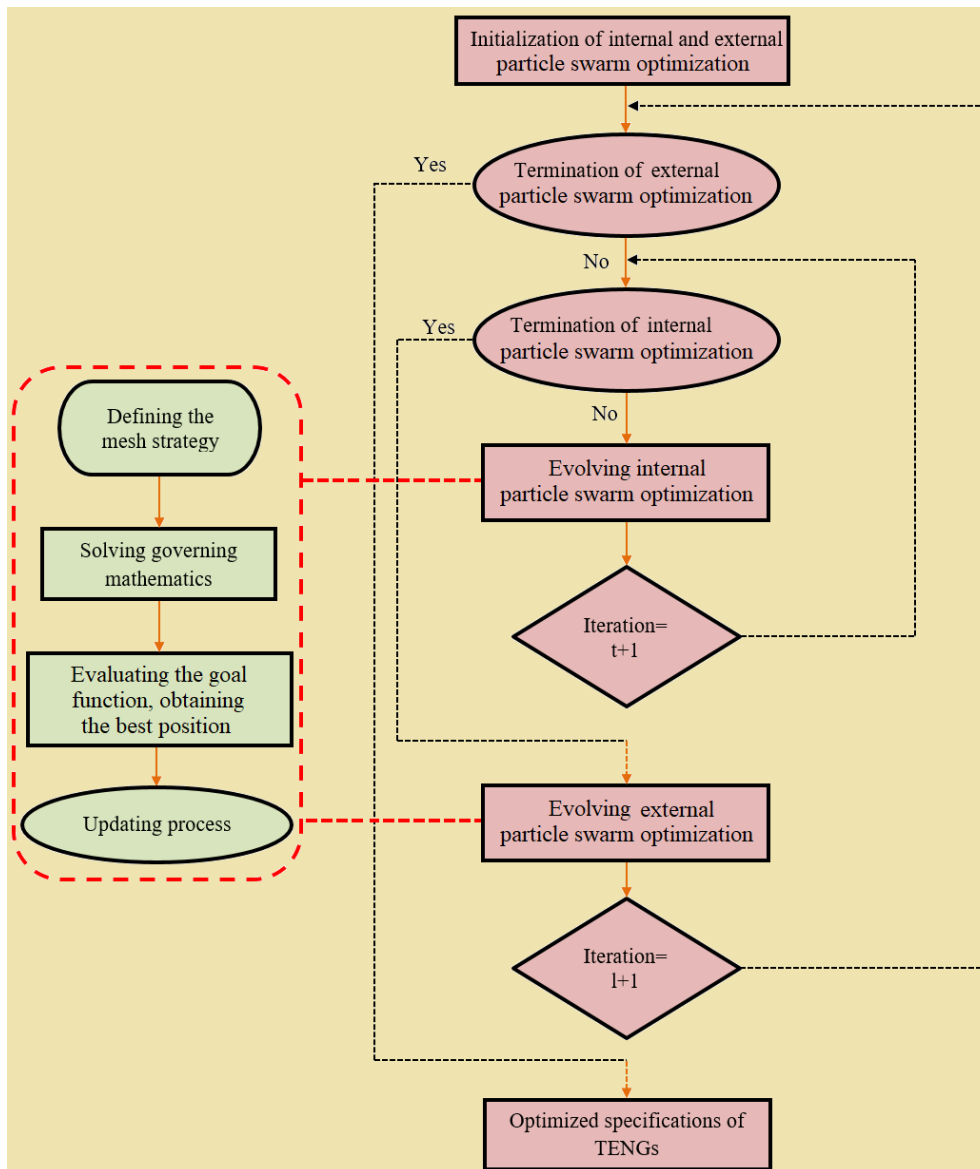


Fig. 4.3: The optimization procedure of the sliding-mode TENGs.

The major difficulty in any optimization scheme is how to find the best responses of variables while all constraints are satisfied. Here, we apply *CPSO* as an advanced optimizer and merge it with *DQ* approach to develop the power output, kinematic, and geometry of TENGs. The main task of the optimization theory is searching for the best answer under the rule of constraints. Meanwhile, a mathematical solver presents the answers for charge, current, and voltage of TENGs. The details regarding the algorithm was described in the previous chapter.

4.5 Simulation results

Here, first a study is conducted to evaluate the accuracy of the proposed algorithm. Then, a various study is presented to characterize the TENGs.

4.5.1 Validity evaluation

First, the validity of the presented algorithm is evaluated by comparing the results of sliding-mode TENGs with experimental outputs reported by Niu et al. [61]. Although many materials can be used practically in TENGs structures, some especial materials, including PTFE, glycol-modified polyethylene terephthalate, polydimethylsiloxane, and polymethyl methacrylate, can be effectively coupled with others such as polyamide, aluminum, silver, and copper to produce a high volume of triboelectric charges in the contact region [61, 184, 185]. As the experiment reported in [61], it is assumed that the dielectric pair consists of Nylon and PTFE. The material properties of the dielectric layers are cited in Table 4.1.

Table 4.1: Properties of dielectric films [61].

Parameter	Value	
Nylon	ρ (kg/m ³)	1150
	ϵ_r	4
PTFE	ρ (kg/m ³)	2200
	ϵ_r	2.1

As reported in [61], in the experiment, the bottom dielectric layer was fixed, and the motion process was guided through a linear motor accelerating and decelerating the top dielectric layer at a constant acceleration. Throughout the experiment using different

resistors, Niu et al. [61] kept all other parameters the same and obtained the curves of the voltage and current in order to maximize the power output of the TENGs. From our application of the proposed algorithm, the calculation is presented and the results for current and voltage are plotted in Fig. 4.4. In comparison with experimental outputs of Ref. [61], the present study produces a very good simulation of the real experimental design.

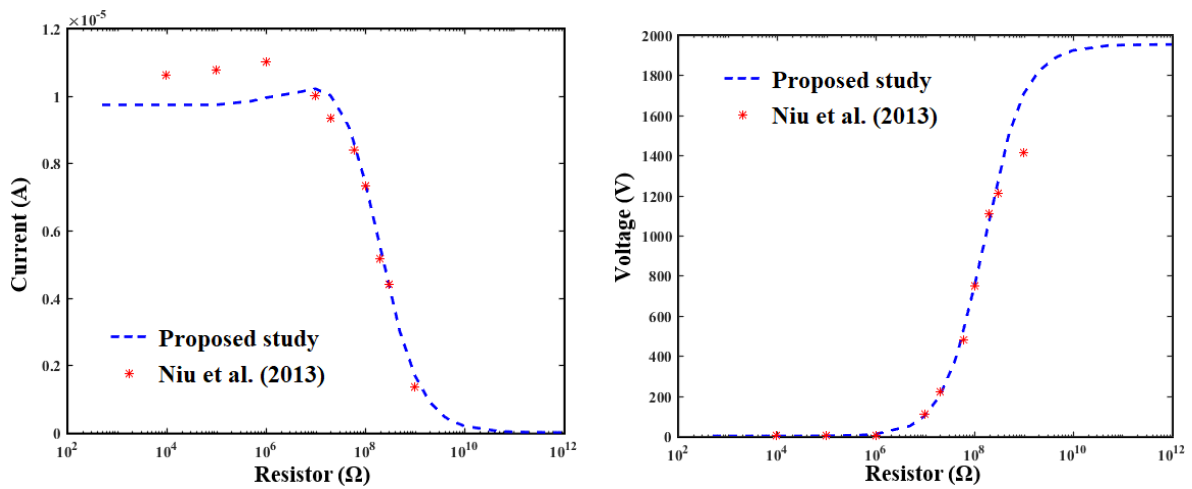


Fig. 4.4: Comparison of results obtained for (a) current and (b) voltage with those of Ref. [61].

Next, a comparison of the simulation outputs with those of our experiment is presented. The dielectric layers are of equal thickness, $d_1=d_2=250 \mu\text{m}$, which are considerably less than the length and width; therefore, the formulation of the capacitance will be valid. It is assumed that the bottom dielectric layer is fixed while the top dielectric layer moves with a constant acceleration/deceleration rate, i. e., $a_c \approx 35 \text{ m/s}^2$. The motion is defined as:

$$\begin{aligned}
x &= 0.5a_c t^2, \quad (t < \sqrt{\frac{x_{\max}}{a_c}}) \\
x &= x_{\max} - 0.5a \{2\sqrt{\frac{x_{\max}}{a_c}} - t\}^2, \quad (\sqrt{\frac{x_{\max}}{a_c}} < t \leq 2\sqrt{\frac{x_{\max}}{a_c}}) \\
x &= x_{\max} - 0.5a \{2\sqrt{\frac{x_{\max}}{a_c}} - t\}^2, \quad (2\sqrt{\frac{x_{\max}}{a_c}} < t \leq 3\sqrt{\frac{x_{\max}}{a_c}}) \\
x &= 0.5a \{4\sqrt{\frac{x_{\max}}{a_c}} - t\}^2, \quad (3\sqrt{\frac{x_{\max}}{a_c}} < t \leq 4\sqrt{\frac{x_{\max}}{a_c}})
\end{aligned} \tag{4.11}$$

Environmental effects, particularly humidity and ambient pressure, can significantly affect the generated power of the TENGs [186-189]. It was demonstrated that the transferred charges during triboelectrification surge 20% when relative humidity decreases from 90% to 10% at the ambient pressure. Furthermore, the amount of transferred charges drops as the air pressure decreases from atmospheric pressure to 50 Torr with a relative humidity of 0%. Also, the optimum working condition of the TENG device shifts to a low pressure when the relative humidity is high. The impacts of humidity are becoming significant where relative humidity exceeds 50%. The effect of different levels of humidity on output power was excluded in the current study. However, to minimize and control the humidity effect, all samples were kept in similar preconditioning using a sealed container before testing and all experiments were performed in the ambient pressure with consistent relative humidity of approximately 40%. In addition, the surface microstructure is another useful route in order to improve the electric performances of TENGs [190-193]. However, the effect of environmental conditions and surface microstructure were excluded of the current study and another study is required to address the associated results. To calculate the surface charge density, we consider four cycles of the sliding process and use the average to find a more accurate value for σ . The integration of current over time results in induced charge during the sliding process. Fig. 4.5 shows the output of the TENG for 4 cycles.

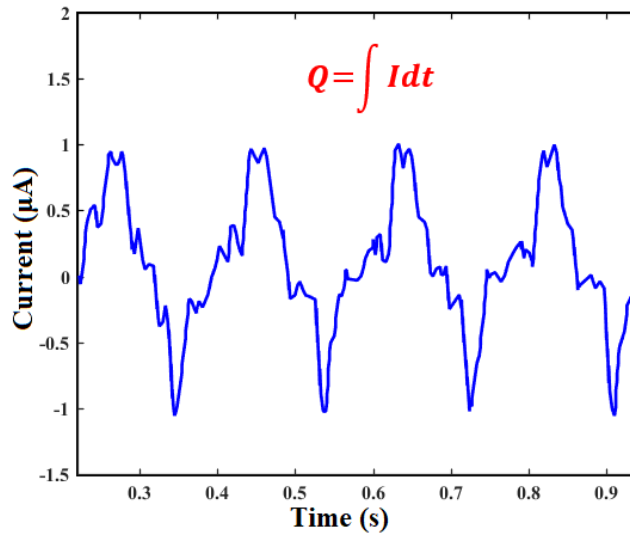


Fig. 4.5: Induced charges generated in four cycles.

In our setup, the size of the triboelectric film is 10 cm by 10 cm. $\sigma=Q/S\approx 5 \mu\text{C}/\text{m}^2$. The results are plotted in Fig. 4.6. When $R=8 \text{ M}\Omega$, temporal curves of the current and voltage are drawn in Figs. 4.6a and 4.6b. As it is evident, good agreement can be found between simulation and experimental data. Furthermore, for various load resistances, the distributions of the maximum values of current and voltage are plotted in Figs. 4.6c and 4.6d, indicating that simulation matches the experiment well.

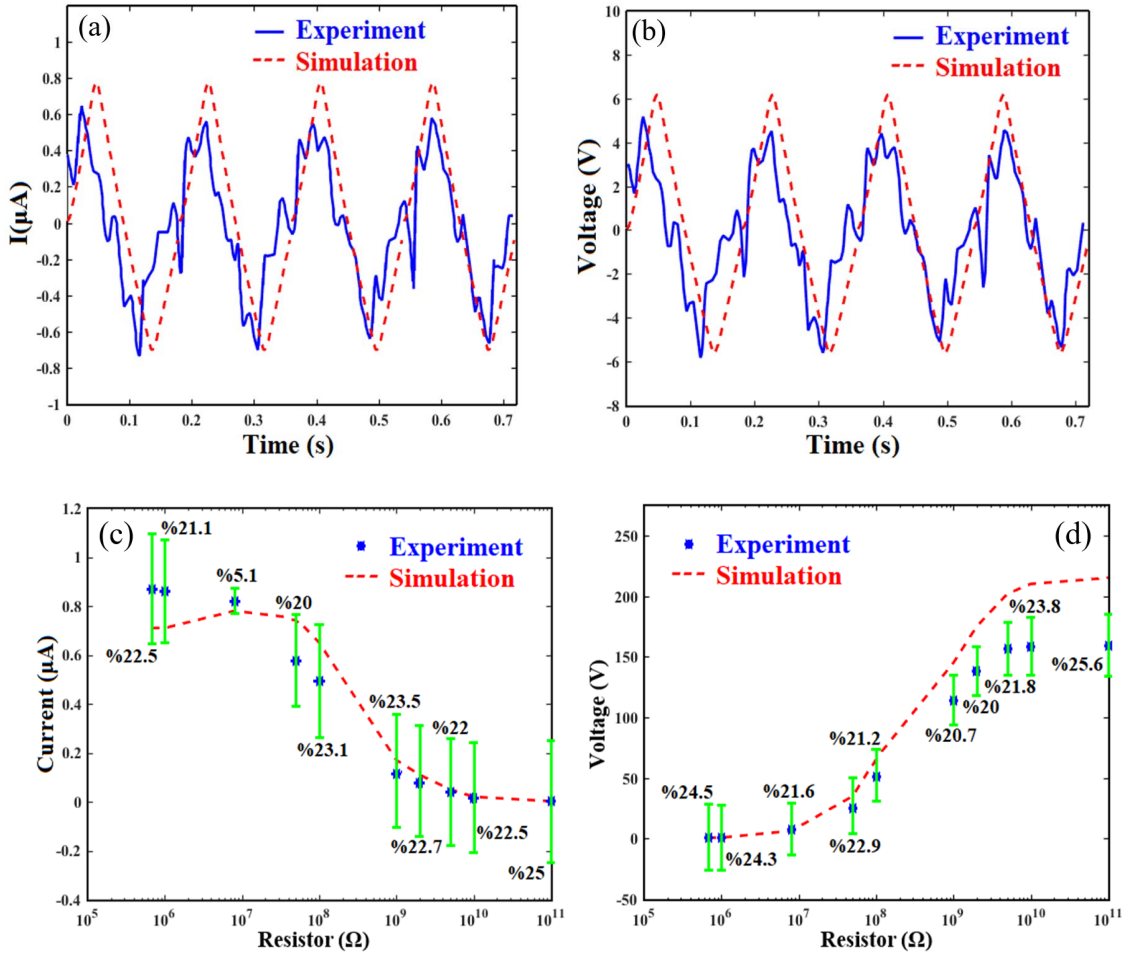


Fig. 4.6: Comparison of the simulation results with our experiment (a) temporal response of the current for $R=8 \text{ M}\Omega$, (b) temporal response of the voltage for $R=8 \text{ M}\Omega$, (c) maximum current, and (d) maximum voltage.

It should be noted that some distortions happened in the experimental curves of the voltage and current in comparison to the simulated results. In fact, through the simulation, we assumed a fully in tight contact between the top and bottom triboelectric films. However, we have imperfect sliding motion. Moreover, electrostatic influences from the environment can affect the results of the TENG, making some distortions in the current and voltage curves. Also, for formulation of the TENG, we had some ideal assumptions which can imply some differences between the simulation and experimental data. In order to derive the formulation, it was assumed that the electrodes work as infinite plates in each region. Under this

circumstance, the electric field will be almost uniform along the vertical direction inside the dielectric films. The distribution of the surface charge density has also been considered uniform in each region. But it does not occur.

The above-mentioned reasons made some differences between the simulation and experimental data. The error bar was displayed in Figs. 4.6c and 4.6d. In fact, open circuit and short circuit conditions are ideal states reflecting more difference between simulation and experimental results. For the regions far from the open circuit and short circuit conditions, the error is almost 20%. However, the accordance in Figs. 4.4 and 4.6 between simulation and experiments proves that the simulation is correct and can be utilized to estimate the experimental cases. Lifetime of TENG is a key parameter that should be taken into consideration. The SEM images of Nylon surface before and after gold coating and the coated surface after 1000, 10,000, and 30,000 cycles of operation are shown in Fig. 4.7. It can be observed that the wear features can be identified on the surface after cycling slide, especially after large number of sliding cycles. However, the microstructure of the gold-coated surfaces was not significantly affected by the huge numbers of cycles to generate electricity, reflecting acceptable durability of the device structure at the microscale.

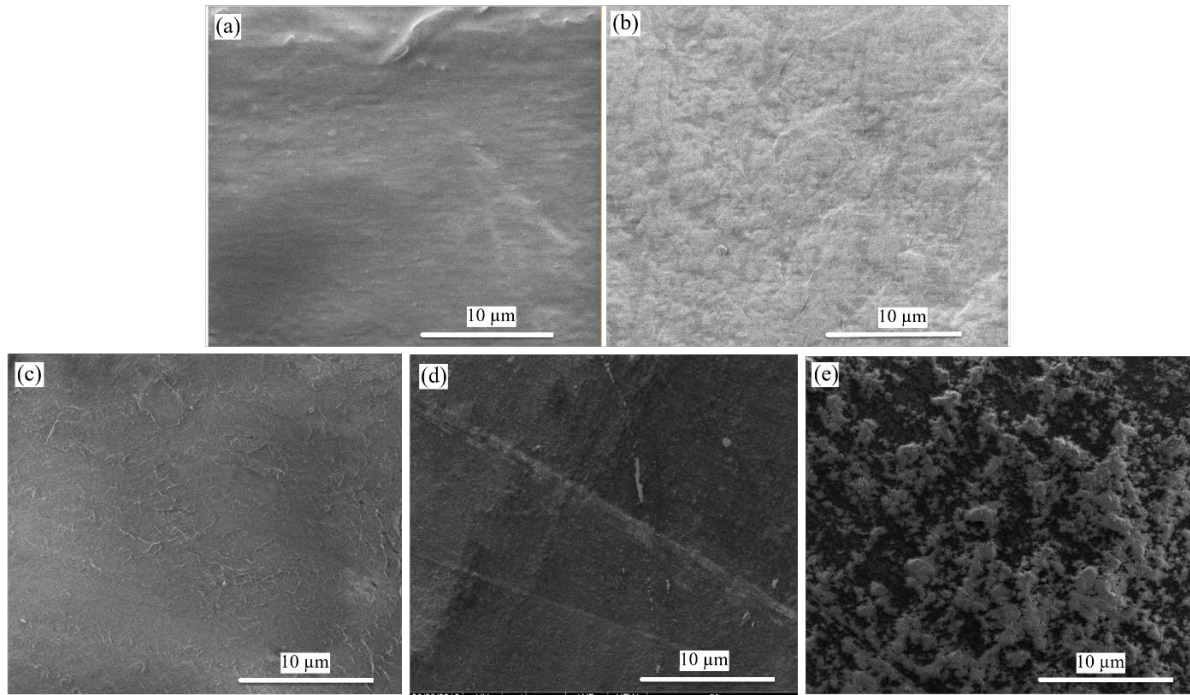


Fig. 4.7: The SEM images of the Nylon surface (a) before and (b) after gold coating and the coated surface after (c)1000 cycles, (d) 15,000 cycles and (e) 30,000 cycles of sliding.

4.5.2 Prediction of TENG's outputs

Because experimentation was not possible for different geometries and loading conditions, it was highly important to numerically predict the behavior of TENGs. In this section, the effects of the thickness of dielectric films and the load resistance on the output of the sliding-mode TENG are investigated.

The variation of the maximum values of the voltage, current, and P_{ave} across various resistors and thicknesses of the triboelectric layers are plotted in Fig. 4.8. As shown in Fig. 4.8a, for a constant thickness, the value of voltage increases as the resistor value rises, reaching its maximum in the open circuit condition. However, the reverse behavior can be observed from Fig. 4.8b, where the maximum current is obtained in the short circuit condition. Fig. 4.8c reflects the fact that the average power output is highly dependent on the load resistance and the thickness of dielectric films. For example, for $d_{Nylon}=d_{PTFE}=50 \mu\text{m}$, the

maximum P_{ave} occurs at $R=1 \text{ G}\Omega$, and its value is almost 1.4 mW. This value increases to 35.7 mW when $d_{Nylon}=d_{PTFE}=1000 \text{ }\mu\text{m}$ and $R=10 \text{ G}\Omega$. Dot points stand for experimental data reported in Ref. [61].

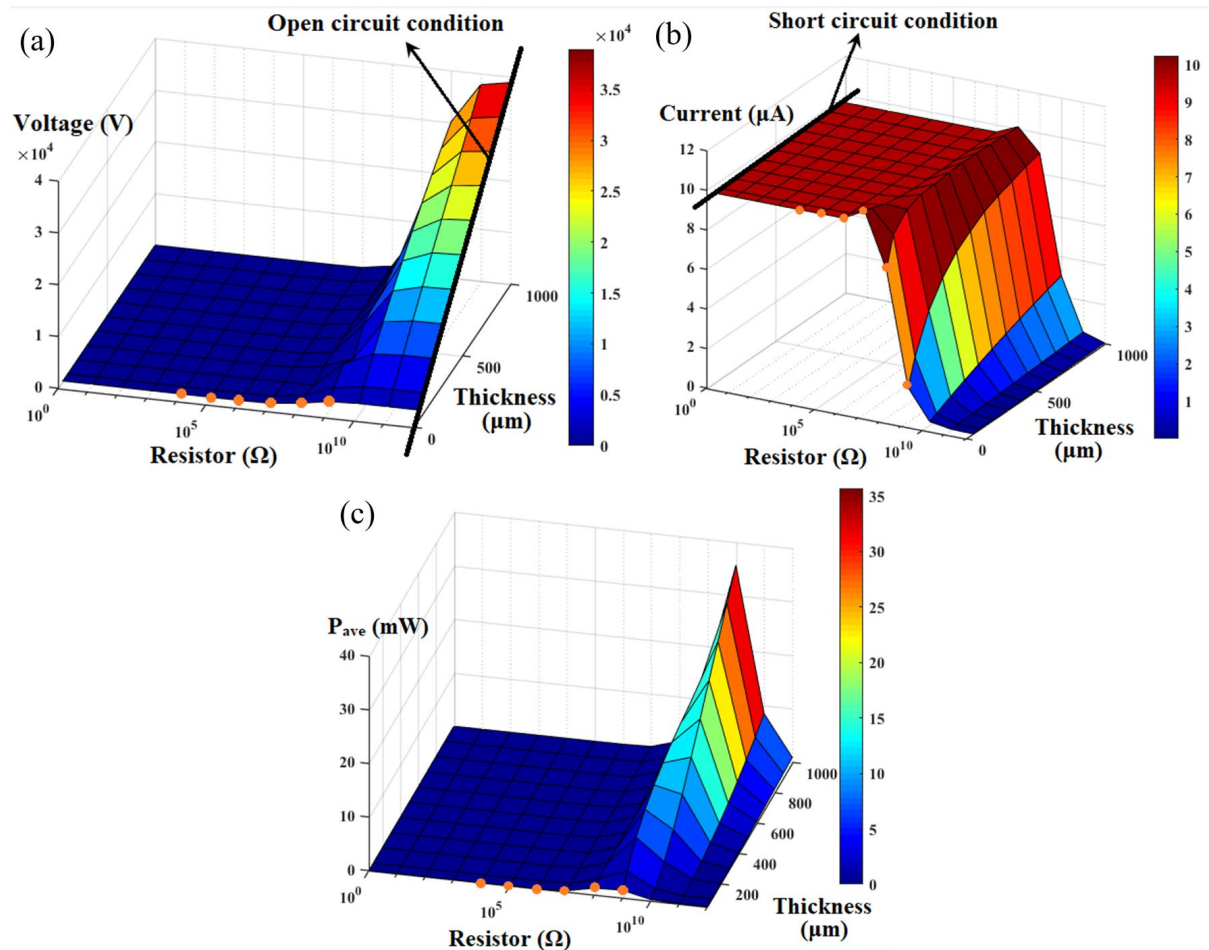


Fig. 4.8: Dependence of TENG's outputs on the resistor and thickness of the triboelectric films: (a) voltage, (b) current, and (c) average power output.

Fig. 4.9 reflects the sensitivity of P_{ave} to change in the resistor and thickness of triboelectric films. The gradient of P_{ave} in respect to the resistor reaches around 17, while only touching 0.045 in respect of thickness. This investigation clearly demonstrates that the output power of TENG can be dominantly affected by the load resistance.

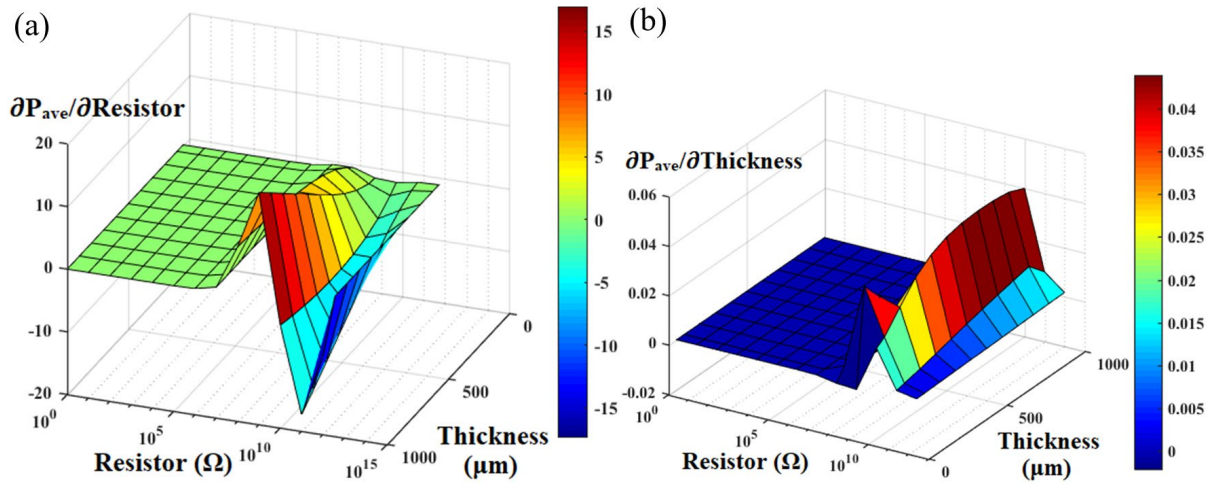


Fig. 4.9: Variation of the average power output in respect to (a) resistor and (b) thickness of triboelectric films.

Next, the impacts of the contact area on the maximum values of the voltage, current, and output power of the TENG are examined in Fig. 4.10. Liu et al. experimental results [61] are shown with dot points on the curves. As expected, voltage, current and average output power increase with the increment of the contact area. The results indicate that the maximum voltage is not a function of the contact area in the open circuit condition. However, the current increases linearly with contact area in the short circuit condition.

The gradient of average power output is calculated in respect of the load resistance and contact area and the results are plotted in Fig. 4.11. The maximum gradient in respect of the resistor is greater than 60, whereas the gradient is always less than 0.08 in respect of the contact area. As clearly evidenced, the resistor is the dominant factor for describing the behaviors of the sliding TENGs.

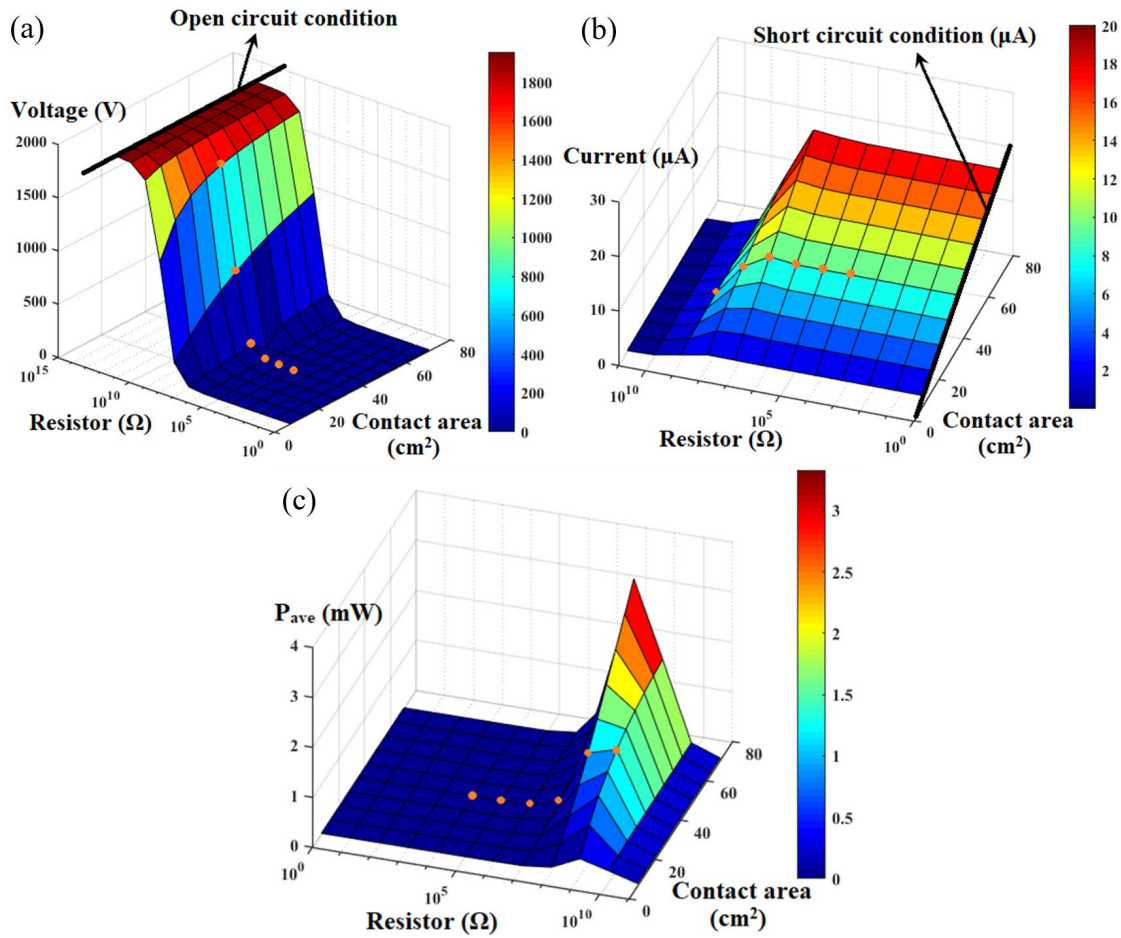


Fig. 4.10: Impacts of the resistor and contact area on outputs of the TENG, including (a) voltage, (b) current, and (c) average power output.

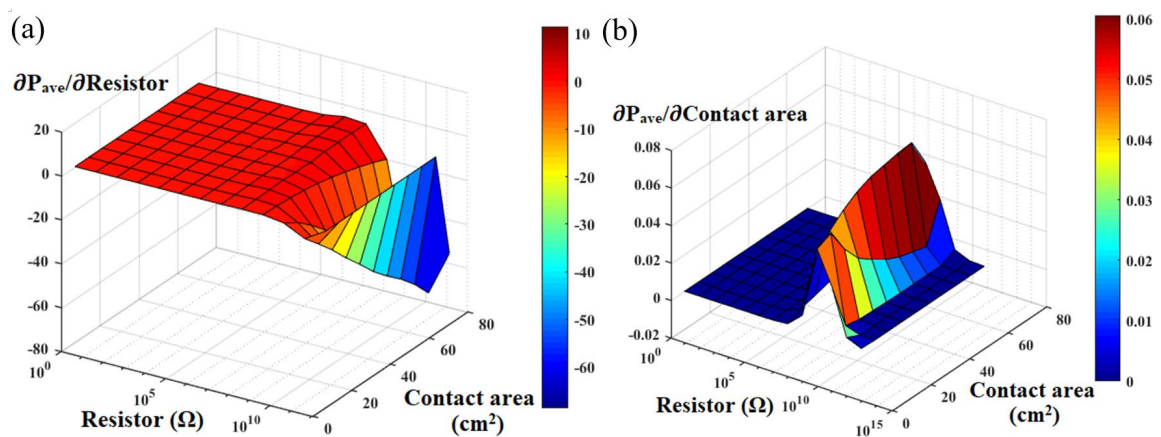


Fig. 4.11: Variation of the average power output in respect of (a) resistor and (b) contact area.

Figs. 4.9 and 4.11 showed that for lower values of the external resistance the variation of contact area and the thickness of dielectric films have a negligible impact on outputs of the TENG. However, when the load resistance is in a range of $\sim 100 \text{ M}\Omega$ to $\sim 10 \text{ G}\Omega$, any change in the thickness or contact area will significantly affect the TENG's output. Fig. 4.12 compares the impacts of the contact area and thickness of the dielectric films for different resistors. The results provided for the dimensionless contact area (A/A_{max} , $A_{max}=71 \text{ cm}^2$) and thickness (t/t_{max} , $t_{max}=1000 \text{ }\mu\text{m}$). This figure clearly shows that when $R=100 \text{ M}\Omega$, the average power output of the TENG is highly dependent on the contact area, and the change of thickness has insignificant effect. In the case $R=1 \text{ G}\Omega$, contact area is still the dominant parameter, however the impacts of thickness increase than the previous case. Fig. 4.12c indicates that the thickness has higher effect on output of the TENG.

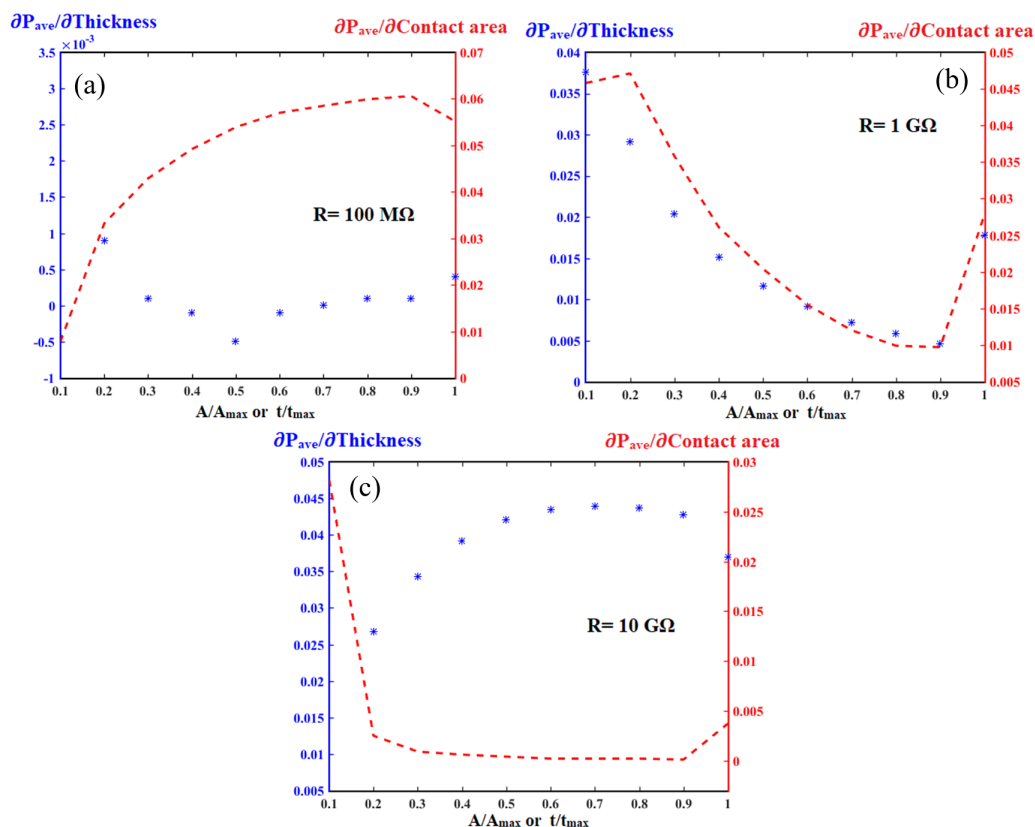


Fig. 4.12: Comparing the impacts of the thickness of the dielectric films and contact area for different load resistances: (a) $R=100 \text{ M}\Omega$, (b) $R=1 \text{ G}\Omega$, and (c) $R=10 \text{ G}\Omega$.

4.5.3 Study of the thickness of dielectric films

The main concept of TENGs is based on the construct of generating electric power from mobile working conditions, such as human motion. In such conditions, miniaturizing the system is vitally important. One of the most important parameters of the electrical responses of TENGs is the thickness of dielectric films. As Eq. (4.9) shows, this geometry has a direct impact on voltage, current, and then power output of TENGs. On the one hand, as already mentioned, the basic performance of TENGs is on the ground of the distinct material properties of dielectric layers. On the other hand, the size and density of dielectric layers overwhelmingly affect the dimensions and total weight of the system. Thus, for driving electronics with predetermined power consumption, it is of great significance to choose the optimum value of thickness.

Here again, we consider Ref. [61], in which an experiment was conducted to obtain the output of a sliding-mode TENG. The width (w) and length (L) of dielectrics are equal to 0.05 m and 0.071 m respectively. Tribo-charge surface density is set at $\sigma=200 \mu\text{C}/\text{m}^2$. It is assumed that the top dielectric film moves in the outward direction with the uniform acceleration of $a=20 \text{ m}/\text{s}^2$. The algorithm is implemented for sliding-mode TENGs working under different load resistors. Through the experiment in [61], an average power output of 1.2 mW was achieved when $R=100 \text{ M}\Omega$. Then, the aim is to determine the thickness of the dielectric films to achieve the predetermined average power output, $P_{ave}=1.2 \text{ mW}$. Fig. 4.13 depicts the results of the convergence study for the thickness of the dielectric films.

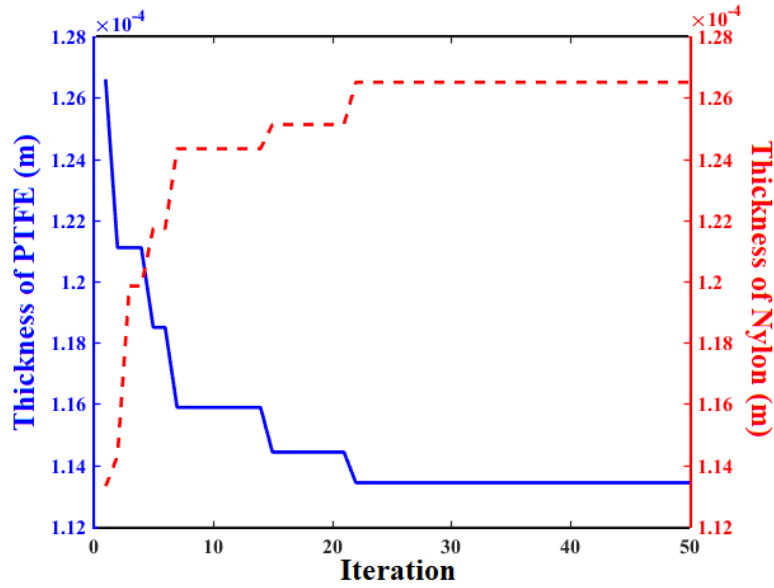


Fig. 4.13: Convergence study of the proposed algorithm.

The results of the simulation under different load resistances are presented in Table 4.2.

Table 4.2: Simulation results for the optimum dielectric thickness of different resistor values.

Load resistance (M Ω)	Thickness of dielectrics (μm)		Weight (gr)
	Nylon	PTFE	
100	107	19.5	5.82
1000	95.8	20	5.38
10000	113	127	14.23
100000	354	375	42.91

Fig. 4.14 shows the changes in the optimal thickness of PTFE and Nylon across different resistors. It is clearly evident that the thickness is almost constant for lower values of R . However, a sharp increase is found near the open circuit condition. In detail, the TENG's output power significantly depends on the match with the resistor. As demonstrated in Fig. 4.8, when the load resistance is low, both collected voltage and the current are almost

constant, close to the short-circuit condition; the reason is infinitely large inner resistance of the TENG. For higher values of the R , the calculated voltage increases, while the current decreases. Therefore, the harvested energy will sharply grow and then drops at higher values of R . Meanwhile, Fig. 4.8 shows that the average power output can increase with increment in the thickness. Consequently, the optimality of the system will be almost constant at lower values of resistance and will increase at open circuit condition.

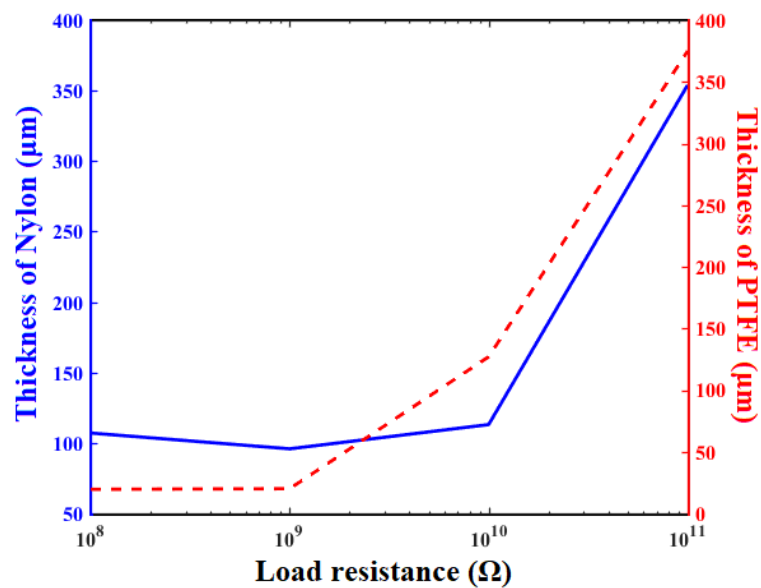


Fig. 4.14: Variation of the optimum thickness of dielectric films with resistor.

The curve responses of the transferred charge, current, voltage, power, and harvested energy of the sliding-mode TENG are plotted in Fig. 4.15. From Fig. 4.15, it is evident that, as soon as the top dielectric film begins to move outwards, the in-plane charge separation, current, voltage, output power, and energy of the TENG begin to increase exponentially until the dielectric layer stops moving. From that moment, the current and output power fall rapidly. As expected, as shown in Figs. 4.15a and 4.15b, the value of the transferred charge and consequently the current between electrodes decreases as the load resistance increases. When the condition is very close to the open circuit condition, i.e., $R=100 \text{ G}\Omega$, the minimum

charge is transferred. The short circuit current reaches around $7.5 \mu\text{A}$. The voltage curve is drawn in Fig. 4.15c, from which it is highlighted that the functional values of the obtained voltage grow as the load resistance rises. In this case, the value of the open-circuit voltage with $R=100 \text{ G}\Omega$ is almost 14000 V . Fig. 4.15d shows the power output of sliding-mode TENGs. From Fig. 4.15e, it can be understood that the maximum functional value for power almost reaches 5.5 mW , but in all cases, $P_{ave}=1.2 \text{ mW}$. The harvested energy reaches approximately 0.25 mJ for all resistors.

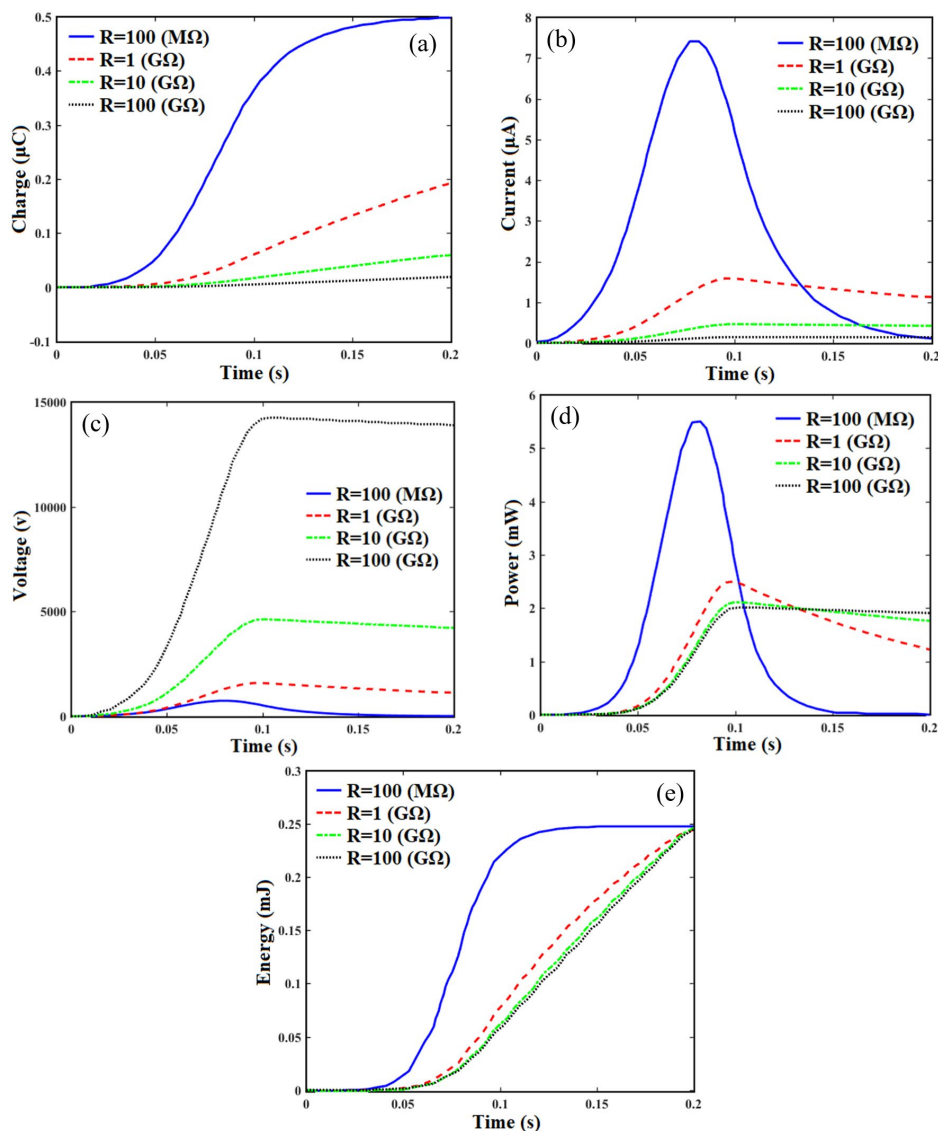


Fig. 4.15: Results of different resistors on electrical outputs of dielectric-to-dielectric sliding-mode NTEGs (a) charge, (b) current, (c) voltage, (d) power, and (e) energy.

4.5.4 Investigation of optimal load resistance

Here, the charge surface density, geometries including width, length, and maximum separation and acceleration rate are the same as in the previous section. For different thicknesses of the dielectric layer, we aim to determine the load resistance in order to achieve the maximum value of average power output. The simulation results are summarized in Table 4.3, from which it is evident that load resistance and consequently average power output increase with the increase in PTFE thickness.

Table 4.3: Optimum load resistance of sliding-mode TENGs for different geometries.

Thickness of triboelectric films (μm)	Load resistance ($\text{M}\Omega$)	Average power output (mW)
50	370	1.8
100	716	3.67
200	1470	7.32
300	2215	11
400	2953	14.6
500	3681	18.31

Fig. 4.16 shows the variation of the optimum resistor and the maximized power output for different thicknesses of PTFE film. As is clearly evident, a linear increase is seen in load resistance and average power output with an increase in thickness of the dielectric film.

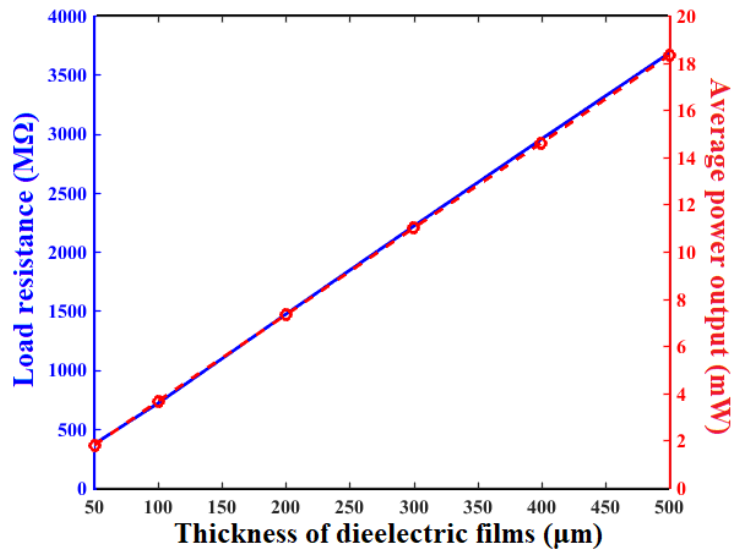


Fig. 4.16: Variation of optimum load resistance and average power output with the thickness of the dielectric film.

The time responses of TENG characteristics are plotted in Fig. 4.17. The variations in the charge and current corresponding to different values of thickness are almost constant, as shown in Figs. 4.17a and 4.17b. The value of the open-circuit voltage changes with variation in thickness of films, as denoted in Eq. (4.4). The temporal curve of voltage demonstrates that its value increases substantially with increase in thickness of the dielectric film. The same pattern can be found in the power distribution of sliding TENG. In fact, with sliding the top dielectric layer on the bottom dielectric, the values of current, voltage, and power begin to increase until the stopping time, at which we have maximum current, voltage, and power. From that moment, the values of the variables decrease. In Fig. 4.17e, feedback of the energy occurs, revealing that its value increases as the thickness increases.

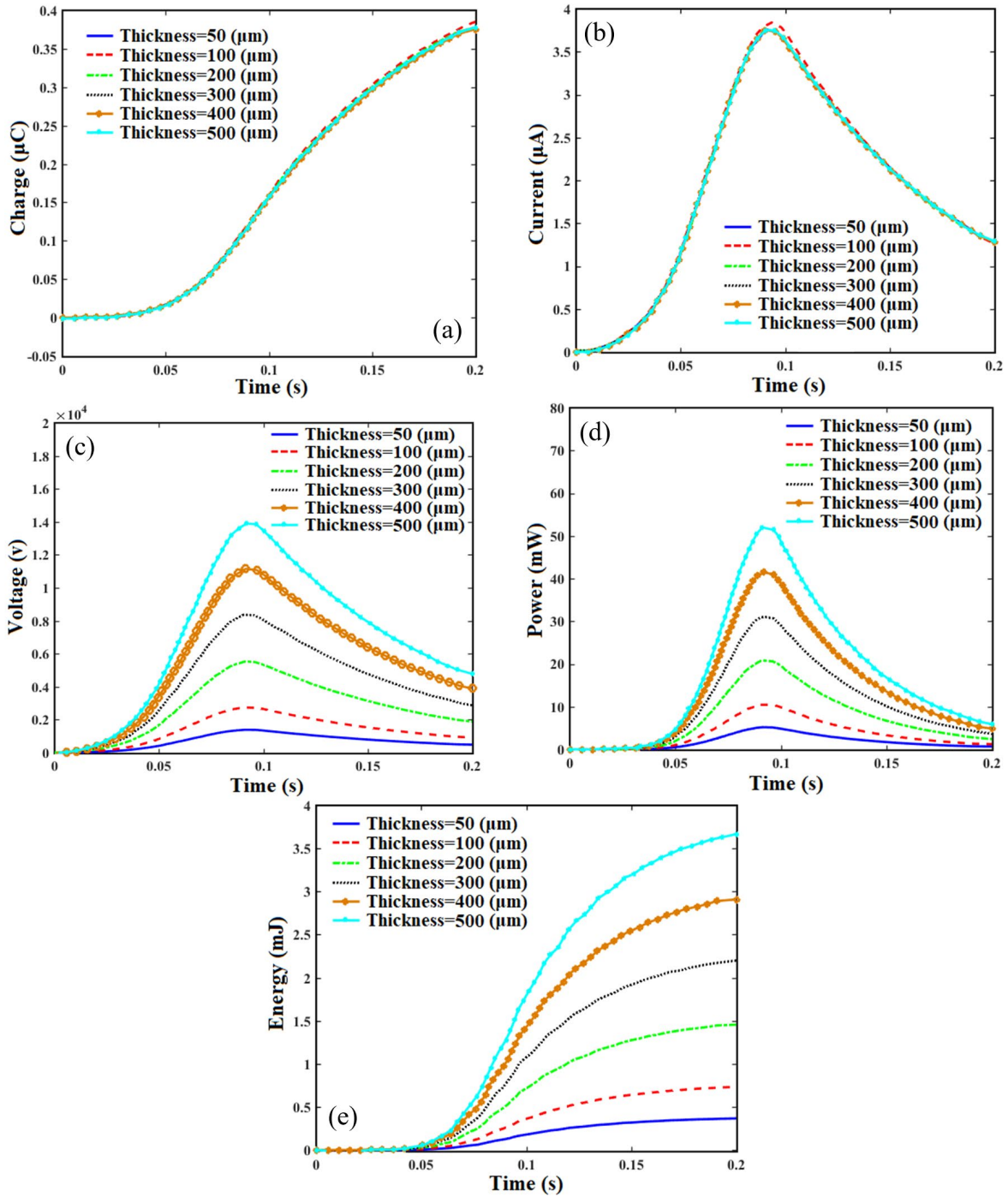


Fig. 4.17: Effects of the thickness of dielectric film on electrical outputs of dielectric-to-dielectric sliding-mode TENGs (a) charge, (b) current, (c) voltage, (d) power, and (e) energy.

4.6. Summary

A simulation modeling for sliding-mode TENG was presented to predict and optimize the harvested energy. Key parameters of TENG encompassing contact area, thickness of

dielectric films, and external load resistance were considered. Beginning with derived equations, a merged algorithm of physical solver and artificial intelligence was introduced. Based on the presented approach, the optimized characteristics of TENG were calculated, where a good overlap was obtained between the simulation calculations and experimental data. Most importantly, the numerical investigation revealed that selection of a proper value for the external resistor could increase the average power output to 18.31 mW at each cycle, whereas setting appropriate values for the dimensions could decrease the weight to 5.82 g. The current work presents useful simulation results that support deep understanding of the correlation between the optimized TENG's characteristics and harvested energy, opening an avenue for accelerating the development of sliding-mode TENGs towards self-powered nanotechnology applications.

Rotary triboelectric nanogenerators

5.1. Introduction

In pervious chapter, sliding-mode TENGs was designed to harvest electric power from periodic reciprocal movements. Another type of motion is the rotational motion. Rotational motion abundantly available in many human-made rotating environments, such as wheels, shafts, gears, and bearings, and has served to establish innovative designs to harvest energy using disk TENGs. The rotary TENGs can be embedded in specific systems to harvest energy from renewable energy resources such as wind power and the water wave. Especially, blue energy is a preferred place for the rotary TENGs since river flow and ocean tides are hugely available. Comparing with sliding-mode TENGs, the rotary design offers some benefits. The rotary device can operate under high rotational speed, resulting in considerably harvested power. Meanwhile, an irritating problem with sliding TENGs is its durability. When triboelectric films are become into physical contact, some wear and deformation is expected. Here the rotary TENGs can smartly be designed to generate power while working in the non-contact mode. In such a condition, the longevity of dielectric films and coatings is substantially extended. To improve the durability and sustainability of the sliding-mode TENGs, I present theoretical and experimental studies on rotary TENGs in this chapter.

Some attempts have been dedicated to present some designs on rotary TENGs. However, a systematic theoretical framework in conjunction with an experimental setup is still lacking. In essence, structural parameters and operating conditions of disk-shaped TENGs significantly affect the generated energy. Hence, the development of a general analytical platform for determining these parameters is of great importance for performance improvement.

The scrutinized design for rotary TENGs can effectively be used for random energy harvesting, particularly for blue energy purposes. To address this need, considering the electric specifications, geometry, and charge conservation law, the dynamics of rotary TENGs are extracted. A merged algorithm of advanced mathematic solvers and optimization theory is presented. This study introduces the characteristics of rotary TENGs at which the highest generated energy can be scavenged. The theoretical investigation is well matched with experimental data, the output of TENGs is predicted under various working conditions and optimized functional values for structural parameters are assigned.

5.2. Theoretical principles of rotary TENGs

Here, the operation principle of the disk TENG is described. Usually, polymers, which are considered waste material in energy scavenging terms, are used in TENG structures. Nylon 66 and PTFE belong in opposite spectra of the triboelectric series, so we choose these materials as triboelectric layers.

5.2.1 Mechanism of operation for rotary TENGs

A schematic drawing of the rotary TENG is presented in Fig. 5.1a. For simplicity, the energy generation process is schematically drawn on one segment of each triboelectric film. Initially, the Nylon serves as a rotating element and is in full physical contact with the PTFE, which is considered a stationary element. Because of the difference in triboelectric polarities, the triboelectric effect leaves net positive and negative charges on the surface of the Nylon and PTFE, respectively. This phenomenon is shown in Fig. 5.1b. Then, the two triboelectric films are brought apart, as depicted in Fig. 5.1c, after which the cycle of energy generation can begin. The energy is harvested through a cycle that includes four different steps. In the initial condition, the Nylon and PTFE have some charges at their surface, as shown in Fig. 5.1c. As

soon as the Nylon segment begins to rotate, a flow of electrons transfers from the top electrode to the bottom electrode, leading to an output of current in the reverse direction, as shown in Fig. 5.1d. This stage continues until the top substrate is entirely in a nonoverlapping condition, as shown in Fig. 5.1e, corresponding to the maximum expected charge. Next, the Nylon film moves toward the adjacent segment of PTFE after which electrons flow from the bottom electrode to the top electrode, resulting in a current in the opposite direction, as shown in Fig. 5.1f. The process continues until the Nylon segment returns to its initial position.

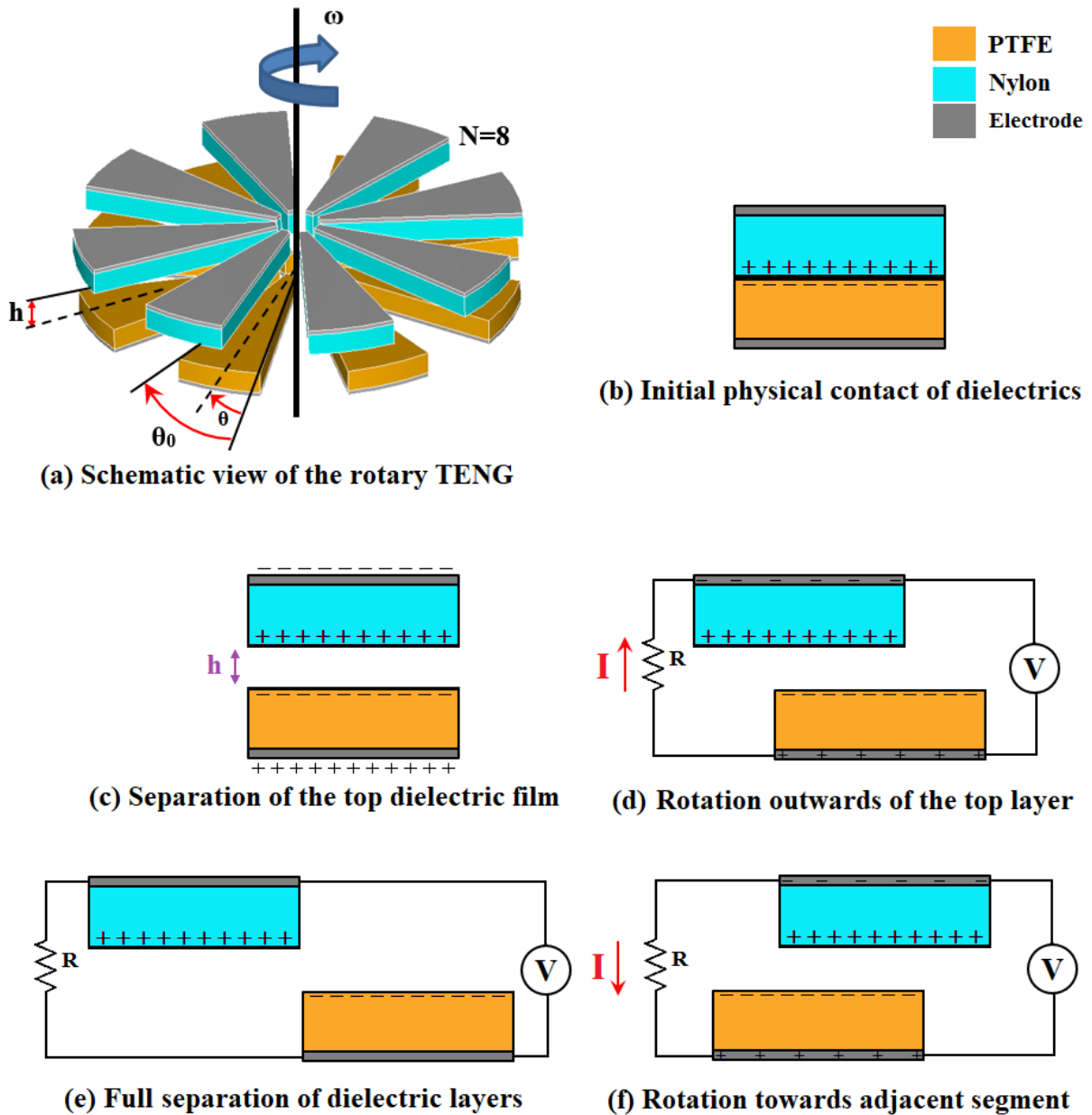


Fig. 5.1: Operating mechanism of rotary TENGs: (a) schematic view, where θ_0 and θ represent the segment and rotation angles in radian, and N , h , and ω stand for grating number, tribo spacing, and rotational speed, respectively, (b) initial physical contact of dielectrics, (c) separation of dielectric films, (d) rotation outwards, (e) full separation of segments, and (f) rotation towards the adjacent segment. (Note: Figures (b-f) show the cross-sectional profile of one segment of a rotary TENGs.)

5.2.2 Experimental setup

In the experimental setup, PTFE and Nylon with thickness of 250 μm were prepared as dielectric films because of their opposite positions in the triboelectric series. First, materials were cut with a laser cutting machine. The inner and outer radii of the dielectric counterparts are 5 mm and 50 mm respectively, and the thickness is 250 μm . Then, materials were twice washed with ethanol carefully to eliminate any undesired agents from the surface. For the coating process, sputter coater (Q300T-D, Quorum, UK) was used to coat the gold with a thickness of 200 nm and the chromium with a thickness of 50 nm at contact and electrode surfaces respectively. Next, the wires were aligned in all segments to guarantee all transferred charge will be collected.

In order to provide the substrate, 3D printing was applied to generate a disk-shaped substrate in accordance with the size of the materials. Then, the dielectric materials were fixed on the substrate with conductive adhesive. It is also noted that a brush and slip rings made of copper flakes were designed to collect the transferred charges between electrodes. Scanning electron microscopy (SEM, Inspect F50, FEI, USA) compared the contact surface before coating and after 10,000 cycles, as shown in Figs. 5.2a and 5.2b. In this case, the rotational speed was 400 rpm, and the tribo spacing was 0. Figs. 5.2c and 5.2d show the experimental setup and the row of serially connected LEDs successfully lit up. The stability of the output power of the rotary TENGs was depicted in Fig. 5.2e. The figure shows an acceptable output power after 10,000 cycles. The drop in the output power is almost 5% after 10,000 cycles. The major reason for this decrement is the fact that the coated gold in the interface of dielectric materials can be removed during the rotation.

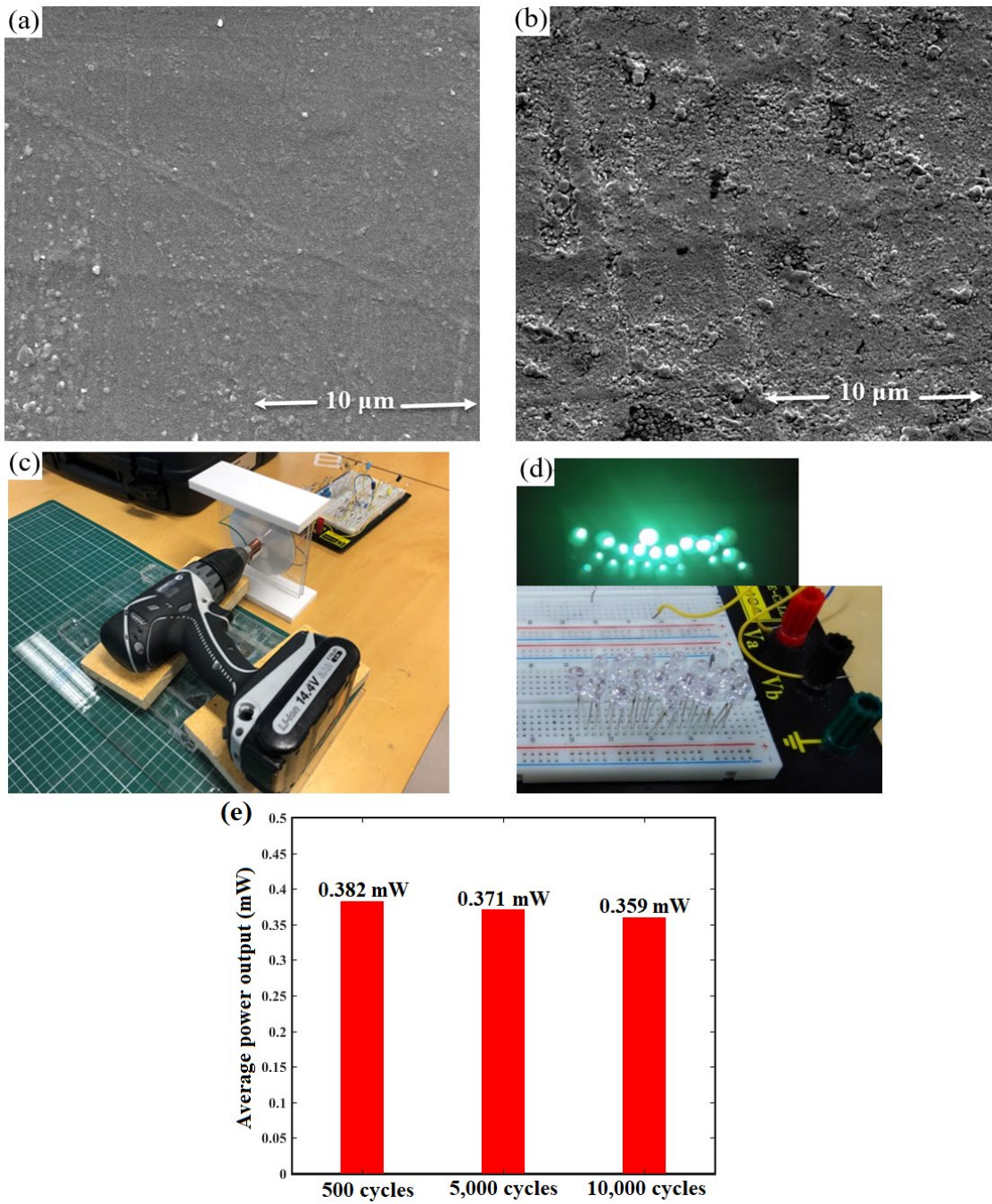


Fig. 5.2: SEM images of the surface (a) before and (b) after contact rotation for 10,000 cycles, (c) photograph of the device, (d) driving serially connected LEDs, and (e) the output power of rotary TENGs after undergoing some cycles.

5.2.3 Fundamental mathematics of TENGs

As already mentioned, the relative rotational motion between triboelectric films leads to an output current through the external circuit. Then, it is of great importance to analyse the resistive load output characteristics. Here the fundamental formulation of the rotary TENG is presented, based on the structural parameters. It should be pointed out that when the rotary TENGs (with different N) rotates a whole cycle, i.e. 360° , the value of the contact area is different. To meet this issue and have a base for comparison purposes, formulations and results are presented for a segment angle ($\theta=[0-2\theta_0]$), as depicted in Fig. 5.1. In this way, we can compare the results for different geometries.

The resistive analysis can be performed by a combination of the general voltage-charge (V-Q) relationship and Ohm's law as below [61]:

$$V = R \frac{dQ}{dt} = \frac{-1}{C} Q + V_{oc} \quad (5.1)$$

where R , C , and V_{oc} are the external resistor, capacitance value, and open-circuit voltage respectively.

The thickness of the triboelectric films is significantly negligible in comparison with other directions, then the theory of parallel plates can be used to present the formulation for capacitance, as below:

$$C = \frac{\epsilon_0 A}{d} \quad (5.2)$$

If ϵ_1 and ϵ_2 account for the permittivity of the dielectric layers, the capacitance of the TENG can be expressed as:

$$C = \frac{\epsilon_0 A}{\frac{d_1}{\epsilon_1} + \frac{d_2}{\epsilon_2} + h} \quad (5.3)$$

where A is the total contact area of all segmentations, and ϵ_0 shows the vacuum permittivity. The above formula gives a good approximation for capacitance. However, the edge effects

have been ignored. Considering the position of the top triboelectric layer, the contact area can be calculated:

$$A = \frac{(\theta_0 - \theta)(r_2^2 - r_1^2)}{2}, \quad \theta < \theta_0$$

$$A = \frac{(\theta - \theta_0)(r_2^2 - r_1^2)}{2}, \quad \theta > \theta_0$$
(5.4)

or simply:

$$A = \frac{|\theta_0 - \theta|(r_2^2 - r_1^2)}{2}$$
(5.5)

where $||$ returns the absolute positive value.

Next, we need to find short circuit transferred charges (Q_{sh}) and V_{oc} .

Q_{sh} can be obtained through [194]:

$$Q_{sc} = Q_{sc,n} - Q_i$$
(5.6)

where Q_i and $Q_{sc,n}$ account for the transferred charges in short circuit conditions at $\theta=0$ (Fig. 5.1c) and a certain angle $\theta \neq 0$ (Fig. 5.1d). Q_i is the same with the short circuit charge of a contact-separation TENG [62], then we have:

$$Q_i = \frac{N\sigma h\theta_0(r_2^2 - r_1^2)}{2\left(\frac{d_1}{\epsilon_1} + \frac{d_2}{\epsilon_2} + h\right)}$$
(5.7)

If $\theta < \theta_0$, the charge density on the electrode in overlapped and nonoverlapped can be written as:

$$\sigma_1 = \sigma \quad \text{for non-overlapped region}$$

$$\sigma_2 = \frac{\sigma h}{\left(\frac{d_1}{\epsilon_1} + \frac{d_2}{\epsilon_2} + h\right)} \quad \text{for overlapped region}$$
(5.8)

Then, $Q_{sc,n}$ can be estimated by:

$$Q_{sc,n} = \sigma_1 \frac{N\theta(r_2^2 - r_1^2)}{2} + \sigma_2 \frac{N(\theta_0 - \theta)(r_2^2 - r_1^2)}{2}$$
(5.9)

Combining Eqs. (5.8) and (5.9) will yield:

$$Q_{sc,n} = \frac{N\sigma\left\{\left(\frac{d_1}{\varepsilon_1} + \frac{d_2}{\varepsilon_2}\right)\theta + \theta_0 h\right\}(r_2^2 - r_1^2)}{2\left(\frac{d_1}{\varepsilon_1} + \frac{d_2}{\varepsilon_2} + h\right)} \quad (5.10)$$

If $\theta_0 < \theta < 2\theta_0$, we have the same scenario. The result will be described:

$$Q_{sc,n} = \frac{N\sigma\left\{(2\theta_0 - \theta)\left(\frac{d_1}{\varepsilon_1} + \frac{d_2}{\varepsilon_2}\right) + \theta_0 h\right\}(r_2^2 - r_1^2)}{2\left(\frac{d_1}{\varepsilon_1} + \frac{d_2}{\varepsilon_2} + h\right)} \quad (5.11)$$

Putting Eqs. (5.7), (5.10) and (5.11) in (5.6) will result in short circuit charge:

$$Q_{sc} = \frac{N\sigma\theta\left(\frac{d_1}{\varepsilon_1} + \frac{d_2}{\varepsilon_2}\right)(r_2^2 - r_1^2)}{2\left(\frac{d_1}{\varepsilon_1} + \frac{d_2}{\varepsilon_2} + h\right)}, \quad \theta < \theta_0 \quad (5.12)$$

$$Q_{sc} = \frac{N\sigma(2\theta_0 - \theta)\left(\frac{d_1}{\varepsilon_1} + \frac{d_2}{\varepsilon_2}\right)(r_2^2 - r_1^2)}{2\left(\frac{d_1}{\varepsilon_1} + \frac{d_2}{\varepsilon_2} + h\right)}, \quad \theta_0 < \theta < 2\theta_0$$

The current is the derivate of the charge with respect to time, then we have:

$$I_{sc} = \frac{dQ_{sc}}{dt} = \frac{N\sigma \frac{d\theta}{dt} \left(\frac{d_1}{\varepsilon_1} + \frac{d_2}{\varepsilon_2}\right)(r_2^2 - r_1^2)}{2\left(\frac{d_1}{\varepsilon_1} + \frac{d_2}{\varepsilon_2} + h\right)}, \quad \theta < \theta_0 \quad (5.13)$$

$$I_{sc} = \frac{N\sigma \frac{d(2\theta_0 - \theta)}{dt} \left(\frac{d_1}{\varepsilon_1} + \frac{d_2}{\varepsilon_2}\right)(r_2^2 - r_1^2)}{2\left(\frac{d_1}{\varepsilon_1} + \frac{d_2}{\varepsilon_2} + h\right)}, \quad \theta_0 < \theta < 2\theta_0$$

where $\omega = d\theta/dt$.

Now we have the expression for capacitance (Eq. (5.3)) and short circuit charge. The open-circuit voltage can easily be calculated:

$$V_{oc} = \frac{\sigma\theta(\frac{d_1}{\varepsilon_1} + \frac{d_2}{\varepsilon_2})}{\varepsilon_0(\theta_0 - \theta)} \quad , \quad \theta < \theta_0$$

$$V_{oc} = \frac{\sigma(2\theta_0 - \theta)(\frac{d_1}{\varepsilon_1} + \frac{d_2}{\varepsilon_2})}{\varepsilon_0(\theta - \theta_0)} \quad , \quad \theta_0 < \theta < 2\theta_0$$
(5.14)

Here the fundamental formula for rotary TENG can be summarized as:

$$V = R \frac{dQ}{dt} = \frac{Q}{\varepsilon_0 \frac{|\theta_0 - \theta|(r_2^2 - r_1^2)}{2}} + \frac{\sigma\theta(\frac{d_1}{\varepsilon_1} + \frac{d_2}{\varepsilon_2})}{\varepsilon_0(\theta_0 - \theta)} \quad , \quad \theta < \theta_0$$

$$V = R \frac{dQ}{dt} = \frac{Q}{\varepsilon_0 \frac{|\theta_0 - \theta|(r_2^2 - r_1^2)}{2}} + \frac{\sigma(2\theta_0 - \theta)(\frac{d_1}{\varepsilon_1} + \frac{d_2}{\varepsilon_2})}{\varepsilon_0(\theta - \theta_0)} \quad , \quad \theta_0 < \theta < 2\theta_0$$
(5.15)

Since the output power of TENG varies with respect to time, the average power is used in our calculations:

$$P_{ave} = \frac{\int_0^T VI dt}{T_t} = \frac{\int_0^T RI^2 dt}{T_t}$$
(5.16)

where T_t is the period.

5.3. Solution strategy

The energy generated through the triboelectrification process depends highly on its materials, geometry, and kinematics. In this study, the effects of geometry and kinematics on output power are investigated. In engineering and physics circles, artificial intelligence plays a vital role in the reduction of hidden marginal costs and the augmentation of inherent characteristics of any problem. Recently, we implemented a new algorithm into a large-scale

engineering problem in order to increase the energy harvested by piezoelectric materials [195]. The process is depicted in Fig. 5.3. The proposed algorithm presented better results in comparison with other artificial intelligence approaches [195].

Here, the algorithm is used to analyse the TENG's output. It has been formulaically shown that the scavenged energy of rotary TENGs depends highly on the grating space, angular velocity, tribo-spacing, and external resistor. The algorithm encompasses the grey wolf as a recently elaborated intelligent method in parallel with different mathematical strategies to meet the fundamental mathematics. The artificial intelligence and the governing mathematics were coded in MATLAB. The algorithm is initiated with the geometry and dimensions as well as the materials and electrical specifications. This artificial intelligent method was originally inspired by the hunting mechanism of grey wolves. Based on some mathematical theory and leadership hierarchy, it undergoes three steps: searching for prey in the search space, surrounding the prey, and attacking the prey. The algorithm is supposed to pass through iterations at which all local and global results are compared in order to introduce the best solution. Meanwhile, two mathematical solvers meet all differential and integration equations in every step of each loop. The simulation process analyzes the impacts of the design variables and identifies the best results at which the maximum energy can be harvested. Details of the simulation process were presented in the previous chapter.

The proposed algorithm offers some benefits to TENGs. First, the algorithm is a general platform and can easily be implemented to analyze the rotary TENGs in various shapes and working conditions (from human-made rotating environments such as turbine shafts to natural power sources including wind and blue energy). In fact, there is no limitation with initial and boundary conditions or geometries. Furthermore, the artificial intelligent method embedded in the algorithm is highly capable of engaging with any prediction and optimization study, introducing the algorithm as a time and cost-effective approach. It should

be noted that the presented algorithm does not get stuck into the local optimization regions, which is the most common issue for many artificial intelligent methods.

It is of the great importance to noted that the outputs of rotary TENGs can considerably be affected by edge effects through two ways: attributing a very large value to a grating number, and also opting a small value for L/d where L is the arc length of the disk and d is the thickness of the dielectric materials. In detail, the edge effects make some interactions between two adjacent segments. This leads to a substantial decrease in the sensitivity of the potential variation in response to the rotation. Consequently, a significant drop can be seen in the output of the TENGs. In order to avoid this undesirable phenomenon, a large value of L/d is selected in our calculations. In this study, a large value of $L/d=125.6$ ($r_1=5$ mm, $r_2=50$ mm, $d=250$ μm) is chosen to avoid all negative edge effects. Also, a maximum grating number of 32 is chosen to avoid the interactions between adjacent segments [72, 196].

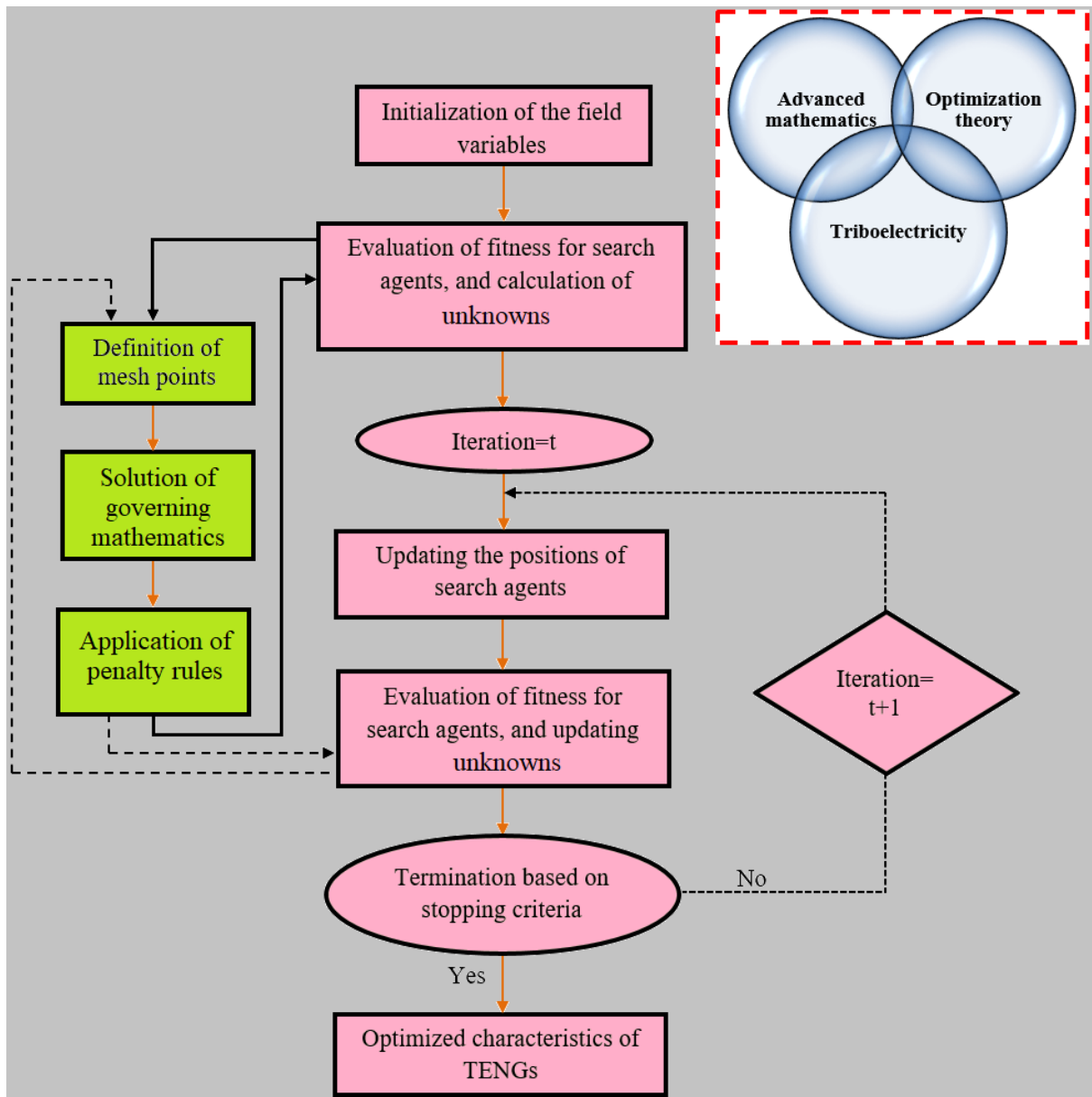


Fig. 5.3: Flow chart of the proposed algorithm for characterizing the contact-mode TENGs.

5.4. Results and discussion

5.4.1 Evaluation

Here, a study is conducted to evaluate the accuracy of the presented simulation. The algorithm is implemented to simulate a reported experiment by Jiang et al. (2016) [197]. This reference was chosen due to some reasons: (i) the experiment was fully described in detail, (ii) all detail of material, in particular surface charge density, were mentioned in the

publication, (iii) the geometry was fully explained by authors. As mentioned in the experimental setup, Al and PTFE, each 100 μm thick, are used as the dielectric films. Also, the inner and outer radii are 5 mm and 50 mm respectively, and the number of gratings is 4. It is assumed that the bottom dielectric layer is fixed while the top part rotates at a constant rate. The curves of short-circuit current and open-circuit voltage are plotted in Fig. 5.4. The short circuit current has been collected under a constant rotational speed of 275 rpm, while the open circuit voltage has obtained at 900 rpm. From application of the proposed algorithm, the calculation is presented and the results for current and voltage are plotted in Fig. 5.4. It is obvious that the results of the current simulation overlap very well with the reported experimental data.

Fig. 5.4a shows a square waveform for distribution of the short circuit current. As was formulated, the short circuit charge has a linear relationship with angle of rotation (θ). In fact, the driving force of this transferred charge is electrostatic force from the triboelectric charges. This driving force produces a specific transferred charge between metal electrodes. When R is very small (near to short circuit condition), the real transferred charge can catch up with this specific transferred charge. Hence, close to short circuit condition, all current curves are similar and have a uniform distribution. However, for higher values of resistor, distribution of Q will deviate from the short circuit curve. This phenomenon happens because the resistor limits the transferred charge speed. Then, the transferred charge cannot catch up with that specific charge transfer rate. In this case, the charge accumulation is slowed down, and more time is required for Q to get saturated.

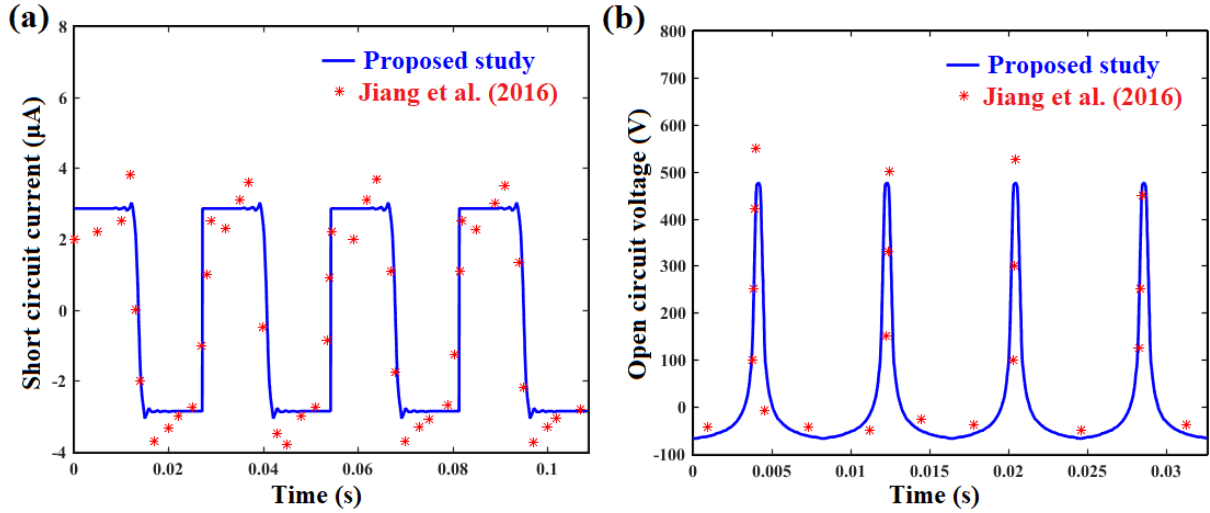


Fig. 5.4: Comparison of results obtained for (a) current and (b) voltage with those of Ref. [197] with inner and outer radii of 5 mm and 50 mm, grating number of 4, triboelectric layers thickness of 100 μm and tribo spacing h of zero.

Next, a comparison of the simulation outputs with those of our experimental results is presented. As in the previous evaluation, one dielectric part acts as the stator while another rotates around the central axis of the TENG with $\omega=400$ rpm. The properties of the dielectric films consisting of Nylon and PTFE are listed in Table 5.1. The dielectric layers are of equal thickness of $d_1=d_2=250$ μm and the inner and outer radii are 5 mm and 50 mm, respectively. The TENG has four segments, and the tribo spacing is equal to 0.

As a critical step in triboelectrification-based energy harvesting, all basic properties should be determined before any further experiment and calculation. This basic information is required through next steps. In particular, surface charge density is the most important property of the TENGs needed to be measured at first. This parameter would be the input in our simulation process as well. Surface charge density can be found by taking the integration of the short circuit current versus the time. In order to obtain more accurate results, the surface charge density (σ) is calculated based on a whole rotation, i.e., 360 degrees, and an

average value is presented. Fig. 5.5 shows the current cure of rotary TENG extracting from the experiment.

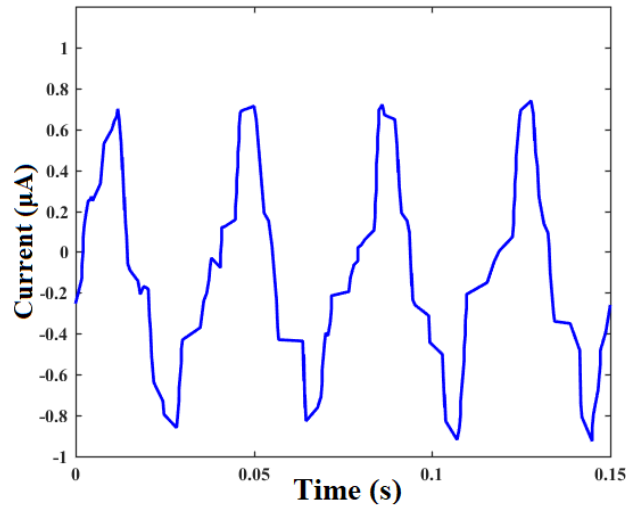


Fig. 5.5. Temporal response of the current for a whole rotation.

The geometry of the dielectrics is an annular disk, then the area can be calculated as:

$$S = \pi(r_2^2 - r_1^2) / 2 = 0.0039 \text{ m}^2$$

Now the surface charge density can be found:

$$\sigma = Q / S \approx 5 \text{ } \mu\text{C/m}^2.$$

Table 5.1: Material properties of dielectric films [61].

Parameter	Value	
Nylon	ρ (kg/m ³)	1150
	E	4
PTFE	ρ (kg/m ³)	2200
	E	2

Theoretical results and experimental measurements are shown in Fig. 5.6. The responses of the current and voltage of the rotary TENG are plotted in Figs. 5.6a and 5.6b for $R=1 \text{ G}\Omega$. As is evident, the simulation outputs follow the experimental data closely. When compared with other theoretical models of TENGs, the current study presents acceptable results [198-202]. The difference between theoretical model and experiment stem from a few sources. Thorough modeling and full contact between dielectrics were assumed. However, because of the shaking and high-speed rotation, is almost impossible to achieve perfect contact in the experimental setup. Also, some ideal assumptions were applied in the theoretical study, including negligible thickness of the dielectrics and absence of electrostatic influences from the environment, features that do not occur in reality. Figs. 5.6a and 5.6b shows a similar pattern for the current and voltage. The reason for this behavior is the fact that the produced voltage is proportional to current based on the Ohm's law. A similar pattern has been presented in references [194, 203, 204]. The maximum values of the current and voltage versus different external loads were calculated and results are depicted in Figs. 5.6c and 5.6d, where it is evident that the simulation pattern matches the measurements from the experiment reasonably well.

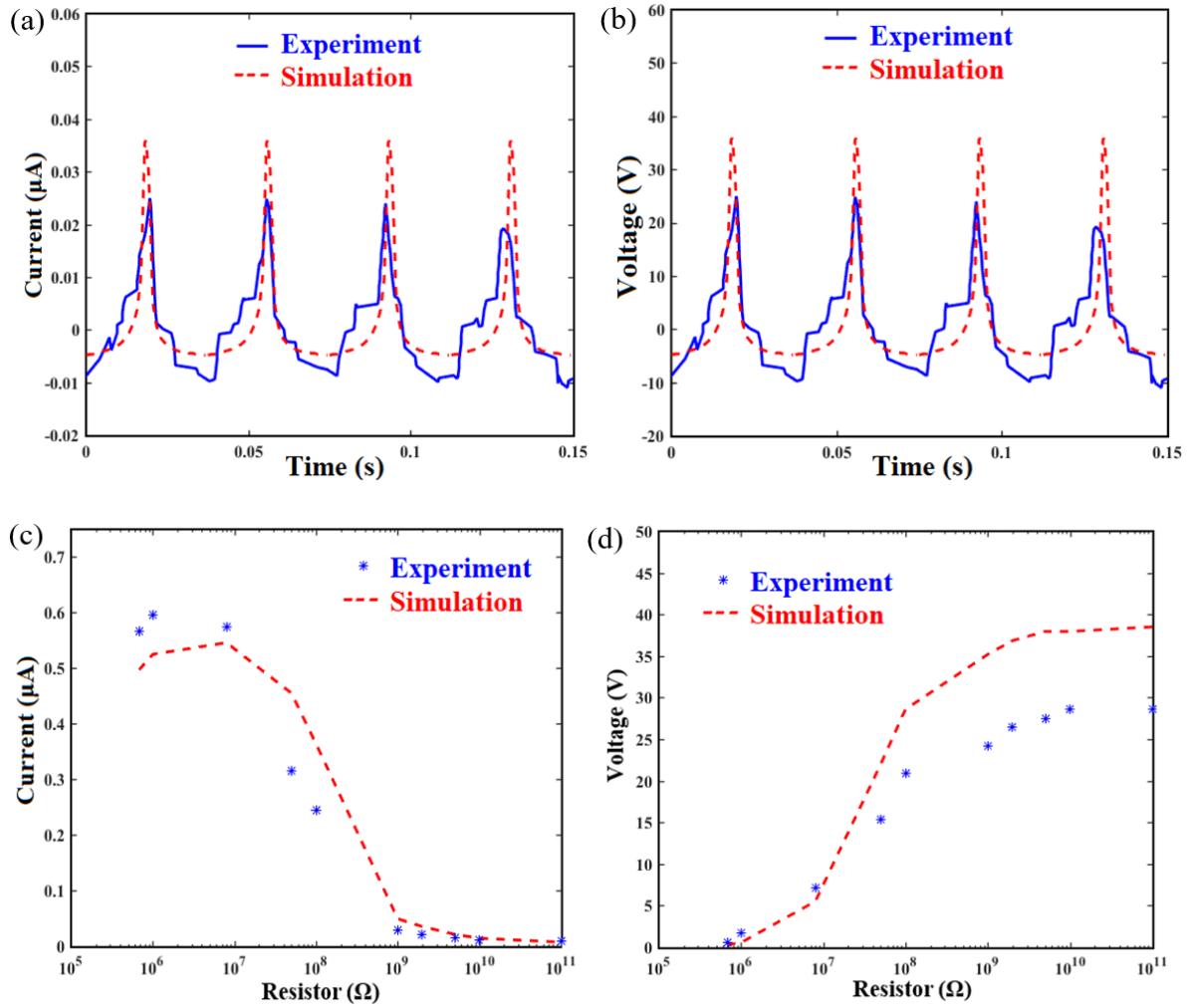


Fig. 5.6: Comparison of the simulation results with our experimental results (a) temporal response of the current for $R=1$ G Ω , (b) temporal response of the voltage for $R=1$ G Ω , (c) maximum obtained current, and (d) maximum obtained voltage. The geometry parameters are $r_1=5$ mm, $r_2=50$ mm, $N=4$, $d_1=d_2=250$ μm , and $h=0$.

5.4.2 Prediction and sensitivity analysis of TENG

In the previous section, it was demonstrated that the presented strategy could effectively simulate the real working condition of the rotary TENGs. Creation of the experimental setup for all loading conditions, materials, geometries, and kinematics would be excessively time-consuming and would impose high costs. But it is of great importance to simulate the output

patterns of TENGs under various working conditions. Here, we present the average power output of the rotary TENG across different resistors, kinematics, and geometries.

By assigning different values to the tribo spacing, number of gratings, and velocity, the variation of P_{ave} is plotted and shown in Fig. 5.7. From this figure, appropriate values for N , h , and ω can be assigned based on the required power. The P_{ave} can reach almost 1.2 mW, when $N=20$. These figures show that, when short-circuit and open-circuit conditions are approached, the TENG's power drops significantly, because of the very low voltage and current in short-circuit and open-circuit conditions respectively. However, an optimum resistance happens within a specific range of R , i.e., $R \sim [10-10^4 \text{ (M}\Omega\text{)}]$ where the output current and voltage are significantly changed.

The dot points in the figures shows the experimental data. The rotary TENGs variables, including N , ω , and h were taken into consideration and the experiment was separately conducted for each variable versus various variation of the load resistance. It means when a variable is measured through the experiment, all other variables are assumed to be constant. On dielectric film was fixed on the substrate while another dielectric layer rotates. In all experiments the inner and outer radii are $r_1=5 \text{ mm}$, $r_2=50 \text{ mm}$. As can obviously be seen, the simulation excellently predicts the experimental data.

Results demonstrate that the average power output increases as the grating number rises. When the grating number increases, the TENG device will get a fine pitch, which leads to increment of the number of charge transfers in a whole cycle, resulting in enhancement of the current. Hence, the value of the output power increases. Also, it should be noted that the power is dominantly affected by the short circuit current and open circuit voltage. According to Eq. (5.13), the short circuit current increases rapidly as the grating number increases. This phenomenon makes the optimum average power output occurs at a lower load resistance as the grating number increases. A similar trend can be found in the case of the angular velocity.

It can be interpreted by considering the linear relationship between the short circuit current and the angular velocity. The larger mechanical energy delivers a higher current output, leading to larger values of the generated power. Moreover, it can be found that the average power output increases at a constant load resistance as the tribo-spacing decreases, and the location of the optimum resistor shifts towards the lower values. This phenomenon happens because the rate of the transferred charges is inversely proportional to the tribo-spacing, demonstrated in Eq. (5.13). The higher tribo-spacing, the less transferred charges and current.

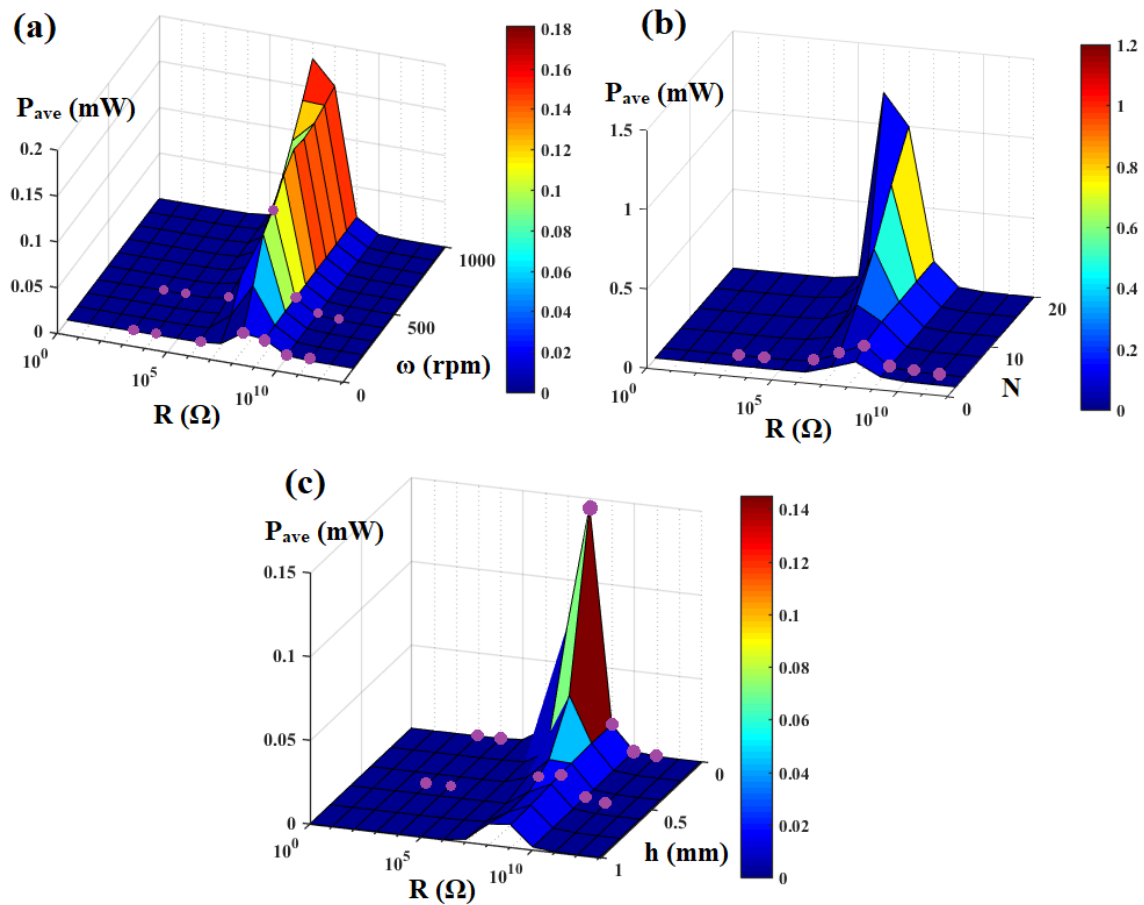


Fig. 5.7: Dependence of TENG outputs on the resistor and (a) angular velocity, (b) tribosurface spacing, and (c) number of gratings. Dot points represent the experimental data obtained in this study with $r_1=5$ mm, $r_2=50$ mm, $d_1=d_2=250$ μ m, angular velocity of 100, 300, 500 and 700 rpm, h of 0, 0.5 and 1 mm, and N of 2 and 4, respectively.

As can be found in Fig. 5.7, changes in design parameters can significantly or slightly affect the P_{ave} . Then, it is of interest to know which parameters can dominantly affect the TENG's generated power. To reveal this, a sensitivity analysis is performed, with the results depicted in Fig. 5.8. As Fig. 5.8 shows, the variation of the output power in respect to the load resistance reaches a maximum value, and then drops to its minimum value. This quantitative data demonstrates the fact that the load resistance is the dominant variable affecting the rotary TENG's output, respectively followed by the tribo-spacing, grating number and angular velocity. In real applications, the TENG device is connected to electronics and the provided data can help with choosing proper specifications, particularly resistor.

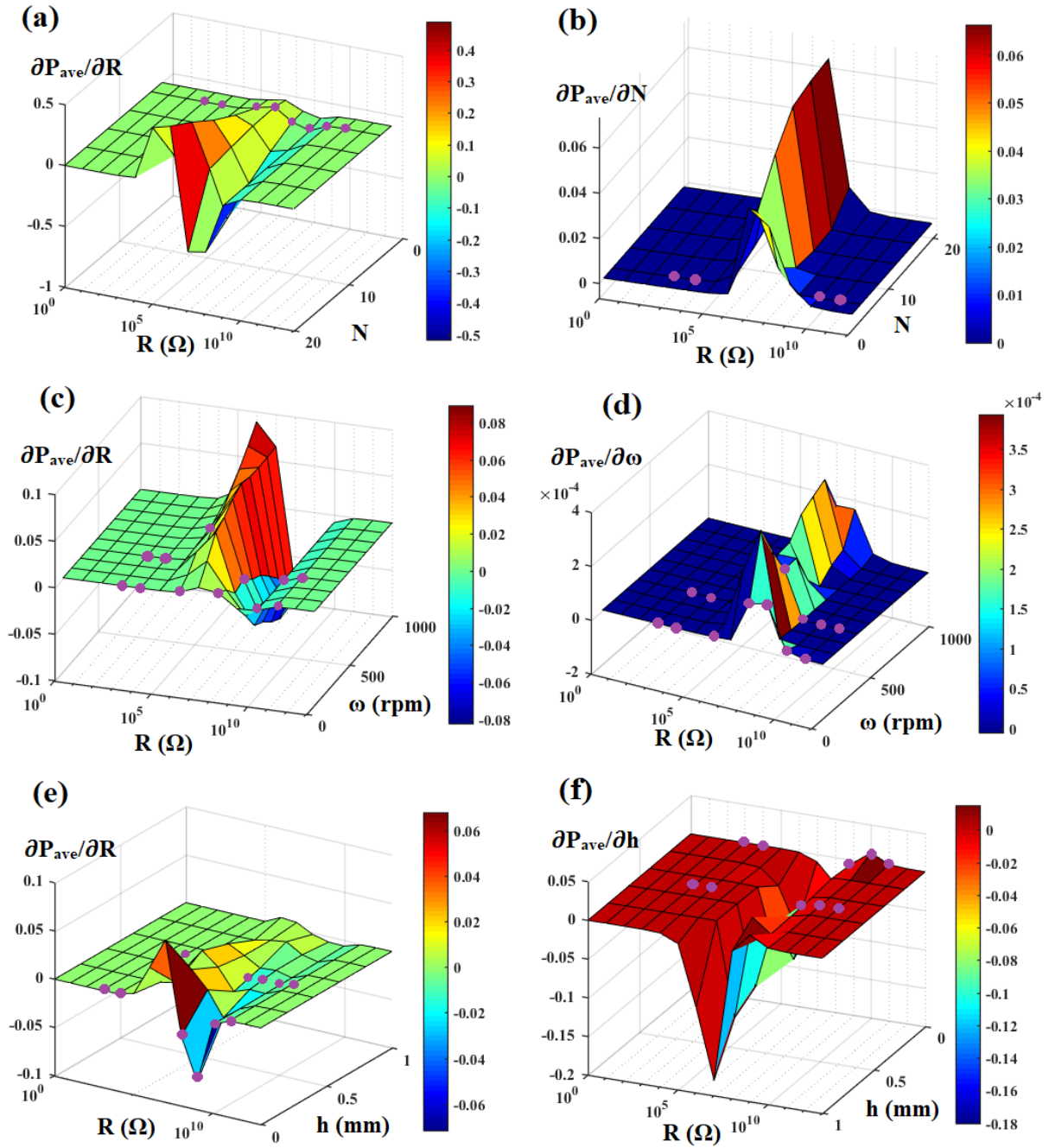


Fig. 5.8: Sensitivity analysis of TENG's generated power with (a) resistance vs different N , (b) angular velocity, (c) resistance vs different ω , (d) number of gratings, (e) resistance vs different h , and (f) tribo-surface spacing.

5.4.3 Study on grating number

As it was shown in the last section, the grating number significantly affect the rotary TENG's power output. Here we consider various grating numbers and introduce the optimum resistors

at which the most energy can be harvested. It is assumed that the top dielectric rotates at a constant angular velocity, i.e. $\omega=400$ rpm. Considering different grating numbers, the algorithm is implemented for rotary TENGs. Fig. 5.9 depicts the results of the convergence study for R and P_{ave} .

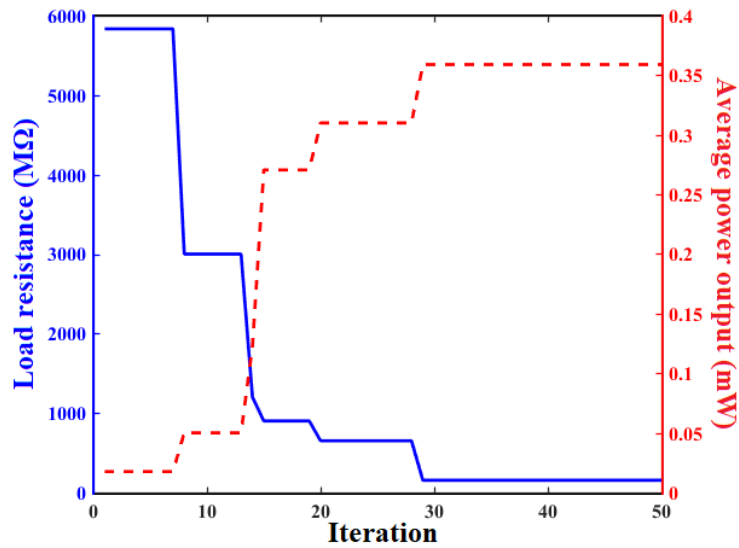


Fig. 5.9: Convergence study of the proposed algorithm.

The optimized characteristics of the TENG are presented in Table 5.2.

Table 5.2: Optimum outputs of rotary TENGs for different values of the grating number.

Grating number	Optimum resistor (MΩ)	Average power output (mW)	Harvested energy in one rotation (mJ)
4	165.82	0.359	0.054
8	153.46	0.610	0.092
16	60.57	1.370	0.206
32	37.74	2.462	0.369

Fig. 5.10 shows the optimum resistors and relevant harvested power across different N . It is clearly evident that the average power output increases linearly with increment in the grating number. However, the optimum values of load resistance show a decreasing pattern. In fact, rotary TENGs work based on the transferred charges between electrodes. The reason for this charge transfer is the change in the contact area between dielectric films. When the TENGs consist of more segmentations, it means the change in the contact area increases. In other words, the frequency of the TENG system rises with increment in grating number. Furthermore, this phenomenon can be explained by the presented formulations. As was demonstrated, the value of the transferred charges is linearly proportional to the grating number. The more segmentations, the more transferred charges.

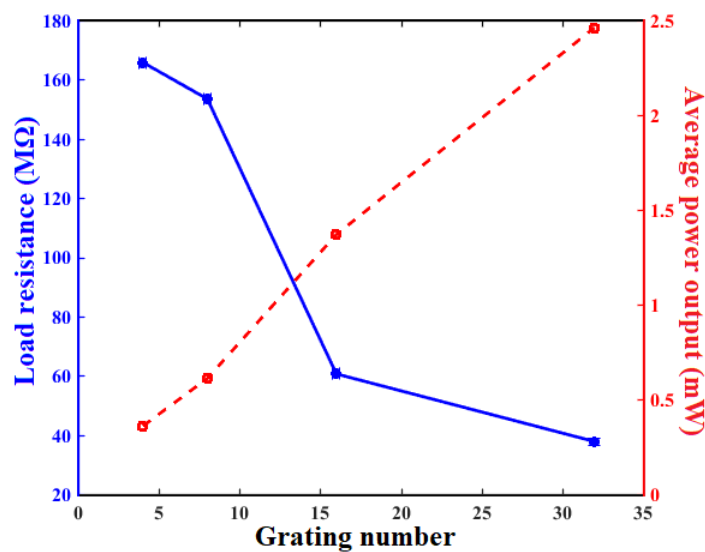


Fig. 5.10: Results of optimized average power output and resistors for different N .

The curve responses of the transferred charge, current, voltage, and output power of the rotary TENG are plotted in Fig. 5.11. This figure shows that increasing the N will result in higher values of the current and voltage. In particular, the maximum point on the current

curve surges from 5 μA at $N=4$ to approximately 30 μA at $N=32$. The pattern of the output power sharply

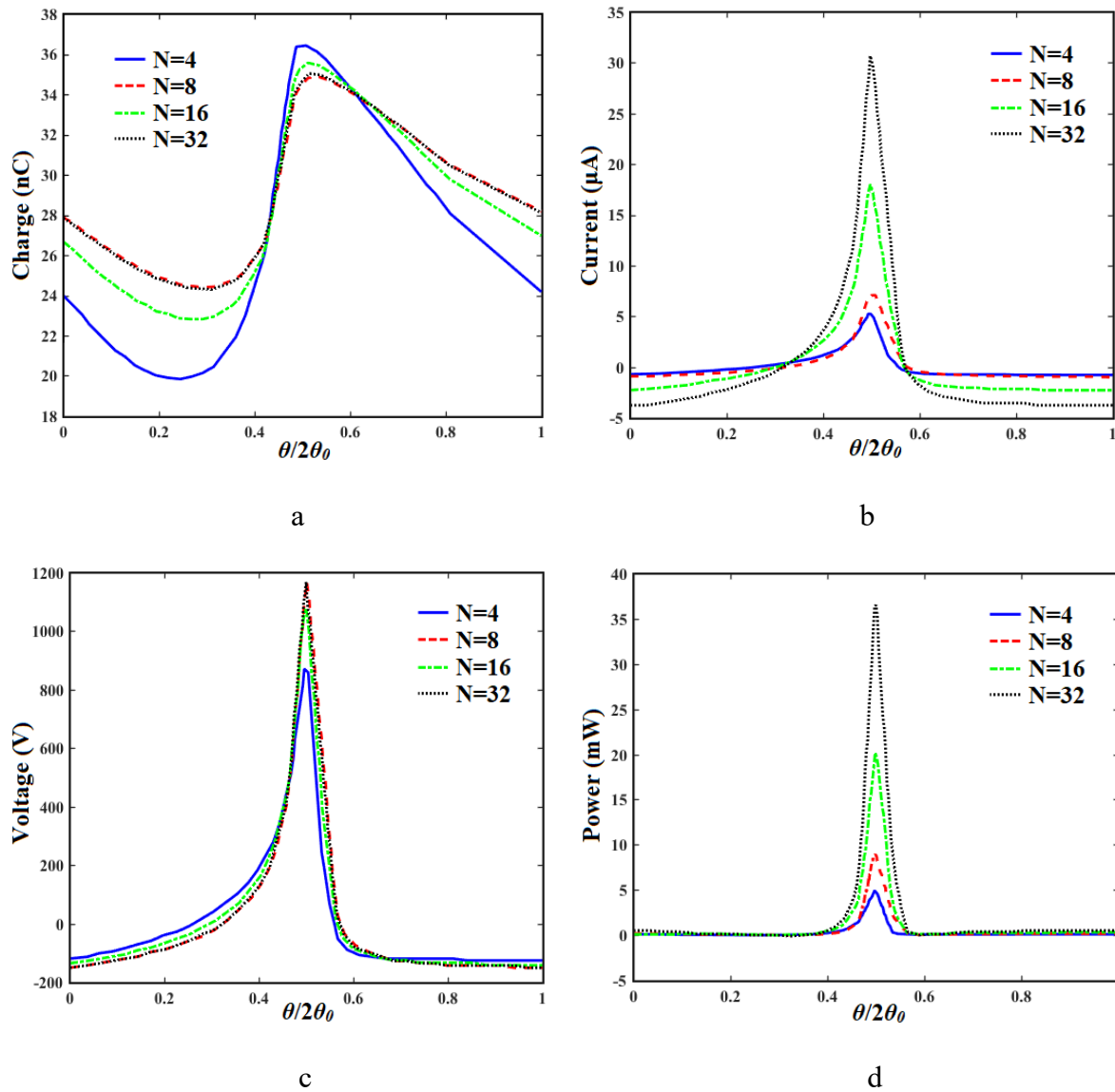


Fig. 5.11: Impacts of the grating number on electrical outputs of rotary NTEGs: (a) charge, (b) current, (c) voltage, and (d) power.

5.4.4 Investigation on the angular velocity

Angular velocity is another important parameter in rotary TENG. In this section, for different values of ω , we aim to determine the load resistance in order to achieve the maximum value

of average power output. The simulation results are summarized in Table 5.3, from which it is evident that load resistance and consequently average power output increase with the increase in PTFE thickness.

Table 5.3: Optimized specification of rotary TENGs for different angular velocity.

Angular velocity (rpm)	Optimum resistor (M Ω)	Average power output (mW)
100	697.87	0.068
400	165.82	0.359
700	87.30	0.565
1000	73.24	0.794

Fig. 5.12 shows the variation of the optimum resistor and the maximized power output for different ω . Similar to the previous, a linear increase is seen in the curve of the average power output while a decreasing behavior can be found in the pattern of the resistor.

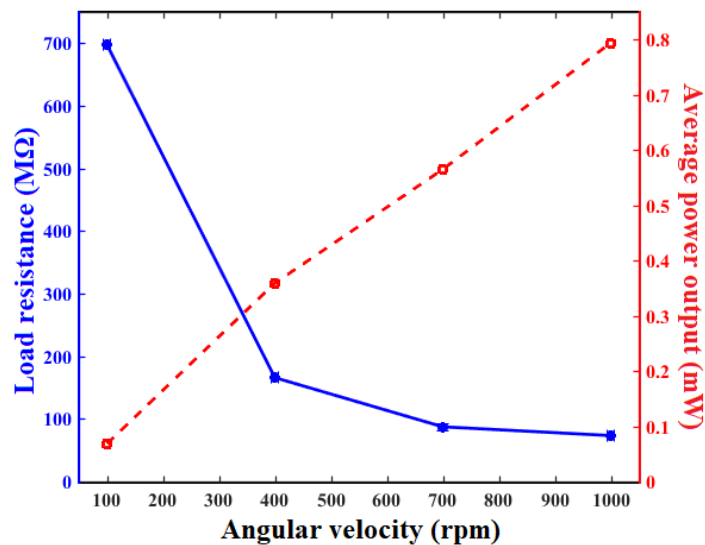


Fig. 5.12: Distribution of the optimized load resistance and average power output with ω .

The responses of rotary TENG with optimized characteristics are plotted in Fig. 5.13. The curve of current demonstrates that its value increases substantially with an increase in angular velocity. The same pattern can be seen in the power output of the TENG. In fact, with the movement of the top dielectric layer on the fixed bottom dielectric, the values of current, voltage, and power begin to increase until the entire separation, at which we have maximum current, voltage, and power. From that moment, the values of the variables decrease.

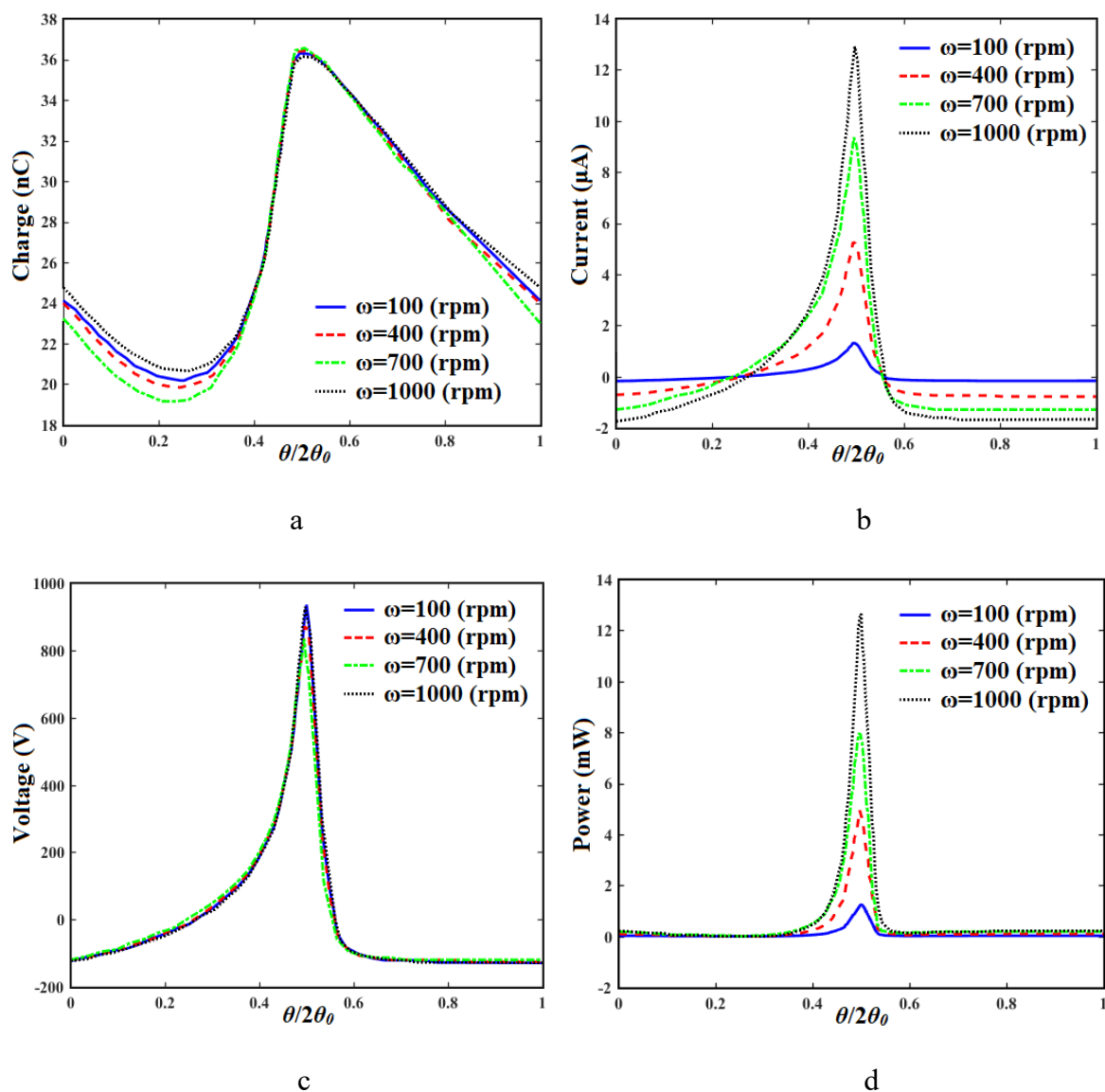


Fig. 5.13: Effects of angular velocity on electrical outputs of rotary TENGs: (a) charge, (b) current, (c) voltage, and (d) power.

5.4.5 Investigation on the tribo-surface spacing

Generally, one of the major issues with TENGs is the durability of the device under working conditions. The triboelectric films and coatings experience some damages when device is used for a long time, as it was observed in the sliding-mode TENGs. To meet this bottlenecking problem, rotary TENGs with non-contact working mechanism was fabricated to guarantee an extended long-life. The triboelectric layers are charged during the initial physical contact. Then, dielectrics are separated and rotations can frequently induce charges on the top and bottom electrodes. In this condition, device presents much more longevity; however, the harvested power drops as the tribo-surface spacing increases (Table 5.4). Meanwhile, the rotary design is capable to undergoes high rotational speeds. In this case, the frequency of the TENGs can considerably be increased, resulting in a sustainable average power output. Finally, the impacts of tribo-spacing on the TENG's output are investigated. Harvested average power output versus different tribo-spacing values is shown in Table 5.4 and its distribution is plotted in Fig. 5.14. As can be seen, for higher values of h , a greater resistor value is necessary to scavenge more power.

Table 5.4: Optimized results for different tribo-spacings.

Tribo Spacing (mm)	Optimal resistor (MΩ)	Average power output (mW)
0	165.82	0.359
0.4	486.45	0.084
0.8	874.56	0.050
1	1047.12	0.042

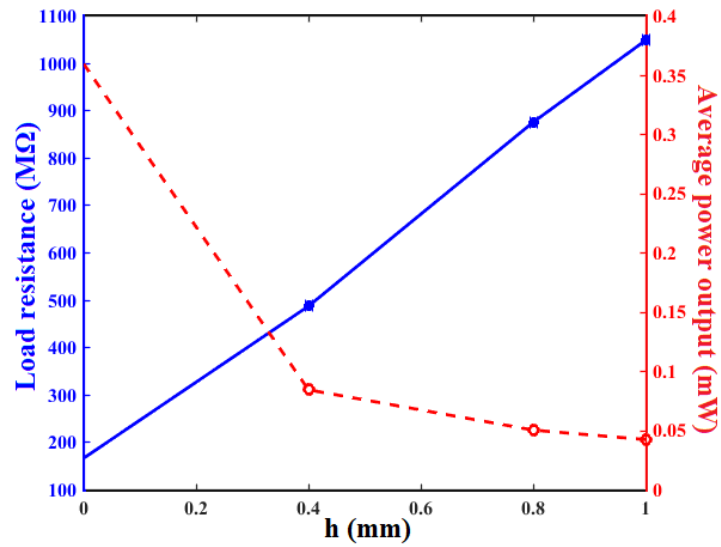


Fig. 5.14: Optimized curves for variation of tribo spacing, h ($r_1=5$ mm, $r_2=50$ mm, $N=4$ and $d_1=d_2=250$ μm).

The optimized curves of charge, current, voltage, and power of TENG are depicted in Fig. 5.15. These figures show that for the contact mode of the TENG, the transferred charge and consequently the current are considerably higher than for the non-contact mode. Similar behavior is evident in the case of power distribution. Although the output power is less in the non-contact mode, its longevity is higher than that of the contact mode, due to the movement without friction.

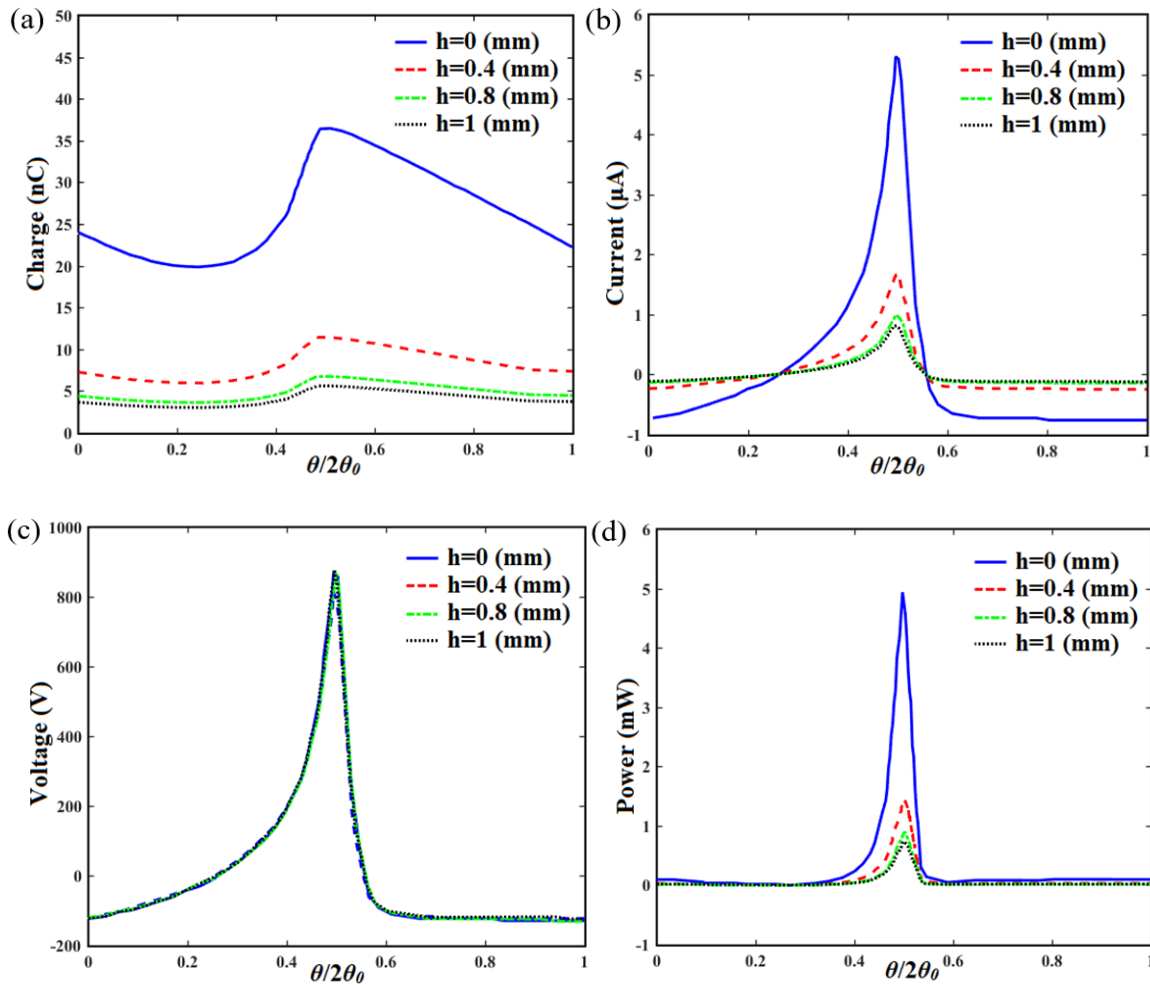


Fig. 5.15: Impacts of tribo spacing of rotary TENGs on (a) charge, (b) current, (c) voltage, and (d) power with geometry parameters of $r_1=5$ mm, $r_2=50$ mm, $N=4$, and $d_1=d_2=250$ μm .

5. Concluding remarks

In this work, the theoretical model and experimental setup of the disk-shaped TENG was investigated. Considering the electric and geometric conditions, the theoretical model was developed, and the dependency of the generated energy on structural parameters was analyzed. The optimal distributions for the charge, voltage, current and harvested energy were plotted. It was found that the harvested energy for optimized rotary TENG can surge to 0.369 mJ in one cycle. The presented paradigm for rotary TENGs can significantly enhance

the applicability of the current TENGs for sustainably renewable energy utilization from the rotating environment.

Conclusion and Future plans

6.1 Conclusion

The aim of this thesis was to develop advanced energy harvesting approaches including piezoelectric and triboelectric based nanogenerators. Since piezoelectrics perfectly respond to the applied pressure and temperature motivations, FGMs piezoelectric shells were introduced to increase the harvested energy. Based on variation of the properties thorough the geometry, the material elements of the media were appropriately functionalized, resulting in a high value of stored energy in the system. An increment of 75% in the stored energy was reported in conjunction with almost 10% reduction in the weight. Comparing with a homogeneous piezoelectric-based energy harvesting system, an inhomogeneous design can deliver 50% more electric potential.

To meet deficiencies of piezoelectric energy harvesters, in particular low-current output and expensive materials, in the next stage, thesis shifted to triboelectric-based energy harvesters. A cost-effective sliding TENG was fabricated. Based on the mathematical modelling and artificial intelligent approaches, a simulation platform was developed, predicting, and optimizing the output power of sliding-mode TENGs under various working conditions. The efficiency of the suggested algorithm was proved by comparing the results with those of the experimental data. A short circuit current and open circuit voltage of $0.9 \mu\text{A}$ and 150 V was observed during the experiment, which was enough to light up a row of LEDs. Thorough sensitivity analysis, the impacts of the thickness of the triboelectric films, contact area and resistor were investigated. It was found that the external load resistance is the dominant design parameter affecting the TENGs output power. Furthermore, as the

thickness of dielectrics increases, the optimum resistor shifts towards the open circuit condition, while shifting towards the short circuit condition in the case of increment of the contact area. The results demonstrated that the proposed sliding-mode TENG can harvest 0.25 mJ at each cycle where the weight is only 42.91 g.

In sliding-mode TENGs, triboelectric films physically touch each other, then the durability is a critical issue. To meet this challenge, application of rotary TENGs in energy scavenging systems was explored. The dielectric layers are physical contacted firstly, then rotate separately. Such a design can extend the longevity of the materials and coatings. In parallel with experimental setup, a theoretical study was presented to predict and optimize the trend of the disk-shaped TENGs. This configuration had capability to be embedded in energy harvesting purposes for blue energy and wind power. An iteration-based optimality system was developed to present high-output rotary TENGs. Simulation results excellently followed that of the experiment. A peak of 0.6 μA and 30 V was obtained for short circuit and open circuit voltage, respectively. Throughout the experimental and theoretical exploration, it was concluded that the power generated by rotary TENGs has been significantly changed by variation of the number of segments, rotational speed, and tribo-surface spacing. Increment of frequency and segments led to increase of harvested power. However, a reversed behaviour was observed in case of tribo-surface spacing. Moreover, sensitivity analysis introduced the tribo-surface spacing as the dominant parameter for rotary TENGs. The optimized characteristics successfully delivered a harvested energy of 0.369 mJ at each cycle.

6.2 Future plans

TENG devices still require more attempts to improve the output power and its adaptability with storage systems. Some suggestions are given in this field.

6.2.1 Improvement in generated current

As discussed in this thesis, in micro/nano scales TENG devices provide relatively higher voltage and current output than other energy harvesting strategies. The output voltage is quite acceptable. However, the generated current is still low because TENGs have a high impedance. One possible solution lies at heart of improving the surface charge density. To enhance the charge density, some ideas were generated including: employing a composite structure for triboelectric film [205, 206], chemically modifying the friction surface [207-209], and bypassing the air breakdown [210, 211]. However, the output current is still low and needs to be enhanced through future studies.

6.2.2 Hybridization of TENGs

Integration of TENGs and energy storage systems is of the great importance for driving portable and wearable electronics. The harvested power is higher than that of each energy scavenging method because of the cooperative operation. A few studies were conducted to show the applicability of the hybridization through coupling electromagnetic-triboelectric nanogenerators [196, 212, 213]. The hybridized nanogenerator sustainably generates power to drive biomechanical and self-powered electronics. This field really needs more studies on the concept, design, materials, and integration techniques, leading to introduce high-output TENGs integrated with high energy storage capability.

6.2.3 Bulk energy generation

Almost 72% of the earth's surface is covered by ocean. The wave energy is the most abundant source of renewable and clean energy, which can potentially revolutionize global energy scheme. Due to low-economic issues, traditional technologies rarely touched this area. Electromagnetic generators dominantly generate electricity from wave energy. However,

heavy magnet, seawater corrosion, and low-efficient turbine are annoying challenges. Some prototypes were reported to scavenge the water wave including enclosed TENGs [214-216], wavy-electrode [217, 218], and spherical design [219, 220]. The fabricated devices successfully drive small electronics. However, for macro scale networks of TENGs are required to harvest blue energy. To meet this idea, some issues should be figured out including connecting TENGs together, transferring the harvested power to land, durability of TENGs to perform in seawater, and so on.

Reference

1. Beeby, S.P., et al., *A micro electromagnetic generator for vibration energy harvesting*. Journal of Micromechanics and Microengineering, 2007. **17**(7): p. 1257-1265.
2. White, N.M., P. Glynne-Jones, and S.P. Beeby, *A novel thick-film piezoelectric micro-generator*. Smart Materials & Structures, 2001. **10**(4): p. 850-852.
3. Roundy, S. and P.K. Wright, *A piezoelectric vibration based generator for wireless electronics*. Smart Materials & Structures, 2004. **13**(5): p. 1131-1142.
4. Liu, H.C., et al., *A MEMS-based piezoelectric cantilever patterned with PZT thin film array for harvesting energy from low frequency vibrations*. International Conference on Optics in Precision Engineering and Nanotechnology (Icopen 2011), 2011. **19**.
5. Kundu, S. and H.B. Nemade, *Modeling and Simulation of a Piezoelectric Vibration Energy Harvester*. International Conference on Vibration Problems 2015, 2016. **144**: p. 568-575.
6. Izadgoshasb, I., et al., *Optimizing orientation of piezoelectric cantilever beam for harvesting energy from human walking*. Energy Conversion and Management, 2018. **161**: p. 66-73.
7. Staaf, L.G.H., et al., *Simulation and experimental demonstration of improved efficiency in coupled piezoelectric cantilevers by extended strain distribution*. Sensors and Actuators a-Physical, 2015. **229**: p. 136-140.
8. Li, W.G., S.Y. He, and S.D. Yu, *Improving Power Density of a Cantilever Piezoelectric Power Harvester Through a Curved L-Shaped Proof Mass*. Ieee Transactions on Industrial Electronics, 2010. **57**(3): p. 868-876.
9. Wang, P.Y.K., et al., *Performance of pre-deformed flexible piezoelectric cantilever in energy harvesting*. Aip Advances, 2016. **6**(5).
10. Dong, K., X. Peng, and Z.L. Wang, *Fiber/Fabric-Based Piezoelectric and Triboelectric Nanogenerators for Flexible/Stretchable and Wearable Electronics and Artificial Intelligence*. Advanced Materials, 2020. **32**(5).
11. J. Kymissis, C.K., J. Paradiso, N. Gershenfeld, *Parasitic Power Harvesting in Shoes, in Digest of Papers, in Second International Symposium on Wearable Computers*. 1998. p. 132–139.
12. Jung, W.S., et al., *Powerful curved piezoelectric generator for wearable applications*. Nano Energy, 2015. **13**: p. 174-181.
13. Turkmen, A.C. and C. Celik, *Energy harvesting with the piezoelectric material integrated shoe*. Energy, 2018. **150**: p. 556-564.
14. Qian, F., T.B. Xu, and L. Zuo, *Design, optimization, modeling and testing of a piezoelectric footwear energy harvester*. Energy Conversion and Management, 2018. **171**: p. 1352-1364.
15. Guido, F., et al., *AlN-based flexible piezoelectric skin for energy harvesting from human motion*. Microelectronic Engineering, 2016. **159**: p. 174-178.
16. Yu, J.B., et al., *Skin-conformal BaTiO₃/ecoflex-based piezoelectric nanogenerator for self-powered human motion monitoring*. Materials Letters, 2020. **269**.
17. Maiti, S., et al., *Bio-waste onion skin as an innovative nature-driven piezoelectric material with high energy conversion efficiency*. Nano Energy, 2017. **42**: p. 282-293.
18. Zhu, M.M., et al., *Highly shape adaptive fiber based electronic skin for sensitive joint motion monitoring and tactile sensing*. Nano Energy, 2020. **69**.
19. Barman, A., *Review on Biocompatibility of ZnO Nano Particles*. Advancements of Medical Electronics, 2015: p. 343-352.
20. Kumar, B. and S.W. Kim, *Energy harvesting based on semiconducting piezoelectric ZnO nanostructures*. Nano Energy, 2012. **1**(3): p. 342-355.
21. Huang, M.H., et al., *Catalytic growth of zinc oxide nanowires by vapor transport*. Advanced Materials, 2001. **13**(2): p. 113-116.
22. Hughes, W.L. and Z.L. Wang, *Formation of piezoelectric single-crystal nanorings and nanobows*. Journal of the American Chemical Society, 2004. **126**(21): p. 6703-6709.
23. Kong, X.Y., et al., *Single-crystal nanorings formed by epitaxial self-coiling of polar nanobelts*. Science, 2004. **303**(5662): p. 1348-1351.

24. Pan, Z.W., Z.R. Dai, and Z.L. Wang, *Nanobelts of semiconducting oxides*. Science, 2001. **291**(5510): p. 1947-1949.
25. Wang, Z.L. and J.H. Song, *Piezoelectric nanogenerators based on zinc oxide nanowire arrays*. Science, 2006. **312**(5771): p. 242-246.
26. Lee, S., et al., *Super-Flexible Nanogenerator for Energy Harvesting from Gentle Wind and as an Active Deformation Sensor*. Advanced Functional Materials, 2013. **23**(19): p. 2445-2449.
27. Hansen, B.J., et al., *Hybrid Nanogenerator for Concurrently Harvesting Biomechanical and Biochemical Energy*. Acs Nano, 2010. **4**(7): p. 3647-3652.
28. Yang, Y., et al., *A hybrid energy cell for self-powered water splitting*. Energy & Environmental Science, 2013. **6**(8): p. 2429-2434.
29. Gu, L., et al., *Flexible Fiber Nanogenerator with 209 V Output Voltage Directly Powers a Light-Emitting Diode*. Nano Letters, 2013. **13**(1): p. 91-94.
30. Jung, J.H., et al., *Lead-Free NaNbO₃ Nanowires for a High Output Piezoelectric Nanogenerator*. Acs Nano, 2011. **5**(12): p. 10041-10046.
31. Kwon, J., et al., *A high performance PZT ribbon-based nanogenerator using graphene transparent electrodes*. Energy & Environmental Science, 2012. **5**(10): p. 8970-8975.
32. Mantini, G., et al., *Equilibrium Piezoelectric Potential Distribution in a Deformed ZnO Nanowire*. Nano Research, 2009. **2**(8): p. 624-629.
33. Ali, F., et al., *Piezoelectric energy harvesters for biomedical applications*. Nano Energy, 2019. **57**: p. 879-902.
34. Dong, L., et al., *In vivo cardiac power generation enabled by an integrated helical piezoelectric pacemaker lead*. Nano Energy, 2019. **66**.
35. Zhang, H., et al., *A flexible and implantable piezoelectric generator harvesting energy from the pulsation of ascending aorta: in vitro and in vivo studies*. Nano Energy, 2015. **12**: p. 296-304.
36. Dagdeviren, C., et al., *Conformal piezoelectric energy harvesting and storage from motions of the heart, lung, and diaphragm*. Proceedings of the National Academy of Sciences of the United States of America, 2014. **111**(5): p. 1927-1932.
37. Ida, N., *Engineering electromagnetics*. 2000, New York: Springer. xvii, 1231 p.
38. Priya, S. and D.J. Inman, *Energy harvesting technologies*. 2009, New York: Springer. xx, 517 p.
39. Williams, C.B., et al., *Development of an electromagnetic micro-generator*. Ieee Proceedings-Circuits Devices and Systems, 2001. **148**(6): p. 337-342.
40. Kulkarni, S., et al., *Design, fabrication and test of integrated micro-scale vibration-based electromagnetic generator*. Sensors and Actuators a-Physical, 2008. **145**: p. 336-342.
41. Donelan, J.M., et al., *Biomechanical energy harvesting: Generating electricity during walking with minimal user effort*. Science, 2008. **319**(5864): p. 807-810.
42. Cepnik, C. and U. Wallrabe, *A flat high performance micro energy harvester based on a serpentine coil with a single winding*, in *Actuators and Microsystems Conference (TRANSDUCERS)*. p. 661-664.
43. Lee, J.H., et al., *Development of an AA size energy transducer with micro resonators*. Proceedings of the 2003 Ieee International Symposium on Circuits and Systems, Vol Iv, 2003: p. 876-879.
44. Halvorsen, E. and S.D. Nguyen, *MEMS Electrostatic Energy Harvesters with Nonlinear Springs*, in *Advances in Energy Harvesting Methods*. 2013, Berlin: Springer.
45. Hoffmann, D., B. Folkmer, and Y. Manoli, *Analysis and characterization of triangular electrode structures for electrostatic energy harvesting*. Journal of Micromechanics and Microengineering, 2011. **21**(10).
46. Tsutsumino, T., et al., *Seismic power generator using high-performance polymer electret*. Mems 2006: 19th Ieee International Conference on Micro Electro Mechanical Systems, Technical Digest, 2006: p. 98-+.

47. Yang, B., et al., *A MEMS rotary comb mechanism for harvesting the kinetic energy of planar vibrations*. Journal of Micromechanics and Microengineering, 2010. **20**(6).
48. Nguyen, S.D. and E. Halvorsen, *Nonlinear Springs for Bandwidth-Tolerant Vibration Energy Harvesting*. Journal of Microelectromechanical Systems, 2011. **20**(6): p. 1225-1227.
49. Davies, D.K., *Charge Generation on Dielectric Surfaces*. Journal of Physics D-Applied Physics, 1969. **2**(11): p. 1533-&.
50. Harper, W.R., *The Volta Effect as a Cause of Static Electrification*. Proceedings of the Royal Society of London Series a-Mathematical and Physical Sciences, 1951. **205**(1080): p. 83-103.
51. Matsusaka, S., et al., *Triboelectric charging of powders: A review*. Chemical Engineering Science, 2010. **65**(22): p. 5781-5807.
52. Murata, Y. and S. Kittaka, *Evidence of Electron-Transfer as the Mechanism of Static Charge Generation by Contact of Polymers with Metals*. Japanese Journal of Applied Physics, 1979. **18**(2): p. 421-421.
53. Diaz, A.F. and R.M. Felix-Navarro, *A semi-quantitative tribo-electric series for polymeric materials: the influence of chemical structure and properties*. Journal of Electrostatics, 2004. **62**(4): p. 277-290.
54. Henniker, J., *Triboelectricity in Polymers*. Nature, 1962. **196**(4853): p. 474-&.
55. Wang, Z.L., *On Maxwell's displacement current for energy and sensors: the origin of nanogenerators*. Materials Today, 2017. **20**(2): p. 74-82.
56. Wang, Z.L., *On the first principle theory of nanogenerators from Maxwell's equations*. Nano Energy, 2020. **68**.
57. Xu, C., et al., *On the Electron-Transfer Mechanism in the Contact-Electrification Effect*. Advanced Materials, 2018. **30**(15).
58. Wang, Z.L., *Triboelectric Nanogenerator (TEG)-Sparking an Energy and Sensor Revolution*. Advanced Energy Materials, 2020. **10**(17).
59. Wang, Z.L. and A.C. Wang, *On the origin of contact-electrification*. Materials Today, 2019. **30**: p. 34-51.
60. Khorsand, M., et al., *Simulation of high-output and lightweight sliding-mode triboelectric nanogenerators*. Nano Energy, 2019. **66**.
61. Niu, S.M., et al., *Theory of Sliding-Mode Triboelectric Nanogenerators*. Advanced Materials, 2013. **25**(43): p. 6184-6193.
62. Niu, S.M., et al., *Theoretical study of contact-mode triboelectric nanogenerators as an effective power source*. Energy & Environmental Science, 2013. **6**(12): p. 3576-3583.
63. Yang, W.Q., et al., *Harvesting Energy from the Natural Vibration of Human Walking*. Acs Nano, 2013. **7**(12): p. 11317-11324.
64. Bai, P., et al., *Integrated Multi layered Triboelectric Nanogenerator for Harvesting Biomechanical Energy from Human Motions*. Acs Nano, 2013. **7**(4): p. 3713-3719.
65. Zurbuchen, A., et al., *Energy Harvesting from the Beating Heart by a Mass Imbalance Oscillation Generator*. Annals of Biomedical Engineering, 2013. **41**(1): p. 131-141.
66. Li, Z., et al., *Muscle-Driven In Vivo Nanogenerator*. Advanced Materials, 2010. **22**(23): p. 2534-2537.
67. Starner, T., *Human-powered wearable computing*. Ibm Systems Journal, 1996. **35**(3-4): p. 618-629.
68. Yu, Y.H., et al., *Biocompatibility and in vivo operation of implantable mesoporous PVDF-based nanogenerators*. Nano Energy, 2016. **27**: p. 275-281.
69. Zheng, Q., et al., *In Vivo Powering of Pacemaker by Breathing-Driven Implanted Triboelectric Nanogenerator*. Advanced Materials, 2014. **26**(33): p. 5851-5856.
70. Ouyang, H., et al., *Symbiotic cardiac pacemaker*. Nature Communications, 2019. **10**.
71. Xie, Y.N., et al., *Rotary Triboelectric Nanogenerator Based on a Hybridized Mechanism for Harvesting Wind Energy*. Acs Nano, 2013. **7**(8): p. 7119-7125.

72. Zhu, G., et al., *Radial-arrayed rotary electrification for high performance triboelectric generator*. Nature Communications, 2014. **5**.
73. Chen, S.W., et al., *Self-powered cleaning of air pollution by wind driven triboelectric nanogenerator*. Nano Energy, 2015. **14**: p. 217-225.
74. Bae, J., et al., *Flutter-driven triboelectrification for harvesting wind energy*. Nature Communications, 2014. **5**.
75. Lin, Z.H., et al., *A multi-layered interdigitative-electrodes-based triboelectric nanogenerator for harvesting hydropower*. Nano Energy, 2015. **15**: p. 256-265.
76. Chen, J., et al., *Networks of Triboelectric Nanogenerators for Harvesting Water Wave Energy: A Potential Approach toward Blue Energy*. Acs Nano, 2015. **9**(3): p. 3324-3331.
77. Liang, Q.J., et al., *Highly transparent triboelectric nanogenerator for harvesting water-related energy reinforced by antireflection coating*. Scientific Reports, 2015. **5**.
78. Lin, Z.H., et al., *Water-Solid Surface Contact Electrification and its Use for Harvesting Liquid-Wave Energy*. Angewandte Chemie-International Edition, 2013. **52**(48): p. 12545-12549.
79. Yang, P.K., et al., *A Flexible, Stretchable and Shape-Adaptive Approach for Versatile Energy Conversion and Self-Powered Biomedical Monitoring*. Advanced Materials, 2015. **27**(25): p. 3817-3824.
80. Seung, W., et al., *Nanopatterned Textile-Based Wearable Triboelectric Nanogenerator*. Acs Nano, 2015. **9**(4): p. 3501-3509.
81. Kim, K.N., et al., *Highly Stretchable 2D Fabrics for Wearable Triboelectric Nanogenerator under Harsh Environments*. Acs Nano, 2015. **9**(6): p. 6394-6400.
82. Wang, Z.L., *Self-powered nanotech*. Sci Am, 2008. **298**(1): p. 82-7.
83. Wang, Z.L., *Self-Powered Nanosensors and Nanosystems*. Advanced Materials, 2012. **24**(2): p. 280-285.
84. Lee, M., et al., *Self-powered environmental sensor system driven by nanogenerators*. Energy & Environmental Science, 2011. **4**(9): p. 3359-3363.
85. Fan, F.R., W. Tang, and Z.L. Wang, *Flexible Nanogenerators for Energy Harvesting and Self-Powered Electronics*. Advanced Materials, 2016. **28**(22): p. 4283-4305.
86. Xu, S., et al., *Self-powered nanowire devices*. Nature Nanotechnology, 2010. **5**(5): p. 366-373.
87. He, Z.Z., et al., *Piezoelectric-Driven Self-Powered Patterned Electrochromic Supercapacitor for Human Motion Energy Harvesting*. Acs Sustainable Chemistry & Engineering, 2019. **7**(1): p. 1745-1752.
88. Yang, W.Q., et al., *Harvesting vibration energy by a triple-cantilever based triboelectric nanogenerator*. Nano Research, 2013. **6**(12): p. 880-886.
89. Yu, A.F., P. Jiang, and Z.L. Wang, *Nanogenerator as self-powered vibration sensor*. Nano Energy, 2012. **1**(3): p. 418-423.
90. Bai, S., et al., *Single crystalline lead zirconate titanate (PZT) nano/micro-wire based self-powered UV sensor*. Nano Energy, 2012. **1**(6): p. 789-795.
91. Lin, L., et al., *Transparent flexible nanogenerator as self-powered sensor for transportation monitoring*. Nano Energy, 2013. **2**(1): p. 75-81.
92. Lee, S., et al., *Flexible hybrid cell for simultaneously harvesting thermal and mechanical energies*. Nano Energy, 2013. **2**(5): p. 817-825.
93. Zhu, G., et al., *Self-Powered, Ultrasensitive, Flexible Tactile Sensors Based on Contact Electrification*. Nano Letters, 2014. **14**(6): p. 3208-3213.
94. Yang, Y., et al., *Human Skin Based Triboelectric Nanogenerators for Harvesting Biomechanical Energy and as Self-Powered Active Tactile Sensor System*. Acs Nano, 2013. **7**(10): p. 9213-9222.
95. Li, Z.L., et al., *beta-cyclodextrin enhanced triboelectrification for self-powered phenol detection and electrochemical degradation*. Energy & Environmental Science, 2015. **8**(3): p. 887-896.

96. Lin, Z.H., et al., *A Self-Powered Triboelectric Nanosensor for Mercury Ion Detection*. *Angewandte Chemie-International Edition*, 2013. **52**(19): p. 5065-5069.
97. Yang, J., et al., *Eardrum-Inspired Active Sensors for Self-Powered Cardiovascular System Characterization and Throat-Attached Anti-Interference Voice Recognition*. *Advanced Materials*, 2015. **27**(8): p. 1316-+.
98. Wu, Y., et al., *A Self-Powered Angle Measurement Sensor Based on Triboelectric Nanogenerator*. *Advanced Functional Materials*, 2015. **25**(14): p. 2166-2174.
99. Foulds, L.R., *Optimization techniques : an introduction*. Undergraduate texts in mathematics. 1981, New York: Springer-Verlag. xi, 502 p.
100. Rao, S.S., *Engineering optimization : theory and practice*. 4th ed. 2009, Hoboken, N.J.: John Wiley & Sons. xix, 813 p.
101. Das, S. and P.N. Suganthan, *Differential Evolution: A Survey of the State-of-the-Art*. *Ieee Transactions on Evolutionary Computation*, 2011. **15**(1): p. 4-31.
102. de Melo, V.V. and G.L.C. Carosio, *Investigating Multi-View Differential Evolution for solving constrained engineering design problems*. *Expert Systems with Applications*, 2013. **40**(9): p. 3370-3377.
103. Zhang, H. and G.P. Rangaiah, *An efficient constraint handling method with integrated differential evolution for numerical and engineering optimization*. *Computers & Chemical Engineering*, 2012. **37**: p. 74-88.
104. Hu, J.F., P. Guo, and K.L. Poh, *Flexible capacity planning for engineering systems based on decision rules and differential evolution*. *Computers & Industrial Engineering*, 2018. **123**: p. 254-262.
105. Babu, B.V. and R. Angira, *Modified differential evolution (MDE) for optimization of non-linear chemical processes*. *Computers & Chemical Engineering*, 2006. **30**(6-7): p. 989-1002.
106. Ronkkonen, J., S. Kukkonen, and K.V. Price, *Real-parameter optimization with Differential Evolution*. 2005 Ieee Congress on Evolutionary Computation, Vols 1-3, Proceedings, 2005: p. 506-513.
107. Langdon, W.B. and R. Poli, *Evolving problems to learn about particle swarm optimizers and other search algorithms*. *Ieee Transactions on Evolutionary Computation*, 2007. **11**(5): p. 561-578.
108. Abu-Mouti, F.S. and M.E. El-Hawary, *Overview of Artificial Bee Colony (ABC) Algorithm and Its Applications*. 2012 Ieee International Systems Conference (Syscon), 2012: p. 590-595.
109. Rao, R.V. and V.J. Savsani, *Mechanical design optimization using advanced optimization techniques*. Springer series in advanced manufacturing. 2012, London ; New York: Springer. xii, 320 p.
110. Mohamed, A.F., M.M. Elarini, and A.M. Othman, *A new technique based on Artificial Bee Colony Algorithm for optimal sizing of stand-alone photovoltaic system*. *J Adv Res*, 2014. **5**(3): p. 397-408.
111. Muthukumar, R. and P. Balamurugan, *A novel power optimized hybrid renewable energy system using neural computing and bee algorithm*. *Automatika*, 2019. **60**(3): p. 332-339.
112. Wu, D.F., F.K. Ren, and W.D. Zhang, *An energy optimal thrust allocation method for the marine dynamic positioning system based on adaptive hybrid artificial bee colony algorithm*. *Ocean Engineering*, 2016. **118**: p. 216-226.
113. ArunKumar, S., B.V. Kumar, and M. Pandi, *Artificial bee colony optimization based energy-efficient wireless network interface selection for industrial mobile devices*. *Computer Communications*, 2020. **154**: p. 1-10.
114. Kalayci, C.B., S. Karagoz, and O. Karakas, *Bee colony intelligence in fatigue life estimation of simulated magnesium alloy welds*. *International Journal of Fatigue*, 2019. **127**: p. 36-44.
115. Chen, J., et al., *Image contrast enhancement using an artificial bee colony algorithm*. *Swarm and Evolutionary Computation*, 2018. **38**: p. 287-294.

116. Ding, M., et al., *Dynamic population artificial bee colony algorithm for multi-objective optimal power flow*. Saudi Journal of Biological Sciences, 2017. **24**(3): p. 703-710.
117. *Proceedings of the International Conference on Computing and Communication Systems*. 2018, New York, NY: Springer Berlin Heidelberg. pages cm.
118. Wang, C.F., K. Liu, and P.P. Shen, *Hybrid Artificial Bee Colony Algorithm and Particle Swarm Search for Global Optimization*. Mathematical Problems in Engineering, 2014. **2014**.
119. Liu, W., *A Multistrategy Optimization Improved Artificial Bee Colony Algorithm*. Scientific World Journal, 2014.
120. Hooker, C.A., *Adaptation in Natural and Artificial Systems - Holland, Jh.* Philosophical Psychology, 1995. **8**(3): p. 287-299.
121. McCall, J., *Genetic algorithms for modelling and optimisation*. Journal of Computational and Applied Mathematics, 2005. **184**(1): p. 205-222.
122. Shu, L.S., et al., *An on-line variable fidelity metamodel assisted Multi-objective Genetic Algorithm for engineering design optimization*. Applied Soft Computing, 2018. **66**: p. 438-448.
123. Fleming, P.J. and C.M. Fonseca, *Genetic Algorithms in Control Systems Engineering*. Automatic Control - World Congress 1993, Vol 2, 1994: p. 605-612.
124. Jo, J.B., Y.Z. Li, and M. Gen, *Nonlinear fixed charge transportation problem by spanning tree-based genetic algorithm*. Computers & Industrial Engineering, 2007. **53**(2): p. 290-298.
125. Ene, S., et al., *A genetic algorithm for minimizing energy consumption in warehouses*. Energy, 2016. **114**: p. 973-980.
126. Deb, K. and D.E. Goldberg, *Analyzing Deception in Trap Functions*. Foundations of Genetic Algorithms 2, 1993: p. 93-108.
127. Davis, L., *Genetic algorithms and simulated annealing*. Research notes in artificial intelligence,. 1987, London
Los Altos, Calif.: Pitman ;
Morgan Kaufmann Publishers. 216 p.
128. Eshelman, L.J., R.A. Caruana, and J.D. Schaffer, *Biases in the Crossover Landscape*. Proceedings of the Third International Conference on Genetic Algorithms, 1989: p. 10-19.
129. Shin, K.G. and P. Ramanathan, *Real-Time Computing - a New Discipline of Computer-Science and Engineering*. Proceedings of the IEEE, 1994. **82**(1): p. 6-24.
130. Kennedy, J. and R. Eberhart, *Particle swarm optimization*. 1995 IEEE International Conference on Neural Networks Proceedings, Vols 1-6, 1995: p. 1942-1948.
131. Kennedy, J.F., R.C. Eberhart, and Y. Shi, *Swarm intelligence*. The Morgan Kaufmann series in evolutionary computation. 2001, San Francisco: Morgan Kaufmann Publishers. xxvii, 512 p.
132. Khorsand, M. and Y.H. Tang, *Design functionally graded rotating disks under thermoelastic loads: Weight optimization*. International Journal of Pressure Vessels and Piping, 2018. **161**: p. 33-40.
133. Kongnam, C. and S. Nuchprayoon, *A particle swarm optimization for wind energy control problem*. Renewable Energy, 2010. **35**(11): p. 2431-2438.
134. Zeng, Z.Q., et al., *Integrating process optimization with energy-efficiency scheduling to save energy for paper mills*. Applied Energy, 2018. **225**: p. 542-558.
135. Kusiak, A., M.Y. Li, and F. Tang, *Modeling and optimization of HVAC energy consumption*. Applied Energy, 2010. **87**(10): p. 3092-3102.
136. Elsied, M., et al., *Optimal economic and environment operation of micro-grid power systems*. Energy Conversion and Management, 2016. **122**: p. 182-194.
137. Renuka, T.K., P. Reji, and S. Sreedharan, *An enhanced particle swarm optimization algorithm for improving the renewable energy penetration and small signal stability in power system*. Renewables: Wind, Water, and Solar, 2018. **5**.

138. Song, M.P. and G.C. Gu, *Research on particle swarm optimization: A review*. Proceedings of the 2004 International Conference on Machine Learning and Cybernetics, Vols 1-7, 2004: p. 2236-2241.
139. Wang, D.S., D.P. Tan, and L. Liu, *Particle swarm optimization algorithm: an overview*. Soft Computing, 2018. **22**(2): p. 387-408.
140. Mirjalili, S., S.M. Mirjalili, and A. Lewis, *Grey Wolf Optimizer*. Advances in Engineering Software, 2014. **69**: p. 46-61.
141. Shilaja, C. and T. Arunprasath, *Internet of medical things-load optimization of power flow based on hybrid enhanced grey wolf optimization and dragonfly algorithm*. Future Generation Computer Systems-the International Journal of Escience, 2019. **98**: p. 319-330.
142. Lara-Montano, O.D. and F.I. Gomez-Castro, *Optimization of a shell-and-tube heat exchanger using the grey wolf algorithm*. 29th European Symposium on Computer Aided Process Engineering, Pt A, 2019. **46**: p. 571-576.
143. Miao, D. and S. Hossain, *Improved gray wolf optimization algorithm for solving placement and sizing of electrical energy storage system in micro-grids*. ISA Trans, 2020. **102**: p. 376-387.
144. Yahiaoui, A., et al., *Grey wolf optimizer for optimal design of hybrid renewable energy system PV-Diesel Generator-Battery: Application to the case of Djanet city of Algeria*. Solar Energy, 2017. **158**: p. 941-951.
145. Golcuk, I. and F.B. Ozsoydan, *Evolutionary and adaptive inheritance enhanced Grey Wolf Optimization algorithm for binary domains*. Knowledge-Based Systems, 2020. **194**.
146. Manshahia, M.S., *Grey Wolf Algorithm based Energy-Efficient Data Transmission in Internet of Things*. 10th Int Conf on Emerging Ubiquitous Syst and Pervas Networks (Euspn-2019) / the 9th Int Conf on Current and Future Trends of Informat and Commun Technologies in Healthcare (Icth-2019) / Affiliated Workops, 2019. **160**: p. 604-609.
147. Qu, C.Z., et al., *A novel hybrid grey wolf optimizer algorithm for unmanned aerial vehicle (UAV) path planning*. Knowledge-Based Systems, 2020. **194**.
148. Gupta, A. and M. Talha, *Recent development in modeling and analysis of functionally graded materials and structures*. Progress in Aerospace Sciences, 2015. **79**: p. 1-14.
149. Mahamood, R.M., M. Shukla, and S. Pityana, *Functionally Graded Material: An Overview*, in *Proceedings of the World Congress on Engineering*. 2012 London, U.K.
150. Fakruddinali, J.Y. and K.S. Badarinarayan, *A survey on aluminum matrix composites*. Indian Journal of Scientific Research & Technology, 2015. **3**: p. 34-42.
151. Kokanee, A.A., *Review on functionally graded materials and various theories*. International Research Journal of Engineering and Technology, 2017. **4**: p. 890-893.
152. Maimunnisa, S., et al., *Role of Centrifugal Casting on Electrochemical Corrosion Behavior of A356-SiCp Composite in 3.5 wt.% NaCl*. Journal of Materials Engineering and Performance, 2018. **27**(8): p. 4210-4224.
153. Petit, C., L. Montanaro, and P. Palmero, *Functionally graded ceramics for biomedical application: Concept, manufacturing, and properties*. International Journal of Applied Ceramic Technology, 2018. **15**(4): p. 820-840.
154. Udupa, G., S.S. Rao, and K.V. Gangadharan, *Functionally graded Composite materials: An overview*. International Conference on Advances in Manufacturing and Materials Engineering (Icamme 2014), 2014. **5**: p. 1291-1299.
155. Tiersten, H.F., *Linear piezoelectric plate vibrations*. 1969, New York: Plenum Press.
156. Alibeigloo, A., *Thermo elasticity solution of functionally graded, solid, circular, and annular plates integrated with piezoelectric layers using the differential quadrature method*. Mechanics of Advanced Materials and Structures, 2018. **25**(9): p. 766-784.
157. Jafari, A.A., A.A. Jandaghian, and R. O., *Transient bending analysis of a functionally graded circular plate with integrated surface piezoelectric layers*. International Journal of Mechanical and Materials Engineering, 2014. **9**: p. 1-14

158. Dai, H.L., T. Dai, and S.K. Cheng, *Transient Response Analysis for a Circular Sandwich Plate with an Fgm Central Disk*. Journal of Mechanics, 2015. **31**(4): p. 417-426.
159. Chau, K.T. and X.X. Wei, *Spherically isotropic, elastic spheres subject to diametral point load strength test*. International Journal of Solids and Structures, 1999. **36**(29): p. 4473-4496.
160. Love, A.E.H., *A Treatise on the Mathematical Theory of Elasticity*. 1944, New York: Dover.
161. Sadd, M., *Elasticity: Theory, applications, and numerics*. 2014, New York: Academic Press.
162. Timoshenko, S., *Theory of plates and shells*. 1989: McGRAW-HILL.
163. Incropera, F.P., et al., *Fundamentals of Heat and Mass Transfer*. 2007, New York: Wiley.
164. Saviz, M.R. and M. Mohammadpourfard, *Dynamic analysis of a laminated cylindrical shell with piezoelectric layers under dynamic loads*. Finite Elements in Analysis and Design, 2010. **46**(9): p. 770-781.
165. Quan, J.R. and C.T. Chang, *New Insights in Solving Distributed System Equations by the Quadrature Method .2. Numerical Experiments*. Computers & Chemical Engineering, 1989. **13**(9): p. 1017-1024.
166. Quan, J.R. and C.T. Chang, *New Insights in Solving Distributed System Equations by the Quadrature Method .1. Analysis*. Computers & Chemical Engineering, 1989. **13**(7): p. 779-788.
167. Shu, C., *Differential quadrature and its application in engineering*. 2000: Springer-Verlag.
168. Shu, C. and B.E. Richards, *Application of Generalized Differential Quadrature to Solve 2-Dimensional Incompressible Navier-Stokes Equations*. International Journal for Numerical Methods in Fluids, 1992. **15**(7): p. 791-798.
169. Wang, F.Z., X.B. Liao, and X. Xie, *Characteristics of the Differential Quadrature Method and Its Improvement*. Mathematical Problems in Engineering, 2015.
170. Wu, X.H. and Y.E. Ren, *Differential quadrature method based on the highest derivative and its applications*. Journal of Computational and Applied Mathematics, 2007. **205**(1): p. 239-250.
171. Eslami, M.R., M.H. Babaei, and R. Poultangari, *Thermal and mechanical stresses in a functionally graded thick sphere*. International Journal of Pressure Vessels and Piping, 2005. **82**(7): p. 522-527.
172. Peng, X.L. and X.F. Li, *Thermoelastic analysis of a cylindrical vessel of functionally graded materials*. International Journal of Pressure Vessels and Piping, 2010. **87**(5): p. 203-210.
173. Alibeigloo, A., *Thermoelastic solution for static deformations of functionally graded cylindrical shell bonded to thin piezoelectric layers*. Composite Structures, 2011. **93**(2): p. 961-972.
174. Chen, W.Q., et al., *3D free vibration analysis of a functionally graded piezoelectric hollow cylinder filled with compressible fluid*. International Journal of Solids and Structures, 2004. **41**(3-4): p. 947-964.
175. Yang, W.D., et al., *Nonlinear delamination buckling and expansion of functionally graded laminated piezoelectric composite shells*. International Journal of Solids and Structures, 2014. **51**(3-4): p. 894-903.
176. Wu, C.P. and T.C. Tsai, *Exact solutions of functionally graded piezoelectric material sandwich cylinders by a modified Pagano method*. Applied Mathematical Modelling, 2012. **36**(5): p. 1910-1930.
177. Sodano, H.A., G. Park, and D.J. Inman, *Estimation of electric charge output for piezoelectric energy harvesting*. Strain, 2004. **40**(2): p. 49-58.
178. Coello, C.A.C., *Use of a self-adaptive penalty approach for engineering optimization problems*. Computers in Industry, 2000. **41**(2): p. 113-127.
179. Michalewicz, Z. and N. Attia, *Evolutionary optimization of constrained problems, in Proceedings of the third Annual Conference on Evolutionary Programming*. 1994. p. 98-108.

180. He, Q. and L. Wang, *An effective co-evolutionary particle swarm optimization for constrained engineering design problems*. Engineering Applications of Artificial Intelligence, 2007. **20**(1): p. 89-99.
181. Richardson, J.T., et al., *Some Guidelines for Genetic Algorithms with Penalty-Functions*. Proceedings of the Third International Conference on Genetic Algorithms, 1989: p. 191-197.
182. Li, X.F., X.L. Peng, and K.Y. Lee, *Radially polarized functionally graded piezoelectric hollow cylinders as sensors and actuators*. European Journal of Mechanics a-Solids, 2010. **29**(4): p. 704-713.
183. Feynman, R.P., R.B. Leighton, and M. Sands, *The Feynman lectures on physics, Mainly electromagnetism and matter*. 1979: Addison-Wesley.
184. Wang, Z.L., *Triboelectric Nanogenerators as New Energy Technology for Self-Powered Systems and as Active Mechanical and Chemical Sensors*. Acs Nano, 2013. **7**(11): p. 9533-9557.
185. Wang, Z.L., J. Chen, and L. Lin, *Progress in triboelectric nanogenerators as a new energy technology and self-powered sensors*. Energy & Environmental Science, 2015. **8**(8): p. 2250-2282.
186. Lee, K.Y., et al., *Hydrophobic Sponge Structure-Based Triboelectric Nanogenerator*. Advanced Materials, 2014. **26**(29): p. 5037-5042.
187. Mule, A.R., et al., *Humidity Sustained Wearable Pouch-Type Triboelectric Nanogenerator for Harvesting Mechanical Energy from Human Activities*. Advanced Functional Materials, 2019. **29**(17).
188. Nguyen, V. and R.S. Yang, *Effect of humidity and pressure on the triboelectric nanogenerator*. Nano Energy, 2013. **2**(5): p. 604-608.
189. Wen, R.M., et al., *Humidity-Resistive Triboelectric Nanogenerator Fabricated Using Metal Organic Framework Composite*. Advanced Functional Materials, 2019. **29**(20).
190. La, M., et al., *Development of the Triboelectric Nanogenerator Using a Metal-to-Metal Imprinting Process for Improved Electrical Output*. Micromachines, 2018. **9**(11).
191. Li, L.X., et al., *Triboelectric performances of self-powered, ultra-flexible and large-area poly(dimethylsiloxane)/Ag-coated chinlon composites with a sandpaper-assisted surface microstructure*. Journal of Materials Science, 2019. **54**(10): p. 7823-7833.
192. Lin, L., et al., *Robust Triboelectric Nanogenerator Based on Rolling Electrification and Electrostatic Induction at an Instantaneous Energy Conversion Efficiency of similar to 55%*. Acs Nano, 2015. **9**(1): p. 922-930.
193. Song, J., et al., *Ultra-Flexible and Large-Area Textile-Based Triboelectric Nanogenerators with a Sandpaper-Induced Surface Microstructure*. Materials, 2018. **11**(11).
194. Niu, S.M., et al., *A theoretical study of grating structured triboelectric nanogenerators*. Energy & Environmental Science, 2014. **7**(7): p. 2339-2349.
195. Khorsand, M. and Y.H. Tang, *Durable pyroelectric shell structures for energy scavenging applications*. Acta Mechanica, 2020. **231**(1): p. 205-220.
196. Zhong, X.D., et al., *Rotating-disk-based hybridized electromagnetic-triboelectric nanogenerator for scavenging biomechanical energy as a mobile power source*. Nano Energy, 2015. **13**: p. 771-780.
197. Jiang, T., et al., *Theoretical study on rotary-sliding disk triboelectric nanogenerators in contact and non-contact modes*. Nano Research, 2016. **9**(4): p. 1057-1070.
198. Dharmasena, R.D.I.G., et al., *A unified theoretical model for Triboelectric Nanogenerators*. Nano Energy, 2018. **48**: p. 391-400.
199. Liu, F., et al., *Electrical analysis of triboelectric nanogenerator for high voltage applications exemplified by DBD microplasma*. Nano Energy, 2019. **56**: p. 482-493.
200. Xia, X., J.J. Fu, and Y.L. Zi, *A universal standardized method for output capability assessment of nanogenerators*. Nature Communications, 2019. **10**.

201. Yang, B., et al., *A Fully Verified Theoretical Analysis of Contact-Mode Triboelectric Nanogenerators as a Wearable Power Source*. *Advanced Energy Materials*, 2016. **6**(16).
202. Zhang, L.B., et al., *Galloping triboelectric nanogenerator for energy harvesting under low wind speed*. *Nano Energy*, 2020. **70**.
203. Niu, S.M., et al., *Theory of freestanding triboelectric-layer-based nanogenerators*. *Nano Energy*, 2015. **12**: p. 760-774.
204. Niu, S.M., et al., *Theoretical Investigation and Structural Optimization of Single-Electrode Triboelectric Nanogenerators*. *Advanced Functional Materials*, 2014. **24**(22): p. 3332-3340.
205. Cui, N.Y., et al., *Dynamic Behavior of the Triboelectric Charges and Structural Optimization of the Friction Layer for a Triboelectric Nanogenerator*. *Acs Nano*, 2016. **10**(6): p. 6131-6138.
206. Lai, M.H., et al., *Enhancing the Output Charge Density of TENG via Building Longitudinal Paths of Electrostatic Charges in the Contacting Layers*. *Acs Applied Materials & Interfaces*, 2018. **10**(2): p. 2158-2165.
207. Li, H.Y., et al., *Significant Enhancement of Triboelectric Charge Density by Fluorinated Surface Modification in Nanoscale for Converting Mechanical Energy*. *Advanced Functional Materials*, 2015. **25**(35): p. 5691-5697.
208. Wang, S.H., et al., *Molecular surface functionalization to enhance the power output of triboelectric nanogenerators*. *Journal of Materials Chemistry A*, 2016. **4**(10): p. 3728-3734.
209. Yu, Y.H. and X.D. Wang, *Chemical modification of polymer surfaces for advanced triboelectric nanogenerator development*. *Extreme Mechanics Letters*, 2016. **9**: p. 514-530.
210. Cheng, L., et al., *A self-improving triboelectric nanogenerator with improved charge density and increased charge accumulation speed*. *Nature Communications*, 2018. **9**.
211. Wang, J., et al., *Achieving ultrahigh triboelectric charge density for efficient energy harvesting*. *Nature Communications*, 2017. **8**.
212. Chen, B., Y. Yang, and Z.L. Wang, *Scavenging Wind Energy by Triboelectric Nanogenerators*. *Advanced Energy Materials*, 2018. **8**(10).
213. Quan, T., et al., *Hybridized Electromagnetic-Triboelectric Nanogenerator for a Self-Powered Electronic Watch*. *Acs Nano*, 2015. **9**(12): p. 12301-12310.
214. Guo, H.Y., et al., *A Water-Proof Triboelectric-Electromagnetic Hybrid Generator for Energy Harvesting in Harsh Environments*. *Advanced Energy Materials*, 2016. **6**(6).
215. Xi, Y., et al., *Multifunctional TENG for Blue Energy Scavenging and Self-Powered Wind-Speed Sensor*. *Advanced Energy Materials*, 2017. **7**(12).
216. Xu, L., et al., *Raman-shifted wavelength-selectable pulsed fiber laser with high repetition rate and high pulse energy in the visible*. *Optics Express*, 2017. **25**(1): p. 351-356.
217. Jiang, T., et al., *Structural Optimization of Triboelectric Nanogenerator for Harvesting Water Wave Energy*. *Acs Nano*, 2015. **9**(12): p. 12562-12572.
218. Yao, Y.Y., et al., *Charging System Optimization of Triboelectric Nanogenerator for Water Wave Energy Harvesting and Storage*. *Acs Applied Materials & Interfaces*, 2016. **8**(33): p. 21398-21406.
219. Su, Y.J., et al., *Fully Enclosed Cylindrical Single-Electrode-Based Triboelectric Nanogenerator*. *Acs Applied Materials & Interfaces*, 2014. **6**(1): p. 553-559.
220. Wang, X.F., et al., *Triboelectric Nanogenerator Based on Fully Enclosed Rolling Spherical Structure for Harvesting Low-Frequency Water Wave Energy*. *Advanced Energy Materials*, 2015. **5**(24).